MATERIALI IN TEHNOLOGIJE

MATERIALS AND TECHNOLOGY

6

MATER. TEHNOL.
LETNIK VOLUME 51
ŠTEV. NO. 6
STR. P. 881-1069
LJUBLJANA SLOVENIJA
NOV.-DEC. 2017

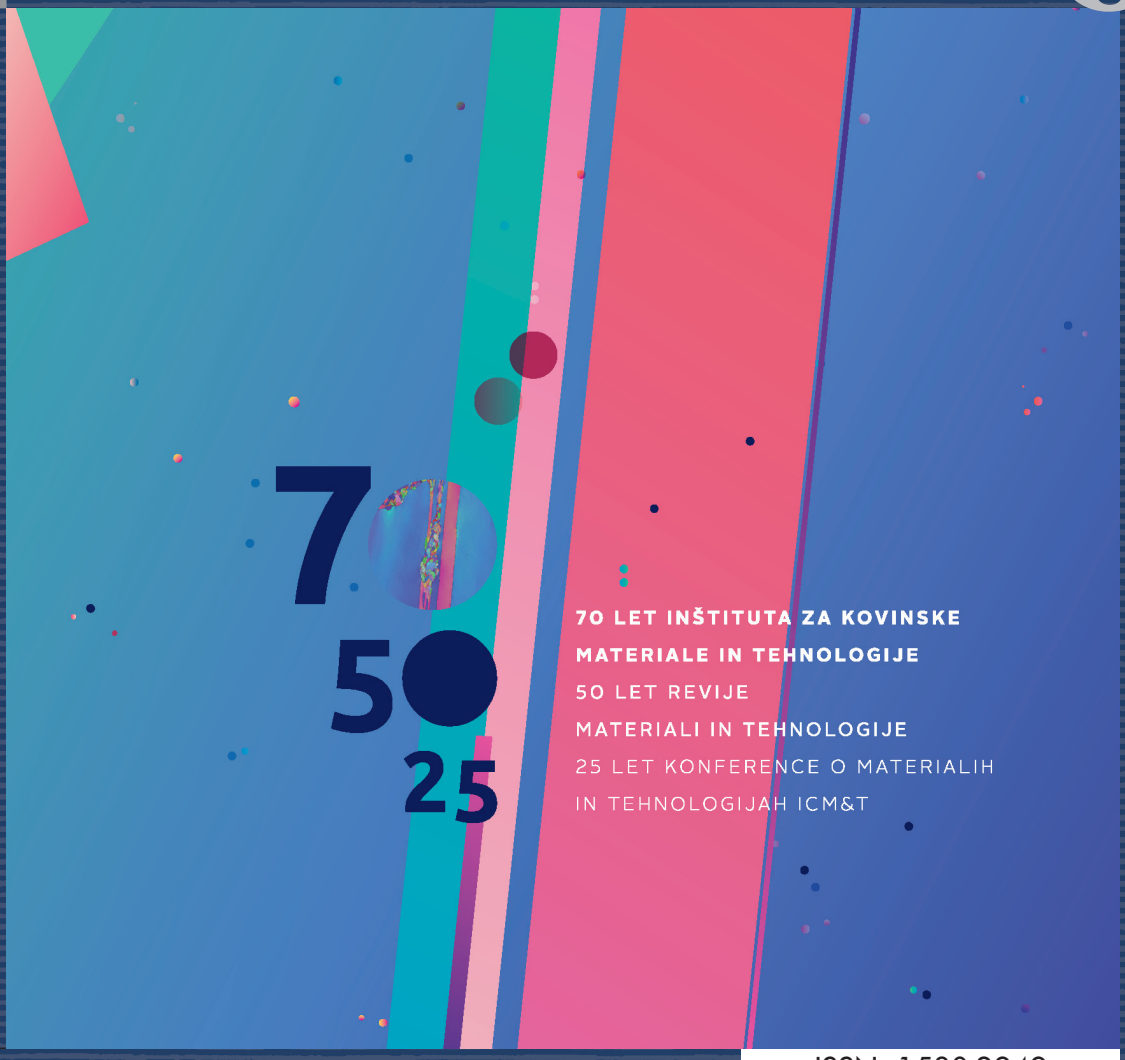

ISSN: 1580-2949
UDK: 669+666+678+53

MATERIALI IN TEHNOLOGIJE
MATERIALS AND TECHNOLOGY

6

MATER. TEHNOL. | LETNIK VOLUME 51 | ŠTEV. NO. 6 | STR. P. 881-1069 | LJUBLJANA SLOVENIJA | NOV.-DEC. 2017

MATERIALI IN TEHNOLOGIJE / MATERIALS AND TECHNOLOGY *so znanstvena serijska publikacija, ki objavlja izvirne in tudi pregledne znanstvene članke ter tehnične novice, ki obravnavajo teoretična in praktična vprašanja naravoslovnih ved in tehnologije na področjih kovinskih in anorganskih materialov, polimerov, vakuumske tehnike in v zadnjem času tudi nanomaterialov.*

The journal MATERIALI IN TEHNOLOGIJE / MATERIALS AND TECHNOLOGY *is a scientific journal, devoted to original scientific papers, reviewed scientific papers and technical news concerned with the areas of fundamental and applied science and technology. Topics of particular interest include metallic materials, inorganic materials, polymers, vacuum technique and lately nanomaterials.*

Izdajatelj (Published for):
Inštitut za kovinske materiale in tehnologije Ljubljana (IMT)

Soizdajatelji (Associated Publishers):
IMPOL Slovenska Bistrica, METAL Ravne, TALUM Kidričevo

Izdajanje **MATERIALI IN TEHNOLOGIJE** sofinancira: Javna agencija za raziskovalno dejavnost Republike Slovenije (ARRS)
(Journal **MATERIALS AND TECHNOLOGY** is financially supported by Slovenian Research Agency (ARRS))

Članki revije Materiali in tehnologije so indeksirani v/Articles published in Materials and Technology are indexed in: SCIENCE CITATION INDEX EXPANDED, MATERIALS SCIENCE CITATION INDEX® AND JOURNAL CITATION REPORTS/ SCIENCE EDITION.
Po bazi podatkov JCR16 ima Materiali in Tehnologije dejavnik vpliva 0,436. / In JCR16 Database Mater. Tehnol. has an impact factor of 0.436.

Članki objavljeni v periodični publikaciji MATERIALI IN TEHNOLOGIJE so indeksirani v mednarodnih sekundarnih virih: (Articles published in journal are indexed in international secondary periodicals and databases):
- DOAJ (Directory of Open Access Journals)
- Google Scholar
- SCIRUS
- CA SEARCH® – Chemical Abstracts®
- METADEX®
- TEME – Technology and management
- Inside Conferences
- Engineered Materials Abstracts®
- Aluminium Industry Abstracts
- SCOPUS
- Civil Engineering Abstracts
- Ceramic Abstracts/World Ceramic Abstracts
- Corrosion Abstracts
- Mechanical & Transportation Engineering Abstracts
- CSA Aerospace & High Technology Database
- Solid State and Superconductivity Abstracts
- Materials Business File
- Referativnyj žurnal: Metallurgija
- COBIB

Izhajanje: 6 številk letno / **Published:** 6 issues per year
Naročnina / Subscription: 42 EUR – **tujina / abroad:** 85 EUR

Naslov uredništva (Editorial Address):
MATERIALI IN TEHNOLOGIJE
IMT Ljubljana
Lepi pot 11
1000 Ljubljana, Slovenija
Telefon: +386 1 470 18 60
Telefax: +386 1 470 19 39
Podračun pri UJP št. 01100-6030344339

Na INTERNET-u je revija MATERIALI IN TEHNOLOGIJE dosegljiva na naslovu (ELECTRONIC ACCESS): http://mit.imt.si

Elektronska pošta (E-mail): mit@imt.si

Oblikovanje ovitka (Design): Ignac Kofol
Oblikovanje plakata na naslovnici (Poster on the Cover): Ajda Schmidt
Računalniški prelom in tisk (Prepress and Printed by):
NONPAREL grafične storitve d.o.o., Škofja Loka
Naklada (Circulation): 400 izvodov/issues

ISSN: 1580-2949
UDK: 669+666+678+53

ISSN 1580-2949
UDK 669+666+678+53 MTAEC9, 51(6)881–1069(2017)

MATER. TEHNOL.	LETNIK VOLUME 51	ŠTEV. NO. 6	STR. P. 881–1069	LJUBLJANA SLOVENIJA	NOV. – DEC. 2017

VSEBINA – CONTENTS

IZVIRNI ZNANSTVENI ČLANKI – ORIGINAL SCIENTIFIC ARTICLES

UDK 620.172.2:621.3.015:519.7
Original scientific article/Izvirni znanstveni članek

ISSN 1580-2949
MTAEC9, 51(6)883(2017)

INCREASING THE TENSILE STRENGTH AND ELONGATION OF 16MnCrS5 STEEL USING GENETIC PROGRAMMING

POVEČEVANJE NAPETOSTNE TRDNOSTI IN RAZTEZKA 16MnCrS5 JEKLA Z UPORABO GENETSKEGA PROGRAMIRANJA

Miha Kovačič[1,2], Ana Turnšek[1], Darja Ocvirk[1], Gašper Gantar[3]

[1]Štore Steel d.o.o., Železarska cesta 3, 3220 Štore, Slovenia
[2]Institute of Metals and Technology, Lepi pot 11, 1000 Ljubljana, Slovenia
[3]College of industrial Engineering, Mariborska cesta 2, 3000 Celje, Slovenia
miha.kovacic@store-steel.si

Prejem rokopisa – received: 2016-09-29; sprejem za objavo – accepted for publication: 2017-05-05

doi:10.17222/mit.2016.293

Štore Steel Ltd. is one of the largest spring-steel producers in Europe. Štore Steel makes more than 1400 steel grades of different chemical composition. Among them is 16MnCrS5 steel. It is generally used for the fabrication of case-hardened machine parts for various applications (e.g., bars, rods, plates, strips, forgings), where a combination of wear resistance, toughness and dynamic strength is essential. These properties can be easily correlated with tensile strength, which depends on the chemical composition and heat treatment after rolling. In addition, the elongation should be taken into account. In the paper, modeling of tensile strength and elongation with genetic programming is presented and compared with linear regression modeling. The chemical composition data (content of C, Mn, S and Cr) and the heat-treatment regime data (GKZ or BG annealing) were used for modeling. The modeling results show that a higher tensile strength with improved elongation were achieved.

Keywords: 16MnCrS5, tensile strength, elongation, modeling, genetic programming, linear regression

Štore Steel je največji proizvajalec vzmetnega jekla v Evropi. Štore Steel izdeluje več kot 1400 različnih kvalitet jekla z različnimi kemijskimi sestavami. Med njmi tudi 16MnCrS5, ki spada v skupino jekel za cementacijo, ki so namenjena za strojno obdelavo različnih delov (npr. palic, plošč, trakov, odkovkov), kjer se zahteva kombinacija obrabne odpornosti, žilavosti ter trajnonihajne trdnosti. Le-te lastnosti lahko povezujemo z natezno trdnostjo, ki je odvisna predvsem od kemične sestave in toplotne obdelave po valjanju. Prav tako je pomemben raztezek. V članku je predstavljeno modeliranje natezne trdnosti in raztezka s pomočjo genetskega modeliranja in linearne regresije. Za modeliranje smo uporabili vsebnosti kemijskih elementov (C, Mn, S in Cr) ter način toplotne obdelave (GKZ ali BG). Glede na rezultate smo povečali natezno trdnost pri izboljšanem raztezku.

Ključne besede: 16MnCrS5, natezna trdnost, raztezek, modeliranje, genetsko programiranje, linearna regresija

1 INTRODUCTION

In the modern steel-production and steel-consumption industry, it is essential to know the material properties and behavior. There are several well-known commercial types of software available for modeling material properties but steel producers are often forced on using inventive experiments, methods and approaches due to their unique production, equipment, time constraints and niche applications.[1–6]

The literature review reveals that tensile strength and elongation optimization of steel products in general incorporates multi-criteria optimization approaches,[1,2,7–9] based also on artificial intelligence methods.[10–14]This is the case for rated material properties in both quantitative and qualitative terms.[1,10]

The required tensile strength and elongation are obtained by changing:

- chemical composition,[2,12,14]
- plastic deformation parameters (i.e., influencing microstructure, grain size),[8,15–17]
- heat-treatment parameters after plastic deformation.[2,7,14]

The article presents the practical implementation of tensile strength and elongation optimization for long-rolled products made of 16MnCrS5 steel, which is generally used for the fabrication of case-hardened machine parts for several applications (e.g., bars, rods, plates, strips, forgings).

First, we provide the experimental background, then the methods used, and, lastly, we present the practical implementation and draw conclusions.

2 EXPERIMENTAL BACKGROUND

In general, production starts with scrap melting in an electro arc furnace (EAF).[18] After the scrap and carburizing agents have been melted, dephosphorization is conducted. The melting bath is heated up to the tapping temperature and, after secondary steel treatment, is discharged into the casting ladle.

After discharging from EAF, the melting bath is deoxidated, desulphurized, the nonmetallic inclusions

are filtered out, the slag metallic oxides are reduced, the hydrogen and nitrogen are partly degassed, the melting bath and temperature field are homogenized, and then the formed slag exchange and the major alloying are carried out. The melt is poured from the casting ladle into the tundish on the continuous casting device, where 180 mm square billets from 2 m to 4 m in length are cast. All billets are cooled before the rolling operation.

The billets are heated, in accordance with the prescribed temperatures, in the continuous heating furnace. After heating, the billets are hot rolled on the rolling stands. Depending on the various shapes and dimensions of the grooves, cylindrical, square or flat steel bars can be produced. Steel bars are cooled on the cooling bed. After cooling they are cut into different lengths using hot shears. During cutting, the samples for examination of the material are taken (e.g., tensile strength, hardenability, micro-cleanliness).

After cooling, the bars can be additionally heat treated in accordance with the customers' orders.

In Štore Steel there are 7 different quality prescriptions (chemical compositions) for 16MnCrS5.[19] Only the most representative one (**Table 1**) was used in the research. From October 2008 to February 2016, 70 consecutively cast batches (orders) with diameters from 20 mm to 55 mm were produced. In all cases the data on tensile strength and elongation is available. For some orders the bars were also heat treated:

- GKZ (Glühen auf kugeligen Zementit) – spheroidization annealing or
- BG annealing – isothermal annealing (for excellent machinability properties and a better micro-structure homogenizing).
- The heat treatment is conducted using the tunnel heat-treatment furnace.[3]

Table 1: Chemical composition in mass fractions (*w*/%) of the most representative quality prescription (17) for 16MnCrS5

	C	Mn	Cr	S	Mo	Ni
Minimum	0.14	1.00	0.8	0.020		
Maximum	0.19	1.30	1.1	0.040	0.08	0.30

During the microstructure examination, also the pearlite content and percentage of spheroidization (after GKZ annealing) were assessed. The micro-cleanliness (*K*3) was determined according to DIN 50602, method K. All the metallurgical examinations and tensile testing were conducted by the head of the metallurgical laboratory and by the person responsible for mechanical testing. The collected data is presented in **Table 2**. In the same table, besides quantitative (i.e., chemical composition, content of pearlite, percentage of spheroidization and micro-cleanliness), also the qualitative parameter is included (heat treatment), where the prediction of material properties is often aggravated.[1,10]

Table 2: The collected data on 16MnCrS5 (quality prescription 17)

Batch #	C (%)	Mn (%)	S (%)	Cr (%)	*K*3	Pearlite (%)	Spherodization (%)	Heat treatment	Rm (N/mm^2)	A (%)
1	0.17	1.26	0.03	1	7	40	0	/	669	24.5
2	0.17	1.22	0.027	0.99	5	40	0	/	604	17.2
3	0.17	1.22	0.027	0.99	6	45	0	/	658	16.1
4	0.18	1.2	0.025	0.97	6	40	0	/	654	16.2
5	0.17	1.19	0.023	0.99	7	45	0	/	666	16.8
6	0.19	1.29	0.023	1.09	9	40	90	GKZ	437	29.5
7	0.15	1.05	0.033	0.82	3	45	80	GKZ	454	30.4
8	0.15	1.02	0.028	0.82	11	40	90	GKZ	440	28.9
9	0.19	1.3	0.019	1.06	9	40	95	GKZ	446	30.5
10	0.19	1.27	0.021	1.07	15	40	0	BG	570	22.2
11	0.15	1.02	0.03	0.85	7	40	0	BG	593	22.3
…	…	…	…	…	…	…	…	…	…	…
70	0.16	1.09	0.029	0.92	5	40	0	/	644	15.2

3 MODELING OF TENSILE STRENGTH AND ELONGATION

In **Table 2** the percentage of spheroidization depends on GKZ (Glühen auf kugeligen Zementit) – spheroidization annealing. Accordingly, both "qualitative" parameters of GKZ and BG annealing can be replaced, respectively, by the quantitative values 0 and 1 (0 for when no heat treatment is used; 1 for when the heat treatment is used).

For the model fitness the average relative deviation between the predicted and the experimental data was selected. It is defined as Equation (1):

$$\Delta = \frac{\sum_{i=1}^{n} \left| E_i - P_i \right|}{n} \tag{1}$$

where n is the size of the collected data, and E_i and P_i are the actual and the predicted total tensile strength or elongation, respectively.

The tensile strength and elongation were modeled using linear regression and genetic programming. The results of the modeling are presented hereafter.

3.1 Linear regression

Based on the linear regression results regarding tensile strength only the percent of spheroidization and heat treatment are statistically significant influential parameters ($p < 0.05$). The average relative deviation between the predicted and the experimental data is 3.06 %. The linear-regression model for the tensile-strength prediction is in Equation (2):

$$R\text{m} = 500.0126 \cdot \text{C} - 198.777 \cdot \text{Mn} + 119.686 \cdot \text{S} + 128.071 \cdot \text{Cr} - 0.0738 \cdot K3 + 1.815 \cdot \text{Pearlite} - 1.66 \cdot \text{Spherodization} + 587.2196 \tag{2}$$

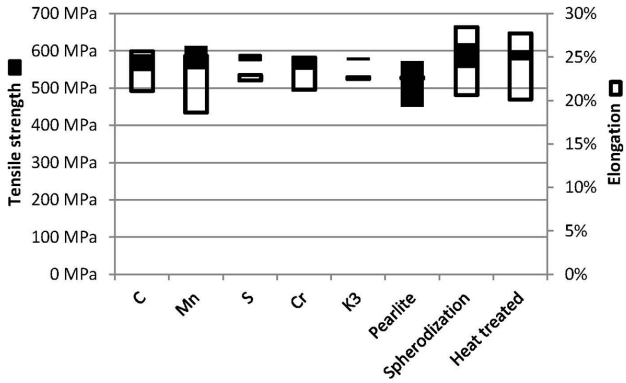

Figure 1: Calculated influences of individual parameters on the tensile strength and elongation, while separately changing them within the range from **Table 2**

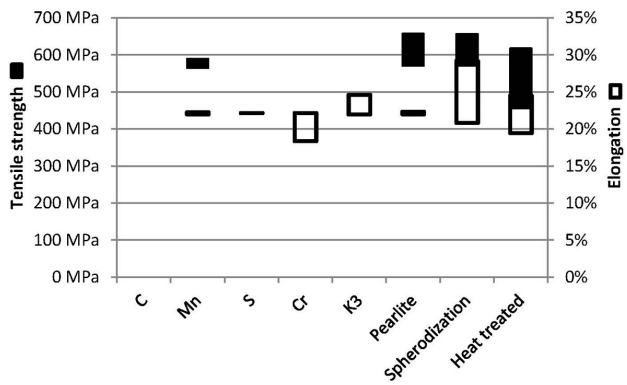

Figure 2: Calculated influences of individual parameters on the tensile strength and elongation, while separately changing them within the range from **Table 2**

During the elongation modeling only the percentage of spheroidization and heat treatment are statistically significant influential parameters ($p < 0.05$). The average relative deviation between the predicted and the experimental data is 7.56 %. The linear regression model for the tensile-strength prediction is:

$$A = -57.295 \cdot C + 21.749 \cdot Mn \pm 44.973 \cdot S - 12.498 \cdot Cr - 0.0093 \cdot K3 - 0.0247 \cdot \text{Pearliten} + 0.07823 \cdot \text{Spherodization} + 16.718 \quad (3)$$

It must be emphasized that the percentage of spheroidization and heat treatment statistically significantly influences both the tensile strength and the elongation. However, it does so conversely (i.e., if tensile strength is increased by the influence of both parameters, the elongation is decreased and vice versa).

Figure 1 shows the calculated influences of individual parameters on the tensile strength and elongation using the developed models, while separately changing the individual parameter within the range from **Table 1**. It can be concluded that the C, Mn, S and Cr content, the percentage of spheroidization and the heat treatment are the most influential factors.

3.2 Genetic programming

Genetic programming has already been found useful for several different applications in Štore Steel Ltd.[3,6,18,19] Genetic programming is a population-based algorithm that is similar to a genetic algorithm and many other heuristic optimization techniques.[20–23] In the present paper 100 models for tensile strength and also for elongation were obtained through a genetic programming method. During the simulated evolution the organisms (with basic ingredients – function and terminal genes) are generated and afterwards changed through different changing algorithms. The following function genes were selected: addition (+), subtraction (-), multiplication (*) and division (/). The selected terminal genes were: weight percentage of C (*C*), Mn (*MN*), S (*S*), Cr (*CR*), the micro-cleanliness K3 (*K*3) determined according to DIN 50602, method K, content of pearlite in % (*PEARLITE*), percentage of spheroidization (*SPHER*) and heat treatment (*HT*).

The AutoLISP-based in-house genetic programming system was run 100 times in order to develop 100 independent civilizations. Each run lasted approximately 4 h and 40 min on a 3.0-GHz processor with 4 GB of RAM.

$$\begin{aligned}
&5.65484 + C + 5.21897\,\text{PEARLITE} + 5.21897\,(\text{Mn} + \text{PEARLITE}) + \\
&\frac{1 - \left(-5.21897 + \frac{27.2376\,\text{HT Mn}}{\text{HT Mn}+\text{PEARLITE}}\right)\left(\text{Mn} - \frac{27.23764(16.1979+2\,\text{Mn})}{-42.2681770815+\text{PEARLITE}} - \frac{0.1916\,\text{Mn}}{\text{SPHER}}\right) - 5.21897\,(\text{Mn} + \text{SPHER})}{\text{PEARLITE}} + \\
&-\text{Mn}\left(-5.21897 + \frac{741.8894\,\text{HT Mn}}{(\text{Mn}+\text{PEARLITE})(\text{HT Mn}+\text{PEARLITE})}\right) + \frac{27.2376(8.09895+2\,\text{Mn})}{\text{PEARLITE}-5.21897\text{SPHER}} - \frac{16.1979+2\,\text{Mn}}{\text{PEARLITE}-5.21897\text{SPHER}} + \frac{\text{Mn}}{\text{SPHER}+\frac{8.09895+\text{HT Mn}+\text{SPHER}}{\text{PEARLITE}}} + \\
&\frac{}{\text{SPHER} + \frac{8.09895+\text{HT Mn}+\text{SPHER}}{\text{PEARLITE}}} \quad (4) \\
&-\text{Mn}\,(-5.21897 + 2\,\text{Mn}\,(\text{HT} + \text{HT Mn})) + \frac{5.21897(\text{PEARLITE}-5.21897\text{SPHER})}{\text{SPHER}} + \frac{\text{Mn}}{5.21897\text{SPHER} - \frac{27.2376\,\text{Mn}}{\text{PEARLITE}+\text{SPHER}} + \frac{\text{Mn}+\text{HT Mn}+\frac{\text{HT SPHER}}{\text{PEARLITE}}}{(-5.21897+\text{HT Mn})\text{SPHER}}} \\
&\frac{}{\text{SPHER} + \frac{8.09895+(-5.21897+2\,\text{Mn}\,(\text{HT}+\text{HT Mn}))(2\,\text{HT Mn}+\text{SPHER})}{\text{PEARLITE}}}
\end{aligned}$$

$$15.70195 + \mathrm{Mn} + 4.96016\left(\mathrm{HT} + \frac{\mathrm{HT} + \mathrm{SPHER} + \frac{\mathrm{Cr}+\mathrm{HT}+\mathrm{SPHER}}{0.3709+2\,\mathrm{HT}+\mathrm{K3}+0.10849\mathrm{SPHER}}}{9.21726 + \frac{\mathrm{SPHER}}{\mathrm{S}} + \frac{\mathrm{Cr}+\mathrm{SPHER}}{\mathrm{PEARLITE\,SPHER}}}\right) + \mathrm{SPHER} + \frac{\mathrm{SPHER}}{\mathrm{K3}} - \frac{-3.41876+\mathrm{Cr}+\mathrm{HT}}{-\mathrm{Cr}+\frac{3.41876}{\mathrm{HT}}+\mathrm{HT}+2\,\mathrm{K3}-\mathrm{PEARLITE}+\frac{\mathrm{SPHER}}{\mathrm{K3}}} + \frac{3.41876}{-\frac{3.41876}{\mathrm{HT}}+\mathrm{K3}-\frac{\mathrm{SPHER}+\frac{\mathrm{SPHER}}{\mathrm{K3}}+\frac{3.41876\,\mathrm{PEARLITE}}{\mathrm{Cr}+\mathrm{SPHER}}}{9.21726+\mathrm{Cr}+\frac{\mathrm{SPHER}}{\mathrm{PEARLITE}}}}$$

$$9.21726 + \mathrm{HT} + \frac{\mathrm{SPHER} + \left(9.21726+\mathrm{Cr}+\frac{1-\frac{3.41876}{\mathrm{HT}}}{9.21726+\mathrm{Cr}+\mathrm{HT}+\mathrm{PEARLITE}}+\frac{3.41876\,\mathrm{HT}}{\mathrm{SPHER}}-\frac{3.41876}{\mathrm{K3\,SPHER}}\right)\left(0.3709+\mathrm{HT}+\mathrm{K3}+\mathrm{SPHER}+\frac{\mathrm{HT}+\mathrm{SPHER}}{9.21726+\mathrm{HT}+0.10849\,\mathrm{SPHER}}\right)}{-9.21726-\mathrm{HT}+\mathrm{K3}+\mathrm{SPHER}-\frac{\mathrm{SPHER}}{\mathrm{PEARLITE}}}}{\mathrm{PEARLITE}} \quad (5)$$

The selected maximum number of generations was 100. The selected size of the population of organisms 100, the reproduction probability 0.4, the crossover probability 0.6, the maximum permissible depth in the creation of the population 6, the maximum permissible depth after the operation of crossover 10, and the smallest permissible depth of the organisms in generating new organisms 2. For the selection of organisms the tournament method with tournament size 7 was used.

For the tensile-strength modeling, the most succesful organism from all of the civilizations is presented in Equation (4).

The average relative deviation between the predicted and the experimental data is 2.89 %. The model consists of 235 genes. Its depth is 14. It must also be emphasized that the parameters (genes) *CR*, *S*, *K*3 are not included in the model.

For elongation modeling, the most succesful organism from all of the civilizations is presented in Equation (5).

The average relative deviation between the predicted and the experimental data is 5.18 %. The model consists of 189 genes. Its depth is 14. It must also be emphasized that parameters (genes) *CR*, *S*, *K*3 are not included in the model.

Figure 2 shows the calculated influences of the individual parameters on the tensile strength and elongation using the genetically developed model (Equations (4) and (5)), while separately changing the individual parameter within the range from **Table 2**. It can be concluded that Cr and pearlite content, the percentage of spheroidization and the heat treatment are the most influential factors.

4 IMPLEMENTATION OF MODELING RESULTS

Up until February 2016, six consecutively cast batches (16MnCrS5, quality prescription 17) were used for the implementation of the modeling results. The collected data are presented in **Table 3**. Depending on the chemical composition and the pearlite content, the plan for the heat treatment is determined in order to achieve the optimal tensile strength at moderate elongation.

Table 3: The collected data on 6 16MnCrS5 (quality prescription 17) consecutively cast batches

Batch #	C (%)	Mn (%)	S (%)	Cr (%)	*K*3	Pearlite (%)
1	0.17	1.09	0.035	0.87	4	40
2	0.17	1.13	0.025	0.86	8	45
3	0.16	1.08	0.026	0.85	6	40
4	0.18	1.09	0.022	0.85	7	40
5	0.15	1.07	0.023	0.87	6	40
6	0.17	1.13	0.025	0.99	7	40

Figure 3 presents the prediction of tensile strength using linear regression and genetic programming for the 6 batches (from **Table 3**). There are statistically significant differences (one-way ANOVA, $p < 0.05$) between the predicted tensile strength when the heat treatment is used and when it is not used – for both methods: linear regression and genetic programming. GKZ annealed material has the statistically significantly lowest tensile strength (one-way ANOVA, $p < 0.05$).

Figure 4 presents the prediction of elongation using linear regression and genetic programming for 6 batches (from **Table 3**). There are statistically significant differences (one-way ANOVA, $p < 0.05$) between the predicted elongation when the heat treatment is used and when the heat treatment is not used – for both methods: linear regression and genetic programming. GKZ annealed ma-

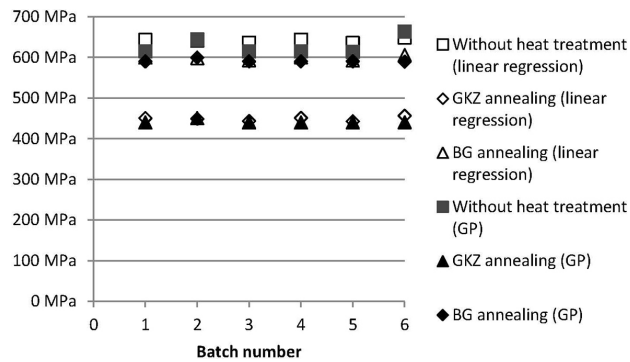

Figure 3: Calculated influences of the individual parameters on the elongation, while separately changing them within the range from **Table 2**

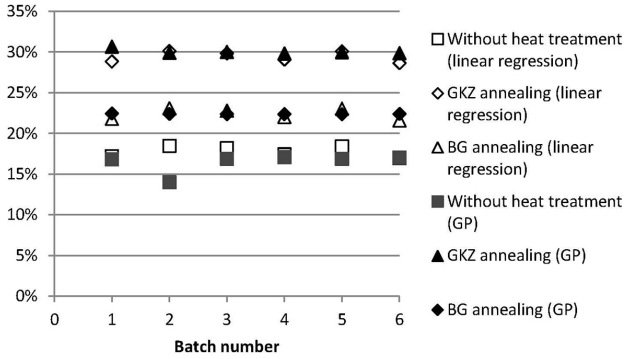

Figure 4: Calculated influences of the individual parameters on the elongation, while separately changing them within the range from **Table 2**

terial has the statistically significantly highest elongation (one-way ANOVA, $p < 0.05$).

In accordance with the predictions presented in **Figures 3** and **4** the BG annealing was selected in order to achieve a higher tensile strength at moderate elongation.

The tensile-test results (tensile strength and elongation) and linear-regression results are presented in **Table 4**.

The average relative deviation between the predicted and the experimental data for the tensile strength for linear regression and genetic programming is 3.55 % and 3.08 %, respectively. The average relative deviation between the predicted and the experimental data for elongation for linear regression and genetic programming is 3.56 % and 2.65 %, respectively.

5 CONCLUSIONS

The 16MnCrS5 steel grade is generally used for the fabrication of case-hardened machine parts for several applications (e.g., bars, rods, plates, strips, forgings), where having a combination of wear resistance, toughness and dynamic strength is essential. These qualities can be easily correlated with tensile test results (e.g., tensile strength, elongation), which depends on the chemical composition and the heat treatment after rolling.

Accordingly, from October 2008 to February 2016, 70 consecutively cast batches with diameters from 20 mm to 55 mm were produced. In all cases the data on the tensile strength and elongation is available. For some orders the bars were also heat treated:

- GKZ (Glühen auf kugeligen Zementit) – spheroidization annealing or
- BG annealing – isothermal annealing (for excellent machinability properties and a better microstructure homogenizing).

The chemical composition (content of C, Mn, S and Cr) and heat-treatment regime (GKZ or BG annealing) data were collected. During the microstructure examination also the pearlite content and the percentage of spheroidization (after GKZ annealing) were assessed. The micro-cleanliness (*K*3) was determined according to DIN 50602, method K.

The tensile strength and elongation were modeled using linear regression and genetic programming.

The ANOVA results obtained using linear regression show that only the percentage of spheroidization and heat treatment are statistically significant influential parameters ($p < 0.05$) for tensile strength. The average relative deviation between the predicted and the experimental data is 3.06 %. At elongation only the percentage of spheroidization and heat treatment are statistically significant influential parameters ($p < 0.05$). The average relative deviation between the predicted and the experimental data is 7.56 %.

The average relative deviation between the predicted and the experimental data for the best genetically developed mathematical model for predicting tensile strength is 2.89 %. The model consists of 235 genes. Its depth is 14.

The average relative deviation between the predicted and the experimental data for the best genetically developed mathematical model for predicting elongation is 5.18 %. The model consists of 189 genes. Its depth is 14.

Up until February 2016, six consecutively cast batches (16MnCrS5, quality prescription 17) were used for the implementation of the modeling results. To achieve the optimal tensile strength at moderate elongation, the plan for the heat treatment has to be determined on the basis of the chemical composition and the pearlite content. The tensile strength and the elongation were predicted using linear regression and genetic programm-

Table 4: The collected data on 6 16MnCrS5 (quality prescription 17) consecutively cast batches

Batch #	C (%)	Mn (%)	S (%)	Cr (%)	*K*3	Pearlite (%)	R_m (MPa)	R_m – linear regression (MPa)	R_m – GP (MPa)	*A* (%)	*A* – linear regression (%)	A – GP (%)
1	0.17	1.09	0.035	0.87	4	40	622.0	600.28	590.53	22.60	21.82	16.85
2	0.17	1.13	0.025	0.86	8	45	641.0	598.63	599.92	22.00	23.10	14.02
3	0.16	1.08	0.026	0.85	6	40	578.0	593.48	590.74	21.90	22.81	16.91
4	0.18	1.09	0.022	0.85	7	40	613.0	600.94	590.54	23.00	22.05	17.10
5	0.15	1.07	0.023	0.87	6	40	607.0	592.67	590.98	22.70	23.05	16.89
6	0.17	1.13	0.025	0.99	7	40	598.0	606.28	589.95	22.30	21.61	17.05

ing. Based on the obtained results the BG annealing was selected in order to achieve a higher tensile strength at moderate elongation.

The average relative deviation between the predicted and the experimental data for the tensile strength for linear regression and genetic programming is 3.55 % and 3.08 %, respectively. The average relative deviation between the predicted and the experimental data for elongation for linear regression and genetic programming is 3.56 % and 2.65 %, respectively.

In the future the proposed concept will be used for analyzing the properties of selected steel grades.

6 REFERENCES

[1] S. Bruschi, T. Altan, D. Banabic, P.F.Bariani, A. Brosius, J. Cao, A. Ghiotti, M. Khraisheh, M. Merklein, A. E. Tekkaya, Testing and modelling of material behaviour and formability in sheet metal forming, CIRP Annals – Manufacturing Technology, 63 (**2014**) 2, 727–749, doi:10.1016/j.cirp.2014.05.005

[2] Q. Zhang, M. Mahfouf, A nature-inspired multi-objective optimisation strategy based on a new reduced space searching algorithm for the design of alloy steels, Engineering Applications of Artificial Intelligence, 23 (**2010**) 5, 660–675, doi:10.1016/j.engappai.2010.01.017

[3] M. Kovačič, B. Šarler, Application of the Genetic Programming for Increasing the Soft Annealing Productivity in Steel Industry, Materials and Manufacturing Processes, 24 (**2009**) 3, 369–374, doi:10.1080/10426910802679634

[4] M. Kovačič, Modeling of Total Decarburization of Spring Steel with Genetic Programming, Materials and Manufacturing Processes, 30 (**2014**) 4, 434–443, doi:10.1080/10426914.2014.961477

[5] M. Kovačič, D. Novak, Prediction of the chemical non-homogeneity of 30MnVS6 billets with genetic programming, Materiali in tehnologije, 50 (**2016**) 1, 69–74, doi:10.17222/mit.2014.280

[6] M. Kovačič, R. Jager, Modeling of occurrence of surface defects of C45 steel with genetic programming, Materiali in tehnologije, 49 (**2015**) 6, 857–863, doi:10.17222/mit.2013.304

[7] Z. Wang, P. Liu, Y. Xu, Y. Wang, Y. Zhan, Hot Stamping of High Strength Steel with Tailored Properties by Two Methods, Procedia Engineering, 81 (**2014**), 1725–1730, doi:10.1016/j.proeng.2014.10.221

[8] A. K. Lakshminarayanan, Enhancing the properties of friction stir welded stainless steel joints via multi-criteria optimization, Archives of Civil and Mechanical Engineering, 16 (**2016**) 4, 605–617, doi:10.1016/j.acme.2016.03.012

[9] X. Kong, L. Lan, Z. Hu, B. Li, T. Sui, Optimization of mechanical properties of high strength bainitic steel using thermo-mechanical control and accelerated cooling process, Journal of Materials Processing Technology, 217 (**2015**), 202–210, doi:10.1016/j.jmatprotec.2014.11.016

[10] R. S. Khabba, B. D. Manshadi, A. Abedian, R. Mahmudi, A simplified fuzzy logic approach for materials selection in mechanical engineering design, Materials and Design, 30 (**2009**) 3, 687–697, doi:10.1016/j.matdes.2008.05.026

[11] D. Pandya, D. Shah, Experimentation and its Prediction of Process Parameters Effects on Elongation in Tensile Test of AISI 1008 Steel Using ANN Model, Procedia Technology, 14 (**2014**), 282–289, doi:10.1016/j.protcy.2014.08.037

[12] I. Mohanty, D. Bhattacharjee, S. Datta, Designing cold rolled IF steel sheets with optimized tensile properties using ANN and GA, Computational Materials Science, 50 (**2011**) 8, 2331–2337, doi:10.1016/j.commatsci.2011.03.007

[13] Y. Y. Yang, M. Mahfouf, D. A. Linkens, Q. Zhang, Tensile Strength Prediction for Hot Rolled Steels by Bayesian Neural Network Model, IFAC Proceedings Volumes, Vol. 42 (**2009**) 23, 255–260, doi:10.3182/20091014-3-CL-4011.00046

[14] J. Chen, M. Mahfouf, G. Sidahmed, A new holistic systems approach to the design of heat treated alloy steels using a biologically inspired multi-objective optimisation algorithm, Engineering Applications of Artificial Intelligence, 37 (**2015**), 103–114, doi:10.1016/j.engappai.2014.08.014

[15] J. Han, H. Li, Z. Zhu, L. Jiang, H. Xu, L. Ma, Effects of processing optimisation on microstructure, texture, grain boundary and mechanical properties of Fe-17Cr ferritic stainless steel thick plates, Materials Science and Engineering: A, 616 (**2014**), 20–28, doi:10.1016/j.msea.2014.07.107

[16] S. Chen, X. Jin, L. Rong, Improving the strength and ductility of reduced activation ferritic/martensitic steel by cold-swaging and post-annealing, Materials Science and Engineering: A, 631 (**2015**), 139–143, doi:10.1016/j.msea.2015.02.044

[17] L. Chen, J, Huang, Y. Zhao, H. Di, F. Zhu, Processing, Microstructures and Mechanical Properties of Ultra-high Strength Steel Sheet, Procedia Engineering, 81 (**2014**), 84–89, doi:10.1016/j.proeng.2014.09.131

[18] S. Klemen, M. Kovačič, P. Kitak, J. Pihler, Electric-arc-furnace productivity optimization, Materiali in tehnologije, 48 (**2014**) 1, 3–7

[19] M. Kovačič, B. Šarler, Genetic Algorithm-Based Batch Filling Scheduling in the Steel Industry, Materials and manufacturing processes, 26 (**2011**) 3, 464–474, doi:10.1080/10426914.2010.525576

[20] J. F. Wang, W. L. Kang, J. L. Zhao, K. Y. Chu, A simulation approach to the process planning problem using a modified particle swarm optimization, Advances in Production Engineering & Management, 11 (**2016**) 2, 77–92, doi:10.14743/apem2016.2.211

[21] S. Ramadan, A bi-objective inspection policy optimization model for finite-life repairable systems using a genetic algorithm, Advances in Production Engineering & Management, 11 (**2016**) 1, 38–48, doi:10.14743/apem2016.1.208

[22] M. Hrelja, S. Klančnik, T. Irgolič, M. Paulič, Z. Jurkovič, J. Balič, M. Brezočnik, Particle swarm optimization approach for modelling a turning process, Advances in Production Engineering & Management, 9 (**2014**) 1, 21–30, doi:10.14743/apem2014.1.173

[23] M. Hrelja, S. Klančnik, J. Balič, M. Brezočnik, Modelling of a Turning Process Using the Gravitational Search Algorithm, International Journal of Simulation Modelling, 13 (**2014**) 1, 30–41, doi:10.2507/IJSIMM13(1)3.248

UDK 67.017:674-419.3:678.686
Original scientific article/Izvirni znanstveni članek

ISSN 1580-2949
MTAEC9, 51(6)889(2017)

DURABILITY OF FRP/WOOD BONDS GLUED WITH EPOXY RESIN

OBSTOJNOST FRP/LESNIH SKLOPOV, LEPLJENIH Z EPOKSI SMOLO

Jan Vaněrek, Milan Šmak, Ivo Kusák, Petr Misák

Brno University of Technology, Faculty of Civil Engineering, Veveří 95, 602 00 Brno, Czech Republic
vanerek.j@fce.vutbr.cz

Prejem rokopisa – received: 2016-11-18; sprejem za objavo – accepted for publication: 2017-04-20

doi:10.17222/mit.2016.321

The paper describes the properties of FRP/wood bonds, made of different wood species commonly used in the timber industry within Central Europe (oak, spruce, pine and larch). An FRP fabric (glass-fiber-reinforced polymer – GFRP, carbon-fiber-reinforced polymer – CFRP) was applied as the reinforcement. The durability of all the reinforced FRP/wood assemblies was verified with short-term exposure tests following the tensile-shear-strength and wood-failure criteria for the shear area of a single-lap joint. To precisely define the effect of the mechanical interlocking mechanism of the bond, analyses of porosity and surface roughness, and SEM were performed.

Keywords: durability, epoxy, FRP, wood adherend

Članek opisuje lastnosti FRP/lesnih sklopov, narejenih iz različnih vrst lesa, ki se običajno uporablja v lesni industriji v Srednji Evropi (hrast, jelka, bor, macesen). FRP-materiali (polimeri, ojačani s steklenimi vlakni – angl. GFRP, polimeri, ojačani z ogljikovimi vlakni, angl. CFRP) so bili uporabljeni za ojačanje. Obstojnost vseh FRP/lesnih sklopov so preverjali s kratkotrajnimi strižnimi preizkusi. Kriterij je bil površina strižnega preloma na enojni prekrivni ploskvi med FRP in lesom. Da bi lahko natančno definirali mehansko trdnost spoja, so izvedli analize poroznosti, površinske hrapavosti in SEM-analize.

Ključne besede: trajnost, epoksi, FRP, lepljivost lesa

1 INTRODUCTION

The main purpose of the FRP usage with timber in the construction industry is generally to improve the stiffness/strength of reinforced items without any influence on their service life or any environmental impact. From the perspective of the timber-reinforcement process, the optimum dimensional stability during moisture changes in wood should be one of the most important criteria for such joints.

Different studies were made for the FRP/wood bond durability using different types of adhesives. The optimum results of adhesion were achieved using formaldehyde-based adhesives;[1–3] different, contrary results were found using epoxy resins.[4,5] The results[1] for the epoxy resins showed an inability to reach the requirement for a cohesive failure of 80 % (in wood) after an exposure to cyclic hygrothermal conditions. Moreover, positive results were found using priming treatments (hydroxymetyl resorcinol – HMR; resorcin-fenol – RF; hexamethylolmelamin metyl ether – MME) before the gluing process.[2] The durability of FRP/wood joints using epoxy has not been completely established. Therefore, the final aim of this experiment was to establish the durability aspect of such joints. The focus was on the observation of the wood adhering parameters having a significant impact on the mechanical interlocking process to understand the impact of mechanical interlocking on the joint durability.

2 EXPERIMENTAL PART

2.1 Materials

Carbon, glass or aramid are common reinforcement-fiber materials used for external polymer-composite systems known as fiber-reinforced polymers (FRPs). Reinforcing of wood with FRP lamellas/fabrics could be applied without any restriction regarding the wood species. To evaluate the influence of wood species, the experiment used glass-fiber-reinforced polymer (GFRP) and carbon-fiber-reinforced polymer (CFRP) fabrics applied to different wood adherents. Oak (*Quercus robur*), spruce *(Picea abies*), pine (*Pinus sylvestris*) and larch (*Larix decidua*) with a uniform thickness of 25 mm were chosen. The fabrics with carbon fibers (Tyfo SCH-41, FYFE Co.) with a width of 1.0 mm and the GFRP with glass fibre (Tyfo-SEH-51A, FYFE Co.) with a width of 1.3 mm were used. As the adhesive, the epoxy resin TYFO S (diglycidyl ether of bisphenol-A, DGEBA) with an amine hardener was used. Pre-treatment including penetration of the wood surface to ensure stabilization of wood cells (200 g/m^2) was applied. Similarly, the FRP fabrics were saturated with epoxy resin (400 g/m^2) on both sides. After 30 min of such

pre-treatments, the FRP strips were applied to the wood surface. After 24 h of the epoxy curing process, the final layer of the epoxy matrix in the amount of 200 g/m^2 was also applied without any pressure. All the applications were carried out at a laboratory ambient temperature of 20 °C. To ensure the post-curing process, the assemblies were exposed to a constant temperature of 60 °C for 72 h. After the post-curing process, the test samples of 20 mm × 8 mm × 150 mm with 3-mm-thick notches in the wood were adhered to the fabrics and the CFRP or GFRP layers were made, defining the shear area.

2.2 Tensile-shear-strength testing

The FRP/wood specimens were subjected to accelerated tests, exposing them to all the climatic treatments and different hygrothermal conditions (classes A2–A5, specified in ČSN EN 302-1, **Table 1**). Tensile-shear tests were performed on the test specimens, for each condition class, and a total of 12 test samples were used. The tests were performed on a Testometric M350-20CT machine (Testometric Company Ltd., UK), digitally recording the test progress at a crosshead speed of 1 mm/min. As an additional evaluation of the bond durability, the wood failures within the shear area (rounded to the nearest value in multiples of 10 %) were visually assessed.

Table 1: Types of exposure treatments prior to the tensile-shear testing

Treatment	Climatic treatment	Specification
A1	Standard climate	7 d 20 °C/65 %
A2	Immersion in cold water	7 d 20 °C/65 % 4 d in water (15±5 °C) Tested in a wet state
A3	Immersion in cold water	7 d 20 °C/65 % 4 d immersion in water (15±5 °C), conditioning at 20 °C/65 % Tested in a dry state
A4	Immersion in boiling water	7 d 20 °C/65 % 6 h in boiling water 2 h immersion in water (15±5 °C), Tested in a wet state
A5	Immersion in boiling water	7 d 20 °C/65 % 6 h in boiling water 2 h immersion in water (15±5 °C) 7 d conditioning at 20 °C/65 % Tested in a dry state

2.3 Microstructural analysis

To assess the effect of mechanical interlocking as a possible aspect of a bond, the microstructures of all the tested wood adherents were analyzed. The sizes of the main structural elements of the transverse wood microtome samples were assessed. Electron scanning microscopy provided an accurate evaluation of a failed bond based on the loss of adhesion.

2.4 Wood-surface-roughness analysis

The surfaces of all the tested wood adherents were scanned using confocal laser microscopy in both the optical and confocal mode. The automatic microscope mode was used to determine the highest and lowest point of the relief of a scanned area. The number of optical sections depended only on the wood, assuming that the other parameters such as magnification and the illumination mode (laser or optical light) remained unchanged. Alternatively, the number of optical sections depended on the illuminated thickness of the wood. Optical cuts from 40 to 60 in the optical mode and from 70 to 90 in the confocal mode were evaluated. The purpose of this analysis was to see if the different surface roughness of each wood species has an impact on the final durability of a FRP/wood bond. The parameters of mean quadratic heights (SRq, SPq) and mean arithmetic heights (SRa, SPa) were assessed in five different appointed places for each tested wood. Surface roughness parameters SRa, SPa, SRq and SPq are based on one-dimensional parameters Ra (the arithmetic mean of roughness), Pa (the arithmetic mean of height of a curve profile), Rq (the root mean square roughness), Pq (the root mean square height of a curve profile). The calculation of these one-dimensional parameters is specified in ČSN EN ISO 4287 and the conversion into surface parameters was calculated based on the data acquired from two perpendicular directions.

2.5 Porosity

The pore size and pore distribution within all the tested wood specimens were evaluated with mercury porosimetry using the PASCAL 140/240, Thermo Finnigan equipment. Wood samples with a volume of approx. 0.75 cm^3 were used. To avoid an overestimation of the portion of smaller pores, a gradual increase in the rate of pressure during the process was chosen.

3 RESULTS

3.1 Tensile-shear-strength testing

The mean strength values obtained are shown in **Figures 1a** to **1d**; it is clear that the sets of dry-wet cycling ageing tests show a reduction in the joint strength. The most significant strength reduction in the dry state for both FRP materials resulted from the specimens subjected to both exposure treatments, providing a significant hygrothermal-stress concentration in the bond line.

To compare the test results, variance tests (ANOVA) were analyzed. The influence of the type of exposure was tested using the one-way ANOVA. Based on this analysis, the tensile strength is significantly influenced by the type of exposure. In addition, the two-way ANOVA was used when both the type of exposure and the type of reinforcement were factors. The purpose of

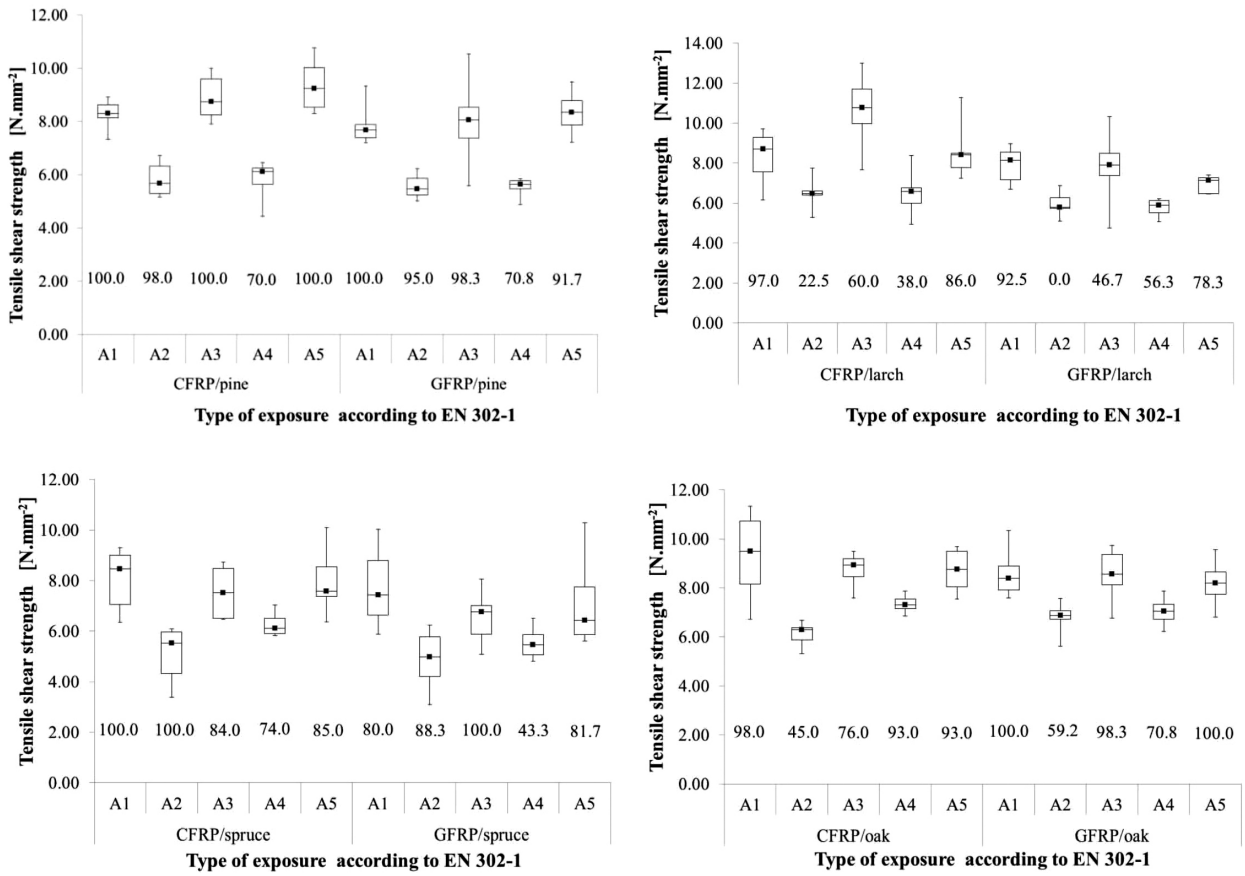

Figure 1: Mean tensile-shear strengths of the samples tested after the exposure to climatic treatment according to EN 302-1; ■ denotes the mean value; the box plot – rectangle shows the interquartile range (IQR) with the median depicted within the box; for each exposure, the value of wood failure is stated

Table 2: Mean values of the wood-element size proportion of the used wood species

	Size (diameter) of wood elements (μm)							
	Lumina					Cell-wall thickness		
	tracheids		vessels		libriform	tracheids		libriform
	early wood	late wood	early wood	late wood		early wood	late wood	
Pine (*Pinus sylvestris*)	26.1	9.7				6.0	11.7	
Larch (*Larix decidua*)	30.7	10.1				4.7	9.2	
Spruce (*Picea abies*)	31.2	10.3				4.0	8.9	
Oak (*Quercus robur*)			245.0	41.9	9.0			4.0

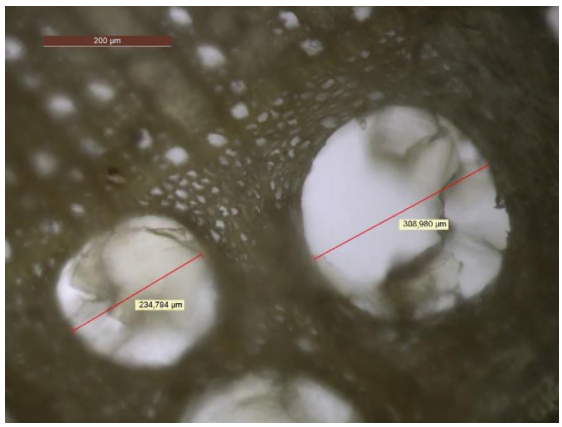

Figure 2: Cross-section of oak wood, apparent vessel elements and libriform cells, magn. 100×

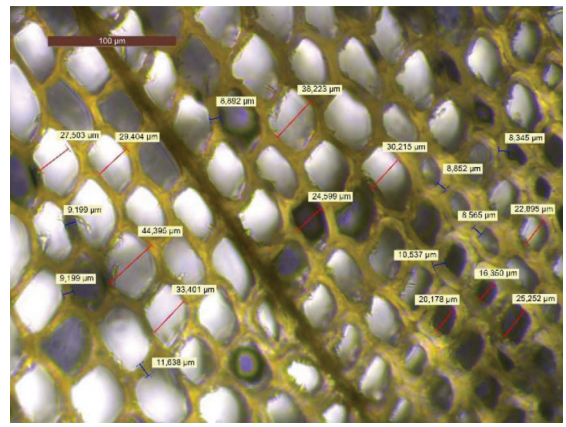

Figure 3: Cross-section of an early part of the annual ring of spruce wood, magn. 200×

this was to establish the individual influences of these factors and the interaction between them. The results of the two-way ANOVA show that each factor is statistically significant for the tensile strength, but the interaction between the factors is not significant. All the statistical tests were carried out at a significance level of 0.05.

3.2 Microstructural analysis

Results of the size-distribution evaluation did not show any significant difference between the coniferous species; the biggest size of the cell-wall thickness was found for the pine species, concurring with the smallest size of the pores (lumina) of tracheid elements. Details of all the observed elements are shown in **Table 2**. The photomicrographs of the hardwood and conifer species with the size measurements are shown in **Figures 2** and **3**.

3.3 Wood-surface-roughness analysis

A comparison of the results of the profile parameters (SPa, SPq) indicates deviations from the interspaced centerline of the test surface; the highest deviations were detected on the oak surface, arising from the existence of open vessel elements (**Figure 5**). The smallest deviation was found on the pine; the drop of the profile-parameter value for the pine was lower by almost 50 % compared to the other coniferous woods.

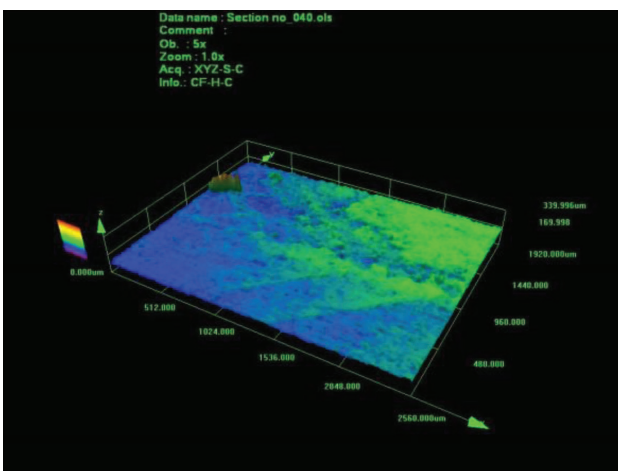

Figure 4: Surface relief of the pine sample used for calculating square roughness parameters (magn. 120×; area of 2560 µm × 1920 µm)

Table 3: Values of selected roughness parameters of used wood species obtained with confocal microscopy

Wood species	Mean values and S. D. of roughness parameters							
	SPa		SRa		SRq		SPq	
Pine	9.14	1.20	5.82	0.18	8.00	0.41	12.31	1.29
Oak	42.89	9.20	9.66	1.04	14.77	1.73	53.68	10.35
Larch	19.95	2.20	8.05	0.95	11.22	1.52	24.84	3.18
Spruce	17.41	3.03	7.47	0.63	11.20	1.26	22.95	3.51

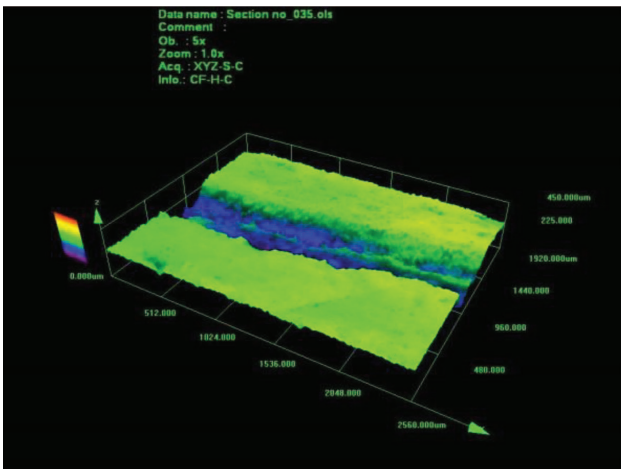

Figure 5: Surface relief of the pine sample used for calculating square roughness parameters (magn. 120×; area of 2560 µm × 1920 µm)

The achieved values of the roughness parameters (SRa, SRq), where the longwave part is eliminated, showed the highest values of the roughness for the oak sample; the highest decrease of nearly 40 % was observed for the pine sample, compared to the other softwood species. All the achieved values are shown in **Table 3**.

3.4 Porosity

Among all the other parameters, porosity has the most significant influence on the impregnability of

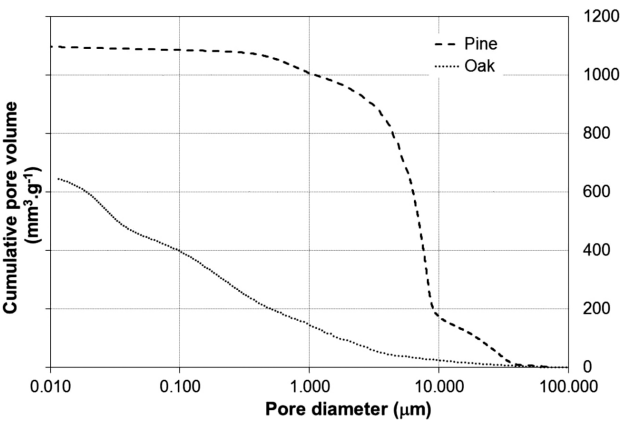

Figure 6: Cumulative pore volume as a function of the pore diameter of softwood and hardwood species

Table 4: Achieved results of mercury porosimetry of tested wood samples

Wood species	Total porosity	Specific density	Bulk density	Cumulative pore volume
	%	kg m^{-3}	kg m^{-3}	mm^3 g^{-1}
Oak	47.6	1410.0	738.6	644.7
Larch	54.0	1518.4	699.2	771.6
Pine	60.3	1381.1	549.0	1097.3
Spruce	62.8	1423.6	528.9	1188.1

wood. Consequently, the bulk density and specific density for each tested sample were established from the other parameters. The resulting values are shown in **Table 4**, confirming the presumption of a decreasing total porosity despite the increasing bulk density. The cumulative pore-volume curves as a function of the pore diameter of oak (hardwood) and pine (softwood) are shown in **Figure 6**.

4 DISCUSSION

4.1 Tensile-shear-strength testing

A stronger effect of the thermal exposure ensuring the hygrothermal exposure for condition classes A4 and A5 compared to the exposure without a thermal effect (A2, A3) was not proven (**Table 5**).

Regarding the type of fabrics, there was no indication of any dependency on the durability aspect. The requirements of the EN standard for strength limits (related to the beech/beech bond) for all the exposures were not exceeded by any of the tested samples. The most significant result of durability was achieved with the pine as an adherent when no losses in the strength occurred under all the severe exposures. Furthermore, the values of the cohesive failure expressed with a higher wood failure (WF) for the pine/FRP bonds supported this durability aspect. The values of the wood failure showed that the minimum limit of 80 % was not reached for the dry test samples of larch as a softwood; also, the WF percentage dropped below the 80 % criterion for the FRP/larch samples tested in a wet condition. Comparing the effects of the strength and wood-failure parameters, it can be clearly indicated that the more decisive criterion for the durability aspect shows exceptional values for the type of failure as shown for the larch/FRP bonds.

4.2 Porosity

The microscopy analysis of the main structural elements showed similar sizes of tracheids for all the softwood species; the highest porosity was established for spruce, the lowest for larch. But differences occurred between the results for the pore distribution as a function of the pore diameter. The differences occurred between the distributions of pores for the softwood species where the biggest drop in the distribution occurred for the pore diameters of 10 μm, contrary to the shape of the distribution curves for the oak as the ring-porous wood, which showed a consistent increase in the pore volume for pore diameters from 12 nm to 100 μm. The distribution of pore diameters for softwood is affected by the amount of tracheids elements, which form the main structure of softwoods. The lowest value of the porosity was established for the oak-wood sample; however, this had no effect on the final durability of the FRP/wood bond. Similar strength decreases were found when comparing the FRP/oak samples with the samples of the other wood species. The values of the pore distribution correlate with similar results,[6] performed for the European wood species.

4.3 Bond-line failure

After the accelerated tests, the FRP/wood bond lines were assessed at the macroscopic and microscopic levels. At the macroscopic level, the adhesive failure occurred mostly in the late part of the annual ring, despite the cohesive failure in the early part of the annual ring for the soft-wood species. For oak as a hardwood, the most cohesive failures were detected at the shear areas of the specimens tested in a dry state.

To precisely specify the mechanism of failure, electron microscopy (SEM) was performed to observe the microscopic structure of the wood at the FRP/wood interphase region. For the softwood species, the adhesion failure did not show the existence of structural tracheid elements in the early parts of the annual rings. Nevertheless, the existence of ray elements filled with resin was observed (**Figure 7**); a deeper penetration of the adhesive was observed due to their perpendicular orientation to the application area, which was wetted by the adhesive. This clearly indicates that the existence and quantity of rays partake in the tensile-shear strength of the softwood species.

For the hardwood species, a good adhesive penetration into the lumina of all the conductive elements (vessel, libriform) was observed. This phenomenon was proven by a higher wood-failure percentage for the specimens tested in a dry state after a hygrothermal

Table 5: Resulting values of decreasing strength after exposing the test samples to different exposure criteria

	Decreasing-strength and wood-failure values (%)				
Exposure	A1	A2 (wet)	A3 (dry)	A4 (wet)	A5 (dry)
Standard requirements for beech	10 MPa	-40	-20	-40	-20
Oak/CFRP (WF)	9.3 (98)	-34.3 (45)	-6.0 (73)	-21.1 (93)	-6.4 (93)
Oak/GFRP (WF)	8.6 (100)	-20.8 (59.2)	-0.5 (98.3)	-18.0 (70.8)	-4.6 (100.0)
Pine/CFRP (WF)	8.3 (100)	-29.7 (98)	7.5 (100)	-29.7 (70)	13.0 (100)
Pine/GFRP(WF)	7.9 (100)	-29.3 (95.0)	1.9 (98.3)	-29.5 (70.8)	6.1 (91.7)
Larch/CFRP (WF)	8.3 (97.0)	-22.0 (22.5)	28.0 (60.0)	-22.3 (38.0)	2.9 (86.0)
Larch/GFRP (WF)	7.9 (92.5)	-24.7 (0)	-1.4 (46.7)	-28.6 (56.3)	12.1 (78.3)
Spruce/CFRP (WF)	8.1 (100)	-36.8 (100)	-6.5 (84)	-22.3 (74.0)	-1.1 (85.0)
Spruce/GFRP (WF)	7.7 (80.0)	-37.0 (88.3)	-15.2 (100.0)	-28.6 (43.3)	-8.2 (81.7)

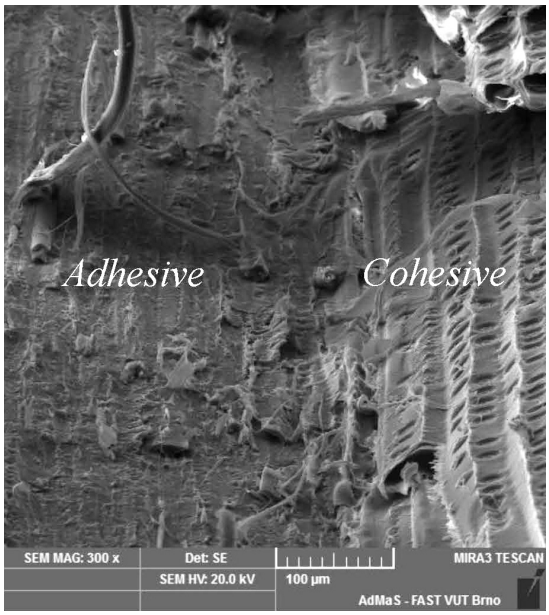

Figure 7: SEM micrograph of the border between early and late larch wood, different types of failure, magn. 300×

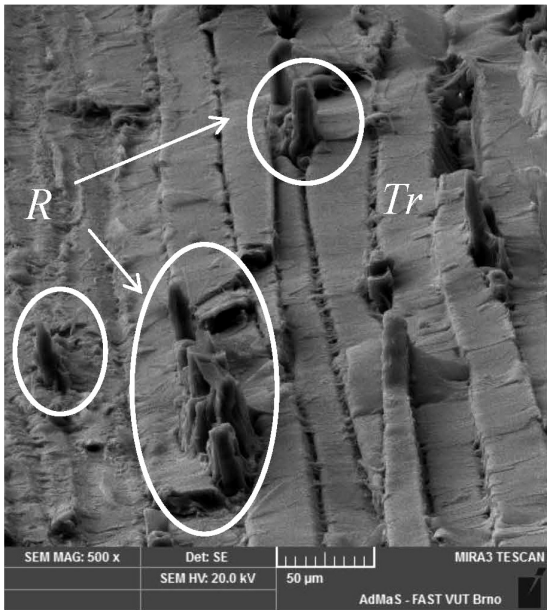

Figure 8: SEM micrograph, typical existence of rays (R) and tracheids (Tr) filled with resin, FRP/pine, magn. 500×

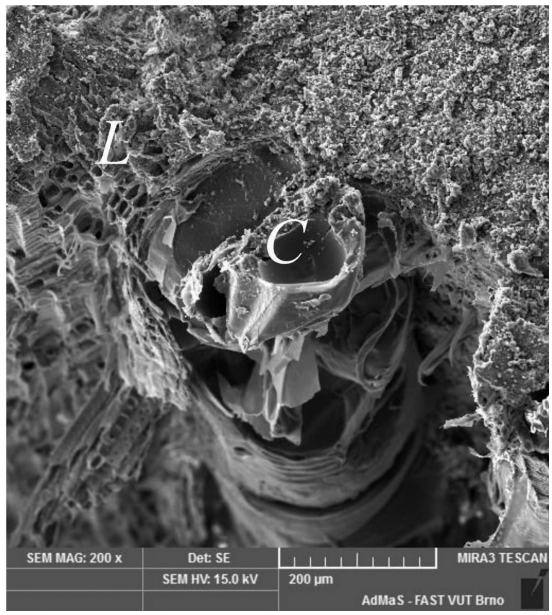

Figure 9: SEM micrograph of adhesive failure for FRP/oak, existence of the adhesive in the lumina of vessels (V) and libriform (L), magn. 200×

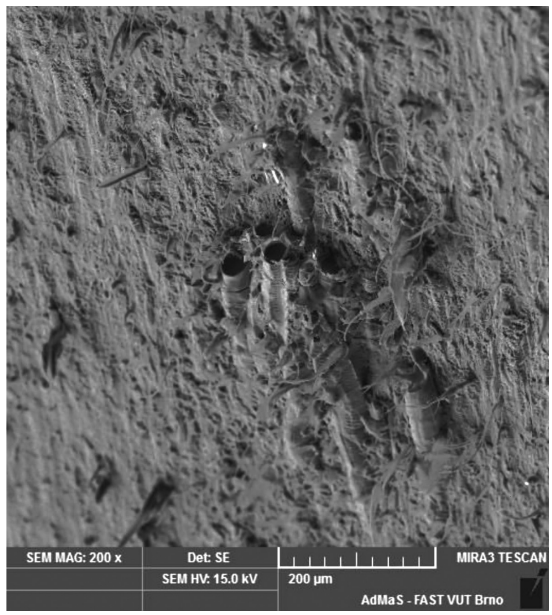

Figure 10: SEM micrograph of adhesive failure for FRP/oak, existence of cohesive failure of vessels, predominant adhesive failure of the FRP/oak bond line, magn. 200×

exposure. Despite this, the proper penetration of the adhesive into the lumina did not show a positive effect on the durability for the A2 and A4 condition classes.

5 CONCLUSIONS

The durability of FRP/wood bonds with different wood adherents was established using accelerated durability tests. According to the EN standard (declared for the beech/beech bond), all the tested samples of GFRP and CFRP fabrics met the standard criterion regardless of the wood species as the adherent. The wood species did not affect the durability of the FRP/wood bonds. The achieved strength for all the tested specimens in the conditions with a thermal exposure (A4, A5) was not significantly different from the one achieved in the conditions without a thermal exposure (A2, A3). Therefore, the inability of epoxy to withstand the volume changes of a wood adherent plays a more dominant role than the temperature influence on a possible resin degradation. The wood failure percentage proved to be a better

means to assess the durability of bonded specimens compared to strength-loss aspects.

The principle of a good adhesion of the FRP/wood bonds via a mechanical interlocking process was considered for the experimental work. The size of the pores is dominant for the permeability of the adhesive into the cell lumina. Therefore, the surface roughness, porosity and size distribution of pores for all the tested wood samples were analyzed. The dependency between the porosity and the FRP/wood bond durability was not proven. The spruce wood having the highest porosity did not exhibit the lowest drop in the strength, or even the biggest value of the cohesive failure. Furthermore, the FRP/wood durability of all the tested softwoods showed no dependency on the pore-size distribution. According to the laser confocal microscopy analysis, it was found that good durability of the FRP/pine wood bonds exhibits a good relationship with the parameters of the surface roughness. A plain surface and elimination of any debris on the surface allow proper adhesive wetting.

All the results showed that the mechanical interlocking of the FRP/wood bond does not have the dominant role anticipated; on the contrary, the chemical bonds of the adhesive contribute to the higher durability of the epoxy/wood bonds. This is because an interpenetrating polymer (adhesive) network occurs in the cell walls and in the mesopores between the cellulose fibers in the cell walls. A proper application technique, ensuring a proper diffusion of the epoxy adhesive between the cellulose microfibrils in the cell walls seems to be necessary for more durable FRP/wood bonds.

Acknowledgment

This paper was prepared with the financial help of project TA04010425 "A complex system of special repair materials using secondary raw materials for industries" supported by The Technology Agency of The Czech Republic; and the internal project of specific research No. FAST-S-16-3772 "Research of an adhesive modification increasing the durability of FRP/wood bonds at moisture exposure" supported by Brno University of Technology, Faculty of Civil Engineering.

6 REFERENCES

[1] B. S. Trimble, Durability and mode-I fracture of fiber-reinforced plastic (FRP)/wood interface bond, Doctoral dissertation, West Virginia University, 1999, 192

[2] H. V. S. Ganga Rao, Sawn and laminated wood beams wrapped with fiber reinforced plastic composites, Wood Design Focus, 8 (**1997**) 3, 13–18

[3] D. J. Gardner, J. F. Davalos, U. M. Munipalle, Adhesive Bonding of Pultruded Fiber-Reinforced Plastic to Wood, Forest Products Journal, 44 (**1994**) 5, 62–66

[4] G. M. Raftery, A. M. Harte, P. D. Rodd, Bond quality at the FRP-wood interface using wood-laminating adhesives, International Journal of Adhesion & Adhesives, 29 (**2009**) 2, 101–110, doi:10.1016/j.ijadhadh.2008.01.006

[5] J. P. Alexander, S. M. Shaler, D. J. Gardner, Evaluating wood/FRP bond durability through chemical kinetics, Proc. of Wood Adhesive, Madison WI, 2000, 289–299

[6] M. Plötze, P. Niemz, Porosity and pore size distribution of different wood types as determined by mercury intrusion porosimetry, European Journal of Wood and Wood Products, 69 (**2011**) 4, 649–657, doi:10.1007/s00107-010-0504-0

UDK 621.793.7:620.192.42
Original scientific article/Izvirni znanstveni članek

ISSN 1580-2949
MTAEC9, 51(6)897(2017)

THERMAL-CYCLING BEHAVIOR OF CoNiCrAlY BONDS COATED WITH THERMAL BARRIER COATINGS (TBCs) PRODUCED WITH ATMOSPHERIC PLASMA SPRAYING (APS)

OBNAŠANJE CoNiCrAlY PREVLEKE MED TERMIČNIM UTRUJANJEM

Mustafa Kaplan[1], Mesut Uyaner[2], Abdullah Cahit Karaoglanli[3]

[1]Selcuk University, Department of Metallurgical and Materials Engineering, Graduate School of Natural and Applied Sciences, Konya, Turkey
[2]Necmettin Erbakan University, Faculty of Aeronautics and Astronautics, Department of Aeronautical Engineering, Konya, Turkey
[3]Bartin University, Faculty of Engineering, Department of Metallurgical and Materials Engineering, Bartin, Turkey
mkaplan5442@gmail.com

Prejem rokopisa – received: 2017-01-23; sprejem za objavo – accepted for publication: 2017-05-12

doi:10.17222/mit.2017.024

Thermal barrier coatings (TBCs) are commonly applied as a thermal insulation in order to protect against environmental influences in the components of high-temperature gas turbines and jet engines. Gas-turbine components are affected by aggressive conditions of the environment during the service, being subjected to failures such as corrosion, thermal shock and oxidation. Plasma-spray technology is used to produce metallic bonds and ceramic top coats as a cost-effective method to prolong the lifetime of TBCs. In the present research, CoNiCrAlY bond-coat and YSZ top-coat powders included in the TBCs were deposited onto Inconel 718 superalloy substrates using atmospheric plasma spraying (APS). The TBCs were exposed to a furnace cycling test at 1150 °C and one-hour cycles. The presence of porosity and cracks facilitating the diffusion of oxygen in the top-coating structure led to the formation of thermally grown oxides (TGOs) at the interface. In addition, the most effective factors of failures were the formation and growth of mixed oxides at the bond/top-coat interface and the presence of imperfections. According to the test results, an increasing number of thermal cycles resulted in a decrease in the lifetime of the TBCs related to the sintering of the top coating due to the effect of high temperature.

Keywords: thermal barrier coatings (TBCs), thermal cycling, Inconel 718 superalloy, atmospheric plasma spraying (APS), CoNiCrAlY, ytrria-stabilized zirconia (YSZ)

Prevleke s toplotno pregrado (angl. TBCs) se običajno uporabljajo kot toplotna izolacija, ki ščiti komponente visoko temperaturnih plinskih turbin ali reaktivnih motorjev. Na komponente plinskih turbin vplivajo agresivni vplivi okolja, katerim so izpostavljene med obratovanjem, zato pride do okvar, kot so: korozija, termični šok in oksidacija. Tehnologija plazemskega naprševanja je cenovno ugodna tehnologija za izdelavo kovinskih in keramičnih prevlek. V članku avtorji predstavljajo raziskavo v kateri sta bila na podlago iz zlitine Inconel 718 s tehnologijo plazemskega naprševanja v zračni atmosferi nanešena vezivna prevleka CoNiCrAlY in prekrivni sloj iz YSZ prahu. Izdelani prevleki sta bili nato izpostavljeni termičnem utrujanju v peči pri 1150 °C z večimi enournimi cikli. Prisotnost poroznosti in razpok olajša difuzijo kisika v zgornjo plast prevleke kar vodi do nastanka termično induciranega oksida (TGO) na površini prevleke. Poleg tega sta bila najpomembnejša dejavnika za nastanek napak tvorba mešanih oksidov na meji med vezno in vrhno plastjo ter prisotnost drugih nepravilnosti. Rezultati preizkusov so pokazali, da povečanje števila termičnih ciklov zmanjšuje dobo trajanja TBC prevlek, zaradi sintranja zgornje plasti pri povišanih temperaturah.

Ključne besede: prevleke s toplotno pregrado, toplotni (termični) cikel, superzlitina Inconel 718, plazemsko naprševanje, CoNiCrAlY, cirkon stabiliziran z itrijem

1 INTRODUCTION

Atmospheric plasma spraying (APS) is one of the most important methods in the thermal-spray family. The APS technique, which is a type of the plasma spray technique, provide many advantages, such as an economic, quick and easy production; besides, almost all materials can be sprayed with this method. Plasma-sprayed particles quickly cool down from very high temperatures to low temperatures. Plasma-spray coatings consist of microstructured, layered and porous structures.[1,2]

Thermal barrier coatings (TBCs) are widely employed in gas turbines and its components operating at high-temperature service conditions. The main function of TBCs is to provide a protective thermal shield to protect the main material components, especially turbine blades and vanes, from the negative effects caused by high temperatures in the environment. There are three main layers in TBC systems, including a nickel-based superalloy substrate, an MCrAlY metallic bond coat and partially yttria-stabilized zirconia (YSZ), acting as the ceramic top coat.[3,4] The bond coat, which consist of MCrAlY (M = Ni and/or Co), is extensively applied to minimize the thermal mismatch between the superalloy substrate and the ceramic top coat.[5,6]

TBCs are subject to sudden temperature changes and thermal stress during service conditions. In high-temperature applications, TBCs are adversely affected and tend to suffer because of failures such as oxidation, hot corrosion and thermal cycling/shock so that they lose structural integrity. Residual stresses due to the thermal-expansion mismatch during the cooling and sintering of

the top coat, and oxidation of the bond coating cause the coating to become damaged during thermal cycling.[7,8]

In this study, the TBC system consists of a CoNiCrAlY metallic bond and YSZ ceramic top coat deposited with the APS technique on an Inconel 718 superalloy substrate. The effects of oxidation and TGO-growth behavior on the thermal durability were investigated through a furnace thermal cyclic test. The microstructure evolution and thermal durability were evaluated before and after the furnace thermal-cycling tests.

2 EXPERIMENTAL PART

2.1 Material

The Inconel 718 nickel-based superalloy was used as the substrate material. Superalloy disk-shaped samples with a diameter of 25.4 mm and thicknesses of 4 mm were used as substrates. The chemical composition of the nickel-based superalloy substrate is given in **Table 1**.

Table 1: Chemical composition of Inconel 718 Ni-based superalloy[9]

Elements, Chemical Composition, in mass fractions (*w*/%)							
Ni	Cr	Nb	Ti	Mo	Al	Co	Si
53.53	18.45	5.31	0.95	3.02	0.48	0.27	0.09
Cu	Mn	C	Ta	P	B	S	Fe
0.04	0.06	0.03	0.005	0.007	0.005	0.001	Balance

2.2 Spraying processes

Commercial CoNiCrAlY metallic bond-coat powder (Amdry 9951, Sulzer-Metco) with a 5–37 μm particle size and ZrO_2 + 8 %Y_2O_3 (YSZ) ceramic top-coat powder (Metco 204NS, Sulzer Metco) with a -45+20 μm particle size were used as the feedstocks. As previously mentioned, the APS technique was used for depositing both the metallic bond and ceramic top coatings. The top layer of YSZ with a thickness of 300 μm was applied on the CoNiCrAlY layer with a thickness of 100 μm on the superalloy substrates.

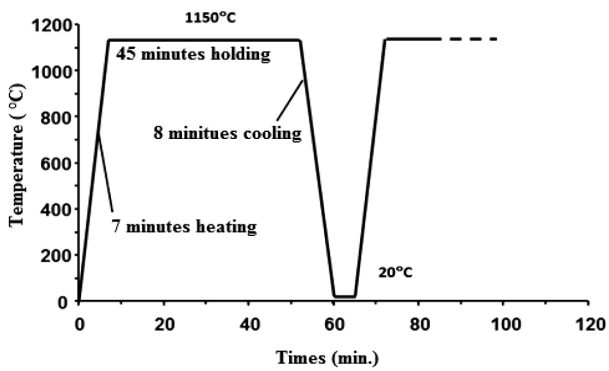

Figure 1: Thermal-cycling diagram during the furnace cycling test

2.3 Furnace thermal-cycling test

The lifetime of the TBCs tested with the furnace thermal-cycling test using rapid temperature furnace 1710 BL was as follows: The samples were heated to 1150 °C in 7 min, held at this temperature for 45 min and then cooled to 20 °C in air within 8 min. The thermal-loading diagram of the samples coated during thermal cycling is given in **Figure 1**. During isothermal-oxidation cycles, the temperature changes in the working furnace did not exceed 5 °C. The coating lifetime was determined with the thermal cycling carried out until the cracking point of the outer ceramic layer. This was considered to be cracked when 25 % of the sample surface was blistering. The surface failure was visually determined based on the percentage of the separation of the outer ceramic layer from the sample surface. At the end of the thermal-cycling tests, the samples were investigated from both the top surface and cross-sectional area via a scanning-electron-microscopy (SEM) analysis.

3 RESULTS AND DISCUSSION

3.1 As-sprayed TBC

A SEM microstructure image of an as-deposited TBC is shown in **Figure 2**. The APS-applied CoNiCrAlY metallic bond and the YSZ top coat exhibit a porous structure and some cracks and open discontinuities due to the deposition process. The metallic-bond and top-coat structures show typically characteristic properties of the plasma-spray technique.

In **Figure 3**, the top surface of the TBC is shown. There are some micro-cracks due to heating and rapid cooling of the sprayed particles during the deposition process as well as melted and unmelted particles.

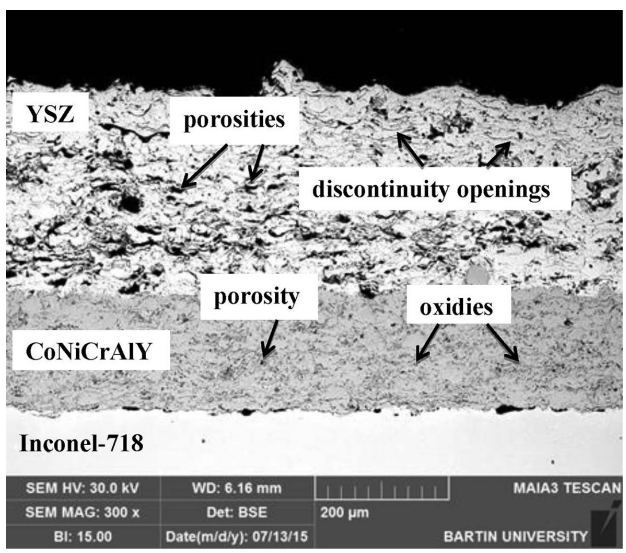

Figure 2: As-deposited TBC cross-sectional SEM microstructure

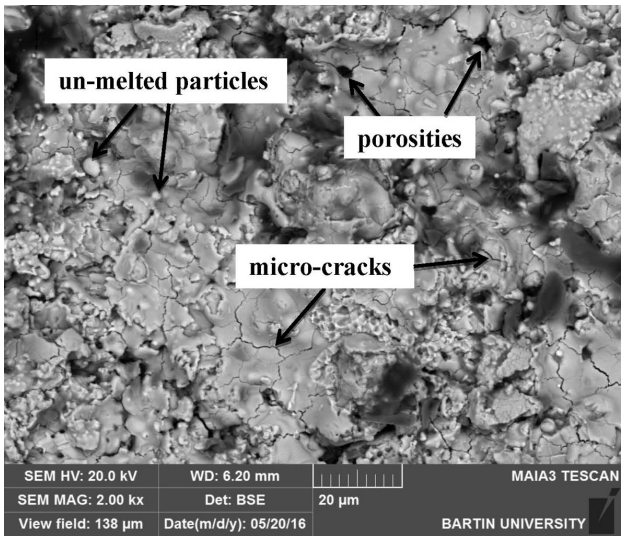

Figure 3: Top-coat SEM image of the as-sprayed TBC

3.2 Thermal-cycling test of the coated specimens

At high temperatures, oxygen can easily diffuse from the top coat to the bond coat due to the ionic conductivity of YSZ. Also, the coating includes many imperfections such as cracks and porosity, which accelerate the penetration of oxygen to the metallic bond coat. As a result, the bond coat oxidizes easily at high temperatures in spite of the ceramic coat. According to the Ellingham diagram, Y and Al are the elements that enter the first reaction with oxygen in the CoNiCrAlY bond coat due to low-standard free energies. With the effect of high temperature, the particles are still oxidized in flight and during the deposition on the substrate material.[10]

Using the APS method, there are many internal oxide formations in the coating because of the excessively high temperatures due to plasma during the deposition of the coating. Since the concentration of the Y element is much lower than those of the other elements, Y can be entirely depleted. Thus, after the deposition of a TBC, Al is oxidized at the interface and Al_2O_3 is formed.[11–13]

In the early stages of the cyclic oxidation, the TGO layer mainly occurred as the Al_2O_3 phase. This oxidation causes thermal stresses at the interface between the bond and the top coat due to both the phase transformations of Al_2O_3 (γ, δ, θ and α) and a lower thermal-expansion coefficient compared to YSZ. Al_2O_3 (especially in the α-Al_2O_3 form) is thermodynamically a very stable phase compared to the other phases such as Cr_2O_3, (Co, Ni)O or $(Co,Ni)(Al,Cr)_2O_4$.[13] In addition, it provides a better resistance against the oxygen expansion into the bond coat. Depending on the time, the Al concentration decreases to a critical level and Cr_2O_3 and (Co, Ni)O phases form at the interface. Afterwards, these oxides react with Al_2O_3 and spinel phases occur. The thermal-expansion coefficient of the spinel phases is relatively lower than that of Al_2O_3, which means it leads to a higher stress.[14,15]

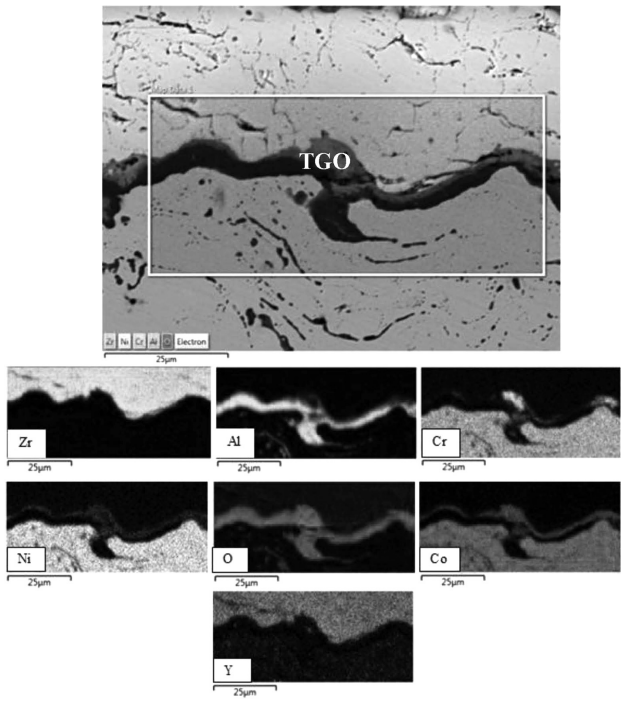

Figure 4: Elemental mapping microstructure belonging to the YSZ TBC after a 40-h thermal-cycling test

In addition, the spinel phases grow faster than Al_2O_3 and show larger volume changes.[16]

In **Figure 4**, an elemental mapping microstructure belonging to the YSZ TBC after a 40-h thermal-cycling test is shown. The coating structure almost preserved its uniformity. At the interface, the Al_2O_3 phase is dominant and a mixture of oxide formations like Cr_2O_3, (Co, Ni)O and spinels can be observed. In the bond coat, dark stringers represent the Al_2O_3 phase. In addition, the top coat was sintered due to the effect of high temperature

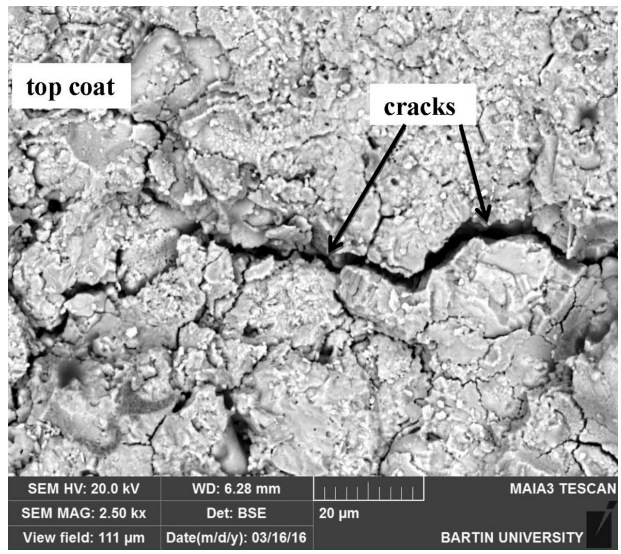

Figure 5: Top-surface SEM image of the TBC after the thermal-cycling test

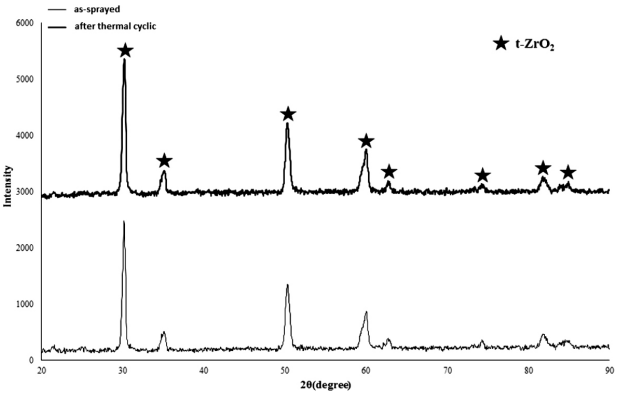

Figure 6: XRD analysis of the TBC before and after the thermal-cycling test

depending on time. This can be explained with decreasing discontinuity openings.

In **Figure 5**, a top-surface SEM image of the TBC after the thermal-cycling test is given. After 40 thermal cycles, the top-surface crack area of the TBC covers approximately 25 %. In **Figure 5**, a failed surface of the TBC is shown. According to Figure 5, there are large crack formations and sintered areas.

Figure 6 shows that there is only one phase in the as-sprayed TBC. After the thermal-cycling test, there is not any phase transformation so the structure is similar to the as-sprayed TBC. The semi-stable tetragonal ZrO_2 phase is durable up to approximately 1200 °C, which means that the crack propagation does not progress into the bond coat.[8] This can also be understood from a cross-sectional SEM image of the failed TBC.

J. A. Haynes et al.[17] applied furnace thermal-cycling tests to YSZ TBCs including a NiCrAlY bond coat produced with the APS method. The tests were carried out for one hour in a furnace at 1150 °C with periods of 15-min heating and 30-min cooling. The test result shows that after 100 thermal cycles, the APS TBCs failed. However, in the present study, the heating and cooling times of the thermal-cycling tests are shorter. Thus, the CoNiCrAlY TBC is exposed to damage earlier than in the above study. R. Chen et al. used the APS technique to produce a CoNiCrAlY bond coated with the YSZ TBC on an Inconel 625 substrate. Their thermal-cycling test at 1050 °C showed a parabolic TGO growth. The growth rate of the TGO structure increased proportionally as the thermal-cycling period increased. This result supports the present study.

A. El-Turki et al.[18] studied the thermal-cycling behavior of a VPS NiCoCrAlY bond coated with APS YSZ at 1050 °C, with 25-min heating, 300-h holding and 30-min cooling. The TBCs were damaged after 21 cycles. The damage of the TBCs started at the same time as the damage to TGO interface areas. The use of the VPS technique allowed a low porosity and oxidation during the deposition of the bond coat, and their total holding time was very long compared to the present study.[19] J. Sun et al.[20] produced their bond coat using the HVOF technique; afterwards they carried out the deposition of APS YSZ. Their thermal cycling was performed at 1100 °C for one hour, with 10-min cooling. After 30 thermal cycles, the TBC underwent a significant failure. In contrast, the present-study condition is more destructive, but the thermal-cycling lifetime is longer. As a result, the used bond-coat powder type, production technique and thermal-cycling conditions can cause significant differences in the lifetime of TBCs.[20] In the present study, the APS TBC separated from the bond-coat surface of the ceramic top coat after 40 h of the thermal cycling and was spalled and damaged. Furthermore, a TGO structure formed during the thermal cycling, causing failure of the TBC systems. The growth of the oxide layer formed the TGO structure and an increase in the stresses increased the failure formation.

4 CONCLUSIONS

In this study, TBCs including CoNiCrAlY bonds and YSZ were deposited using the APS technique. Furnace thermal-cycling tests were performed to predict the thermal-cycling lifetime of the TBCs and to observe their microstructural changes. The results obtained at the end of the observations are given below.

TBCs were damaged, with their cracks covering 25 % of the top coat after 40 cycles.

The most effective factor of failure was the formation of mixed oxides and spinels at the interface of the bond and the top coat, according to the cross-sectional investigations.

The porosity and cracks of the top coat caused the formation of TGOs at the interface.

The top coat was sintered as a result of high temperature depending on time.

At the interface, the Al_2O_3 phase is dominant, but a mixture of oxide formations like Cr_2O_3, (Co, Ni)O and spinels is also observed. In the bond coat, dark stringers represent the Al_2O_3 phase. The mixture of oxides formed at the interface was mainly responsible for the failure of the TBCs after the thermal cycling.

Acknowledgements

The present study was derived from the Ph.D. thesis of Mustafa Kaplan at the Selcuk University Graduate School of Natural and Applied Sciences, Konya, Turkey. The study was also supported by Selcuk University Scientific Research Projects under the Grant Number of 15201071.

5 REFERENCES

[1] L. Pawlowski, The Science and Engineering of Thermal Spray Coatings, 2nd ed., John Wiley & Sons, England, 2008, 656

[2] K. M. Doleker, A. C. Karaoglanli, Comparison of oxidation behavior of shot-peened plasma spray coatings with cold gas dynamic spray coatings, Oxidation of Metals, (**2016**), 1–12, doi:10.1007/s11085-016-9691-3

[3] K. E. Schneider, V. E. Belashchenko, M. Dratwinski, S. Siegmann, A. Zagorski, Thermal spraying for power generation components, John Wiley & Sons, England, 2006, 285

[4] Z. Gao, G. Jin, Z. Cai, Y. Fu, X. Cui, Thermal cycling property of supersonic atmospheric plasma sprayed thermal barrier coatings reinforced by Ni-coated YSZ fibers, Surface and Coatings Technology, (2017), doi:10.1016/j.surfcoat.2017.01.041

[5] A. C. Karaoglanli, K. M. Doleker, B. Demirel, A. Turk, R. Varol, Effect of shot peening on the oxidation behavior of thermal barrier coatings, Applied Surface Science, 354 (**2015**) 2, 314–322, doi:10.1016/j.apsusc.2015.06.113

[6] A. C. Karaoglanli, K. M. Doleker, Y. Ozgurluk, State of the art thermal barrier coating (TBC) materials and TBC failure mechanisms, properties and characterization of modern materials, Adv. Struct. Mater., 33 (**2017**), 441–452, doi:10.1007/978-981-10-1602-834

[7] A. N. Khan, J. Lu, Behavior of air plasma sprayed thermal barrier coatings, subject to intense thermal cycling, Surface and Coatings Technology, 166 (**2003**), 37–43, doi:10.1016/S0257-8972(02) 00740-5

[8] K. M. Doleker, A. C. Karaoglanli, Comparison of oxidation behavior of YSZ and $Gd_2Zr_2O_7$ thermal barrier coatings (TBCs), Surface and Coatings Technology, (2016), doi:10.1016/j.surfcoat.2016.12.078

[9] F. Pusavec, H. Hamdi, J. Kopac, I. S. Jawahir, Surface integrity in cryogenic machining of nickel based alloy – Inconel 718, Journal of Materials Processing Technology, 211 (**2011**) 4, 773–783, doi:10.1016/j.jmatprotec.2010.12.013

[10] K. Yuan, R. L. Peng, X. H. Li, S. Johansson, Y. D. Wang, Some aspects of elemental behaviour in HVOF MCrAlY coatings in high-temperature oxidation, Surface and Coatings Technology, 261 (**2015**), 86–101, doi:10.1016/j.surfcoat.2014.11.053

[11] O. Kovářík, P. Haušild, J. Siegl, T. Chráska, J. Matějíček, Z. Pala, M. Boulos, The influence of substrate temperature on properties of APS and VPS W coatings, Surface and Coatings Technology, 268 (**2015**), 7–14, doi:10.1016/j.surfcoat.2014.07.041

[12] I. Milas, B. Hinnemann, E. A. Carter, Diffusion of Al, O, Pt, Hf, and Y atoms on alpha-Al_2O_3(0001): implications for the role of alloying elements in thermal barrier coatings, Journal of Materials Chemistry, 21 (**2011**) 5, 1447–1456. doi:10.1039/c0jm02212h

[13] J. Liu, Y. H. Sohn, K. S. Murphy, Microstructural evolution of durable thermal barrier coatings with Hf and/or Y modified CMSX-4^{TM} superalloy substrates, Materials Science Forum, 539–543 (**2007**), Thermec 2006, 1206–1211, doi:10.4028/www.scientific.net/MSF.539-543.1206

[14] L. Y. Ni, C. Liu, H. Huang, C. G. Zhou, Thermal cycling behavior of thermal barrier coatings with HVOF NiCrAlY bond coat, Journal of Thermal Spray Technology, 20 (**2011**) 5, 1133–1138, doi:10.1007/s11666-011-9647-8

[15] C. Zhou, C. Wang, Y. Song, Evaluation of cyclic oxidation of thermal barrier coatings exposed to NaCl vapor by finite element method, Materials Science and Engineering A, 490 (**2008**) 6, 351–358, doi:10.1016/j.msea.2008.01.050

[16] S. Laxman, B. Franke, B. W. Kempshall, Y. H. Sohn, L. A. Giannuzzi, K. S. Murphy, Phase transformations of thermally grown oxide on (Ni,Pt)Al bondcoat during electron beam physical vapor deposition and subsequent oxidation, Surface and Coatings Technology, 177 (**2004**), 121–130, doi:10.1016/j.surfcoat.2003.08.072

[17] J. A. Haynes, M. K. Ferber, W. D. Porter, Thermal cycling behavior of plasma-sprayed thermal barrier coatings with various MCrAlX bond coats, Journal of Thermal Spray Technology, 9 (**2000**) 38, 38–48, doi:10.1361/105996300770350041

[18] R. Chen, X. Wu, D. Dudzinski, Influence of thermal cycle frequency on the TGO growth and cracking behaviors of an APS-TBC, Journal of Thermal Spray Technology, 21 (**2012**) 6, 1294–1299, doi:10.1007/s11666-012-9824-4

[19] A. El-Turki, G. C. Allen, C. M. Younes, J. C. C. Day, An investigation of the effect of thermal cycling on plasma-sprayed zirconia/NiCoCrAlY thermal barrier coating, Materials and Corrosion, 55 (**2004**) 1, 24–29, doi:10.1002/maco.200303709

[20] J. Sun, L. L. Zhang, D. Zhao, Microstructure and thermal cycling behavior of nanostructured yttria partially stabilized zirconia (YSZ) thermal barrier coatings, Journal of Rare Earths, 28 (**2010**) 1, 198–201, doi:10.1016/S1002-0721(10)60

UDK 669.017.3:67.017:669.018.2
Original scientific article/Izvirni znanstveni članek

ISSN 1580-2949
MTAEC9, 51(6)903(2017)

PHASE-TRANSFORMATION BEHAVIOR AND MICROMECHANICAL PROPERTIES OF A DUAL-PHASE STEEL AFTER CHEMICAL MODIFICATIONS

FAZNE SPREMEMBE IN MIKROMEHANSKE LASTNOSTI DVOFAZNIH JEKEL PO KEMIJSKIH PRILAGODITVAH

Aijuan Zhao[1], Guoxin Zhao[2], Haijie Sun[1], Hairong Gao[1], Shaoqing Wang[1], Xiuli Chen[1]

[1]School of Chemistry and Chemical Engineering, Zhengzhou Normal University, Zhengzhou 450044, Henan, China
[2]Institute of Chemical Industry and Food, Zhengzhou Institute of Technology, Zhengzhou 450044, Henan, China
mkyj2017@163.com

Prejem rokopisa – received: 2017-01-31; sprejem za objavo – accepted for publication: 2017-05-30

doi:10.17222/mit.2017.017

In this work, the phase-transformation behavior and micromechanical properties of a dual-phase steel after chemical modifications were investigated theoretically and experimentally. In particular, the micromechanical behavior of the steel was modeled, based on the effects of the microstructure, phase fractions, local compositions of single phases and their area shapes. The developed model was used for predicting the damage behavior of a specimen. It was demonstrated that the tensile strength increased with the increasing temperature due to an increase in the amount of martensite in the steel, but the hardening behavior of this specimen was affected by the microstructure. Furthermore, the flow curves of the steel under different intercritical temperatures could be well predicted based on the real microstructures. The subsequent simulation results showed that while higher stress concentrated on the martensite, the shear-band appearance strongly depended on the microstructures of the phases. In addition, for the prediction of damage behaviors, the true stress/true strain curves of macroscale simulations showed good agreement with the experiments involving differently heat-treated steels.

Keywords: intercritical treatment, steel, micro model

V tem delu so teoretično in eksperimentalno preiskovali fazne spremembe in mikromehanske lastnosti dvofaznega jekla po kemijskih prilagoditvah. Še posebej je bilo modelirano mikromehansko obnašanje jekla glede na mikrostrukturo, deleže posameznih faz, lokalno sestavo posameznih faz in njihovo morfologijo. Razviti model je bil uporabljen za napoved poškodb vzorca. Dokazano je bilo, da se natezna trdnost povečuje z naraščajočo temperaturo zaradi naraščanja vsebnosti martenzita v jeklu, vendar je na kaljivost tega vzorca vplivala mikrostruktura. Nadalje je bilo ugotovljeno, da je možno krivulje tečenja jekla pri različnih interkritičnih temperaturah dobro napovedati na podlagi dejanskih mikrostruktur. Nadalje so rezultati simulacij pokazali, da so višje napetosti koncentrirane na martenzitu in istočasna prisotnost strižnih pasov, močno odvisne od mikrostruktur posameznih faz. Poleg tega je za napoved poškodb pomembno, da se prave krivulje napetost-deformacija, dobljene s pomočjo simulacij na makronivoju, dobro ujemajo z eksperimentalnimi, dobljenimi pri različno toplotno obdelanih jeklih.

Ključne besede: interkritična obdelava, jeklo, mikromodel

1 INTRODUCTION

In the past few decades, HSLA steels were widely used in the fields of pipelines, pressure vessels, heavy machinery, buildings, cars, bridges, offshore platforms and ships.[1] However, with the development of the technology and deterioration of the environment, an even better performance of advanced steel was required, especially for the automotive industry.[2] As a result, DP steels were developed. The matrix of DP steels consists of two different phases: ferrite and martensite; the former shows great plasticity and toughness, while the later shows high strength. Combining the two great performances, DP steels show great mechanical properties.[3]

The intercritical heat treatment, which involves holding in the two-phase (α+γ) region, followed by quick cooling, is frequently applied to obtain ferrite and martensite phases in a low-alloy steel.[4–8] Previous investigations suggested that different chemical compositions, thermomechanical processing routes or heat treatments lead to different microstructural configurations, different phase-space distributions and other microstructure characteristics, affecting the deformation and failure behaviors of DP steels.[9,10]

Recently, researchers obtained the flow curves of the composite phases using micromechanical modelling based on the RVEs selected from a real microstructure.[11–19] The flow behavior of a DP steel mainly depends on the properties of ferrite and martensite and the volume fractions of different phases. As steel has the same chemical composition, when modelling heat-treated steels, the model mainly focuses on the effects of strengthening methods and the grain size on the strength of different phases. With respect to material modeling, two equations, the Ashby–Orowan equation and

Table 1: Chemical composition of Gr.65 steel

Elements	C	Si	Mn	P	S	Al	V	Ti	Cr	Nb	Fe
w/%	0.13	0.3	1.4	0.014	0.002	0.03	0.043	0.014	0.06	0.031	Balance

Hall-Petch equation, were taken into account when describing the flow-stress behavior of steel.[12]

Moreover, in actual engineering, the predictions of deformation and failure behaviors of DP steels are the final purpose. Some of the available damage models such as the ones of the aforementioned failure mechanisms, the Gurson–Tvergaard–Needleman (GTN) damage model, the extended finite-element model (XFEM), the cohesive-zone model and so on, were closely estimated for the experiments.[20–23]

A. Ramazani et al. investigated the effect of an inhomogeneous morphology on the mechanical properties of a welded joint.[15] 2D RVEs simulated flow curves were corrected to 3D ones, taking into account the effects of the microstructure, the chemical composition and the area fraction on the macroscopic mechanical properties of the welded joint. Finally, the tensile test of the welded material with the inhomogeneous morphology was simulated and good agreement between the experimental and predicted flow curves was achieved.

The aim of this work was to predict the damage behavior of an HSLA steel under different intercritical-temperature conditions and to establish a relational model presenting the connection between the microstructure and macromechanics of materials to provide guidance for material design based on the microstructure.

2 EXPERIMENTAL PART

The as-received material was the Gr.65 steel, a high-strength low-alloy structural steel (with a yield strength of 460MPa), supplied as a hot-roll plate. **Table 1** gives the chemical composition of the steel. The initial microstructure mainly consisted of ferrite with a small amount of pearlite, shown in **Figure 1**.

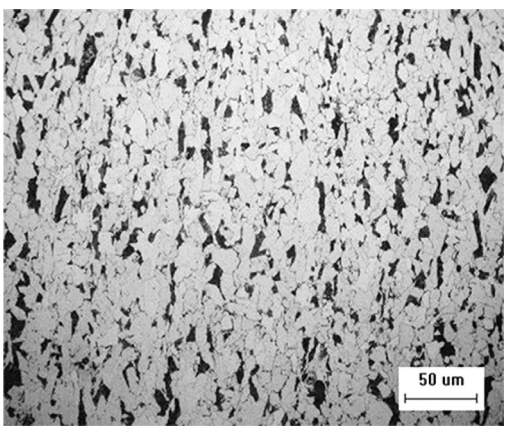

Figure 1: Original microstructure of Gr. 65 steel in OM

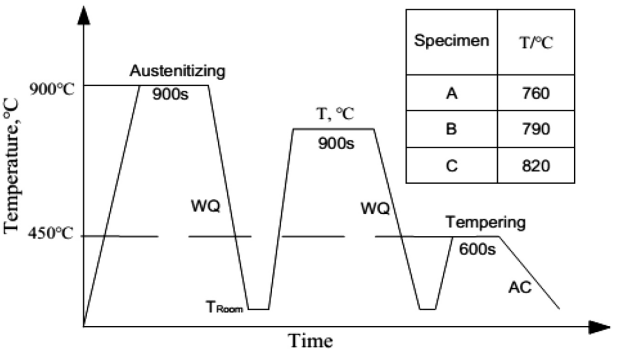

Figure 2: Heat-treatment regime for the samples

All of the specimens cut along the rolling direction of the plate, with dimensions of 70 mm × 40 mm × 4 mm (length, width and thickness) underwent heat treatment in a resistance furnace, and the heat-treatment regime is illustrated on **Figure 2**. The specimens were first austenitized at 900 °C for 15 min, followed by water cooling to get the martensite phase, then reheated to different intercritical temperatures (760, 790 and 820) °C for 15 min and water cooled again to get a ferrite-martensite microstructure. Then, all the specimens were tempered at 450 °C for a holding time of 10 min and air cooled to room temperature. After the heat treatments, the specimens were ground, polished and etched for metallographic analyses.

Figure 3 shows the geometry of the specimens for tensile testing. The tensile specimens were tested at a strain rate of 0.00033 s^{-1}. The force and displacement curves were recorded by means of a load cell and extensometer (in this study, the length of the extensometer was 12.5 mm) during the tests. Later, the stress/strain curves of the steels were calculated at room temperature.

3 NUMERICAL APPROACH

3.1 Micromechanical modeling

Recently, the model based on the Ashby-Orowan equation and Hall-Petch equation was usually used to

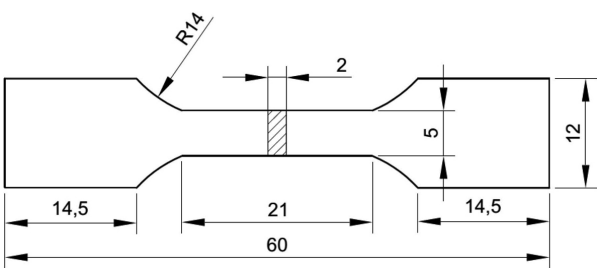

Figure 3: Geometry of a specimen for tensile testing

predict the flow-stress behavior of each phase in the steel.[11–15,18] The former equation represents the material strengthening due to the carbon content and other alloying elements' carbide precipitation, while the latter is based on the dislocation theory determining the effects of the grain size.[12] The approach can be expressed as Equation (1):

$$\sigma = \sigma_0 + \Delta\sigma_s + \alpha M \mu \sqrt{b} \sqrt{\frac{1-\exp(-Mk\varepsilon)}{kL}} \quad (1)$$

where σ is the flow stress and ε is the true strain. The first term σ_0 takes care of the Peierls stress and the effects of the elements in a solid solution (Equation (2)). The second term is the solid-solution strengthening due to the carbon content (Equations (3) and (4)). α is the material constant, M is the Taylor factor, μ is the shear modulus, b is the Burgers vector, k is the recovery rate and L describes the dislocation mean free path.

$$\sigma_0 \text{ (in MPa)} = 77 + 750(\%P) + 60(\%Si) + 80(\%Cu) + \\ + 45(\%Ni) + 60(\%Cr) + 80(\%Mn) + 11(\%Mo) \quad (2)$$

From the literature, the values for parameters α, M, μ, and b were 0.33, 3, 80000 MPa, and $2.5 \cdot 10^{-10}$ m. For ferrite, the k value used is $10^{-5}/d_\alpha$, where d_α is the ferrite gain size. For martensite, two constants, 41 and 0.038, were used to define k and L.[11,13,15,18]

The second term is the solid-solution strengthening due to the carbon and nitrogen contents. For ferrite, it is:

$$\Delta\sigma_s = 5000(\%C_{ss}^{f} + \%N_{ss}^{f}) \quad (3)$$

while for martensite, it is

$$\Delta\sigma_s = 3605(\%C_{ss}^{m} + \%N_{ss}^{m}) - 161 \quad (4)$$

where C_{ss}^{f} and $\%N_{ss}^{f}$ denote the carbon and nitrogen contents in the solid solution (w/%) in ferrite, C_{ss}^{m} and $\%N_{ss}^{m}$ are the carbon and nitrogen contents in the solid solution in martensite, respectively. The values of the carbon and nitrogen contents were computed with software JMatPro.

3.2 Macromechanical modeling

2D RVE was generated based on real micrographs and can involve all the microstructural features in the calculations. However, a specimen deforms three-dimensionally during the uniaxial tensile test and 2D-modeling approaches are not able to predict the flow curve of a material precisely. Therefore, in order to study the effects of microstructural features on the mechanical properties of a heat-treated steel, the predicted flow curves of 2D modeling should be correlated to the 3Ds by introducing a correlation factor. A. Ramazani et al.[11] introduced a function as σ_{3D}/σ_{2D} to describe the correlation between the 2D and 3D flow-curve modelling of DP steels. The function mainly considered the effect of the martensite volume fraction and the equivalent plastic strains under the 2D FE simulation and provided some influence exponentials, as shown in Equation (5). Therefore, the developed flow curves from 2D RVE calculations were corrected to 3D curves using Equation (5). These corrected flow curves are used as input data for macromechanical modeling.

$$\sigma_{3D}/\sigma_{2D} = 2\times10^{-4} \times (\varepsilon_{eq}^{p})^2 \times V_m^3 + 1\times10^{-7} V_m^3 + \\ + 0.0218 \times (\varepsilon_{eq}^{p})^2 \times V_m^2 + 7\times10^{-5} \times V_m^2 + 0.18 \times (\varepsilon_{eq}^{p})^2 \times \\ \times V_m + 0.007 \times (\varepsilon_{eq}^{p})^2 \times V_m + 0.0036 \times (\varepsilon_{eq}^{p})^2 \times V_m + 1 \quad (5)$$

where σ_{3D} and σ_{2D} are the 3D and 2D flow stresses, V_m and ε_{eq}^{p} are the martensite volume fraction and equivalent plastic strains under the 2D FE simulation.

In order to study the microstructure-based failure of the intercritically heat-treated HSLA steel, a GTN model was applied to investigate the damage behavior of the material at the macroscale. The GTN model is formulated as Equation (6):

$$\Phi_{GTN} = \left(\frac{\sigma_v}{\sigma_y}\right)^2 + 2q_1 \cdot f^* \cosh\left(\frac{3}{2} q_2 \frac{\sigma_H}{\sigma_y}\right) - (1 + q_3 f^{*2}) = 0 \quad (6)$$

where σ_v, σ_y and σ_H are the von Mises equivalent stress, the matrix-material yield stress and the hydrostatic stress; q_1, q_2 and q_3 are the model parameters, in practice, $q_1 = 1.5$, $q_2 = 1$ and $q_3 = (q_1)^2 = 2.25$.[24] Function f^* was introduced by V. Tvergaard and A. Needleman[25] to describe the effect of a void interaction starting during the failure process (Equation (7)):

$$f^* = \begin{cases} f; & f \le f_c \\ f_c + \dfrac{1/q_1 - f_c}{f_F - f_c}(f - f_c); & f > f_c \end{cases} \quad (7)$$

were f, f_c and f_F are the void volume fraction, the critical void volume fraction at the onset of void coalescence, and the void volume fraction at failure, respectively. The whole void-volume-fraction development is defined as the sum of the growth of the existing voids: $\dot{f}_{growth}$ and the nucleation of new voids $\dot{f}_{nucleation}$.

As the matrix material is considered to be incompressible, $\dot{f}_{growth}$ is defined by the volumetric part of the plastic-strain rate $\dot{\varepsilon}_{kk}$:

$$\dot{f}_{growth} = (1-f) \cdot \dot{\varepsilon}_{kk} \quad (8)$$

C. C. Chu and A. Needleman[26] assumed that the strain controlled the void-nucleation mechanism, following a normal distribution. $\dot{f}_{nucleation}$ is defined by the rate of the equivalent plastic strain $\dot{\bar{\varepsilon}}$ in Equation (9):

$$\dot{f}_{nucleation} = A \cdot \dot{\bar{\varepsilon}} \quad (9)$$

where

$$A = \frac{f_N}{s_N \sqrt{2\pi}} \exp\left[-\frac{1}{2}\left(\frac{\bar{\varepsilon} - \varepsilon_N}{S_N}\right)^2\right] \cdot \dot{\bar{\varepsilon}},$$

f_n is the volume fraction of the secondary voids, ε_N and S_N are the mean value and the standard deviation of the

characteristic plastic-strain distribution, $\bar{\varepsilon}$ and $\dot{\bar{\varepsilon}}$ are the equivalent plastic strain and the rate of the equivalent plastic strain, respectively.

Finally, the damage-evolution law is given as:

$$f = \dot{f}_{\text{growth}} + \dot{f}_{\text{nucleation}} = (1-f)\cdot\dot{\varepsilon}_{\text{kk}} + \\ + \frac{f_{\text{N}}}{s_{\text{N}}\sqrt{2\pi}} \exp\left[-\frac{1}{2}\left(\frac{\bar{\varepsilon}-\varepsilon_{\text{N}}}{S_{\text{N}}}\right)^2\right]\cdot\dot{\bar{\varepsilon}} \quad (10)$$

In this damage model, ε_{N} and S_{N} were assumed to be 0.3 and 0.1, while the other parameters were determined with a calibration of the numerical results using experimental data. [24]

3.3 Macro/microscopic finite-element model and boundary conditions

All the associated numerical models were performed with the finite-element software ABAQUS. **Figure 4a** shows the macroscopic finite-element model for a tensile-test specimen, and the specimen was modeled with solid, reduced-integration element C3D8R. The boundary condition and the load plan, according to which the upper part of the specimen was stretched and the bottom was fixed was consistent with the real condition.

In the case of the macroscopic finite-element simulations, all the specimens were generally considered as continuous and homogeneous. On the microscale, each constituent character of the microstructure of a steel specimen needed to be incorporated. RVE was applied to take into account the influences of different deformation behaviors of each phase on the resulting mechanical properties. The 2D RVE models were generated from real microstructures modeled with plane strain element CPE4R in ABAQUS. The selection requirement is that the volume percent of martensite is the same with the real microstructure in 2D RVE. The boundary condition and load plan are shown in **Figure 4b**; the bottom of 2D RVE is fixed and the top of it is pulled.

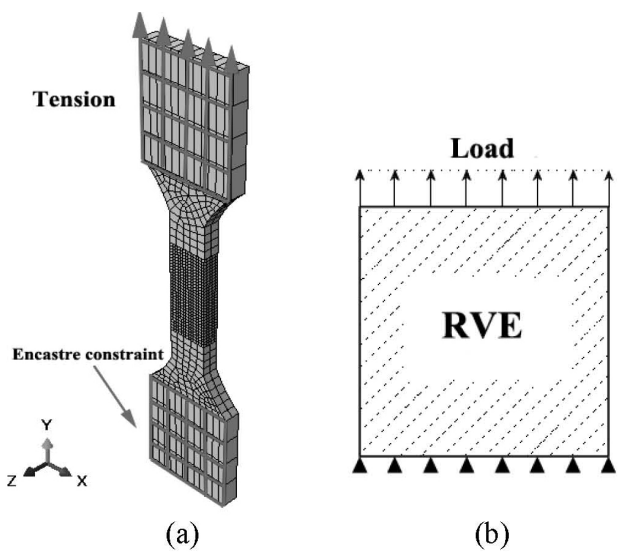

Figure 4: a) Macrostructural finite-element mode, b) microstructural finite-element model

4 RESULTS AND DISCUSSION

4.1 Microscale simulation results

Intercritical temperature T, ferrite grain size d_α, martensite fraction V_{m}, along with the carbon content in ferrite C_{ss}^{f} and in martensite C_{ss}^{m} are listed in **Table 2**. After calculating the nitrogen content, we found that the effect of the nitrogen content on the solid-solution strengthening was extremely minimal, so we ignored the nitrogen contents in ferrite and martensite. In general, the parameter has a monotonous trend with an increase in the temperature (760 °C to 820 °C), except for the ferrite grain.

Table 2: Model parameters for the flow-curve prediction for individual phases

Specimen	T(°C)	d_α (m)	V_{m} (%)	C_{ss}^{f} (%)	C_{ss}^{m} (%)
A	760	5.28	48%	0.00688	0.33
B	790	2.31	57%	0.0059	0.21
C	820	4.17	69%	0.00455	0.13

Figure 5 exhibits the stress/strain curve for micromechanical modelling. It can be seen that ferrite shows a ductile hardening behavior, whereas martensite is more brittle and also shows a higher strength. In this study, the grain size and the carbon content played important roles in the computed yield curves for ferrite and materials. From **Table 2** and **Figure 5**, the solute carbon content limits the yield strength of martensite, while the ultimate stress of ferrite is dependent on the grain size.

The microstructure in OM and the selections of 2D RVEs from the real microstructures at different intercritical temperatures are displayed in **Figure 6**. The phases of all the specimens were ferrite and martensite, and after different intercritical temperatures, the phases

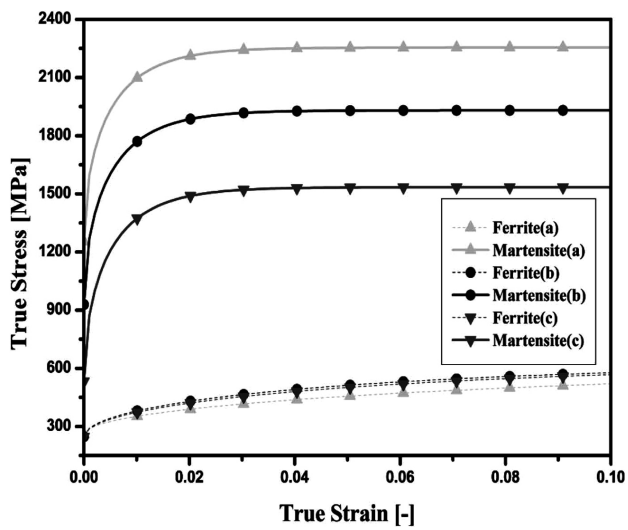

Figure 5: Flow curves for ferrite and martensite phases in a specimen

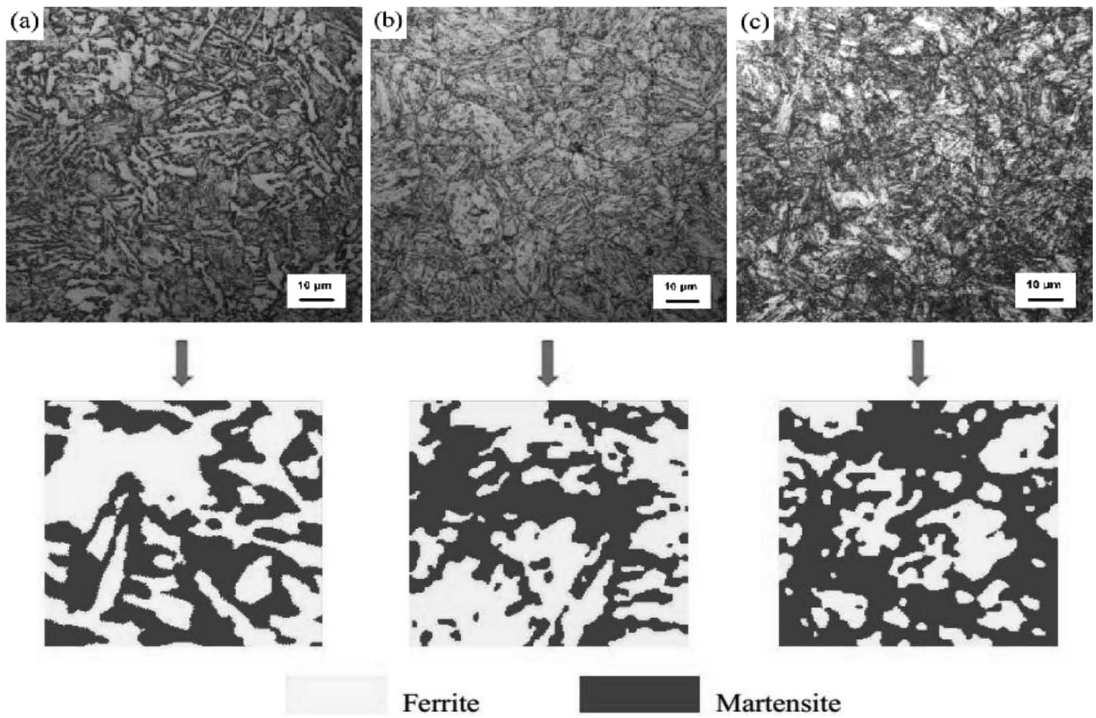

Figure 6: Microstructure in OM and selections of 2D RVEs from real microstructures at different intercritical temperatures: a) 760 °C, b) 790 °C and c) 820 °C

presented different microstructures. After the heat treatment (at 760 °C), lath martensite and banded ferrite coexisted in steel, as shown in **Figure 6a**. When the second quenching temperature was 790 °C, the grain boundaries were clear and the parallel lath martensite was distributed in the grains (**Figure 6b**). The amount of lath martensite increased and the grain boundaries disappeared at 820 °C (**Figure 6c**).

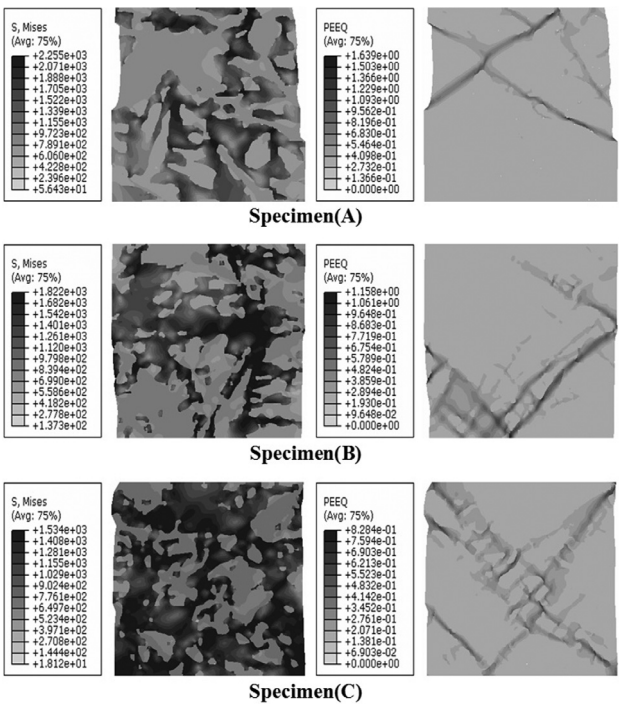

Figure 7: Von Mises stress distributions (left) and equivalent plastic-strain distributions (right) on 2D RVEs

After a 5 % deformation, the von Mises stress and equivalent plastic-strain distributions for the specimens were simulated; the results are shown in **Figure 7**. It can be clearly concluded that the stress is mainly carried by martensite, and a higher stress difference exists between the ferrite and martensite phases due to the von Mises stress distributions. For the first specimen, the maximum stress mainly focuses on the small connecting belt among the martensite grains (**Figure 7a**). Regarding the second specimen, the maximum stress is mainly distributed along the lath martensite (**Figure 7b**). The last specimen's maximum stress is distributed uniformly in martensite (**Figure 7c**). Furthermore, the equivalent plastic-strain distributions show shear bands in the ferrite areas; it is easily seen that the amount of shear bands of specimen (A) is low, while more shear bands consist in specimen (C).

Because of different microstructures, there are some differences in the shape of fracture surfaces. On the first specimen, there are more shear-fracture dimples on the fracture face and a tearing dimple is shown (**Figure 8a**). For the second specimen, tear dimples are obviously seen from the fracture morphology; its fracture tearing edge is higher and the tearing dimple is deeper (**Figure 8b**). For the third specimen, the micro-fracture morphology shows some large equiaxed dimples (**Figure 8c**).

Therefore, the effective stress/strain and work-hardening-rate/true-strain curves from the 2D RVE calculations were corrected to 3D curves using Equation

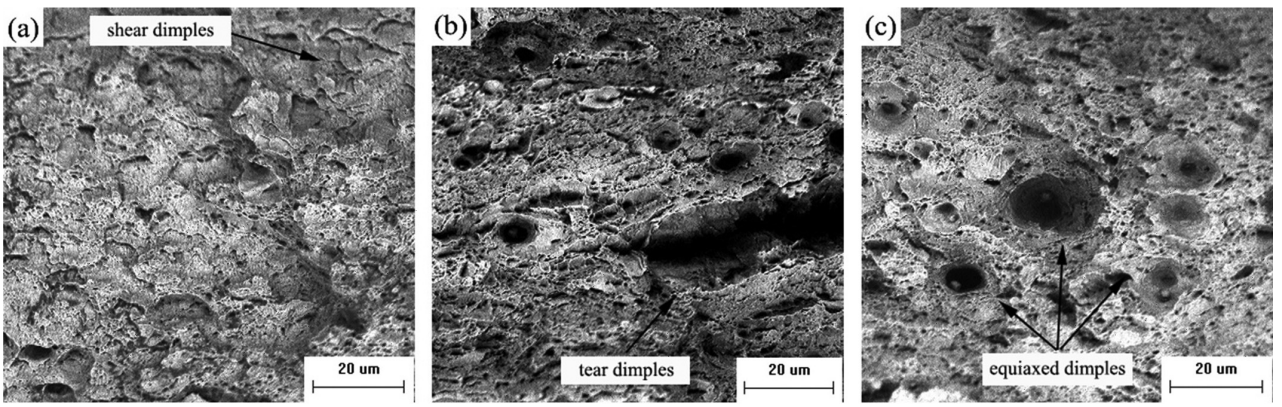

Figure 8: Fracture surfaces of the heat-treated specimens at different intercritical temperatures: a) 760 °C, b) 790 °C and c) 820 °C

(5). These corrected curves are shown in **Figure 9**; specimen (B) shows the highest work hardening behaviors, higher stress level and yield stress.

4.2 Macroscale simulation results

The flow curves were obtained through micromechanical modeling and inputted into the macromechanical model. Subsequently, the GTN damage model was applied to investigate the failure behavior of the material. After macromechanical modeling, the stress/strain curves of the simulation were compared with the experimental curves, as shown in **Figure 10**. It can be observed that the macromechanical model based on the flow curves of micromechanical modeling provides very good estimates for the experimental results.

The equivalent plastic-strain distribution and void-volume-fraction distribution in tensile samples (1/2 part of the extensometer measurement) at a 6 % deformation are shown in **Figure 11**. After the deformation due to the engineering strain of 6 %, the plastic strain and void

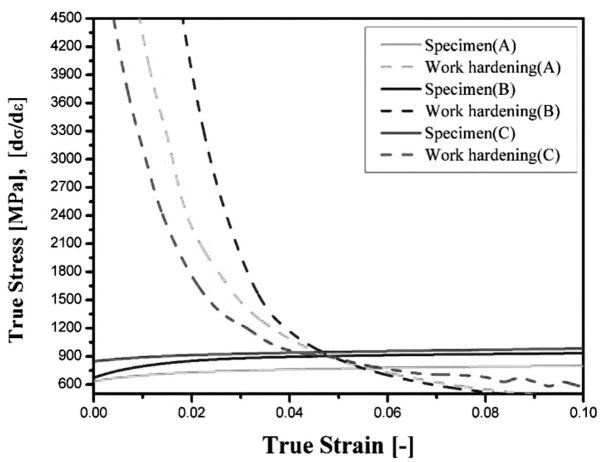

Figure 9: True stress/strain and work-hardening curves obtained through micromechanical modeling

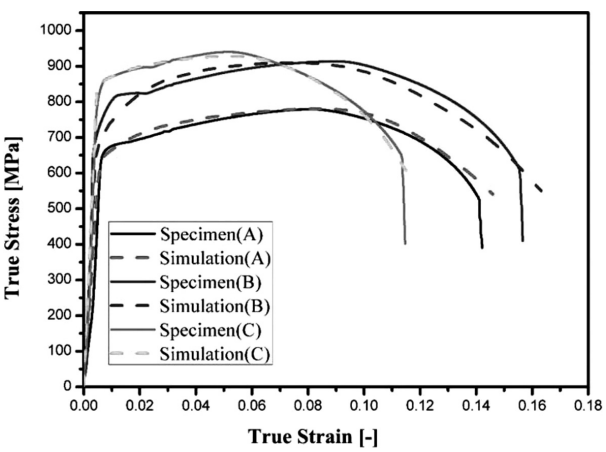

Figure 10: Experimental and simulated stress/strain curves of intercritically heat-treated steels

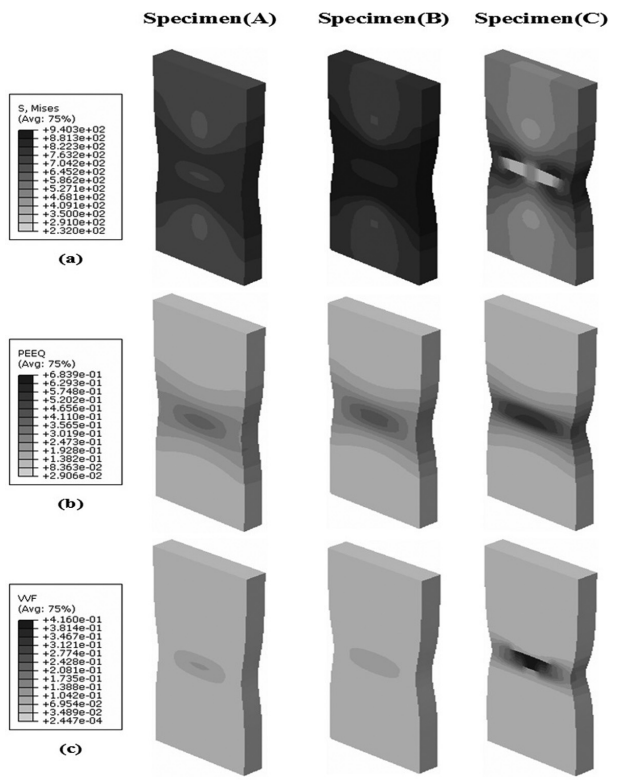

Figure 11: a) Equivalent plastic-strain distribution, b) void-volume-fraction distribution in 1/2 part of the extensometer measurement, at a deformation of 6 %

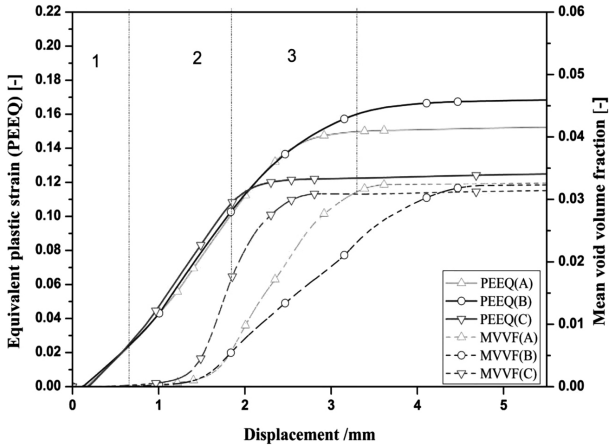

Figure 12: Comparison between the equivalent plastic strain and mean void volume fraction during loading

volume fraction mainly focus on the core of a specimen. For specimen (A), the equivalent plastic strain is the smallest, but the void volume fraction is the largest for specimen (C).

In addition, development curves of the equivalent plastic strain and the mean void volume fraction were calculated during the simulation process. With an increase in the displacement, the development trends of the equivalent plastic strain and the mean void volume fraction for different specimens were similar, as shown in **Figure 12**. It can be seen that there are three processes (we took the third specimen as an example).

During the first stage, the growth rate of the equivalent plastic strain is almost constant and the mean void volume fraction initially remained unchanged, followed by a slow increase, which shows that the specimen is in the state of uniform deformation. After the first stage, the equivalent plastic strain increases rapidly and the volume fraction of voids increases greatly, which means the specimen goes into the inhomogeneous deformation stage and a lot of voids begin to form and grow up. During the last stage, the mean volume fraction of voids and the equivalent plastic strain continue to increase, followed by a slow increase, and come to be maximum in the end. This illustrates that the coalescence of voids plays an import part in the third stage. For the specimen, large cracks are formed and the sample finally breaks. After the comparison between the equivalent plastic strain and the mean void volume fraction, we can see that specimen (B) shows a great elongation performance because of the lowest void-volume-fraction growth rate (**Figure 12**).

5 CONCLUSIONS

The Gr.65 steel underwent an intercritical heat-treatment process. The micromechanical properties of the heat-treated steel were predicted, taking into account the effects of the microstructure, phase fractions, local compositions of single phases and their area shapes. The GTN model was used for predicting the damage behavior of the specimens for the macromechanical model. The following points could be drawn:

1) The tensile strength increased with the increasing temperature due to an increase in the amount of martensite in the steel, but the hardening behavior of this specimen was affected by the microstructure.
2) The flow curves of the Gr.65 steel at different interitical temperatures could be well predicted using the 2D FE simulation based on real microstructures. Simulation results showed that higher stress concentrated on the martensite; at the same time, the shear-band appearance strongly depended on the microstructures of the phases.
3) For the prediction of damage behaviors, the true stress/true strain curves of macroscale simulations showed good agreement with the experiments involving differently heat-treated steels.

6 REFERENCES

[1] H. J. Jun, J. S. Kang, D. H. Seo, F. K. Kim, Effects of deformation and boron on microstructure and continuous cooling transformation in low carbon HSLA steels, Materials Science and Engineering A, 422 (**2006**) 1, 157–162, doi:10.1016/j.msea.2005.05.008

[2] S. Oliver, T. B. Jones, G. Fourlaris, Dual phase versus TRIP strip steels: comparison of dynamic properties for automotive crash performance, Materials Science and Technology, 23 (**2007**) 4, 423–431, doi:10.1179/174328407X168937

[3] Y. I. Son, Y. K. Lee, K. T. Park, Ultrafine grained ferrite–martensite dual phase steels fabricated via equal channel angular pressing: microstructure and tensile properties, Acta Materialia, 53 (**2005**) 11, 3125–3134, doi:10.1016/j.actamat.2005.02.015

[4] L. Shi, Z. Yan, Y. Liu, D. G. Li, Improved toughness and ductility in ferrite/acicular ferrite dual-phase steel through intercritical heat treatment, Materials Science and Engineering A, 590 (**2005**), 7–15, doi:10.1016/j.msea.2005.10.006

[5] J. Kang, C. Wang, G. D. Wang, Microstructural characteristics and impact fracture behavior of a high-strength low-alloy steel treated by intercritical heat treatment, Materials Science and Engineering A, 553 (**2012**), 96–104, doi:10.1016/j.msea.2012.05.098

[6] Z. J. Xie, S. F. Yuan, W. H. Zhou, G. D. Wang, Stabilization of retained austenite by the two-step intercritical heat treatment and its effect on the toughness of a low alloyed steel, Materials & Design, 59 (**2014**), 193–198, doi:10.1016/j.matdes.2014.02.035

[7] M. A. Maleque, Y. M. Poon, H. H. Masjuki, The effect of intercritical heat treatment on the mechanical properties of AISI 3115 steel, Journal of Materials Processing Technology, 153 (**2004**), 482–487, doi:10.1016/j.jmatprotec.2004.04.391

[8] W. H. Zhou, X. L. Wang, P. K. C. Venkatsurya, R. F. Shi, Structure–mechanical property relationship in a high strength low carbon alloy steel processed by two-step intercritical annealing and intercritical tempering, Materials Science and Engineering A, 607 (**2014**), 569–577, doi:10.1016/j.msea.2014.03.107

[9] M. Azuma, S. Goutianos, N. Hansen, D. F. White, Effect of hardness of martensite and ferrite on void formation in dual phase steel, Materials Science and Technology, 28 (**2012**) 9, 1092–1100, doi:10.1179/1743284712Y.0000000006

[10] B. C. Hwang, T. Y. Cao, S. Y. Shin, F. H. Kim, Effects of ferrite grain size and martensite volume fraction on dynamic deformation behaviour of 0.15C–2.0Mn–0.2Si dual phase steels, Materials Science and Technology, 21 (**2005**) 8, 967–975, doi:10.1179/174328405X47609

[11] A. Ramazani, K. Mukherjee, H. Quade, D. H. Gray, Correlation between 2D and 3D flow curve modelling of DP steels using a microstructure-based RVE approach, Materials Science and Engineering A, 560 (**2013**), doi:10.1016/j.msea.2012.09.046

[12] P. Phetlam, V. Uthaisangsuk, Microstructure based flow stress modeling for quenched and tempered low alloy steel, Materials & Design, 82 (**2015**), 189–199, doi:10.1016/j.matdes.2015.05.068

[13] A. Ramazani, K. Mukherjee, U. Prahl, Modelling the effect of microstructural banding on the flow curve behaviour of dual-phase (DP) steels, Computational Materials Science, 52 (**2012**) 1, 46–54, doi:10.1016/j.commatsci.2011.05.041

[14] M. R. Ayatollahi, A. C. Darabi, H. R. Chamani, 3D Micromechanical Modeling of Failure and Damage Evolution in Dual Phase Steel Based on a Real 2D Microstructure, Acta Mechanica Solida Sinica, 29 (**2016**) 1, 95–110, doi:10.1016/S0894-9166(16)60009-5

[15] A. Ramazani, K. Mukherjee, A. Abdurakhmanov, Micro–macro-characterisation and modelling of mechanical properties of gas metal arc welded (GMAW) DP600 steel, Materials Science and Engineering A, 589 (**2014**), 1–14, doi:10.1016/j.msea.2013.09.056

[16] S. M. K. Hosseini, A. Zarei-Hanzaki, M. J. Y. Panah, A. G. Amire, ANN model for prediction of the effects of composition and process parameters on tensile strength and percent elongation of Si–Mn TRIP steels, Materials Science and Engineering A, 374 (**2004**) 1, 122–128, doi:10.1016/j.msea.2004.01.007

[17] M. I. Latypov, S. Shin, B. C. De Cooman, Micromechanical finite element analysis of strain partitioning in multiphase medium manganese TWIP+ TRIP steel, Acta Materialia, 108 (**2016**), 219–228, doi:10.1016/j.actamat.2016.02.001

[18] A. Ramazani, M. Abbasi, U. Prahl, Failure analysis of DP600 steel during the cross-die test, Computational Materials Science, 64 (**2012**), 101–105, doi:10.1016/j.commatsci.2012.01.031

[19] B. Berisha, C. Raemy, C. Becker, Multiscale modeling of failure initiation in a ferritic–pearlitic steel, Acta Materialia, 100 (**2015**), 191–201, doi:10.1016/j.actamat.2015.08.035

[20] A. L. Gurson, Continuum theory of ductile rupture by void nucleation and growth: Part I – Yield criteria and flow rules for porous ductile media, Journal of Engineering Materials and Technology, 99 (**1977**) 1, 2–15, doi:10.1115/1.3443401

[21] V. Tvergaard, A. Needleman, Analysis of the cup-cone fracture in a round tensile bar, Acta Metallurgica, 32 (**1984**) 1, 157–169, doi:10.1016/0001-6160(84)90213-X

[22] A. Needleman, V. Tvergaard, An analysis of ductile rupture modes at a crack tip, Journal of the Mechanics and Physics of Solids, 35 (**1987**), 151–183, doi:10.1016/0022-5096(87)90034-2

[23] N. Vajragupta, V. Uthaisangsuk, B. Schmaling, S. F. Shaw, A micromechanical damage simulation of dual phase steels using XFEM, Computational Materials Science, 54 (**2012**), 271–279, doi:10.1016/j.commatsci.2011.10.035

[24] M. Abendroth, M. Kuna, Determination of deformation and failure properties of ductile materials by means of the small punch test and neural networks, Computational Materials Science, 28 (**2003**) 3, 633–644, doi:10.1016/j.commatsci.2003.08.031

[25] J. Faleskog, X. Gao, C. F. Shih, Cell model for nonlinear fracture analysis – I. Micromechanics calibration, International Journal of Fracture, 89 (**1998**) 4, 355–373, doi:10.1023/A:1007421420901

[26] C. C. Chu, A. Needleman, Void nucleation effects in biaxially stretched sheets, Journal of Engineering Materials & Technology, 102 (**1980**) 3, 249–256, doi: 10.1115/1.3224807

UDK 621.793.5:620.1:669.018.26
Original scientific article/Izvirni znanstveni članek

ISSN 1580-2949
MTAEC9, 51(6)911(2017)

EIS AND SKP STUDY ON IMPROVEMENT OF THE PROTECTION PERFORMANCE OF AN ALKYD-VARNISH COATING MODIFIED WITH AIR-PLASMA TREATMENT ON Q235 STEEL

EIS IN SKP ŠTUDIJA IZBOLJŠANJA ZAŠČITE Z ALKIDNO PREVLEKO, MODIFICIRANO S PLAZEMSKO OBDELAVO NA Q235 JEKLU

Chuanbo Zheng[1], Haoyang Qu[1], Wei Wang[2]

[1]Jiangsu University of Science and Technology, School of Materials Science and Engineering, Mengxi Road 2, Zhenjiang, Jiangsu Province, 212003, China
[2]State Key Laboratory for Marine Corrosion and Protection, Luoyang Ship Material Research Institute (LSMRI), 149-1 Zhuzhou Road, Laoshan District, Qingdao, 266101, China
15952802516@139.com

Prejem rokopisa – received: 2017-02-16; sprejem za objavo – accepted for publication: 2017-05-30

doi:10.17222/mit.2017.022

Electrochemical impedance spectroscopy (EIS) and scanning Kelvin probe (SKP) were used to study the failure of the coating modified with air-plasma treatment in 3.5 % mass fraction of NaCl. The results show that the failure process can be divided into three stages including water penetration, accumulation of corrosion products at the location of a defect, water penetration of the entire coating and coating failure. The EIS results show that the plasma-treated samples exhibit an additional electrical double-layer capacitor that delays the coating failure during the second stage. The potential of the non-plasma-treated samples decrease faster than that of the plasma-treated samples according to the SKP study. As the transition layer, air plasma delays the coating failure due to the chemical bond between the metal substrate and the coating.

Keywords: air-plasma treatment, electrochemical impedance spectroscopy, scanning Kelvin probe, coating failure, hydrostatic pressure

Elektrokemijsko impedančno spektroskopijo (angl. EIS) in vrstično Kelvinovo sondo (SKP) smo uporabili za preučevanje poškodb na prevleki, modificirani s plazmo, v 3,5 mas. % raztopini NaCl. Rezultati kažejo, da se nastajanje poškodb lahko razdeli na tri faze, vključno s penetracijo vode: na akumulacijo korozijskih produktov na mestu napake, na prodiranje vode v dele celotne prevleke in na odpoved prevleke. Rezultati EIS kažejo, da imajo vzorci, obdelani v plazmi, dodaten električni dvoslojni kondenzator, ki v drugi fazi upočasni poškodbo prevleke (premaza). SKP-analize so pokazale, da se potencial plazemsko neobdelanih vzorcev zmanjšuje hitreje kot tistih vzorcev, ki so bili obdelani s plazmo. Kot prehodna plast, obdelava z zračno plazmo upočasni poškodbo premaza zaradi kemijske vezi med kovinskim substratom in prevleko.

Ključne besede: obdelava s plazmo, elektrokemijska impedančna spektroskopija, skeniranje s sondo Kelvin, odpoved prevleke, hidrostatični tlak

1 INTRODUCTION

With the exploration and development of marine research, problems of the corrosion and protection of structural materials and organic coatings in marine environments have increasingly gained attention.[1–3] Thus, the corrosion problems of the materials under deep-ocean conditions must be considered. The environment of the deep ocean is a complicated system, including hydrostatic pressure, differently dissolved oxygen (DO), all kinds of salts, water velocity and suspended silt. Coating deterioration, delamination, blistering and penetration are likely to occur in the deep-sea environment.[4–6] How to improve the coating quality is an urgent need for deep-ocean resource exploitation.

Due to the fact that air-plasma treatment[7–10] does not alter the overall performance of the substrate, the chemical and physical activities of a material surface remains constant. During a reaction, polar oxygen groups with single or double bonds can be incorporated into the surface of the substrate, enhancing the wettability of the substrate surface.[11,12] After the air-plasma treatment, the hydrophobicity and spreading ability of the material surface were also found to improve. In addition, porosity is effectively reduced on the substrate surface due to a better wettability of the organic coating. Therefore, the coating in combination with the surface of the substrate allows a better modification process.[7,8,13]

Many researchers effectively modified surfaces with plasma-processing techniques in order to increase hydrophobicity and alter only the surface properties of the material. L. Wang et al.[14] prepared a column-like nano/micro-scale topography surface via trichloro(octyl)silane (TCOS) vapor deposition on a polydimethylsiloxane oxidized with air plasma. Their results showed a successful assembly of TCOS on a polydimethylsiloxane surface. An addition of n-heptanol to alkylsiloxane also helps regulate the scale and roughness of the column-like nano/micro-scale topography. C. Riccardi et al.[15] induced

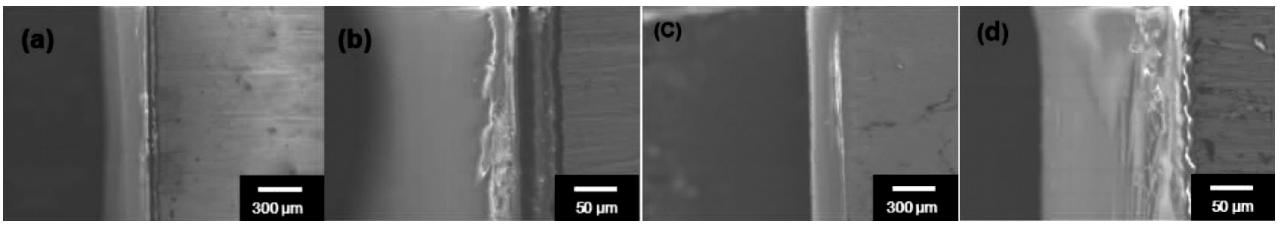

Figure 1: Cross-sections of alkyd-varnish coatings with and without plasma treatment; a), b): with plasma treatment; c), d): without plasma treatment

chemical and physical surface modifications of poly (ethylene terephthalate) fibers using radio-frequency air-plasma treatments. After the treatment, the fibers demonstrated significant increases in hydrophilicity, accompanied by extensive etching and an incorporation of both polar oxygen- and nitrogen-containing groups. Air-plasma treatment was applied extensively and with excellent results when treating organic compounds. However, the cases of the air-plasma treatment being applied to metal substrates are rare.

In this work, for the transition layer, air-plasma treatment was performed on a metal surface. The effect of the plasma treatment on the failure process of alkyd-varnish coatings (AVCs) with defects under deep-ocean conditions was investigated. EIS[16–19] and SKP[20–24] were used as electrochemical macroscopic and microscopic characterization methods, respectively. The depth-from-defocus method was also applied as an intuitive approach to observing the changes in the defects and the coating.

2 EXPERIMENTAL PART

2.1 Materials

The Q235 carbon steel was produced by Shanghai BaoSteel. The water used in all the experiments was produced by the Milli-Q plus 185 purification system. Q235 carbon-steel samples with dimensions of 1 cm × 1 cm × 1 cm were used as substrates and sealed with epoxy resin. The substrates were first ground with 400–1200-grade SiC paper, degreased ultrasonically in acetone and rinsed with double-distilled water.

Some samples were treated with air plasma and the reactor employed for the plasma treatment was APJD-1000. The alkyd varnish was applied to the substrate surface with a controlled thickness of approximately 50 μm, using the roller-coating method. The coatings were then dried in air and pinholes were formed in the center of the coatings with a needle whose diameter was 100 μm, using a friction-and-wear machine.

Figure 1 shows the cross-sections of the specimens prepared with (a and b) and without (c and d) air-plasma treatment.

2.2 Experiment condition

To simulate a 450-meter deep-sea condition of low temperature and low oxygen, an autoclave corrosion-testing machine of SSRT (constant load, low-cycle fatigue) produced by Cortest Inc. was adopted in the experiment. The hydrostatic pressure in the reactor was 4.5 MPa, the temperature in the reactor was controlled to be 10±2 °C, and the content of dissolved oxygen in water was controlled to be 4.0±0.5 mg/L, using the oxygen-concentration detector included in the equipment.

2.3 Experimental techniques

2.3.1 Depth-from-defocus method

To observe the process of the coating failure from an optical point of view, the depth-from-defocus method was adopted using a KH-8700 digital microscope produced by HIROX Co. Ltd. (Tokyo, Japan). Every sample was observed in the mid-range with a 140× magnification.

2.3.2 Electrochemical measurements

Bipotentiostat PGSTAT302N Metrohm Autolab was used for the EIS measurements. The EIS measurements were carried out using a conventional three-electrode cell. The working-electrode area was 1 cm^2. A saturated calomel electrode (SCE) and a platinum wire were employed as the reference and counter electrodes, respectively. An aqueous solution with a 3.5 % mass fraction of NaCl (pH = 7) prepared with ultrapure water and reagent-grade chemicals was used as the electrolyte. All the experiments were conducted at room temperature and N_2 was bubbled through the electrolyte for 30 min before the testing and during the experiment.

Prior to impedance measurements, the open-circuit potential (OCP) was measured. When the fluctuation of the OCP was less than 500 μV over a period of 60 s, the OCP was considered to be in a stable state, allowing the EIS measurement to be carried out. Frequencies between 100 kHz and 10 mHz were used, with the amplitude signal set to 10 mV to guarantee a linear response.

VersaSCAN, produced by Princeton Inc. (USA), was used for the SKP measurements. During the experiments, the working electrode must be parallel to the workbench and kept level at a distance of 100 nm from the probe. The probe scans two dimensions (*X* and *Y*) in the range of 0–4000 μm relative to the point of origin. The pinhole was located at the center of the scanning scope. In addition, the scanning steps of the *X* and *Y* axes were 200 μm and 400 μm, respectively.

3 RESULTS AND DISCUSSION

3.1 Coating-failure morphology observed with the depth-from-defocus method

Figures 2 and **3** show the coating-failure process with and without air-plasma treatment. An accumulation of corrosion products in the pinhole and an increase in the area of disbonding over time were observed. However, the corrosion production volume and the disbonding area of the plasma-treated sample were smaller than those of the non-plasma-treated sample. Therefore, the protection performance of the alkyd varnish was improved with air-plasma treatment.

3.2 EIS

The EIS measurements of the coatings at different immersion times were important for evaluating the conditions of the coatings. Using the EIS spectra for each immersion time, we were able to divide the coating-failure process into several stages and fit electrical circuits (EC) in order to analyze this process.

The coating-failure process of the non-plasma-treated samples with a pinhole can be divided into three stages: water penetration and accumulation of corrosion products located at the defect (**Figure 4a** to **4c**), water penetration of the overall coating (**Figure 4d** to **4f**) and coating failure (**Figure 4g** to **4i**). There are two time constants in the first stage (**Figure 4a** to **4c**) corresponding to the small capacitive loop at high frequencies and the big capacitive loop at medium frequencies. The small and big capacitive loops serve as electrical double-layer capacitors between the coating and the solution and between the coating and the surface of the metal, respectively. In this stage, due to adequate coating protection, water penetration is effectively blocked and the numerical value of $|Z|_{f=0.01}$ is large. Moreover, water can penetrate easily to the metal substrate because of the pinhole, allowing the formation of an electrical double-layer capacitor between the coating and the metal, causing corrosion to occur along the defect. Consequently, the value of $|Z|_{f=0.01}$ declines from 8 MΩ cm^2 to 1 MΩ cm^2.

In the second stage, there were also two time constants corresponding to the electrical double-layer capacitors between the coating and the solution and between the coating and the surface of the metal, respectively (**Figures 4d** to **4f**). However, accumulation of the corrosion products at the defect blocks its ability to serve as a transport channel for water causing the value of $|Z|_{f=0.01}$ to increase to approximately 8 MΩ cm^2. In this process, water transport only occurs slowly through micropores in the coatings. These results indicate that there is a large Warburg diffusion coefficient occurring during the second stage.

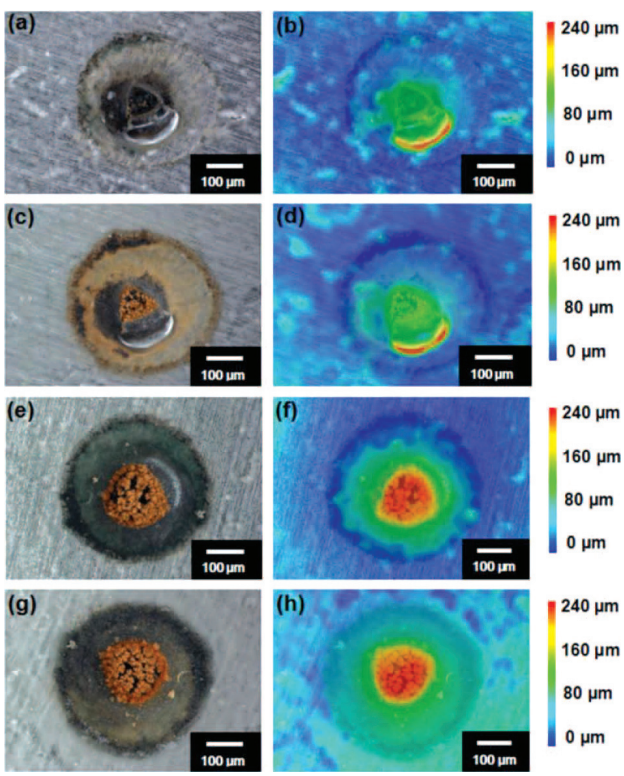

Figure 2: Photos made with the depth-from-defocus method showing the development of the coating failure for non-plasma-treated Q235 steel with crevice AVCs; photos b), d), f), and h) show the contour maps corresponding to photos a) 12.5 h, c) 26.5 h, e) 68.5 h, and g) 102.5 h, respectively

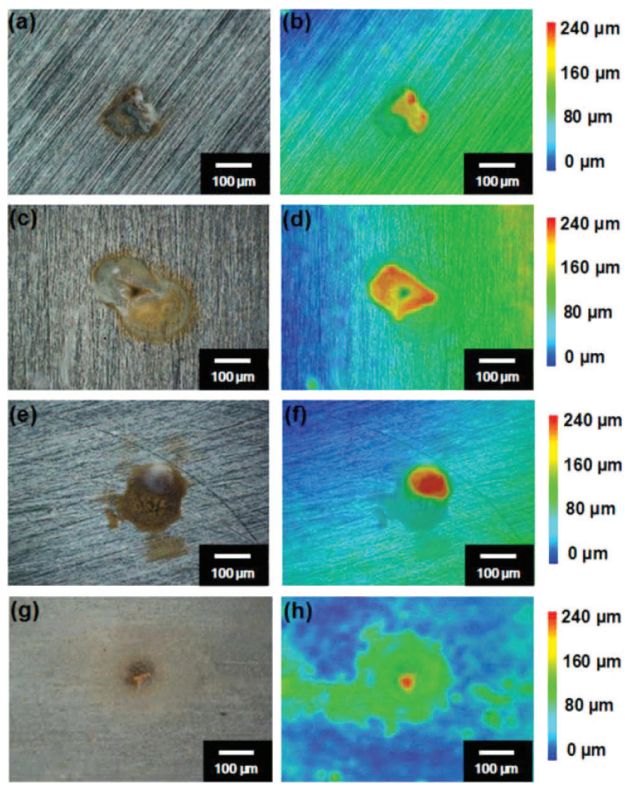

Figure 3: Photos made with the depth-from-defocus method showing the development of the coating failure for plasma-treated Q235 steel with crevice AVCs; photos b), d), f), and h) show the contour maps corresponding to photos a) 13 h, c) 36.5 h, e) 98 h, and g) 143 h, respectively

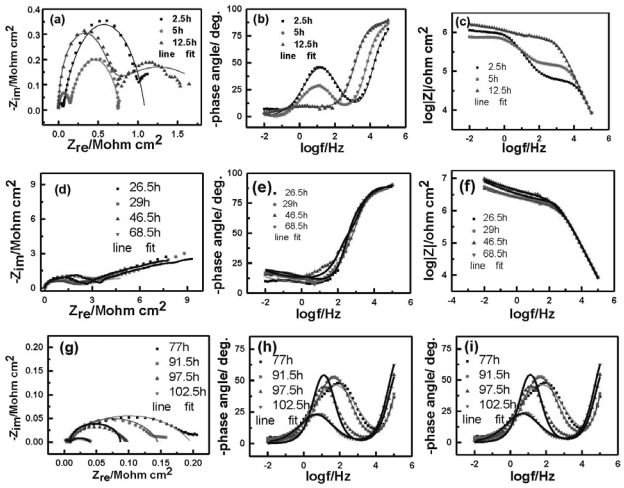

Figure 4: Nyquist and Bode plots of non-plasma-treated Q235 steel with crevice AVCs and different immersion times in a 3.5 % NaCl solution. The stages of the coating failure for non-plasma-treated samples include water penetration and accumulation of corrosion products located at the defect (a, b, and c), water penetration of the overall coating (d, e and f) and coating failure (g, h and i).

In the third stage, continued water transport though the micropores of the coatings causes them to grow, allowing additional water transport to the surface of the metal and causing the Warburg diffusion coefficient to disappear (**Figure 4g** to **4i**). In this stage, local cathodic disbonding appears between the coatings and the metal substrate and the value of $|Z|_{f=0.01}$ decreases rapidly below 0.1 MΩ cm^2.

The coating-failure process of a plasma-treated sample with a pinhole can also be divided into three stages. The two time constants in the first stage (**Figure 5a** to **5c**) correspond to the electrical double-layer capacitors between the coating and the solution and between the coating and the surface of the metal. The Warburg diffusion coefficient impedes the electron transport at the interface of the metal and the coatings. In this stage, an adequate protection of the coating effectively blocks water penetration and the value of $|Z|_{f=0.01}$ is large. However, the presence of the pinhole allows water to penetrate easily to the metal substrate and form an electrical double-layer capacitor between the coatings and the metal, causing corrosion to occur along the defect.

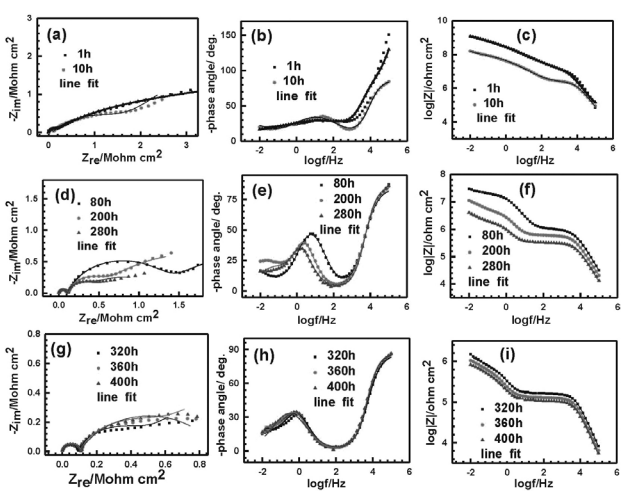

Figure 5: Nyquist and Bode plots of air-plasma-treated Q235 steel with crevice AVCs and different immersion times in a 3.5% NaCl solution. The stages of the coating failure for plasma-treated samples include water penetration and accumulation of corrosion products located at the defect (a, b, and c), water penetration of the overall coating (d, e, and f), and coating failure (g, h, and i).

During the second stage, water begins to gradually permeate along the microporous coatings to the metal oxide layer. There are three time constants associated with this stage (**Figure 5d** to **5f**) that correspond to the electrical double-layer capacitors of the water and the coatings, the coatings and the plasma layer, and the plasma layer and the metal substrate. The increase in the corrosion products at the defect effectively blocks the water transport and increases the value of $|Z|_{f=0.01}$.

In the third stage (**Figure 5g** to **5i**), the coatings lose nearly all of their protection efficiency with continued water transport and the value of $|Z|_{f=0.01}$ also decreases below 1 MΩ cm^2. However, the protection of the metal oxide film causes the $|Z|_{f=0.01}$ value to decrease relatively slowly. We therefore conclude that the metal oxide film can inhibit the coating failure and corrosion of the metal substrate.

The impedance data was fit with suitable equivalent circuit models to explain different electrochemical processes occurring at the electrode-electrolyte interface.

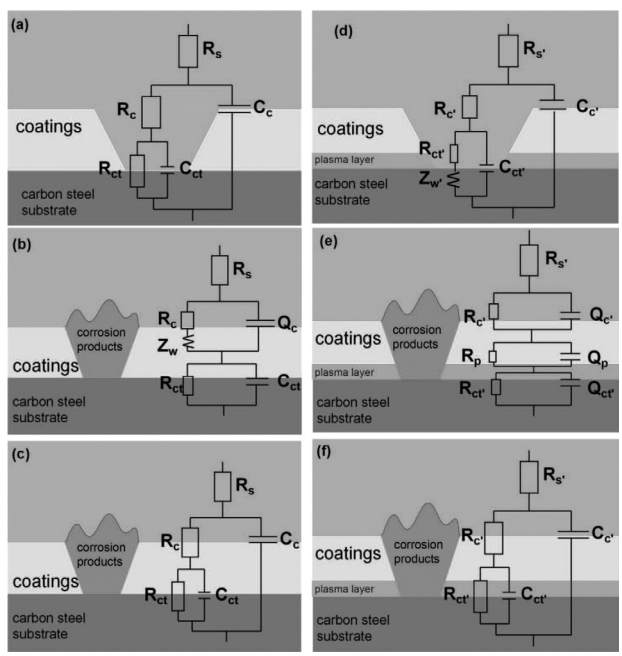

Figure 6: Equivalent circuit models used to fit the experimental impedance data of non-plasma-treated (a, b and c) and plasma-treated (d, e and f) Q235 steel with crevice AVCs. The three stages (water penetration and accumulation of corrosion products located at the defect, water penetration of the overall coating and coating failure) of the coating failure for non-plasma- and plasma-treated samples are shown in a–c and d–f.

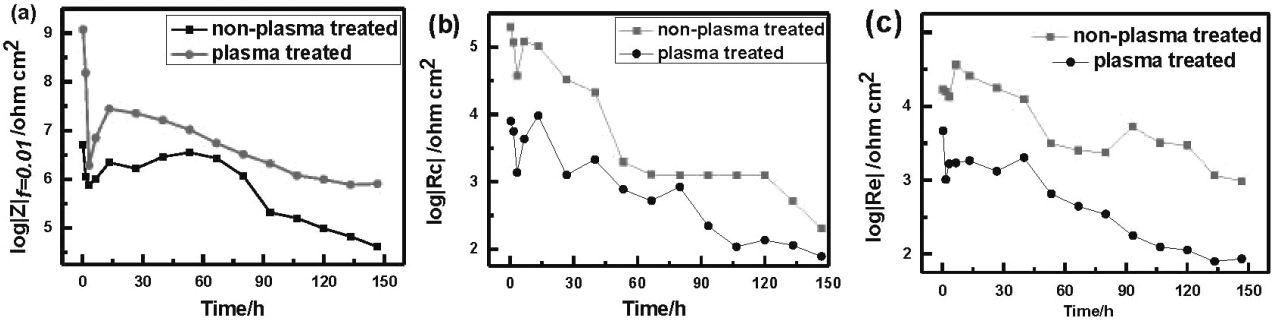

Figure 7: Change in $|Z|_{f=0.01}$, R_c and R_e values (a, b and c, respectively) of plasma- and non-plasma-treated Q235 steel with crevice AVCs over time

The proposed electrical circuits (EC) are presented in **Figure 6**, showing that the model results significantly resemble the experimental data where R_s and R_s' are the resistances of the NaCl electrolyte solution for the non-plasma- and plasma-treated samples, respectively; R_c and R_c' are the coating resistances of the non-plasma- and plasma-treated samples, respectively; R_{ct} and R_{ct}' are the metal charge-transfer resistances of the non-plasma- and plasma-treated samples, respectively; R_p' is the resistance of the plasma layer; C_c and C_c' are the electrical double-layer capacitances of water and coatings of non-plasma and plasma treated samples, respectively; and C_{ct} and C_{ct}' are the electrical double-layer capacitances of the metal charge transfer of the non-plasma- and plasma-treated samples, respectively.

The CPE (constant phase element), denoted as Q in the equivalent circuit, is introduced instead of the pure capacitance during our simulations to obtain good agreement between the simulated and experimental data. The CPE impedance can be defined as $Z_{CPE} = Y_0^{-1} \cdot (j\omega)^{-n}$, where Y_0 is the CPE constant; j is the imaginary unit ($j^2 = -1$); ω is the angular frequency ($\omega = 2\pi f$, where f is the frequency); and n is the exponent of the constant phase element. The CPE depends on both the Y_0 parameter and the exponent n. In general, $0 < n < 1$. When $n = 1$, the CPE behaves as an ideal capacitor with conventional double-layer capacitance; and when $n = 0$, the CPE behaves as a resistor.

Q_c and Q_c' are the constant phase elements related to the coating capacitance of the non-plasma- and plasma-treated samples, respectively. Q_p and Q_{ct}' are the constant phase elements related to the capacitance of the plasma-treated layer and metal charge transfer, respectively. Z_w and Z_w' are the Warburg diffusion coefficients of the non-plasma- and plasma-treated samples, respectively.

Compared to the EIS and fitted-equivalent-circuit results, an additional capacitance (Q_p) also occurs during the second stage after the plasma treatment and delays the water penetration and corrosion of the metal substrate, increasing the time for the coating to fail.

Since the information regarding the low frequencies in the Bode diagram mainly reflects the impedance of the coating, the impedance at low frequencies ($|Z|_{f=0.01}$) can be used to evaluate the coating's ability to prevent corrosion. **Figure 7a** shows a significant peak for both the non-plasma- and plasma-treated samples; however, there is an overall declining trend of the curves. The $|Z|_{f=0.01}$ value is increased due to the covering of the pinholes by the increasing amounts of corrosion products, blocking any further infiltration of water. In addition, there is a smaller decrease in the value of $|Z|_{f=0.01}$ for the plasma-treated sample compared to the non-plasma-treated sample. The time it takes for this value to decrease to 1×10^5 Ω cm^2 is also significantly longer for the plasma-treated sample compared to the non-plasma-treated sample. R_c and R_e values showed a trend similar to $|Z|_{f=0.01}$ (**Figures 7b** and **7c**) and an overall decreasing trend for the curve. The R_c and R_e values for the plasma-treated samples were significantly larger than those of the non-plasma-treated samples after 100 h. These effects may be induced by the plasma treatment, leading to the conclusion that the surface plasma treatment can delay coating failure in 3.5 M NaCl aqueous solutions.

3.3 SKP measurements of the coating failure

The SKP measurements of the development of coating failure for plasma- and non-plasma-treated Q235 steel with crevice AVCs are shown in **Figures 8** and **9**. After 13 h of immersion, the water permeates through the pinhole located at the center of the coating on the metal substrate and the metal substrate begins to corrode. Corrosion products accumulate over time, which reduces the potential at the center of the coatings and creates a potential difference. Based on **Figures 8** and **9**, we observe that the blue area at the center of the coating and the overall yellow and red area of the intact coating are significantly different. There are several successive equipotential circles from the inside to the outside. The defect located at the center of the circle is where the potential is the lowest while the outside area has a higher potential. We also observe the occurrence of the potential difference for the non-plasma-treated sample. Over time, the potential of the intact area becomes much smaller. As more water and oxygen penetrate the surface, the resistance of the coating declines and the capacity of the

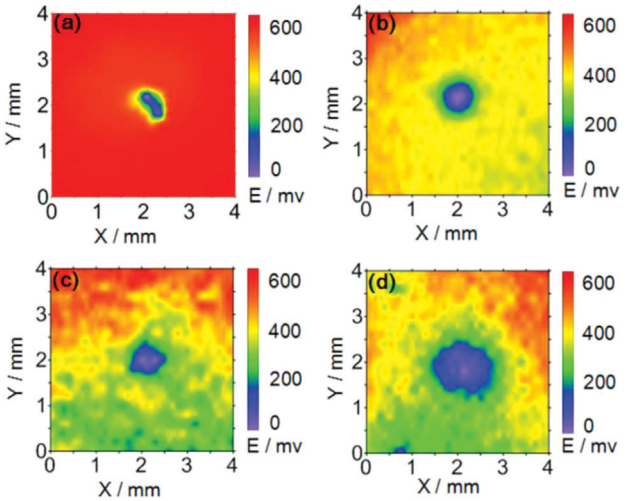

Figure 8: SKP study of the development of coating failure for non-plasma-treated Q235 steel with crevice AVCs where a, b, c and d correspond to: a) 12.5 h, b) 26.5 h, c) 68.5 h and d) 02.5 h, respectively

coating rises. **Figures 8d** and **9d** show that most of the coating disbonded and the potential decreased to approximately the value of the defect, indicating an absolute coating failure.

Compared to the plasma-treated sample, the expending trend of the lower potential value for the non-plasma-treated sample is significantly faster, indicating that the rate of the coating failure for the non-plasma-treated samples is higher than that of the plasma-treated samples. In addition, the lower area for the non-plasma-treated samples is larger than that of the plasma-treated samples during all the periods, demonstrating that the area of the coating failure for the non-plasma-treated samples is larger compared to the plasma-treated samples.

A sectional view of the varnish-coating-failure process without plasma treatment, at Y = 2 mm and at

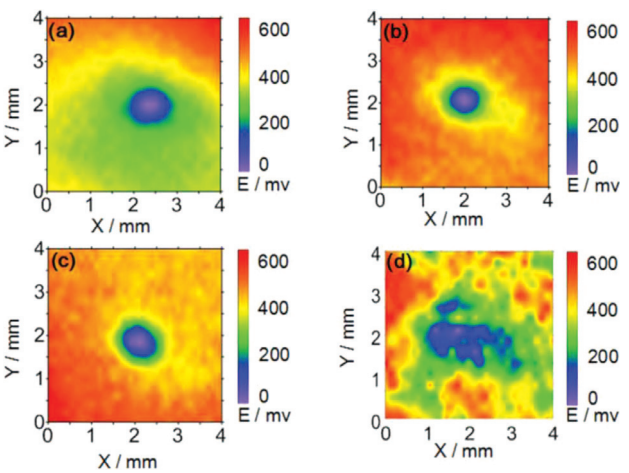

Figure 9: SKP study of the development of coating failure for plasma-treated Q235 steel with crevice AVCs where a, b, c and d correspond to: a) 13 h, b) 36.5 h, c) 98 h and d) 143 h, respectively

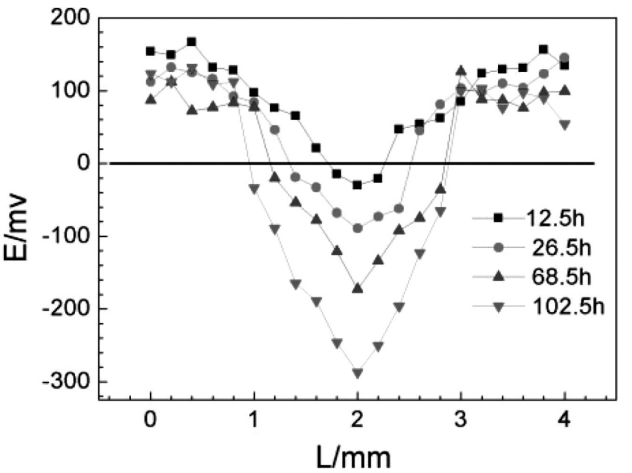

Figure 10: SKP sectional view of coating without plasma treatment at Y = 2 mm at different times

different times (an SKP map) is shown in **Figure 10**, and a sectional view of the varnish-coating-failure process with plasma treatment, at Y = 2 mm and at different times (an SKP map) is shown in **Figure 11**.

As we can see from the figure, with an increase in the time, the electric potential becomes lower and the low potential range is growing. The growth rate of the low potential region is proportional to the failure rate of the coating.

Figure 12 shows the trend chart of the change in the X-axis length of the SKP, with the electric potential below 0 mV. It can be seen from the figure that the curve of the coating without plasma treatment is above the curve of the plasma-treated coating. It shows that the low potential range of the coating without plasma treatment is larger than that of the coating with plasma treatment. In addition, the slope of the curve of the coating without plasma treatment is larger than the slope of the curve of the coating with the plasma treatment. It also shows that the growth rate of the low electric potential without

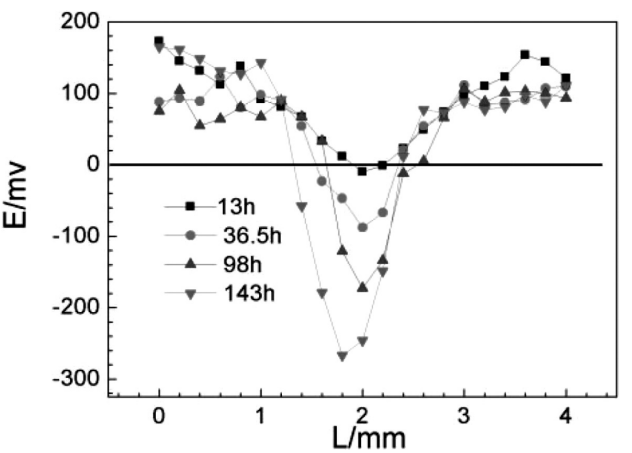

Figure 11: SKP sectional view of coating with plasma treatment at Y = 2 mm at different times

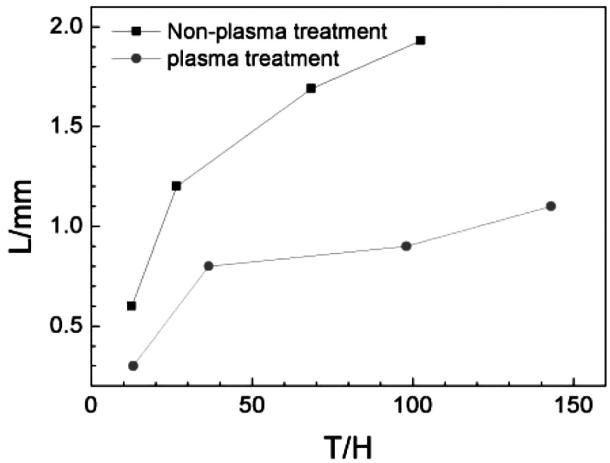

Figure 12: Trend chart of the change in the length of the SKP with the electric potential below 0 mV

plasma treatment is larger than the growth rate of the one with plasma treatment.

All of these results show that the failure rate of the plasma coating is lower than the failure rate of the coating without plasma treatment. Together, they show that the plasma treatment can delay the failure rate of the coating.

L. Yang et al.[8] treated stainless-steel electrodes with air plasma and observed an increase in the relative oxygen and nitrogen contents (atom %) of the electrodes from 3 % to 17.4 % and from 0 % to 2.7 %, respectively, compared to the non-plasma-treated electrodes. V. Prysiazhnyi et al.[25] treated aluminum surfaces with air plasma and observed a significant increase in the amount of -OH groups on the surfaces as well as a decrease in the surface roughness. M. A. Samad et al.[26] also observed that air-plasma treatment significantly improves the adhesion between an ultra-high-molecular-weight-polyethylene (UHMWPE) film and a steel substrate by enhancing the surface energy, which in turn results in good tribological characteristics of the film. The wear life of the plasma-treated steel sample coated with the UHMWPE film increased by 10 to 12 fold compared to the untreated steel samples.

Figure 13 shows the plasma treatment process and the reaction between the alkyd resin and plasma layer. Air-plasma treatment results in connections between the metal substrates and hydroxyl(-OH), carbonyl(-CO) and other functional groups. These functional groups can react with functional groups within the alkyd resin, including -C=C-, R-OH, R-OOH, R-OOR and other functional groups. Therefore, the binding force between a metal substrate and its coating is not only due to physical adhesion but also chemical binding.[8,25,10]

4 CONCLUSIONS

Air-plasma treatment delays the failure rate of a coating and corrosion of a metal substrate under deep-ocean conditions. Air-plasma treatment results in connections between a metal substrate and hydroxyl(-OH), carbonyl(-CO) and other functional groups. These functional groups can react with the functional groups within the alkyd resin, including -C=C-, R-OH, R-OOH, R-OOR and other functional groups. Therefore, the binding force between a metal substrate and its coating is due to both physical adhesion and chemical binding. EIS measurements of the plasma- and non-plasma-treated samples show the formation of an additional plasma layer/coating interface in the EC for the plasma-treated sample. The plasma-treated sample also exhibits a longer failure time and a faster decrease in the value of $|Z|_{f=0.01}$ compared to the non-plasma-treated sample under deep-ocean conditions. The air-plasma-treated sample exhibits a larger resistivity (Zre [MΩ<cm^2]) and a longer failure time even after a four-time-longer immersion.

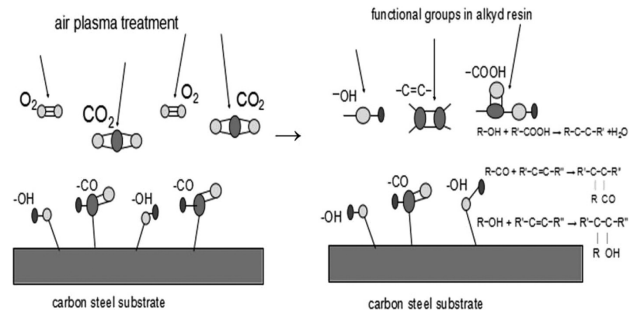

Figure 13: Air-plasma-treatment process and the reaction between the alkyd resin and plasma layer

Acknowledgements

This paper was supported by the National Natural Science Foundation of China (No. 51401185), the Natural Science Foundation of Jiangsu Province, China (No. BK20141292), and Excellent Middle-Aged and Youth Scientist Award Foundation of Shandong Province (No. BS2014CL005).

5 REFERENCES

[1] N. Fredj, S. Cohendoz, X. Feaugas, S. Touzain, Ageing of marine coating in natural and artificial seawater under mechanical stresses, Progress in Organic Coatings, 74 (**2012**) 2, 391–399, doi:10.1016/j.porgcoat.2011.10.002

[2] C. Zheng, G. Yi, Investigating the influence of hydrogen on stress corrosion cracking of 2205 duplex stainless steel in sulfuric acid by electrochemical impedance spectroscopy, Corrosion Reviews, 35 (**2017**) 1, 23–33, doi:10.1515/corrrev-2016-0060

[3] C. B. Zheng, L. Cai, Z. J. Tang, The inhibition effect of the molybdate on hydrogen permeation of 2205 duplex stainless steel, Surface & Coatings Technology, 287 (**2016**) 2, 153–159, doi:10.1016/j.surfcoat. 2015.12.077

[4] X. Lu, X. Feng, Y. Zuo, P. Zhang, C. Zheng, Improvement of protection performance of Mg-rich epoxy coating on AZ91D magnesium alloy by DC anodic oxidation, Progress in Organic Coatings, 104 (**2017**) 2, 188–198 doi:10.1016/j.porgcoat.2016.11.001

[5] C. B. Zheng, H. K. Jiang, Y. L. Huang, Hydrogen permeation behaviour of X56 steel in simulated atmospheric environment under loading, Corrosion Engineering Science & Technology, 46 (**2011**) 4, 365–367, doi:10.1179/147842209X12559428167689

[6] C. Zheng, G. Yi, Temperature effect on hydrogen permeation of X56 steel, Materials Performance, 50 (**2011**) 4, 72–76

[7] M. Schweda, T. Beck, J. Malzbender, Effect of support material creep on the delamination failure of air plasma sprayed thermal barrier coatings, Surface & Coatings Technology, 259 (**2014**) 5, 543–550, doi:10.1016/j.surfcoat.2014.10.033

[8] L. Yang, Z. Shi, W. Yang, Enhanced capacitive deionization of lead ions using air-plasma treated carbon nanotube electrode, Surface & Coatings Technology, 251 (**2014**) 29, 122–127, doi:10.1016/j.surfcoat.2014.04.012

[9] X. Lu, X. Feng, Y. Zuo, C. Zheng, S. Lu, Evaluation of the micro-arc oxidation treatment effect on the protective performance of a Mg-rich epoxy coating on AZ91D magnesium alloy, Surface & Coatings Technology, 270 (**2015**) 2, 227–235, doi:10.1016/j.surfcoat.2015.02.052

[10] Y. Wu, C. Han, J. Yang, Polypropylene films modified by air plasma and feather keratin graft, Surface and Coatings Technology, 206 (**2011**) 3, 506–510, doi:10.1016/j.surfcoat.2011.07.073

[11] F. Ghadami, M. H. Sohi, S. Ghadami, Effect of bond coat and post-heat treatment on the adhesion of air plasma sprayed WC-Co coatings, Surface & Coatings Technology, 261 (**2015**) 2, 289–294, doi:10.1016/j.surfcoat.2014.11.016

[12] M. Afzal, A. N. Khan, T. B. Mahmud T. I. Khan, M. Ajmal, Effect of Laser Melting on Plasma Sprayed WC-12 wt.%Co Coatings, Surface & Coatings Technology, 266 (**2015**) 1, 22–30, doi:10.1016/j.surfcoat.2015.02.004

[13] L. Yang, F. Yang, Y. Long, Y. Zhao, X. Xiong, Evolution of residual stress in air plasma sprayed yttria stabilised zirconia thermal barrier coatings after isothermal treatment, Surface & Coatings Technology, 251 (**2014**) 29, 98–105, doi:10.1016/j.surfcoat.2014.04.009

[14] L. Wang, C. Lin, L. Yang, J. Zhang, J. Zheng, Preparation of nano/micro-scale column-like topography on PDMS surfaces via vapor deposition: Dependence on volatility solvents, Applied Surface Science, 258 (**2011**) 1, 265–269, doi:10.1016/j.apsusc.2011.08.044

[15] C. Riccardi, R. Barni, E. Selli, G. Mazzone, M. R. Massafra, Surface modification of poly(ethylene terephthalate) fibers induced by radio frequency air plasma treatment, Applied Surface Science, 211 (**2003**) 4, 386–397, doi:10.1016/s0169-4332(03)00265-4

[16] C. B. Zheng, B. H. Yan, K. Zhang, Electrochemical investigation on the hydrogen permeation behavior of 7075-T6 Al alloy and its influence on stress corrosion cracking, International Journal of Minerals Metallurgy and Materials, 22 (**2015**) 7, 729–737, doi: 10.1007/s12613-015-1128-5

[17] A. E. Bolzán, L. M. Gassa, Comparative EIS study of the adsorption and electro-oxidation of thiourea and tetramethylthiourea on gold electrodes, Journal of Applied Electrochemistry, 44 (**2014**) 2, 279–292, doi:10.1007/s10800-013-0621-7

[18] R. I. Tucceri, Deactivation of poly(o -aminophenol) film electrodes by storage without use in the supporting electrolyte solution and its comparison with other deactivation processes, A study employing EIS, Journal of Applied Electrochemistry, 45 (**2015**) 10, 1123–1132, doi:10.1007/s10800-015-0851-y

[19] B. Ter-Ovanessian, C. Alemany-Dumont, B. Normand, Single frequency electrochemical impedance investigation of zero charge potential for different surface states of Cu–Ni alloys, Journal of Applied Electrochemistry, 44 (**2014**) 3, 399–410, doi:10.1007/s10800-013-0642-2

[20] P. P. Deshpande, N. G. Jadhav, V. J. Gelling, D. Sazou, Conducting polymers for corrosion protection: a review, Journal of Coatings Technology and Research, 11 (**2014**) 4, 473–494, doi:10.1007/s11998-014-9586-7

[21] M. A. Domínguez-Crespo, A. M. Torres-Huerta, E. Onofre-Bustamante et al., Corrosion studies of PPy/Ni organic–inorganic hybrid bilayer coatings on commercial carbon steel, Journal of Solid State Electrochemistry, 19 (**2015**) 4, 1–17, doi:10.1007/s10008-014-2712-8

[22] F. Deflorian, S. Rossi, M. D. C. Vadillo, M. Fedel, Electrochemical characterisation of protective organic coatings for food packaging, Journal of Applied Electrochemistry, 39 (**2009**) 11, 2151–2157, doi:10.1007/ s10800-009-9818-1

[23] X. Pan, J. Wu, Y. Ge, K. Xiao, H. Luo, Preparation and characterization of anticorrosion Ormosil sol–gel coatings for aluminum alloy, Journal of Sol-Gel Science and Technology, 72 (**2014**) 1, 8–20, doi:10.1007/s10971-014-3414-5

[24] R. Rajamohan, S. K. Nayaki, M. Swaminathan, A Study on Host-Guest Complexation of 5-Amino-2-Mercaptobenzimidazole with β-Cyclodextrin, Journal of Solution Chemistry, 40 (**2011**) 5, 803, doi:10. 1007/s10953-011-9691-5

[25] V. Prysiazhnyi, P. Vasina, N. R. Panyala, J. Havel, M. Cemak, Air DCSBD plasma treatment of Al surface at atmospheric pressure, Surface & Coatings Technology, 206 (**2012**) 12, 3011–3016, doi:10.1016/j.surfcoat.2011.12.039

[26] M. A. Samad, N. Satyanarayana, S. K. Sinha, Tribology of UHMWPE film on air-plasma treated tool steel and the effect of PFPE overcoat, Surface & Coatings Technology, 204 (**2010**) 9, 1330–1338, doi:10.1016/j.surfcoat.2009.09.011

UDK 620.192.42:621.785.36:536:6
Original scientific article/Izvirni znanstveni članek

ISSN 1580-2949
MTAEC9, 51(6)919(2017)

EFFECT OF THE MODE AND DYNAMICS OF THERMAL PROCESSES ON DSC-ACQUIRED PHASE-CHANGE TEMPERATURE AND LATENT HEAT OF DIFFERENT KINDS OF PCM

UGOTAVLJANJE VPLIVOV VRSTE IN DINAMIKE TERMIČNIH PROCESOV NA RAZLIČNE PCM-MATERIALE S POMOČJO DIFERENCIALNE VRSTIČNE KALORIMETRIJE (DSC)

Jan Fořt[1], Zbyšek Pavlík[1], Anton Trník[1,2], Milena Pavlíková[1], Robert Černý[1]

[1]Czech Technical University Prague, Faculty of Civil Engineering, Department of Materials Engineering and Chemistry, Thákurova 7, 166 29 Prague 6, Czech Republic
[2]Constantine the Philosopher University in Nitra, Department of Physics, Faculty of Natural Sciences, A. Hlinku 1, 949 74 Nitra, Slovakia
pavlikz@fsv.cvut.cz

Prejem rokopisa – received: 2017-02-27; sprejem za objavo – accepted for publication: 2017-05-12

doi:10.17222/mit.2017.026

Thermal-energy-storage systems utilizing phase-change materials (PCMs) can find use in many fields, such as solar-energy storage, waste-heat recovery or smart air conditioning in buildings. However, their incorporation into certain building elements and possible utilization of thermal energy are related to the proper understanding of phase-change processes. In this paper, thermophysical properties of five different PCMs were characterised in order to find suitable materials for incorporation into lightweight plasters capable of moderating the interior microclimate of buildings. A DSC analysis as the main investigation method was applied in the range of –10 °C to 55 °C, with the heating/cooling rates of (1, 5, 10 and 20) °C /min. Based on the DSC data, the temperatures and enthalpies of the phase change were determined as functions of both the modes and dynamics of the simulated thermal process. The obtained results were discussed and proper PCM candidates for an application in lightweight interior plasters were identified.

Keywords: phase-change materials, differential scanning calorimetry, phase-change temperature

Sistemi za skladiščenje toplotne energije, ki izkoriščajo fazne spremembe v materialih (angl. PCMs; Phase Change Materials), se uporabljajo na mnogih področjih, kot na primer pri pridobivanju in skladiščenju sončne energije, izkoriščanju odpadne toplote, ali v inteligentnih prezračevalnih sistemih stavb. Kakorkoli, njihova vgradnja v določene gradbene elemente in možno izkoriščanje odpadne toplote, je povezana z ustreznim razumevanjem faznih sprememb. V tem prispevku so bile določene termo-fizikalne lastnosti petih različnih PC materialov, da bi našli ustrezne materiale za vključitev v lahke omete, ki bi bili sposobni uravnavati notranjo mikroklimo stavb. Kot glavna preiskovalna metoda je bila uporabljena DSC (diferencialna vrstična kalorimetrija) analiza v temperaturnem območju med –10 °C in 55 °C, s hitrostjo ogrevanja/hlajenja (1, 5, 10 in 20) °C/min. Glede na podatke DSC-analize, so bile določene temperature in entalpije faznih sprememb v odvisnosti od obeh načinov in dinamike simuliranega termičnega procesa. Dobljeni rezultati so bili preštudirani in najdeni so bili ustrezni PCM-materiali za uporabo v lahkih notranjih ometih.

Ključne besede: materiali s faznimi spremembami, diferenčna dinamična kalorimetrija, temperatura fazne spremembe

1 INTRODUCTION

The International Energy Agency noted in its World Energy Outlook[1] that the building sector is responsible for approx. 30 % of the total energy consumption in the US and Europe, whereas in developing countries, this consumption is even higher, about 41 %. A substantial part of energy is consumed by a building's cooling and heating in order to ensure a high living standard of the building occupants. Nowadays, building energy efficiency and a decrease in greenhouse-gas emissions are of particular importance. Techniques known as passive cooling are extensively studied and used in environmentally friendly technologies for moderation of interior climate.

Modern lightweight buildings bring many advantages compared to the standard heavyweight constructions, such as construction speed, economic benefits and architectural flexibility. Nevertheless, lightweight building envelopes are more sensitive to the temperature fluctuation because of their low thermal-storage capacity.[2] A decrease in the thermal-storage capacity leads to a higher need for moderation of interior climate due to the external and/or internal thermal load. Incorporation of PCMs into the lightweight building envelopes can result in a more stable interior temperature with lower requirements on additional heating/cooling equipment.[3] Latent-heat-storage (LHS) systems can be utilized for the optimization of the ambient temperature, especially during summer and winter temperature peaks or daily and nightly fluctuations. These fluctuations are accompanied by high energy consumption, creating demands on air-conditioning systems in order to satisfy the requirements on indoor comfort temperature.[4] The efficiency of LHS

is strongly connected with the parameters of applied PCMs which must comply with thermophysical, chemical and economic requirements.

PCM characteristics provided by manufacturers without any exact information on the measurement methodology can often be misrepresented, inaccurate, or too optimistic, thus they require further study. Reliable parameters of PCMs are essential for the design of building materials and components for latent-heat storage and moderation of the interior climate. For a proper use of PCMs, the temperature dependence of the enthalpy around the phase transition has to be known with a good accuracy. Analysis techniques used to study the phase change are mainly conventional calorimetry, differential scanning calorimetry (DSC) and differential thermal analysis (DTA). However, other methods, e.g., the T-history method proposed by J. M. Marín[5], also found use in PCM tests. For the measurement of the PCM thermal conductivity, the hot-disk method is often used.[6] As mentioned by B. Zalba,[7] there is considerable uncertainty about the property values provided by the manufacturers (who give values of pure substances) and it is therefore advisable to use DSC to obtain more accurate values. In DSC, a reference sample is made to increase (or decrease) its temperature at a constant rate and the PCM sample is forced to follow this rate by changing the power delivered to it. This allows one to extract the heat capacity as a function of temperature. The transition heat is then determined by integrating the heat-capacity curve. The shape of the specific heat-capacity function depends significantly on the heating and cooling rates used in the measurements. Different scanning rates ranging from 0.2 K/min to 10 K/min were employed in DSC tests to investigate the thermophysical properties of PCMs.[8] Frequently, the enthalpy function or the apparent heat capacity of a PCM is determined on the basis of DSC measurements made at too high heating/cooling rates.[9] It was found that the standards used in calorimetry designed for the materials other than PCMs are not suitable for PCM testing due to the high heating rate, affecting the melting/solidification range and stored heat. When DSC runs at a higher scanning rate, it will give design information that may not be sufficiently accurate. In addition, the data on the measurements using different scanning rates are not comparable.[10] H. Mehling et al.[11] proposed summarizing the standards for PCM testing, in order to ensure the reproducibility and comparability of PCM products. However, although many studies on the PCM experimental characterization were conducted, no universal methodology for the DSC tests of PCMs have yet been developed. This is partially due to the variety of PCM compositions as they are composed of paraffins, fatty acids, hydrated salts, etc. For example, a characteristic of most paraffins and salt hydrates is that the phase change occurs in the temperature range, rather than at a constant temperature as would be expected for pure substances.

On this account, a detailed testing of five PCMs on a paraffin basis was done in our research to describe the materials' thermal behaviour, taking into account the temperature-change rate and the mode of the thermal process (heating or cooling). The presented experimental work aimed also at a comparison of two different groups of PCMs prepared using microencapsulation and dispersion in water.

2 EXPERIMENTAL PART

For the evaluation of the PCM potential for the heat storage in lightweight building elements, five types of commercially produced PCMs were examined. Two of them were polymethyl methacrylate microencapsulated paraffin mixtures produced by BASF. They were in the form of fine powders (a particle size of 50–300 μm) having the solid content of 97–100 % (according to DIN EN ISO 3251) and water content ≤ 3 %. According to the data provided by BASF, the first product, Micronal DS 5038 X, has a melting temperature of about 26 °C and an enthalpy of fusion of 110 J/g. The second one, Micronal DS 5040 X, has a slightly lower melting temperature of 23 °C and an enthalpy of fusion of 100 J/g.[12] The second group of the materials was produced by Rubitherm. These materials were also based on a paraffin mixture encapsulated in a polymer shell, but they were delivered in the form of water dispersion with the solid content of about 35 %. The company product labels of these materials are RT 21 HC, RT 22 HC and RT 25 HC. They have the main peak of the phase-change temperature at (21, 22 and 25) °C, respectively. The heat-storage-capacity values declared by the producer are (190, 200 and 230) J/g.[13]

For the basic characterization of the tested PCMs, measurements of bulk and powder densities were done. The bulk and powder densities were obtained from the measurement of the sample volume and mass. Powdered materials were characterized by the powder density and the PCMs in the form of water dispersion were characterized by their bulk density. The relative expanded uncertainty of these tests was 3.4 %.

Thermal conductivity was measured with an Isomet 2114 device (applied precision) which operates on a transient-measurement principle. The measurement range of the thermal conductivity was from 0.015 W/mK to 6.0 W/mK with the accuracy of 5 % of the reading + 0.001 W/mK. For the measurement, a needle probe that was inserted into the examined PCMS was used. The expanded combined uncertainty was 4.3 %.

A DSC 822e (Mettler Toledo) device was employed in the experiments, together with a Julabo FT 900 cooling device. Temperature and heat-flow calibrations are very important for the accuracy of the data obtained with DSC.[14] The calibration of the measuring apparatus was done according to ISO 11357-1.[15] To avoid wasting time while keeping the data accuracy satisfactory, we

used "smart" temperature programs proposed by A. Shimkin for the calibration.[16] The samples (~10 mg for the BASF materials and ~30 mg for the Rubitherm PCMs) were placed into an aluminum crucible with a volume of 40 mm^3. During the measurement, the following temperature regimes were applied: 5 min of the isothermal regime, cooling at (1, 5, 10 and 20) °C/min from 55 °C to –10 °C, 5 min of the isothermal regime, heating at (1, 5, 10 and 20) °C/min from –10 °C to 55 °C, 5 min of the isothermal regime. All the experiments were done in an air atmosphere with a flow rate of 40 mL/min. The enthalpy of fusion was obtained by integrating the peak area between the start and end temperatures of the peak. The measurement of the heat capacity was carried out using sapphire as the reference sample. Thus, the procedure for measuring the heat capacity consisted of three identical steps: 1. measurement of the blank (the empty crucible), 2. measurement of the sapphire, 3. measurement of the studied sample. Then, the heat capacity was calculated with Equation (1):

$$C_{\mathrm{p}} = C_{\mathrm{pr}} \frac{m_{\mathrm{r}}(H_{\mathrm{s}} - H_{\mathrm{b}})}{m_{\mathrm{s}}(H_{\mathrm{r}} - H_{\mathrm{b}})} \quad (1)$$

where C_{pr} (J/gK) is the heat capacity of the reference sample (sapphire), m_{r} (g) is the mass of the reference sample (sapphire), m_{s} (g) is the mass of the studied sample, and H_{b}, H_{r}, and H_{s} (W/g) are the heat flows of the blank, the reference sample (sapphire) and the studied sample, respectively. The onset and endset temperatures and the enthalpy of fusion were assessed as the average of three independent measurements, while the endset and onset temperatures were identified according to ISO 11357-3:2011.[17] According to this ISO standard, the extrapolated onset temperature is where the extrapolated baseline is intersected by the tangent to the curve at the point of inflection and corresponds to the start of the transition; the extrapolated endset temperature is where the extrapolated baseline is intersected by the tangent to the curve at the point of inflection and corresponds to the end of the transition; the peak temperature is the temperature, at which the peak reaches the maximum (or minimum).

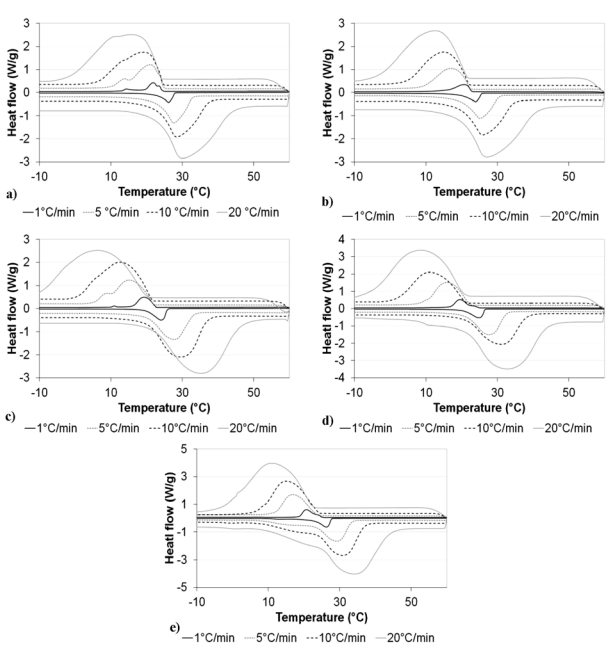

Figure 1: Heat flow during heating and cooling of: a) Micronal DS 5038 X, b) Micronal DS 5040 X, c) Rubitherm RT 21, d) Rubitherm RT 22, e) Rubitherm RT 25

3 RESULTS AND DISCUSSION

The basic physical properties of the studied materials are given in **Table 1**. The data represents the average values from five measurements. The data was obtained in laboratory conditions of 23.0 ± 2 °C and 30.0 ± 2 % RH.

Table 1: Basic physical properties and thermal conductivity of the studied PCMS

PCM	Powder density	Bulk density	Thermal conductivity
	(kg/m^3)	(kg/m^3)	(W/m K)
Micronal DS 5038 X	361	–	0.080
Micronal DS 5040 X	365	–	0.079
Rubitherm RT 21	–	787	0.442
Rubitherm RT 22	–	789	0.445
Rubitherm RT 25	–	787	0.444

The powder densities of both BASF materials were very similar, while the examined Rubitherm materials exhibited almost identical values of the bulk density. For both powdered BASF materials, the thermal conductivity values were very low due to the presence of air gaps between the particles. The assumed incorporation of the PCM into the silicate matrix (cement or cement-lime plasters) with almost no air between the PCM particles is, of course, supposed to result in an increased thermal conductivity as presented, for example, by Z. Wang et al.[18] On the other hand, the thermal conductivities of the PCM dispersions were much higher. This was due to the presence of more than 60 % of water in the dispersion. From a practical point of view, a high thermal conductivity of PCMs ensures their effective thermal performance, thus the optimum usage of the latent heat.

Figure 1 describes the results of the DSC analysis used for the determination of the phase-change temperature, the enthalpy of phase transition and the specific heat capacity of the examined materials. A significant effect of the heating and cooling rate on the monitored temperature of the phase-change transition was observed in all the cases. Generally, with the increasing heating/cooling rate, the phase-change-transition range was more spread; this feature was more remarkable for the materials based on dispersion. A similar PCM performance with respect to the heating rate applied in a DSC analysis was observed, e.g., by G. Feng et al.[19] who analysed capric acid of high purity (≥ 99.9 %) so that the influence of the material impurity on DSC results was

neglected. G. Feng et al.[19] applied heating rates of (10, 5, 1, 0.5 and 0.1) °C/min. When the heating/cooling rate increased from 0.1 °C/min to 10 °C/min, the biggest deviations in solid- and liquid-transition temperatures were 1.1 °C and 6.4 °C, respectively.

In our case, when the heating or cooling rate increased from 1 °C/min to 20 °C/min, the biggest difference in the onset of the liquid-transition temperature was 1.9 °C (measured for Rubitherm RT 21) and it was 2.8 °C for the onset of the solidification temperature (for Rubitherm RT 25). On the other hand, sharp boundaries of the phase-change transition were found for the lower rates of the heating. In this case, it was easy to identify the onset and endset temperatures of the phase change and to calculate its corresponding enthalpy.

The onset and endset temperatures used for the assessment of the enthalpy of the phase transition are given in **Table 2**. Comparing the measured onset and endset temperatures with the phase-change temperatures declared by the producers, the mean values measured for the lower heating/cooling rates corresponded to those provided on PCM product sheets.

Table 2: Phase-change temperatures

PCM	Temperature-change rate (°C/min)	Heating (°C)		Cooling (°C)	
		Onset	Endset	Onset	Endset
Micronal DS 5038 X	1	23.3	27.8	23.7	19.5
	5	23.2	32.8	24.7	14.0
	10	22.9	37.4	24.6	6.2
	20	22.8	44.1	24.2	–1.7
Micronal DS 5040 X	1	19.6	25.5	22.7	15.9
	5	19.5	30.4	22.4	17.0
	10	19.4	34.5	22.1	4.7
	20	19.3	41.1	21.6	–3.5
Rubitherm RT 21 HC	1	19.6	25.7	22.5	16.2
	5	19.9	33.2	21.9	8.4
	10	20.1	37.0	21.5	12.6
	20	21.5	46.2	19.9	–10.1
Rubitherm RT 22 HC	1	20.4	26.4	22.7	16.9
	5	20.7	32.5	22.3	9.9
	10	20.7	38.3	21.0	2.0
	20	21.0	43.7	20.6	–4.9
Rubitherm RT 25 HC	1	22.7	27.6	24.9	18.7
	5	22.0	33.1	23.5	12.0
	10	21.7	36.9	23.8	8.7
	20	21.0	44.3	22.1	1.7

Considering the DSC plots, we can see that during the heating process all the measured heat flux vs. temperature curves exhibited a unimodal character. On the other hand, during the cooling, bimodal or even trimodal shapes were obtained for materials Micronal DS 5038 X and Rubitherm RT 21 HC. In the past, bimodal shapes of DSC curves were found by other investigators as well. J. Jeon et al.[20] reported on two phase-change peaks of paraffin. The first phase-change peak in the cooling process was high, corresponding to the liquid-solid transition of paraffin, but the second peak was much lower. As it was analysed in detail by N. Ukrainczyk et al.[21], this smaller endotherm corresponds to the solid-solid transition when the close-packed hexagonal system of paraffin transforms into the orthorhombic or monoclinic (depending on the number of carbon atoms in a molecule) crystalline structure.

Considering the findings of the other investigators mentioned above, the shapes of the DSC plots of Micronal DS 5038 X and Rubitherm RT 21 in the cooling phase can be explained with two main effects. First, the paraffin underwent two phase transitions.[20,21] Second, due to the high cooling rate adopted for the DSC analysis, the super-cooling phenomena could also contribute to the appearance of the bimodal (or/and trimodal) shape of the DSC plots.[22]

In **Table 3**, the enthalpies of fusion and crystallization in dependence on the heating and cooling rate are presented. The PCMs produced by BASF exhibited substantially lower enthalpies, as compared to the values obtained for the materials delivered by Rubitherm. While the enthalpy values of the BASF products varied from 93 J/g to 103 J/g, the Rubitherm materials yielded the enthalpy in a range of 113–183 J/g. Enthalpy values similar to those shown in Table 4 were obtained, e.g., by J. Jeon et al.[20] and X. Liu at al.[23] who obtained, for paraffinic waxes, enthalpies of fusion of 144.6 J/g and 153.5 J/g, respectively. Comparing the measured data with the enthalpy values provided on product sheets, the values obtained in our case were lower, especially for the Rubitherm materials.

Table 3: Phase-change enthalpies

PCM	Temperature-change rate (°C/min)	Enthalpy (J/g)	
		Heating	Cooling
Micronal DS 5038 X	1	99.5	102.6
	5	101.2	103.4
	10	98.9	103.6
	20	97.9	103.9
Micronal DS 5040 X	1	97.7	100.3
	5	94.0	96.1
	10	95.2	98.8
	20	96.0	103.2
Rubitherm RT 21 HC	1	124.3	131.6
	5	125.5	128.8
	10	126.9	131.3
	20	113.0	119.0
Rubitherm RT 22 HC	1	134.0	128.2
	5	131.9	134.2
	10	126.0	130.6
	20	125.8	131.3
Rubitherm RT 25 HC	1	175.0	166.8
	5	177.3	167.8
	10	178.5	171.1
	20	174.9	183.2

The heating/cooling-rate change resulted in only small differences between the measured enthalpies of fusion and crystallization (< 7 %) up to 10 °C/min. For 20 °C/min, the differences were higher in some cases (Rubitherm RT 21 HC for both the heating and cooling phase, Rubitherm RT 25 HC for the cooling phase) which could be attributed to the higher uncertainty of the measurement of higher temperature-change rates and the difficulty to distinguish the endset and onset temperatures of the phase change. The differences between the enthalpies of fusion and crystallization of particular tested materials were small in all the cases, up to 6 %; they were well within the measurement uncertainty.

Figure 2 shows the specific-heat-capacity plots obtained from the DSC tests. The data represents the average values of three measurements. All the tested materials exhibited an increase in the specific-heat capacity during the melting. Similar to the heat-flow plots shown in **Figures 1** to **5**, a remarkable increase in the specific-heat capacity with the decreasing temperature-change rate was observed in the temperature ranges corresponding to the solid-liquid phase transitions. For instance, for the heating rate of 1 °C/min, the specific-heat-capacity function of Micronal DS 5038 X reached the maximum at 30.1 J/g K. When the heating rate of 20 °C/min was used, the specific-heat-capacity maximum was only 8.5 J/g K. This finding can have significant consequences for the practical capabilities of particular PCMs to moderate the interior climate of a building exposed to different exterior climatic loads as well as to moderate technological processes, energy recuperation, etc.

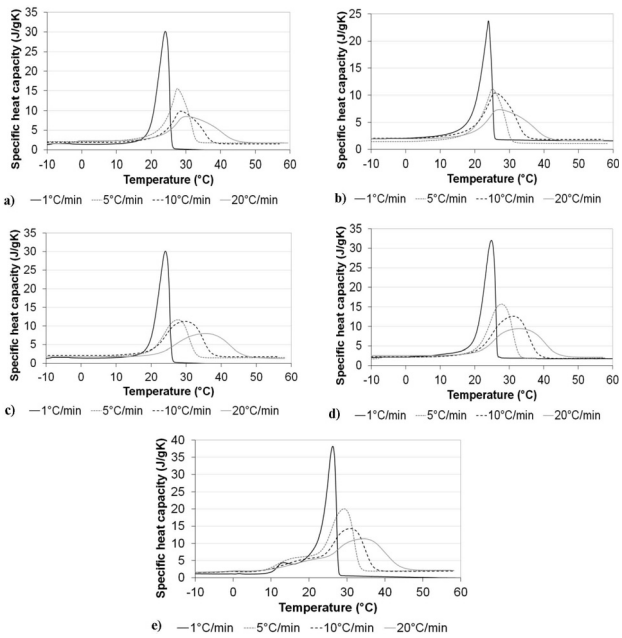

Figure 2: Specific-heat capacity during heating: a) Micronal DS 5038 X, b) Micronal DS 5040 X, c) Rubitherm RT 21, d) Rubitherm RT 22, e) Rubitherm RT 25

From a quantitative point of view, the measured values of the specific-heat capacity corresponding to melting are very high, making the studied PCMs well applicable for effective heat storage in building and construction elements. For lower temperatures, for example 10 °C, the measured specific-heat capacity dropped and reached values of 1.4–2.6 J/g K. Similar results for paraffin E_{53} were reported by E. M. Anghel et al.[24] who obtained, at 10 °C, a specific heat capacity of 1.6 J/g K. Similarly, D. Zhou et al.[25] reported on the specific-heat capacity of Rubitherm 25 that was 2.1 J/g K.

4 CONCLUSIONS

A thermophysical analysis of several different PCMs in the form of a fine powder and water dispersion was done, taking into account the effects of the mode and dynamics of a DSC-simulated thermal process on phase-change characteristics.

The main results of the experimental work can be summarized in the following points:

- The choice of a proper heating/cooling mode of the DSC test was of particular importance for the evaluation and generalization of the PCM thermal performance. In this respect, it was found that a universal methodology for testing PCMs with an assumed application in the construction industry is actually missing although the low-temperature change rate looks promising for a detailed description of phase-change processes.
- A significant effect of the heating and cooling rate on the monitored temperature of the phase-change transition was observed for all the studied PCMs. Generally, with the increasing rate of the temperature change, the phase-change-transition range was more spread; this feature was more remarkable for the materials based on dispersion.
- The temperature-rate change resulted in only small differences between the measured enthalpies of fusion and crystallization up to 10 °C/min.
- The powdered PCMs produced by BASF exhibited substantially lower phase-change enthalpies, when compared to the water-dispersed PCMs delivered by Rubitherm. This was in agreement with the data provided by PCM producers. However, all the studied materials were found to be suitable candidates for application in lightweight interior plasters.
- An increase in the heating rate led to a decrease in the maximum specific-heat capacity in the desired operational range of the examined PCMs. From the point of view of their assumed application for the moderation of a building's interior climate, their effectiveness is better for slower temperature changes, as in common climatic conditions.
- Based on the findings presented above, it can be concluded that from a practical point of view, aiming at an effective use of PCMs in the conditioning of a

building's interior climate, the most crucial is the monitoring of temperature fluctuations in the interior and the performance of a DSC analysis according to the measured indoor-temperature-rate change. In this way, the choice of a proper PCM will consider the actual conditions of a building, and the thermal envelope with the incorporated PCM will be "tailor-made".

Acknowledgment

Authors gratefully acknowledge the financial support of the Czech Science Foundation, under project No P105/12/G059.

5 REFERENCES

[1] World Energy Outlook 2010, OECD/IEA, SOREGRAPH, Paris Cedex 2010, 731

[2] Y. Zhang, S. Zhuang, Q. Wang, J. He, Experimental research on the thermal performance of composite PCM hollow block walls and validation of phase transition heat transfer models, Adv. Mater. Sci. Eng., (2016), doi:10.1155/2016/6359414

[3] A. G. Entrop, H. J. H. Brouwers, A. H. M. E. Reinders, Experimental research on the use of micro-encapsulated phase change materials to store solar energy in concrete floors and to save energy in Dutch houses, Sol. Energy, 85 (**2011**), doi:10.1016/j.solener.2011.02.017

[4] F. Agyenim, N. Hewitt, P. Eames, M. Smyth, A review of materials, heat transfer and phase change problem formulation for latent heat thermal storage systems (LHTESS), Renew. Sust. Energ. Rev., 14 (**2010**), doi:10.1016/j.rser.2009.10.015

[5] J. M. Marín, B. Zalba, L. F. Cabeza, H. Mehling, Determination of enthalpy–temperature curves of phase change materials with the temperature-history method: improvement to temperature dependent properties, Measurement Sci. Technol., 14 (**2003**), doi:10.1088/0957-0233/14/2/305

[6] L. Gao, J. Zhao, Q. An, D. Zhao, F. Meng, X. Liu, Experiments on thermal performance of erythritol/expanded graphite in a direct contact thermal energy storage container, Appl. Therm. Eng., 113 (**2017**), doi:10.1016/j.applthermaleng.2016.11.073

[7] B. Zalba, J. M. Marín, L. F. Cabeza, H. Mehling, Review on thermal energy storage with phase change: materials, heat transfer analysis and applications, Appl. Therm. Eng., 23 (**2003**), doi:10.1016/S1359-4311(02)00192-8

[8] P. Losada-Pérez, C. S. P. Tripathi, J. Leyes, G. Cordoyiannis, C. Glorieux, J. Thoen, Measurement of heat capacity and enthalpy of phase change materials by adiabatic scanning calorimetry, Int. J. Thermophys., 32 (**2011**), doi:0.1007/s10765-011-0984-0

[9] C. Arkar, S. Medved, Influence of accuracy of thermal property data of a phase change material on the result of a numerical model of a packed bed latent heat storage with spheres, Thermochim. Acta, 438 (**2005**), doi:10.1016/j.tca.2005.08.032

[10] B. He, V. Martin, F. Setterwall, Phase transition temperature ranges and storage density of paraffin wax phase change materials, Energy, 29 (**2004**), doi:10.1016/j.energy.2004.03.002

[11] H. Mehling, H. P. Ebert, P. Schossig, Development of standards for materials testing and quality control of PCM, 7th IIR Conference on Phase Change Materials and Slurries for Refrigeration and Air Conditioning, Dinan 2006, 1–9

[12] Product Overview, BASF company, http://product-finder.basf.com, 6.4.2017

[13] PCM RT-Line, Rubitherm, https://www.rubitherm.eu, 6.4.2017

[14] E. Gmelin, S. M. Sarge, Temperature, heat and heat flow rate calibration of differential scanning calorimeters, Thermochim. Acta, 347 (**2000**), doi:10.1016/S0040-6031(99)00424-4

[15] ISO 11357-1:2016 Plastics – Differential scanning calorimetry (DSC) – Part 1: General principles, ISO Committee, Geneve

[16] A. Shimkin, Optimization of DSC calibration procedure, Thermochim. Acta, 566 (**2013**), doi:10.1016/j.tca.2013.04.039

[17] ISO 11357-3:2011 Plastics – Differential scanning calorimetry (DSC) – Part 3: Determination of temperature and enthalpy of melting and crystallization, ISO Committee, Geneve

[18] Z. Wang, H. Su, S. Zhao, N. Zhao, Influence of phase change material on mechanical and thermal properties of clay geopolymer mortar, Constr. Build. Mater., 120 (**2016**), doi:10.1016/j.conbuildmat.2016.05.091

[19] G. Feng, K. Huang, H. Xie, H. Li, X. Liu, S. Liu, DSC test error of phase change material (PCM) and its influence on the simulation of the PCM floor, Renew. Energy, 87 (**2016**), doi:10.1016/j.renene.2015.07.085

[20] J. Jeon, S. G. Jeong, J. H. Lee, J. Seo, S. Kim, High thermal performance composite PCMs loading xGnP for application to building using radiant floor heating system, Sol. Energ. Mater. Sol. C., 101 (**2012**), doi:10.1016/j.solmat.2012.02.028

[21] N. Ukrainczyk, S. Kurajica, J. Sipusic, Thermophysical comparison of five commercial paraffin waxes as latent heat storage materials, Chem. Biochem. Eng. Q., 24 (2010)

[22] Z. Pavlík, J. Fořt, M. Pavlíková, J. Pokorný, A. Trník, R. Černý, Modified lime-cement plasters with enhanced thermal and hygric storage capacity for moderation of interior climate, Energ. Buildings, 126 (**2016**), doi:10.1016/j.enbuild.2016.05.004

[23] X. Liu, H. Liu, S. Wang, L. Zhang, H. Cheng, Preparation and thermal properties of form stable paraffin phase change material encapsulation, Energ. Convers. Manage., 47 (**2006**), doi:10.1016/j.enconman.2005.10.031

[24] E. M. Anghel, A. Georgiev, S. Petrescu, R. Popov, M. Constantinescu, Thermo-physical characterization of some paraffins used as phase change materials for thermal energy storage, J. Therm. Anal. Calorim., 117 (**2014**), doi:10.1007/s10973-014-3775-6

[25] D. Zhou, C. Y. Zhao, Y. Tian, Review on thermal energy storage with phase change materials (PCMs) in building applications, Appl. Energ. 92 (**2012**), doi:10.1016/j.apenergy.2011.08.025

UDK 67.017:621.793.3:669.721.5
Original scientific article/Izvirni znanstveni članek

ISSN 1580-2949
MTAEC9, 51(6)925(2017)

CHARACTERIZATION OF Ni-P COATING PREPARED ON A WROUGHT AZ61 MAGNESIUM ALLOY VIA ELECTROLESS DEPOSITION

KARAKTERIZACIJA Ni-P PREVLEKE, PRIPRAVLJENE Z NEELEKTRIČNO DEPOZICIJO NA KOVANI MAGNEZIJEVI ZLITINI AZ61

Martin Buchtík[1], Petr Kosár[1], Jaromír Wasserbauer[1], Pavel Doležal[1,2]

[1]Brno University of Technology, Faculty of Chemistry, Purkyňova 464/118, 602 00 Brno, Czech Republic
[2]Brno University of Technology, Faculty of Mechanical Engineering, Technická 2896/2, 602 00 Brno, Czech Republic
xcbuchtik@fch.vutbr.cz

Prejem rokopisa – received: 2017-03-08; sprejem za objavo – accepted for publication: 2017-04-20

doi:10.17222/mit.2017.029

A low-phosphorous Ni-P coating was prepared on a wrought AZ61 magnesium alloy via electroless deposition for 1 h after an adequate substrate-surface pre-treatment. The prepared coating with a thickness of 10 μm was characterized by the uniform distribution of Ni (95.4 % mass fraction) and P (4.6 % mass fraction) in the cross-section. Microcavities present in the coating resulted in quite a low corrosion resistance of the coated magnesium alloy in a 0.1 M NaCl solution. On the other hand, the coating exhibits a high degree of adhesion, as evidenced by a scratch test, and significantly improves the AZ61 magnesium-alloy microhardness.

Keywords: electroless nickel, magnesium alloy, AZ61, characterization of Ni-P coatings

Malo porozna Ni-P prevleka je bila pripravljena na površini kovane AZ61 magnezijeve zlitine. Prevleka je bila pripravljena z enourno neelektrično depozicijo na predhodno ustrezno obdelani površini zlitine. Pripravljena prevleka debeline 10 μm je imela v prečnem prerezu enakomerno porazdelitev Ni (95,4 % masnih odstotkov) in P (4,6 % masnih odstotkov). Zaradi prisotnosti mikropraznin v izdelani prevleki je korozijska odpornost prevlečene magnezijeve zlitine v 0,1 M NaCl raztopini slaba. Preizkusi razenja prevleke pa so po drugi strani pokazali zelo dober oprijem izdelane prevleke s površino zlitine in znatno izboljšanje mikrotrdote AZ61 magnezijeve zlitine.

Ključne besede: brezelektrično nikljanje, magnezijeva zlitina, AZ61, karakterizacija Ni-P prevlek

1 INTRODUCTION

Due to their low density, magnesium alloys are ranked among the lightest constructional metallic materials. Magnesium alloys concurrently have a high specific strength, toughness and good casting properties. They find their application in the automotive and aerospace industry.[1–4] A high chemical reactivity, low corrosion resistance and low hardness are their negative properties.[4] Therefore, it is necessary to protect magnesium alloys against the effects of external environment. There are several ways of protecting magnesium alloys such as galvanic or electroless deposition of coatings, conversion coatings, organic coatings and varnishing.

Electroless-deposited Ni-P coatings improve the coated-material resistance to corrosive environments and material mechanical and wear resistance. Deposited Ni-P coatings have a higher corrosion resistance, physico-mechanical and tribological properties compared to non-treated magnesium alloys.[5–7] Generally, the industry identifies three groups of electroless Ni-P coatings according to their phosphorus contents. Low-phosphorus coatings contain 2–5 % mass fractions of phosphorus, medium-phosphorus Ni-P coatings contain 6–9 % mass fractions of phosphorus and high-phosphorus Ni-P coatings contain 10–13 % mass fractions of phosphorus.[8] Low-phosphorus Ni-P coatings are predominantly used to increase the hardness of the coated substrate.[1] In general, the hardness, crystallinity and density of electroless Ni-P coatings decrease with the increasing content of phosphorus in the coatings. However, the corrosion resistance of Ni-P coatings increases with the increasing content of phosphorus.[1,9]

The hardness of deposited low-phosphorus Ni-P coatings can be additionally increased by heat treatment.[5] During heat treatment, the deposited coating consisting of an amorphous Ni-P phase decomposes due to a gradual increase in the temperature to form crystalline particles of phosphide (Ni_3P). Fine crystalline particles of phosphide (Ni_3P) are formed simultaneously, predominantly in the form of precipitates.[9] The highest value of the hardness of Ni-P coatings is reached after the heat treatment at 400 °C for 1 h, when the hardness reaches a value of up to 1300 HV.[10] The hardness of Ni-P coatings can also be increased by reducing the phosphorus content by changing the ratio of the components contained in the nickel bath and by changing the coating-process

conditions.[1] However, the Ni-P coating corrosion resistance increases with the increasing content of phosphorus.[1] The phosphorus content in a deposited Ni-P coating can be controlled by adding suitable surfactants into the nickel bath. As mentioned in reference,[11] an addition of SDS (sodium dodecyl sulfate) causes an increase in the phosphorus content from 6 % to 9 %. It was observed that the hardness of the Ni-P coating increased with an increase in the SDS concentration up to its critical micelle concentration (CMC) and then decreased. The hardness of the Ni-P coating without a surfactant was 450 HV 0.2 and, in the presence of SDS, the hardness increased up to 685 HV 0.2. The change is due to the change in the coating crystalline structure. In the case of the absence of SDS, the structure of the Ni-P coating is purely crystalline. With an addition of SDS, the structure changes into a mixture of nanocrystalline and amorphous structure. At SDS concentrations higher than CMC, the phosphorus content is 9–10 %. The same effect was observed for CTAB (cetyltrimethylammonium bromide). An addition of CTAB caused an increase of phosphorus in the deposited coating of 7.5–12 % and the hardness of the Ni-P coating increased up to 675 HV 0.2.

In general, the addition of some filler to the Ni-P coating matrix is another possible way to increase the hardness of Ni-P coatings. SiC, Al_2O_3,[12–13] SiO_2, TiO_2[14–15] particles and carbon nanotubes can be used as a suitable filler for the Ni-P matrix, improving the coating properties.

The adhesion of the coatings to the substrate is significantly affected by appropriately selected pre-treatments of the substrate surface.[13] The presented paper deals with the characterization of electroless-deposited Ni-P coatings prepared on an wrought AZ61 magnesium alloy. The influence of the coated-substrate pre-treatment and the coating chemical composition on the coating tribological properties and corrosion resistance was the main objective of the study. A 0.1 M NaCl solution was used for immersion tests to analyze the coated magnesium alloy corrosion resistance and corrosion mechanism.

2 EXPERIMENTAL MATERIAL AND PROCEDURES

2.1 Experimental material

Specimens of the wrought AZ61 magnesium alloy with dimensions of 20 mm × 20 mm × 0.8 mm were used as substrates for the deposition of the Ni-P coating. The EDS-measured chemical composition of the AZ61 magnesium alloy is shown in **Table 1**. The measured chemical composition corresponds to standard ASTM B107M.[16] The microstructure of the alloy is shown in **Figure 1**. The microstructure was documented using a light optical microscope (LM) and the microstructural features were identified using a scanning electron microscope (SEM) with EDS. To reveal the magnesium alloy microstructure, ground and polished metallographic samples were poured into a picral etchant (consisting of 4.2 g picric acid, 10 mL acetic acid, 10 mL water and 70 mL ethanol) for 5 s. The microstructure is formed by δ substitutional solid-solution grains (a solid solution of Al in Mg) and γ particles corresponding to the chemical composition of $Mg_{17}(Al,Zn)_{12}$. As shown in **Figure 1b**, the presence of AlMn-based intermetallic phases (apparently Al_4Mn) was also evident in the microstructure.

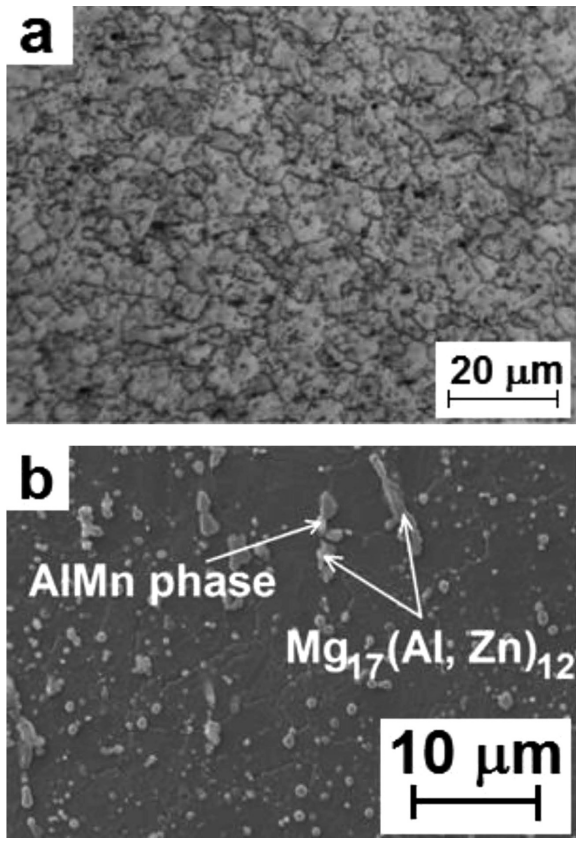

Figure 1: Microstructure of wrought AZ61 magnesium alloy, etched with picral etchant: a) structure of AZ61 magnesium alloy, LM; b) alloy phases, SEM

Table 1: Measured elemental composition of the uncoated wrought AZ61 magnesium alloy

Alloy	Elements (w/%)								
	Al	Zn	Mn	Si	Fe	Ni	Cu	Mg	others
AZ61	5.8-7.2	0.4-1.5	0.15-0.5	max. 0.15	max. 0.005	max. 0.005	max. 0.05	bal.	max. 0.3

2.2 Deposition of the Ni-P coating

Before the Ni-P coating deposition, a specific pre-treatment was required to reach the adequate surface roughness and activity. The samples of the AZ61 magnesium alloy were ground using SiC paper no. 1200. Next, the samples were degreased in an alkaline degreasing bath containing soil-releasing agents. The following pickling in an acid pickling bath was performed to activate the surface with partial etching (removing of the

oxide layer). Rinsing the samples with distilled water and isopropanol and drying them with a stream of hot air were performed between the steps of the pre-treatment.

The electroless Ni-P coating deposition, following the sample-surface pre-treatment, proceeded for 60 min. The electroless nickel bath was composed by a nickel source ($NiSO_4 \cdot 6H_2O$), a reducing agent ($NaH_2PO_2 \cdot H_2O$), a complexing agent and an $H_2PO_2^-$ activating substance. The samples were kept in the middle of the bath to ensure a uniform coating formation.

2.3 Characterization of the Ni-P coating

The microhardness of the deposited Ni-P coating was carried out using a Vickers microhardness tester LECO AMH43. Loading of 25 g for 10 s was used for the indentation according to the standard.[17] To obtain the average value, ten indentations were performed on the coating cross-section. The average thickness of the deposited Ni-P coating used for microhardness testing was about 30 μm.

The physicochemical properties of the deposited Ni-P coating were evaluated using a CSM Instruments REVETEST scratch tester with the progressive-load-type method and a Rockwell diamond indenter with the top angle of 120° and the top radius of 200 μm. For the evaluation of the physicochemical properties, the surface of the substrate was polished to the roughness of $R_a \approx 0.25$ μm using diamond pastes during the pre-treatment after the grinding. The friction force, the friction coefficient, the penetration depth and the acoustic emission were recorded along with the adhesion during the scratch test. The applied normal force was set in a range of 1–20 N. The speed of the indenter was 1.58 mm min^{-1} and the total length of the trace was 3 mm.[18]

A Zeiss Evo LS-10 scanning electron microscope (SEM) equipped with an EDS Oxford Instruments Xmax 80 mm^2 detector and the AZtec software was used to determine the average contents of nickel and phosphorus in the deposited Ni-P coatings. SEM observations were also used to evaluate the mechanism of the corrosion degradation of the magnesium substrate and the deposited Ni-P coating after an exposure to 0.1 M NaCl.

For the evaluation of the mechanism of the corrosion degradation of the magnesium substrate and the deposited Ni-P coating, the samples were immersed into a 0.1 M solution of NaCl for 20 min. After this time, the surface of a sample was analyzed using the scanning electron microscope and the mechanism of corrosion degradation was determined on the cross-section of the sample.

3 RESULTS AND DISCUSSION

3.1 Characterization of the deposited Ni-P coatings

Uniform Ni-P coatings were deposited on the AZ61 magnesium alloy substrate. **Figure 2a** shows the nodular

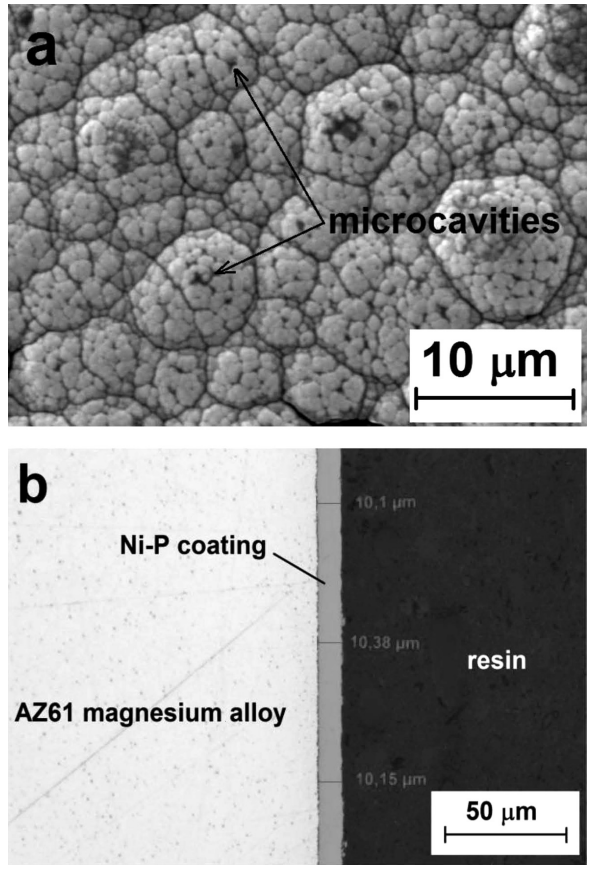

Figure 2: Microstructure of Ni-P coating: a) surface morphology of Ni-P coating, b) cross-section morphology of Ni-P coating on AZ61 magnesium alloy

structure of the Ni-P coating with a typical cauliflower-like pattern. Between these nodular cusps, a certain amount of microcavities is present. These microcavities are nucleation sites for micropitting in the case of material exposure to a corrosive environment. However, no macrodefects were observed in the deposited Ni-P coatings, neither at the Ni-P/substrate interface. **Figure 2b** shows the cross-section morphology of the deposited Ni-P coating. It shows that the Ni-P coating is uniform and compact. The average thickness of the deposited Ni-P coating used for the microhardness testing was about 30 μm and the average thickness of the deposited Ni-P coating used for the EDS analysis and the scratch test was about 10 μm.

Using the EDS analysis, it was determined that the content and distribution of individual components in the deposited Ni-P coating were homogeneous throughout the entire cross-section (**Figure 3**). The analysis showed that the nickel content in the deposited Ni-P coating was 95.4±0.1 % mass fraction and the phosphorus content was 4.6±0.1 % mass fraction. Based on references,[8,10] this coating can be classified as a low-phosphorus Ni-P coating. The homogenous distribution of individual elements in the coating is a sign of a continual coating growth.

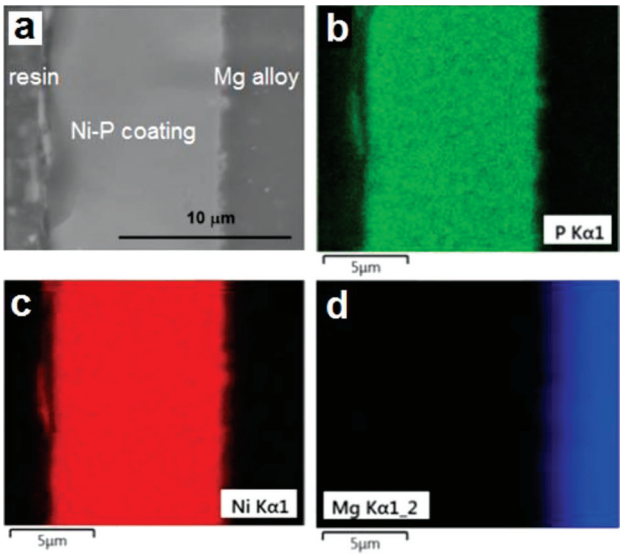

Figure 3: Mapping of Ni-P coating on AZ6 alloy: a) structure of Ni-P coating, b) phosphorus, c) nickel, d) magnesium

3.2 Mechanical and physicochemical properties of the deposited Ni-P coating

The resulting average microhardness value of the prepared electroless-deposited low-phosphorous Ni-P coating is 700±40 HV 0.025, as measured on 10 random places on the coating cross-section. The microhardness of the plain magnesium substrate is 79±6 HV 0.025, so the microhardness of the Ni-P coating is around nine times higher than that of the AZ61 magnesium substrate.

The obtained value is higher when compared to the microhardness of the coating reported on in reference[19]. On the other hand, a positive influence of the filler addition and heat treatment on the coating microhardness was observed in reference.[19] An increase in the microhardness from 380±10 HV 0.1 to 540±10 HV 0.1 was observed when adding SiO_2 nanoparticles to the Ni-P coating[19]; however, this value is still lower when compared to the presented coating. The microhardness of the electroless-deposited composite coating reported on in reference[19] increased to 970±10 HV 0.1 when applying a heat treatment to the coated component at 400 °C.

A similar effect was observed in the work reported in reference[20] where the hardness of the plain Ni-P coating reached a value of 608±12 HV. With the addition of a TiO_2 colloidal solution to the nickel bath, followed by a co-deposition of TiO_2 particles into the Ni-P coating, the hardness value of the Ni-P/TiO_2 composite coating increased to 685±18 HV, which is comparable with the presented coating. The increase in the hardness of the deposited Ni-P/TiO_2 composite coating to 1325±40 HV was observed by following the application of a heat-treatment.[20]

The obtained values of critical normal forces L_{c1} and L_{c2} and adequate values of friction forces F_{t1} and F_{t2} at normal forces L_{c1} and L_{c2}, respectively, are shown in **Table 2**. The record of the scratch test of the Ni-P coating on the AZ61 magnesium alloy is shown in **Figure 4**. Details of the Ni-P coating on the AZ61 magnesium alloy after the scratch test for normal forces L_{c1} and L_{c2} are shown in **Figures 5a** and **5b**, respectively.

The determined value of critical normal force L_{c1} was 6.9 N. The formation of oblique and parallel cracks were observed at L_{c1}, **Figure 5a**. The determined value of critical normal force L_{c2} was 11.9 N. The formation of transverse arch cracks was observed at L_{c2}, **Figure 5b**. Ductile failure of the coating due to the internal tensile stresses occurs during the scratch test.

Table 2: Values of critical normal forces and friction forces of Ni-P coatings and a comparison of these values with the published data

Lit.	Sub-strate	Coating	L_{c1} (N)	L_{c2} (N)	F_{t1} at L_{c1} (N)	F_{t2} at L_{c2} (N)
This work	AZ61	Ni-P	6.9	11.9	0.8	2.2
(21)	AZ31	Ni-P	7.3	12.3	1.1	2.6
(2)	AZ91	Ni-P	-	17.6 (L_c)	-	-
(23)	AZ61	PEO	2.69 ± 0 .10	-	-	-
(24)	AZ61	Ti/Ti (C,N)/ (TiAl)N	3	10	-	-

Comparing critical loads L_{c1} and L_{c2} of the experimental Ni-P coating deposited on the AZ61 magnesium alloy with the Ni-P coating deposited on the AZ31 magnesium alloy from[21], it became clear that the Ni-P coating on the AZ61 magnesium alloy achieved lower critical values L_{c1} and L_{c2}. Oblique, parallel and transverse arch cracks were also observed on the Ni-P coating on the AZ31 magnesium alloy.[21] This effect can be attributed to a slight difference between the methods of the pre-treatment of the magnesium substrate before the deposition process.

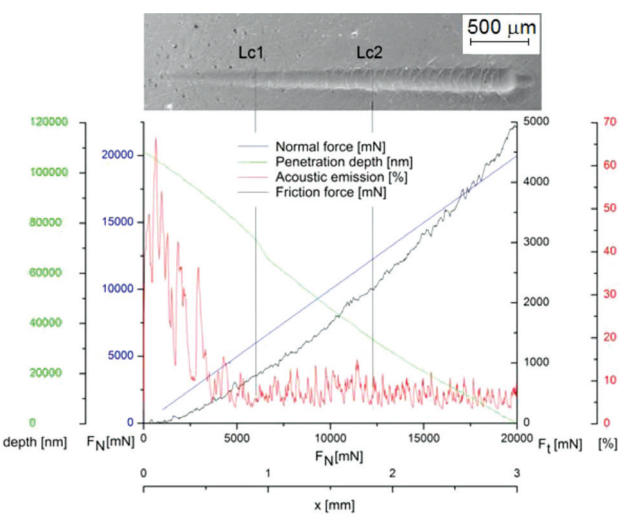

Figure 4: Evaluation of scratch tests for Ni-P coating on AZ61 magnesium alloy

The adhesion of the deposited heat-treated Ni-P coating prepared on the AZ91 magnesium alloy was evaluated in reference.[2] The first cracks on the heat-treated Ni-P coating deposited on the AZ91 magnesium alloy were observed at a load of 17.6 N and their characteristics were the same for all the heat-treated samples. However, the character of the cracks is slightly different compared to the experimental samples (Ni-P on AZ61) due to the heat treatment of the Ni-P coating. Heat-treated coatings are more brittle compared to the non-treated coatings.[1] Moreover, it was observed that the abundance of cracks increased with the increasing applied load.

In literature[2], critical load value L_c, where the first cracks were observed, is higher than that of the Ni-P coatings deposited on the AZ61 magnesium alloy (**Table 2**) and the samples of AZ31 described in reference[21]. This fact can be attributed to several factors. The progressive-load-type method of the scratch test was chosen for the evaluation of the adhesion of the experimental Ni-P coating on an AZ61 alloy and the Ni-P coating on an AZ31 alloy in [21]. However, the constant-load-type method of the scratch test was chosen for the evaluation of the adhesion of a heat-treated Ni-P coating in literature [2]. Moreover, the initial load for the evaluation of the heat-treated Ni-P coatings on the AZ91 magnesium alloy was determined to be 8.80 N and the load was increased five times to 44.0 N. The heat treatment can affect the adhesion of the coating to the substrate. As indicated in literature[22], the creation of Al-Ni intermetallic phases can significantly reduce the adhesion of Ni-P coatings to the AZ91 magnesium alloy after the heat treatment. However, this effect was not observed in the research from reference[2]. This can be attributed to the fact that the presence of these phases is limited to small areas of the γ phase ($Mg_{17}Al_{12}$) present on a substrate surface. The content of the γ phase is dependent on the Al content in the substrate. Clearly, a low amount of Al in AZ91 used in the research from reference[2] did not have a detrimental effect on the coating adhesion.

As shown in **Table 2**, it was observed that the adhesion of the PEO (plasma electrolytic oxidation) coating on the AZ61 magnesium alloy mentioned in reference[23] is lower with respect to the Ni-P coatings deposited on the AZ61 magnesium alloy in this work. In particular, a significantly lower value of critical load L_{c1} resulting in coating damage was measured in the research from literature[23], with respect to the present work.

It can be noted that the deposited Ni-P coating showed a higher adhesion to the magnesium-alloy substrate with respect to the PEO or plasmatic composite coatings.[24] These composite coatings and plasma-deposited layers are more brittle than the deposited coatings. In addition, the adhesion of coatings to the substrate is negatively affected by the stresses at the matrix/filler interface created during the coating formation.[25]

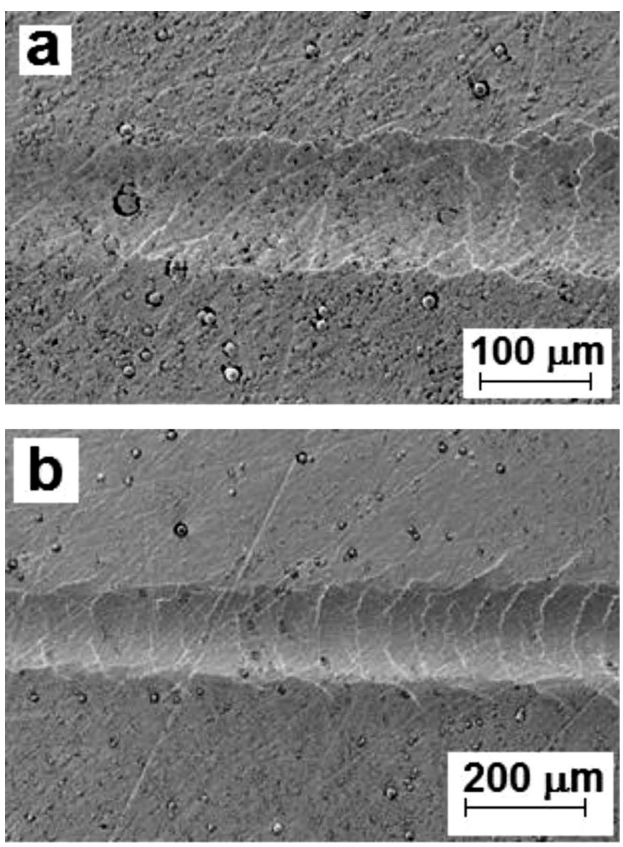

Figure 5: Details of Ni-P coating after scratch tests: a)L_{c1}, b) L_{c2}

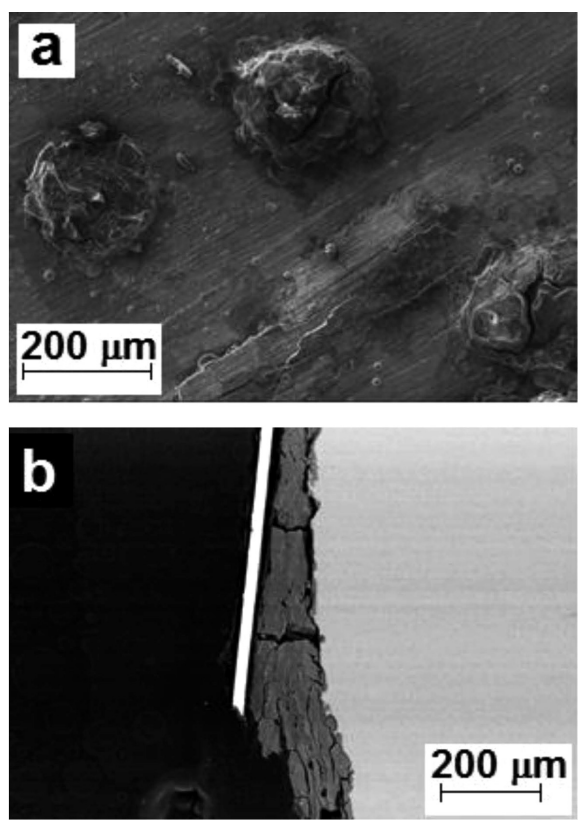

Figure 6: Ni-P coating on AZ61 magnesium alloy after an exposure to 0.1 M NaCl: a) surface, b) cross-section

3.3 Exposure of the samples to a corrosive environment

Figure 6 shows a corrosion degradation of the AZ61 magnesium alloy with the Ni-P coating after an exposure to a 0.1 M NaCl solution for 20 min. The low-phosphorus coatings are characterized by a higher hardness and crystallinity but also by a lower corrosion resistance when compared to the high-phosphorous Ni-P coatings.[10]

The deposited Ni-P coating was characterized by a structure with nodular cusps (**Figure 2a**). An imperfect nickel deposition may occur among these cusps, causing the Ni-P coating to have a certain amount of microcavities in its volume. These microcavities are the nucleation sites for a corrosion attack and micropitting in the case of an exposure to a corrosive environment. The transport of corrosive agents to the surface of the magnesium substrate occurs through these microcavities. The corrosion process starts at the magnesium substrate/Ni-P coating interface. Chemical reactions occur due to the interaction between the corrosive agents and the magnesium-alloy substrate. The formed corrosion products accumulating on the magnesium alloy under the Ni-P coating lead to a local destruction of the coating as shown in **Figure 6**. An EDS analysis revealed that these corrosion products are predominantly formed by the oxides and chlorides of magnesium.

The presence of microcavities in Ni-P coatings can be eliminated or removed by adding suitable surfactants to the nickel bath. Such suitable surfactants can be sodium dodecyl sulfate, sodium benzenesulfonate or CTAB.[11,26–27]

4 CONCLUSION

An electroless-deposited low-phosphorous Ni-P coating was successfully prepared on a wrought AZ61 magnesium alloy by applying a pre-treatment process. The deposited Ni-P coating was characterized in terms of elemental composition, mechanical and physicochemical properties.

In terms of the chemical composition, the deposited 10-μm-thick Ni-P coating treated for 1 h shows a high degree of homogeneity over the entire cross-section with a phosphorus content of 4.6±0.1 % and a nickel content of 95.4±0.1 %. The microhardness of the deposited Ni-P coating reached a value of 700±40 HV 0.025. In terms of physicochemical properties, the deposited Ni-P coating was characterized by a high degree of adhesion. The adhesion was determined from the corresponding critical normal forces L_{c1} (6.9 N) and L_{c2} (11.9 N). The mechanism of corrosion degradation of Ni-P applied on the AZ61 magnesium alloy substrate was determined based on a metallographic observation of a corrosion attack with the subsequent degradation of the magnesium substrate due to the microcavities present in the coating, allowing the contact of the corrosive environment with the substrate.

Acknowledgement

This work was supported by project Nr. LO1211, Materials Research Centre at FCH BUT – Sustainability and Development (National Programme for Sustainability I, Ministry of Education, Youth and Sports).

5 REFERENCES

[1] W. Riedel, ASM International, Electroless Nickel Plating, Reprint ed., Finishing Publications, London 1991, 320

[2] M. Novák, D. Vojtěch, P. Novák, T. Vítů, Tribological properties of heat-treated electroless Ni–P coatings on AZ91 alloy, Appl. Surf. Sci., 257 (**2011**) 23, 9982–9985, doi:10.1016/j.apsusc.2011.06.119

[3] E. Altuncu, H. Alanyali, The applicability of sol-gel oxide films and their characterization on a magnesium alloy, Mater. Tehnol., 48 (**2014**) 2, 289–292

[4] M. Madaj, M. Greger, V. Karas, Magnesium-alloy die forgings for automotive applications, Mater. Tehnol., 49 (**2015**) 2, 267–273, doi:10.17222/mit.2013.174

[5] B. Panja, S. K. Das, P. Sahoo, Tribological Behavior of Electroless Ni–P Coating in Brine Environment, J. Inst. Eng., 95 (**2014**) 2, 153–159, doi:10.1007/s40033-014-0041-9

[6] A. Grosjean, M. Rezrazi, P. Bercot, M. Tachez, Adaptation of a mathematical model to the incorporation of silicon carbide particles in an electroless nickel deposit, Met. Finish., 96 (**1998**) 4, 14–17, doi:10.1016/S0026-0576(97)86615-9

[7] A. I. Aydeniz, A. Göksenli, G. Dil, F. Muhaffel, C. Calli, B. Yüksel, Electroless Ni-B-W coatings for improving hardness, wear and corrosion resistance, Mater. Tehnol., 47 (**2013**) 6, 803–806

[8] R. Parkinson, Properties and applications of electroless nickel, Nickel Development Institute, 1997, 37

[9] M. Buchtík, P. Kosár, J. Wasserbauer, M. Zmrzlý, Electroless Deposition of Ni-P/SiO2 Composite Coating, Acta U. Agr. Silvi. Mendel. Brun., 64 (**2016**) 5, 1459–1464, doi:10.11118/actaun201664051459

[10] G. O. Mallory, J. B. Hajdu, Electroless Plating: Fundamentals and Applications, Reprint ed., NY, Knoyes Publications/William Andrew Publishing, Norwich 2009, 575

[11] R. Elansezhian, B. Ramamoorthy, P. K. Nair, Effect of surfactants on the mechanical properties of electroless (Ni–P) coating, Surf. Coat. Tech., 203 (**2008**) 5–7, 709–712, doi:10.1016/j.surfcoat.2008.08.021

[12] C. Li, Y. Wang, Z. Pan, Wear resistance enhancement of electroless nanocomposite coatings via incorporation of alumina nanoparticles prepared by milling, Mater. Design., 47 (**2013**), 443–448, doi:10.1016/j.matdes.2012.12.021

[13] Y. Xin, K. Huo, T. Hu, G. Tang, P. K. Chu, Mechanical properties of Al2O3/Al bi-layer coated AZ91 magnesium alloy, Thin Solid Films, 517 (**2009**) 17, 5357–5360, doi:10.1016/j.tsf.2009.03.101

[14] E. Georgiza, J. Novakovic, P. Vassiliou, Characterization and corrosion resistance of duplex electroless Ni-P composite coatings on magnesium alloy, Surf. Coat. Tech., 232 (**2013**), 432–439, doi:10.1016/j.surfcoat.2013.05.047

[15] S. Afroukhteh, C. Dehghanian, M. Emamy, Preparation of the Ni–P composite coating co-deposited by nano TiC particles and evaluation of its corrosion property, Appl. Surf. Sci., 258 (**2012**) 7, 2597–2601, doi:10.1016/j.apsusc.2011.10.101

[16] ASTM B107 / B107M-13 – Standard Specification for Magnesium-Alloy Extruded Bars, Rods, Profiles, Tubes, and Wire, ASTM International, West Conshohocken

[17] ISO 6507-1:2005(E) – Metallic materials, Vickers hardness test – Part 1: Test method, Prepared by Technical Committee ISO/TC 164, Geneva

[18] ASTM C1624 – 05(2010) – Standard Test Method for Adhesion Strength and Mechanical Failure Modes of Ceramic Coatings by Quantitative Single Point Scratch Testing, ASTM International, West Conshohocken

[19] A. Sadeghzadeh-Attar, G. Ayubikia, M. Ehteshamzadeh, Improvement in tribological behavior of novel sol-enhanced electroless Ni-P-SiO2 nanocomposite coatings, Surf. Coat. Tech., 307 (**2016**), 837–848, doi:10.1016/j.surfcoat.2016.10.026

[20] X. Wu, J. Mao, Z. Zhang, Y. Che, Improving the properties of 211Z Al alloy by enhanced electroless Ni–P–TiO2 nanocomposite coatings with TiO2 sol, Surf. Coat. Tech., 270 (**2015**), 170–174, doi:10.1016/j.surfcoat.2015.03.006

[21] M. Buchtík, P. Kosár, J. Wasserbauer, P. Doležal, Characterization of Ni-P coating prepared via electroless deposition on wrought AZ31 magnesium alloy, Corros. Mater. Pr., 61 (**2017**) 1, doi:10.1515/kom-2016-0026

[22] M. Novák, D. Vojtěch, T. Vítů, Influence of heat treatment on tribological properties of electroless Ni–P and Ni–P–Al2O3 coatings on Al–Si casting alloy, Appl. Surf. Sci., 256 (**2010**) 9, 2956–2960, doi:10.1016/j.apsusc.2009.11.057

[23] A. Němcová, P. Skeldon, G. E. Thompson, S. Morse, J. Čížek, B. Pacal, Influence of plasma electrolytic oxidation on fatigue performance of AZ61 magnesium alloy, Corros. Sci., 82 (**2014**), 58–66, doi:10.1016/j.corsci.2013.12.019

[24] T. Tański, Characteristics of Hard Coatings on AZ61 Magnesium Alloys, J. Mech. Eng., 59 (**2013**) 3, 165–174, doi:10.5545/sv-jme.2012.522

[25] K. Tohgo, G. J. Weng, A Progressive Damage Mechanics in Particle-Reinforced Metal-Matrix Composites Under High Triaxial Tension, J. Eng. Mater. Technol., 116 (**1994**) 3, 414–420, doi:10.1115/1.2904307

[26] R. Elansezhian, B. Ramamoorthy, P. K. Nair, The influence of SDS and CTAB surfactants on the surface morphology and surface topography of electroless Ni–P deposits, J. Mater. Process. Tech., 209 (**2009**) 1, 233–240, doi:10.1016/j.jmatprotec.2008.01.057

[27] B.-H. Chen, L. Hong, Y. Ma, T.-M. Ko, Effects of Surfactants in an Electroless Nickel-Plating Bath on the Properties of Ni-P Alloy Deposits, Ind. Eng. Chem. Res., 41 (**2002**) 11, 2668–2678, doi:10.1021/ie0105831

UDK 621.178.6:67.017:620.193.16
Original scientific article/Izvirni znanstveni članek

ISSN 1580-2949
MTAEC9, 51(6)933(2017)

CAVITATION EROSION PROPERTIES OF A NICKEL-FREE HIGH-NITROGEN Fe-Cr-Mn-N STAINLESS STEEL

RAZISKAVE ODPORNOSTI PROTI KAVITACIJSKI EROZIJI Z DUŠIKOM LEGIRANEGA Fe-Cr-Mn-N NERJAVNEGA JEKLA

Yanxin Qiao[1], Xiang Cai[1], Yipeng Chen[1], Jie Cui[2], Yanbing Tang[3], Huabing Li[4], Zhouhua Jiang[4]

[1]Jiangsu University of Science and Technology, School of Materials Science and Technology, No.2 Mengxi Road, Zhenjiang, China
[2]Jiangsu University of Science and Technology, School of Naval Architecture and Ocean Engineering, No.2 Mengxi Road, Zhenjiang, China
[3]Jiangsu University of Science and Technology, Marine Equipment and Technology Institute, No.2 Mengxi Road, Zhenjiang, China
[4]Northeastern University, School of Metallurgy, No.2 Wenhua Road, Shenyang, China
yxqiao@just.edu.cn, cuijie2006@hotmail.com

Prejem rokopisa – received: 2017-03-22; sprejem za objavo – accepted for publication: 2017-05-12

doi:10.17222/mit.2017.034

The cavitation erosion behaviour of a nickel-free high-nitrogen stainless steel was investigated using 20-kHz vibratory cavitation test equipment and analysed by scanning electron microscopy (SEM). The potentiodynamic polarization was measured to clarify the role of corrosion on the cavitation erosion of tested steel. The results indicated that the cavitation erosion damage in tested steel occurred initially at the grain boundary, twin boundary and interface between the precipitate and the matrix. Cavitation shifted the corrosion potential to the cathodic direction in 0.5-M NaCl solution and leading to a corrosion-current density almost two orders higher than that under static conditions. In the total cumulative mass loss under cavitation erosion–corrosion conditions, the mechanical effect played a key role in a 0.5-M NaCl solution and the synergistic effect induced by electrochemical and mechanical amounts to 14.78 % of the total mass loss.

Keywords: cavitation erosion, high-nitrogen stainless steel, corrosion, synergistic effect

Za raziskave odpornosti proti kavitacijski eroziji z dušikom brez niklja, legiranega nerjavnega jekla, so uporabili preizkuse z 20 kHz vibracijsko kavitacijo in vrstično elektronsko mikroskopijo (SEM). Zato, da bi pojasnili vlogo kavitacijske korozije pri preiskovanem jeklu, so izmerili potenciodinamsko polarizacijo. Rezultati so pokazali, da so se poškodbe zaradi kavitacijske erozije začele na mejah med zrni, mejah dvojčkov in na mejah med izločki in matrico. Preizkus v 0,5 M NaCl raztopini je pokazal, da je kavitacija premaknila korozijski potencial v katodni smeri, ki vodi h skoraj za dve stopnji višji korozijski gostoti električnega toka, kot je tisti v statičnih pogojih preizkušanja. V celoti je za kumulativno izgubo mase v 0,5 M NaCl raztopini pod kavitacijsko erozijsko-korozijskimi pogoji ključno odgovoren mehanski učinek. Celotna izguba mase je znašala 14,78 % zaradi istočasnega elektrokemijskega in mehansko induciranega delovanja.

Ključne besede: kavitacijska erozija, močno legirano dušikovo nerjavno jeklo, korozija, vpliv sinergijskega delovanja

1 INTRODUCTION

Cavitation erosion (CE) is a common problem in engineering parts in contact with a liquid. Plastic deformation and erosion damage on the metal surfaces are caused by the combination of shock loading and fatigue as a result of the stress generated by the repeated growth and collapse of cavities in the sheared liquid.[1] High-nitrogen stainless steel (HNSS) has attracted much attention during the past several decades due to its well-balanced combination of excellent mechanical properties such as high strength and ductility, high work-hardening ability, high stress-induced martensite transformation and corrosion resistance.[2,3] These attractive properties make HNSS good candidates for use in severe CE conditions.

HNSSs have been reported as suitable materials for applications in which erosive damage caused by CE, leading to a decrease in the large maintenance costs characteristics of hydraulic systems.[4,5] S. Z. Luo[6] found that the excellent CE resistance of CrMnN was related to the good mechanical properties of the austenitic phase and the consumption of CE energy by plastic deformation involving slip and twinning. W. Liu[7] found that the high CE resistance of CrMnN was mainly attributed to their high work-hardening ability and favourable cavitation crack propagation, i.e., parallel rather than perpendicular to the specimen surface. H. Berns[8] attributed the better CE performance of HNSS to the effect of nitrogen in lowering the stacking-fault energy (SFE), leading to an increase in plasticity and work hardening. According to W. T. Fu[9] the high CE resistance of HNSS is related to its good mechanical properties induced by changes in the dislocation configurations, CE-induced mechanical twinning or formation of stacking faults and CE-induced phase transformation. P. Niederhofer[10] found that the superior CE resistance of HNSS is caused by the strengthening effect of N and the low stacking-fault energy leading to intense cold work hardening. W. T. Fu[11] studied the CE behaviour of CrMnN and showed that CE could induce a new martensite structure and delayed the progress of damage due to CE. D. J. Mill and

R. D. Knutsen[12] observed that the CE rate of CrMnN decreased with increasing amounts of cold working. They stressed the importance of the increase in yield strength, leading to a decrease of the plastic deformation inside individual grains during the early CE stages, to a delay of the onset of grain-boundaries extrusion and to a delay of the fatigue damage nucleation and growth. J. F. Santos[13] found that the superior CE resistance of nitride 304L stainless steel is attributed to the high elastic energy. D. H. Mesa[14] found that the high CE resistant of HNSS is due to its high hardness and great resistance to plastic deformation. The energy transferred by the shock waves caused by imploding bubbles, during the earliest stages of CE, is greatly consumed elastically without leaving traces of plastic deformation on the surface.

In practice, many flow-handling components including pumps and valves operate in corrosion environments, where they are apparently subjected to the combined action of CE and corrosion. Although the stainless steel has a dense passive film, the corrosions still happen to some components contacting liquids in fluid machinery and become more obvious in the presence of CE, which causes a more serious damage of components because of the synergism of CE and corrosion.[15,16] C. T. Kwok[17] studied the CE behaviour of stainless steel in 3.5 % NaCl and found that corrosion and corrosion/erosion synergism play a negligible role.

Although a lot of publications on the CE performance of HNSS have been published, a systematic investigation of the effect of corrosion on the CE characteristics of HNSS was rarely reported in the literature. The aim of this study was to investigate the relative importance of CE, corrosion and the synergism between them in the overall CE-corrosion damage of HNSS.

2 EXPERIMENTAL PART

2.1 Materials and specimen preparation

The HNSS used in this study was made by the dissolution of the raw materials in a high-vacuum furnace, followed by forging, hot rolling, cold rolling and then air cooling to room temperature. The HNSS was in the form of a round bar with a diameter of 20 mm. The chemical composition of HNSS is listed in **Table 1**.

Table 1: Chemical composition of HNSS used in this study (*w*/%)

C	Si	Mn	P	S	Cr	Mo	N	Fe
0.048	0.24	15.96	0.004	0.017	18.44	2.23	0.66	Bal.

The shape and dimension of the specimen used has been given in a previous study.[15] Test surfaces were gradually ground down to 1000 grit and polished using 1.5-μm alumina powder before the CE test to observe the response of different phases to CE later. Specimens were degreased by immersion in acetone in an ultrasonic bath and were rinsed with distilled water, then dried and stored in desiccators. The specimens used for the microstructure observation was electrolytically etched in 10 % ethanedioic acid reagent at 12 V for 90 s.

2.2 Test method

CE was produced by a magnetostrictive-induced cavitation facility (Sonicator XL 2020) resonating at 20 kHz with a peak-to-peak amplitude of 60 μm. This test followed ASTM Standard G32-92. The cavitation tests were performed in distilled water and 0.5-M NaCl. Reagent grade NaCl and distilled water were used. The temperature of the tested solution was maintained in the range 20±1 °C.

For the CE test, the specimen was screwed into the horn and immersed into the test medium to a depth of 15 mm. After each test period, the specimen was degreased, rinsed, dried, and weighed using an analytical balance (Sartorius BT25S) with an accuracy of 0.1 mg. To ensure the reproducibility of the results, every test was repeated three times. The potentiodynamic polarization tests were performed with a CS350 workstation (Corrtest Instrument, China). Using a platinum plate as the counter-electrode and a saturated calomel electrode (SCE) as the reference electrode, a classic three-electrode system was used in the electrochemical measurements. Potentiodynamic polarization was started after CE for 15 min and swept from –400 mV relative to corrosion potential at a fixed rate of 1 mV/s until a current density of 10 mA/cm^{-2} was reached.

In order to investigate the mechanism of material removal during CE, specimens were examined after fixed cavitation intervals. The microstructures of HNSS and the eroded surfaces of the samples examined using XL20 scanning electron microscopy (SEM). The crystal structures of the HNSSs were studied by XRD (Philips PW3710), using Cu-K_α radiation generated at 40 kV and 35 mA.

3 RESULTS AND DISCUSSION

3.1 Material characterization

Figure 1 shows the SEM morphology of the as-received HNSS. It is clear that HNSS consisted of a typical γ (austenitic) phase matrix with twin boundaries and precipitated Cr_2N.[18,19] The EDS of HNSS and precipitated particles were shown in **Table 2**. The XRD analysis in **Figure 2** shows that HNSS was in a single γ phase, while the dispersed precipitated Cr_2N cannot be detected.

Table 2: EDS of as-received HNSS and Cr_2N, in mass fractions (*w*/%)

Area	Fe	Cr	Mn	Mo	Si	N
1	5.01	78.83	4.03	0.72	0.58	10.83
2	61.32	18.33	17.37	2.98	-	-

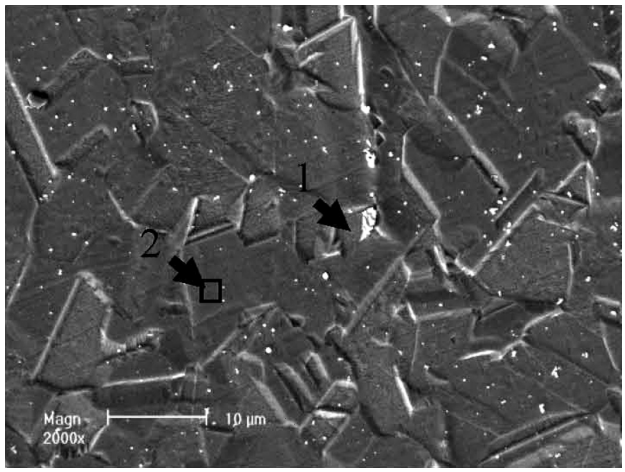

Figure 1: SEM micrograph of as-received HNSS

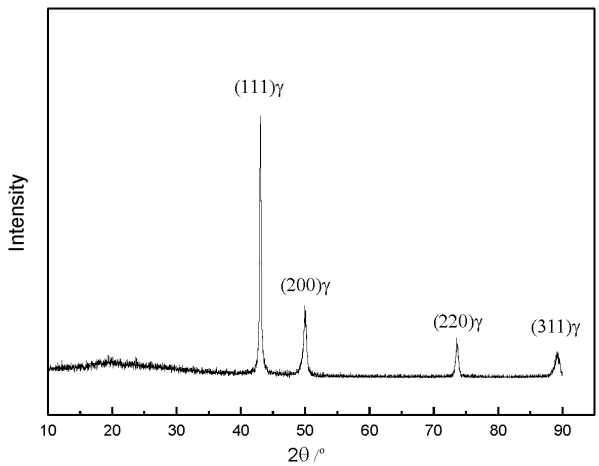

Figure 2: XRD of as-received HNSS

3.2 Mass loss

Figure 3 presents the mass-loss curve versus CE time, which indicates that the CE resistance can be influenced by the corrosivity of the tested solution. After CE for 8 h, the mass loss of HNSS in 0.5-M NaCl was 1.17 times that in distilled water. In distilled water, the mass loss rate curves of HNSS could be divided into two stages. The mass loss rate was characterized by a very low value and kept almost constant within 4 h, and it could be regarded as an incubation period. After a CE time of 4 h the mass-loss rate increased quickly and linearly with the CE time. Generally, it is believed that the duration of incubation time depends on how long microcracks need to initiate by collapse. Material with longer incubation periods is considered to have a superior CE resistance. In contrast, the mass loss rate was characterized by a high value in the 0.5-M NaCl solution. After CE for 2 h, the mass-loss rate reached a constant stage. This indicated that the CE resistance of HNSS in distilled water was better than that in a NaCl solution. The initiation and propagation of microcracks can be facilitated by corrosion media. This could be further confirmed by SEM observation in the later stages.

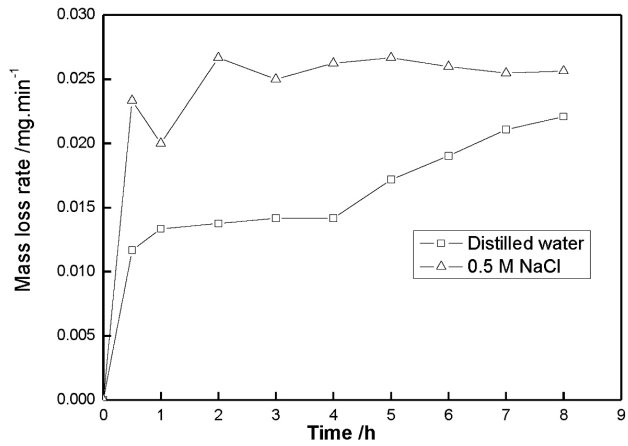

Figure 3: Mass-loss rate for HNSS in tested solutions under CE condition

3.3 Electrochemical behaviour

In order to investigate the effect of corrosion on CE behaviour of HNSS, polarization curves were tested under static and CE conditions in 0.5-M NaCl and shown in **Figure 4**. It can be seen that the corrosion behaviour of the HNSS under both static conditions and CE conditions exhibited similar polarization behaviour. The anodic current density gradually increased by increasing the electrode potential under both static and CE conditions. The corrosion potential under static and CE condition was –212.05 mV_{SCE} and –506.96 mV_{SCE}, respectively. The corrosion current density (i_{corr}) of HNSS under static and CE conditions is 1.39 μA/cm^2 and 133.97 μA/cm^2, respectively. The results obtained indicating that cavitation shifted the corrosion potential to a negative direction and increased the anodic current densities by two orders of magnitude. The corrosion of HNSS in the static condition was controlled by the

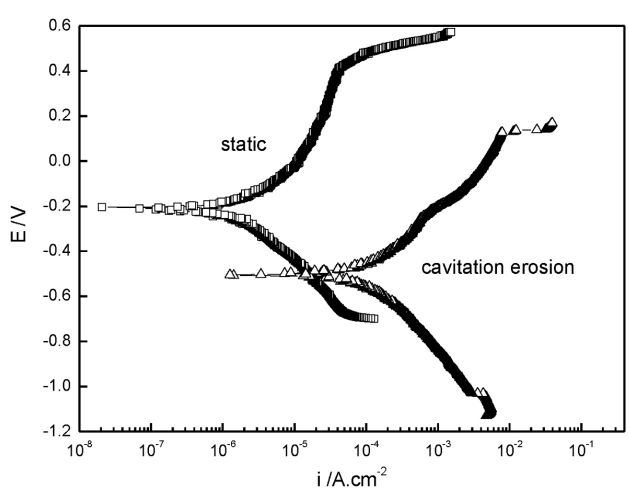

Figure 4: Potentiodynamic polarization curves for HNSS in 0.5 M NaCl and 0.5 MHCl solution under static and CE condition

dissolution of the passive film and repassivation of the metal. The passive film on the surface of HNSS can be damaged locally by a random collapse of bubbles and results in the dissolution of material and will cause the total anodic current density to increase a lot. The influence of CE on the corrosion potential is attributed to the reason that a relatively stronger influence on anodic reaction than that of cathodic reaction.[20,21] It is well known that chloride ions will induce pitting corrosion in stainless steels in static conditions. Under CE conditions, stirring of the electrolyte and film destruction occur simultaneously,[22] both upsetting the local environment for pit growth. Thus the effect of cavitation remains mechanical, even in the presence of chloride ions.[17]

3.4 Evolution of CE damage of HNSS

The microstructure change of HNSS in each period was observed continuously. **Figure 5** shows the surface micrographs of HNSS after CE for different time intervals in distilled water. **Figure 5a** shows the appearance of the surface after a CE time of 1 h. The eroded surface was characterized by the formation of surface undulations, labelled A, and cavities, labelled B, caused by material removal appeared along grain boundaries can be clearly seen. This provided evidence that CE damage was firstly initiated at grain boundaries and is consistent with the results reported by S. Z. Luo,[6] who reported that CE damage arising from material extrusions at grain boundaries in polycrystalline materials. Slip lines, labelled C, and deformed twins, labelled D, can also be seen clearly inside austenite grains. The surface exhibited plastic deformation in the form of surface undulations as well as the appearance of grain boundaries, slip bands, and twin boundaries in incubation periods.[10,12] **Figure 5b** shows the appearance of the surface after a CE time of 3 h. It can be seen that material removal was preferentially at the grain boundaries and cavities, then growth towards the inner region of the grains. The mass removal inside the grains starts at slip lines and deformed twins. This is consistent with the results reported by Mills and Knutsen[12]. It could also be seen that some grains are much more deformed than others, indicating significant plasticity anisotropy at the mesoscale, which can be addressed to different values of the resolved shear stress inside each grain.[15] The damaged surface after CE for 5h is shown in **Figure 5c**, in which craters about 2-5 μm in diameter and cracks can be observed. The craters were created due to the removal of material by a combined effect of microfatigue and microcrack formation. After CE for 8 h, the propagation and connection of the microcracks by fatigue at continuous impact of bubble collapse, give to the larger craters and wide cracks, as shown in **Figure 5d**. This is consistent with the mass-loss rate presented in **Figure 3** that larger bulk material was lost in this period.

The morphologies of the eroded surfaces in 0.5-M NaCl were slightly different to that in distilled water for the same time intervals. **Figure 6** shows surface micrographs of HNSS after CE for different time intervals in 0.5-M NaCl. **Figure 6a** indicates that plastic deformation and surface undulations are more serious than that in distilled water, more slip lines formed inside grains and discontinuous at grain boundaries. The active dissolution of HNSS can be clearly seen on the surface, especially at site of slip line intersections. After CE for 3 h, the cavitated surface was very rough and only a little original surface be preserved, deep gaps and cracks due to the material removal at the grain boundaries can be clearly seen, as shown in **Figure 6b**. These results suggested that mass loss of HNSS in 0.5-M NaCl solution was significantly enhanced and consistent with the results that mass loss is almost constant in 0.5-M NaCl solution after the initial increase. **Figure 6c** and **6d** shows the surface of HNSS after CE for 5 h and 8 h. The eroded surface of the HNSS was found to be similar to that in distilled water in that they are all characterized by the formation of craters and fatigue cracks on the sample

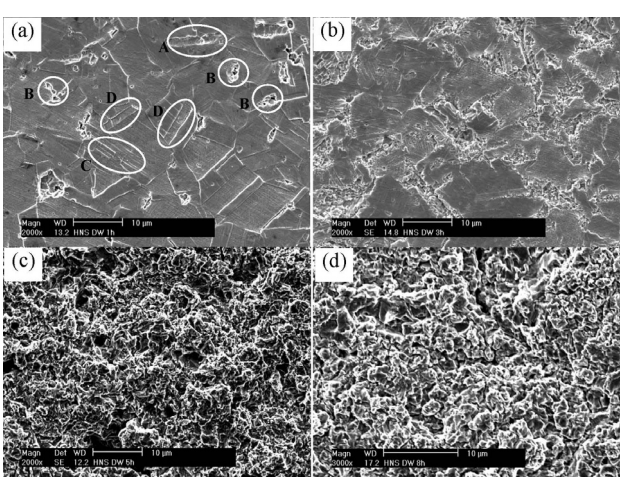

Figure 5: SEM images of HNSS after CE for : a) 1 h, b) 3 h , c) 5 h and d) 8 h in distilled water: A- surface undulations, B- cavities, C- slip lines, D-deformed twins

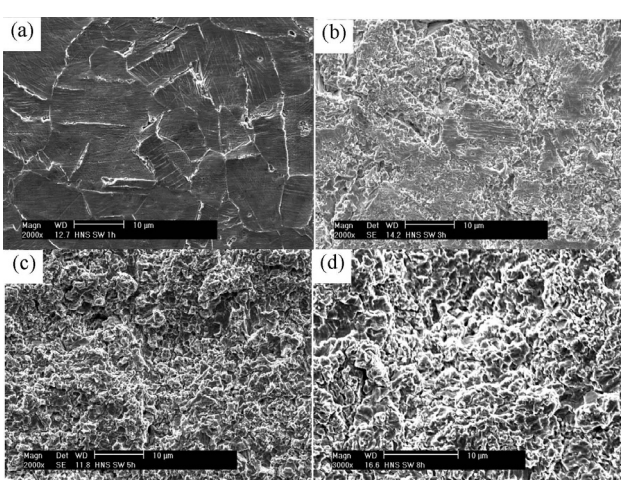

Figure 6: SEM images of HNSS after CE for: a)1 h, b)3 h, c)5 h and d) 8 h in 0.5 M NaCl solution

surface. The size of cater is smaller than that in the distilled water. This indicates corrosion played an important role in that it can promote the crack initiation and propagation of the cracks.

The overall CE rate is constituted by an erosion rate, a corrosion rate and a synergistic effect of erosion and corrosion.[15–17,23–25] The synergistic effect of electrochemical and mechanical factor produced far more damage than if each acted separately in a large number of systems. The total mass loss is composed of erosion mass loss, corrosion mass loss and synergistic effect of erosion and corrosion. In corrosive media the total material loss can be expressed by:[20]

$$W_T + W_E + W_C + W_S = W_C + W_E + W_{CIE} + W_{EIC} \quad (1)$$

where W_T is the total CE material loss, W_E is the component of pure erosion part, W_C is the fraction of pure corrosion under static condition, W_S is volume loss rate of synergism, W_{EIC} is the fraction of erosion induced corrosion, W_{CIE} is the fraction of erosion induced corrosion.

Table 3: Mass loss induced by pure corrosion (W_C), pure erosion (W_E), erosion-induced corrosion (W_{EIC}) and corrosion induced erosion (W_{CIE}) and ratios of each factor for HNSS in 0.5 M NaCl

Mass loss (mg)					Damage fraction (%			
W_T	W_C	W_E	W_{EIC}	W_{CIE}	f_C	f_E	f_{EIC}	f_{CIE}
12.45	0.01	10.60	1.10	0.74	0.08	85.14	8.83	5.95

Note: f_C ratio of pure corrosion, f_E ratio of pure erosion, f_{EIC} ratio of erosion-induced corrosion, f_{CIE} ratio of corrosion-induced erosion, W_T mass loss induced by CE

In present work, W_T was the cumulative mass loss under CE conditions for 8 h in 0.5-M NaCl. W_E were the cumulative mass loss under CE condition for 8 h in distilled water. W_C was calculated from the i_{corr} in the polarization curve under static conditions according to Faraday's law. W_{EIC} was calculated from the i_{corr} in the polarization curve under CE and W_{CIE} could be obtained from Equation (1). **Table 3** lists the parameters described above. It indicated that the contribution of the synergistic component (W_{EIC} and W_{CIE}) to W_T was 14.78 %, which meant that the mechanical effect was the main factor for the CE–corrosion behaviour of HNSS, but at the same time the contribution of corrosion cannot be neglected.

4 CONCLUSION

The cumulative mass loss of the HNSS in 0.5-M NaCl was about 1.17 times that in distilled water. CE shifted the corrosion potential of HNSS to cathodic direction in 0.5-M NaCl. The anodic reactions under cavitation conditions were two orders of magnitude faster than that in quiescent conditions. Cavitation erosion damage began at the grain, twin boundaries and interfaces between Cr_2N. In the total cumulative mass loss under CE corrosion conditions, the mechanical effect played a key role for HNSS and the synergistic component was 14.78 % in 0.5-M NaCl. The propagation and connection of cracks can be facilitated by the corrosivity of the tested media.

Acknowledgements

We wish to express our gratitude to the financial support of the National Natural Science Foundation of China (Nos.51401092, 51409129, 51131008, 51434004, U1435205 and 51304041) and Natural Science Foundation of Jiangsu Province (BK20140504) for the finance support of this research.

5 REFERENCES

[1] A. Karimi, J. L. Martin, Cavitation erosion of materials, Int. Mater. Rev., 31 (**2013**), 1–26, doi:10.1179/imtr.1986.31.1.1

[2] M. Moallemi, A. Zarei-Hanzaki, H. S. Baghbadorani. Evolution of microstructure and mechanical properties in a cold deformed nitrogen bearing TRIP-assisted duplex stainless steel after reversion annealing. Mater. Sci. Eng. A, 683 (**2016**), 83–89, doi:10.1016/j.msea.2016.10.105

[3] F. Y. Dong, P. Zhang, J. C. Pang, Y. B. Ren, K. Yang, Z. F. Zhang, Strength, damage and fracture behaviors of high-nitrogen austenitic stainless steel processed by high-pressure torsion, Scripta Mater., 96 (**2015**), 5–8, doi:10.1016/j.scriptamat.2014.09.016

[4] Y. G. Zheng, S. Z. Luo, W. Ke, Cavitation erosion–corrosion behaviour of CrMnB stainless overlay and 0Cr13Ni5Mo stainless steel in 0.5M NaCl and 0.5M HCl solutions, Tribol. Int., 41 (**2008**), 1181–1189, doi:10.1016/j.triboint.2008.02.011

[5] H. Hänninen, J. Romu, R. Ilola, J. Tervo, A. Laitinen, Effects of processing and manufacturing of high nitrogen-containing stainless steels on their mechanical, corrosion and wear properties, J. Mater. Process. Technol., 117 (**2001**), 424–430, doi:10.1016/S0924-0136(01)00804-4

[6] S. Z. Luo, Y. G. Zheng, W. Liu, H. M Jing, Z. M Yao, W. Ke, Cavitation erosion behavior of CrMnN duplex stainless steel in distilled water and 3% NaCl solution, J. Mater. Sci. Technol., 19 (**2003**), 346–350, doi:10.3321/j.issn:1005-0302.2003.04.016

[7] W. Liu, Y. G. Zheng, C. S. Liu, Z. M. Yao, W. Ke, Cavitation erosion behavior of Cr-Mn-N stainless steels in comparison with 0Cr13Ni5Mo stainless steel, Wear, 254 (**2003**), 713–722, doi:10.1016/S0043-1648(03)00128-5

[8] H. Berns, S. Siebert, High nitrogen austenitic cases in stainless steels. ISIJ Inter., 36 (**1996**), 927–931, doi:10.2355/isijinternational.36.927

[9] W. T. Fu, Y. Z. Zheng, X. K. He, Resistance of a high nitrogen austenitic steel to cavitation erosion, Wear, 249 (**2001**), 788–791, doi:10.1016/S0043-1648(01)00811-0

[10] P. Niederhofer, L. Richrath, S. Huth, W. Theisen, Influence of conventional and powder-metallurgical manufacturing on the cavitation erosion and corrosion of high interstitial CrMnN austenitic stainless steels, Wear, 360–361 (**2016**), 67–76, doi:10.1016/j.wear.2016.04.017

[11] W. T. Fu, Y. B. Yang, T. F. Jing, Y. Z. Zheng, M. Yao, The resistance to cavitation erosion of CrMnN stainless steels, J. Mater. Eng. Perform., 7 (**1998**), 801–804, doi:10.1361/105994998770347396

[12] D. J. Mills, R.D. Knutsen, An investigation of the tribological behaviour of a high-nitrogen Cr-Mn austenitic stainless steel, Wear, 215 (**1998**), 83–90, doi:10.1016/S0043-1648(97)00273-1

[13] J. F. Santos, C. M. Garzón, A. P. Tschiptschin, Improvement of the cavitation erosion resistance of an AISI 304L austenitic stainless steel by high temperature gas nitriding, Mater. Sci. Eng. A, 382 (**2004**), 378–386, doi:10.1016/j.msea.2004.05.003

[14] D. H. Mesa, C. M. Garzón, A. P. Tschiptschin, Influence of cold-work on the cavitation erosion resistance and on the damage mechanisms in high-nitrogen austenitic stainless steels, Wear, 271 (**2011**), 1372–1377, doi:10.1016/j.wear.2011.01. 063

[15] Y. X. Qiao, S. Wang, B. Liu, Y. G. Zheng, H. B. Li, Z. H. Jiang, Synergistic effect of corrosion and cavitation erosion of high nitrogen stainless steel, Acta Metall. Sin., 52 (**2016**), 233–240, doi:10.11900/0412.1961.2015.00282

[16] A. Al-Hashem, P. G. Cacere, A. Abdullah, H. M. Shalaby, Cavitation corrosion of duplex stainless steel in seawater, Corrosion, 53 (**1997**), 103–113, doi:10.5006/1.3280438

[17] C. T. Kwok, F. T. Cheng, H. C. Man, Synergistic effect of cavitation erosion and corrosion of various engineering alloys in 3.5% NaCl solution, Mater. Sci. Eng. A, 290 (**2000**), 145–154, doi:10.1016/S0921-5093(00)00899-6

[18] T. H. Lee, C. S. Oh, C. G. Lee, S. J. Kim, S. Takaki, Precipitation of σ-phase in high-nitrogen austenitic 18Cr-18Mn-2Mo-0.9N stainless steel during isothermal aging, Scripta Mater., 50 (**2004**), 1325–1328, doi:10.1016/j.scriptamat.2004.02.013

[19] H. Y. Ha, H. S. Kwon. Effects of Cr_2N on the pitting corrosion of high nitrogen stainless steels, Electrochimica Acta, 52 (**2007**), 2175–2180, doi:10.1016/j.electacta.2006.08.034

[20] S. Z. Luo, M. C. Li, W. Ke, Z. M. Yao, Y. G. Zheng, Effect of cavitation on corrosion behavior of 20SiMn low-alloy steel in 3% sodium chloride solution, Corrosion, 59 (**2003**), 597–605, doi:10.5006/1.3277590

[21] Y. G. Zheng, S. Z. Luo, W. Ke, Effect of passivity on electrochemical corrosion behavior of alloys during cavitation in aqueous solutions, Wear, 262 (**2007**), 1308–1314, doi:10.1016/j.wear.2007.01.006

[22] B. Vyas. I. L.H. Hansson, The cavitation erosion-corrosion of stainless steel, Corro. Sci., 30 (**1990**), 761–770, doi:10.1016/0010-938X(90)90001-L

[23] J. Basumatary, M. Nie, R. J. K. Wood, The Synergistic Effects of cavitation erosion–corrosion in ship propeller materials, J. Bio. Tribo. Corro., 1 (**2015**), 1–12, doi:10.1007/s40735-015-0012-1

[24] R. J. K. Wood, S. A. Fry, The synergistic effect of cavitation erosion and corrosion for copper and cupro-nickel in seawater, J. Fluids Eng., 111 (**1989**), 271–277, doi:10.1115/1.3243641

[25] S. Hong, Y. P. Wu, J. Zhang, Y. G. Zheng, J. Lin, Synergistic effect of ultrasonic cavitation erosion and corrosion of WC-CoCr and FeCrSiBMn coatings prepared by HVOF spraying, Ultrason. Sonochem., 31 (**2016**), 563–569. doi:10.1016/j.ultsonch.2016.02.011

UDK 620.1:620.193.95:669.1.017:621.926
Original scientific article/Izvirni znanstveni članek

ISSN 1580-2949
MTAEC9, 51(6)939(2017)

INVESTIGATION OF THE WEAR BEHAVIOUR OF AN AISI 1040 FORGED STEEL SHAFT WITH PLASMA-SPRAY CERAMIC-OXIDE COATINGS FOR SUGAR-CANE MILLS

RAZISKAVA OBRABE AISI 1040 KOVANE JEKLENE GREDI S KERAMIČNIMI OKSIDNIMI PREVLEKAMI ZA MLINE ZA MLETJE SLADKORNEGA TRSA

Duraisamy Revathi Ponnusamy Rajarathnam[1], Murugesan Jayaraman[2]

[1]Paavai Engineering College, Department of Mechanical Engineering, Namakkal District, India
[2]Velalar College of Engineering and Technology, Department of Mechanical Engineering, Erode District, India
drprajamalathi@yahoo.co.in

Prejem rokopisa – received: 2017-03-27; sprejem za objavo – accepted for publication: 2017-05-19

doi:10.17222/mit.2017.035

In this investigation, ceramic oxide powders, alumina, titania, chromia, alumina-titania, alumina-chromia and titania-chromia, were coated for a thickness of 200 μm on an AISI 1040 forged steel substrate by means of an atmospheric plasma spraying method. Ni-Cr was used as an intermediate bond coat of thickness 20 μm over the substrate to improve the coating adhesion. Pin-on-disc apparatus was employed for a dry wear test as per the American Society for Testing and Materials G99 standards for a constant load of 10 N, at different sliding distances of 1000 m, 2000 m and 3000 m, respectively. The investigation shows that the microstructure, coating thickness, porosity, surface roughness and hardness influence the wear rate. Before and after the wear tests, surface roughness measurements were carried out by using a talysurf instrument on the specimens. It is shown that the highest value (20.89 μm) was obtained for the coating of alumina-titania. The practical results show that the pure chromia coated specimen has a very good wear-resistance property compared to the ceramic oxides. This suggests that surface coating with pure chromia on the top mill roll shaft of sugar industries enhanced the wear resistance.

Keywords: alumina, titania, chromia, atmospheric plasma spray, pin-on-disc, wear, Talysurf profilometer

V raziskavi so bili oksidni praški: glinica, titan, krom, aluminijev oksid, aluminij-krom, prevlečeni z 200 μm na AISI 1040 podlago kovanega jekla z metodo napršev anja s plazmo. Ni-Cr smo uporabili kot vmesni vezni premaz z debelino 20 μm nad podlago za izboljšanje oprijemljivosti prevleke. Pin-on-disk aparat je bila uporabljen za preskus suhe obrabe, v skladu s standardi G99 Ameriškega združenja za testiranje in materiale, s konstantno obremenitvijo 10 N, na različnih drsnih razdaljah 1000 m, 2000 m in 3000 m. Preiskava je pokazala, da so mikrostruktura, debelina prevleke, poroznost, površinska hrapavost in trdota vplivali na stopnjo obrabe. Pred in po testih obrabe, so bile meritve vzorcev površinske hrapavosti izvedene z uporabo Talysurf instrumenta. Izkazalo se je, da je največja vrednost (20,89 μm), pridobljena s prevleko iz aluminijevega oksida-titanovega dioksida. Praktični rezultati kažejo, da ima s čistim kromom prevlečen vzorec zelo dobro odpornost na obrabo kot tisti s keramičnimi oksidi. Kaže, da površinska prevleka s čistim kromom na zgornji gredi mlina v sladkorni industriji poveča odpornost proti obrabi.

Ključne besede: aluminij, titan, krom, atmoferski plazma sprej, spoj na disk, obraba, Talysurf profilometer

1 INTRODUCTION

In many sugar industries, the top mill roller shaft, used to crush sugarcane, is made up of AISI 1040 forged carbon steel as this medium carbon, tensile steel shows good strength, toughness and wear resistance. The roller shaft has to operate under critical working conditions such as heavy load, high speed, temperature and chemical environment, while it crushes the raw sugar cane to extract the sugar cane juice. Hence, surface hardening of the shaft is a must to improve the wear resistance as they suffer from various types of degradation. Generally, the shaft diameter will decrease due to continuous rotation with a speed of 4 min^{-1} and accumulation of various impurities such as bagasse, ferrous and non-ferrous metals and also due to improper lubrications in between the journal bearing and the shaft. Hence, the shaft surface at the pinion end should be coated with ceramic materials with a good wear-resistance property.

The coating layer is very important because it enhances the wear resistance of the metal substrate of AISI 1040 forged steel to increase its life and efficiency. Some of the most commonly used ceramic materials in industrial applications are alumina (Al_2O_3), titania (TiO_2), Chromia (Cr_2O_3). S.-H. Yao[1] studied nanostructured Al_2O_3 with 13 % of mass fractions of TiO_2 coatings and found that they showed better performance in hardness and wear. Y. Sert et al.[2] studied the wear resistance of the plasma sprayed alumina – titania, titania, chromia and chromia – titania and found the effect of TiO_2 content on Al_2O_3–TiO_2 and Cr_2O_3–TiO_2 coatings on Al-based substrate, and concluded that hardness, coating density and wear resistance changed with the TiO_2 content.

B. A. Khan et al.[3] studied the microstructural, surface roughness and tribological properties of a coated specimen with alumina, titania and alumina-titania coating materials and the results showed that pure alumina has better wear properties than other coating materials, and it was observed that the thermal barrier coating decreases the wear rate compared to the parent metal. M. H. Korkut et al.[4] studied the wear behaviour of the ceramic surfaces over different test durations on AISI 1040 mild steel and found that the pure chromium III oxide (Cr_2O_3) has a higher wear resistance than pure Al_2O_3 and its compositions with TiO_2, they concluded that wear resistance decreased with an increase in the percentage of TiO_2 powder in Al_2O_3 mixture.

S. Islak et al.[5] investigated the effect of TiO_2 rate in an Al_2O_3–TiO_2 composite coating on SAE 1040 steel and observed that the phase transformations take place from stable α-Al_2O_3 and anatase TiO_2 to metastable γ-Al_2O_3, rutile TiO_2 and Al_2TiO_5 phase and as a result the microhardness value was found to be 3 to 4.5 times higher than that of SAE 1040 steel substrate materials due to a decrease in pore content when the TiO_2 powder rate increased in the composition. S. Salman et al.[6] investigated the thermal shock resistance of various ceramic oxides coated on a cast iron substrate and found that zirconia coated samples deformed at 1040 °C after 37 s when compared to Cr_2O_3 which deformed at 960 °C after 33 s. It was concluded that the Al_2O_3 coated specimen has less thermal shock resistance since it deformed at 920 °C in 31 s.

M. S. Kumar et al.[7] analyzed the tribological properties of thermally sprayed WC – 12 % of mass fractions of Co and Al_2O_3 – 13 % of mass fractions of TiO_2 on AISI 1040 steel used in the automobiles and found that the wear failure mechanism gets influenced more at higher temperatures around 600 °C. It was also observed that a carbide coating exhibited denser microstructured and higher hardness than ceramic oxide coatings. G. Bolleli et al.[8] investigated the wear behaviour of plasma-sprayed ceramic coatings (Al_2O_3, Al_2O_3 – 13 % of mass fractions of TiO_2 and Cr_2O_3) and found that the Cr_2O_3 coating was the hardest and most anisotropic among the other plasma-sprayed ceramics due to the low interlamellar cohesion, whereas the Al_2O_3 – 13 % of mass fractions of TiO_2 was less hard and tough due to the formation of a glassy phase and turns out to be quite brittle.

A. Prasad et al.[9] investigated the hardness of a Ni/La_2O_3 composite powder that was cladded over AISI 1040 steel through microwave irradiation to improve the wear resistance and observed the averaged Vickers microhardness was about 319HV. It was further stated that the hardness value depends upon the particle size, microwave power and microwave exposure time. M. S. Gök[10] studied the microstructure and abrasive wear performance of an AISI 1040 steel surface coated with different ceramic materials and observed that a higher rate of Cr_2O_3 in the composition produced a better and higher microhardness value than other ceramic coating materials. They also showed that increasing the proportion of TiO_2 in the composition affects the microhardness value of the specimen.

P. Gadhari et al.[11] studied the wear behaviour of a N-P-Al_2O_3 composite coating on AISI 1040 steel and showed that a change in the parameters like higher annealing temperature 500 °C and reducing agent concentration (25 g/L) improved the wear resistance of the coating. The amount of alumina content affects the wear resistance property of the composite coating. M. Yunus et al.[12] investigated the wear behaviour of ceramic coatings on a mild-steel substrate which has vast applications in aerospace, gas turbine engines and power generators. The result showed that the partially stabilized zirconia (PSZ) has more thermal barrier and thermal cycling resistance than alumina-titania and alumina. The coating temperature (1000 °C), types of coating and thickness of coating affect or influence the thermal barrier against the ceramic coating materials.

2 EXPERIMENTAL PART

2.1 Substrate preparation

AISI 1040 forged steel was used as a substrate material provided by M/s.Coimbatore Metal Mart. The substrate AISI 1040 forged steel was made into circular pins of 8 mm diameter and 30 mm length by performing turning and facing operations in the lathe machine from its original dimension of 30 mm diameter and 40 mm length. Three types of coating materials were used: ceramic oxide powders (99 % of mass fractions) Al_2O_3 as fused, primarily α-phase with particle -325 mesh size, (99 % of mass fractions) TiO_2 traces metal basis with particle – 325 mesh size, (98 % of mass fractions) Cr_2O_3 with particle size 5 μm provided by Sigma Aldrich Chemicals Pvt Ltd, Bangalore, India. The mixtures formed with six different compositions are shown in **Table 1**.

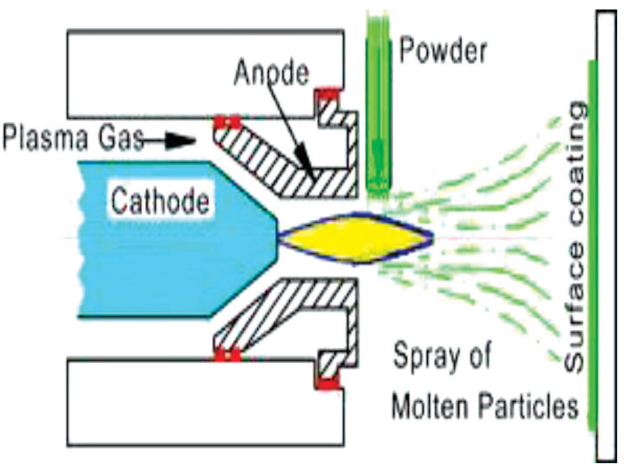

Figure 1: Schematic picture of plasma spray coating

Table 1: Chemical compositions (*w*/%) of ceramics for surface coating

Specimen No.	Al_2O_3	TiO_2	Cr_2O_3
S1	99	-	-
S2	-	99	-
S3	-	-	99
S4	45	55	-
S5	55	-	45
S6	-	45	55

Before spraying, the substrate was cleaned with acetone. In the present work NiCr bond coat of 20 μm thickness was deposited on the substrate surface materials so as to compose an intermediate surface for the purpose of best adhesion property and the coating thickness with 200 μm was deposited by plasma spraying process as shown in **Figure 1**.

2.2 Thermal spraying equipment

Sulzer Metco 3 MB spraying guns were used for the deposition of ceramic oxide layers provided by M/s. SprayMet Technologies Pvt Ltd, Bangalore, India. The parameters used for the deposition of ceramic oxide coatings by thermal spraying process are shown in the **Table 2**.

Table 2: Guidelines of plasma spray process

Gun	METCO 3MB
Nozzle	GH
Arc flow rate	80–90 L/min
Arc pressure	100–120 psi
Auxiliary gas flow rate	20–35 L/min
Auxiliary gas pressure	100 psi
Spray rate	2.0–6.5 kg/h
Arc voltage	60–70V
Arc current	490–590A
Spray distance	3–5 inches
Powder feed	40–50 grams/min

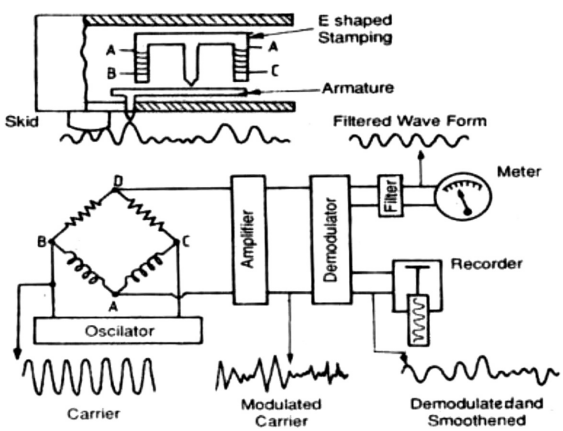

Figure 2: Schematic diagram of Talysurf instrument

2.3 Characterization of coatings

The microstructures of the specimens coated with Al_2O_3, TiO_2, Cr_2O_3 and other compositions were characterized under a Scanning Electron Microscope (SEM) to study the microstructure of the substrate.

2.4 Microhardness of the ceramic oxide coatings

Hardness measurements were carried out to find the microhardness value of the AISI 1040 steel substrate and coated samples. The hardness test was carried out on the top surface of the coatings with a load of 250 g and dwell time period of 10 s and the average of three readings are shown in the **Table 3**.

Table 3: Hardness value of the specimen

Specimens	Vickers hardness number (HV)
AISI 1040	230
Al_2O_3	776
TiO_2	340
Cr_2O_3	960
45 % Al_2O_3 + 55 % TiO_2	448
55 % Al_2O_3 + 45 % Cr_2O_3	560
45 % TiO_2 + 55 % Cr_2O_3	652

2.5 Surface roughness measurements

Talysurf instrument schematic sketch shown in **Figure 2** was used to measure the surface roughness of the specimens before and after wear tests. The cut-off length was chosen as 0.8 mm for the instrument and a mean value of five readings was calculated.

2.6 Wear test and evaluation

Ceramic oxide coated specimens were subjected to dry wear tests by using a pin-on-disc wear testing device as per ASTM G99-04 standards. The 8 mm diameter and 30 mm length cylindrical pin samples coated with alumina, titania, chromia and combination of 45 % Al_2O_3 + 55 % TiO_2, 55 % Al_2O_3 + 45 % Cr_2O_3, and 45 % TiO_2 +

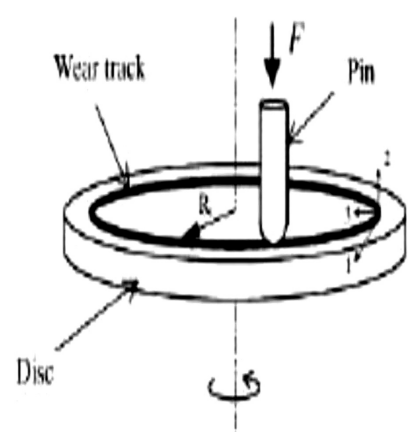

Figure 3: Pin-on-disc geometry

55 % Cr_2O_3 oxides of coating thickness 200 µm were used as test materials. Counter face material made from hardened steel was used as a disc. For each sample dry-sliding wear tests were carried out three times against a constant load of 10 N for a sliding speed of 260 min^{-1}, 525 min^{-1} and 790 min^{-1} under a sliding distance of 1000 m, 2000 m and 3000 m respectively. The corresponding weight losses of the coated specimens were calculated by means of an electronic weighing balance. The microstructural characteristics and wear behaviour were identified by means of the wear scars observed by using SEM for both the coated and uncoated specimens. The pin-on-disc geometry was shown in **Figure 3**.

3 EXPERIMENTAL RESULTS AND DISCUSSION

3.1 Microstructure of ceramic oxide coating

Scanning Electron Microscope (SEM) images of the AISI 1040 forged steel substrate and ceramic oxide powder samples at 200× magnification are shown in **Figure 4**. **Figure 4a** shows various elements present in AISI 1040 forged steel substrate and the increase of the ferrite grain size at the inner regions and ferrite, for example, similar to white regions and perlite, for example, similar to dark side regions were found. **Figures 4b** to **4d** represent the morphological structure of the Al_2O_3, TiO_2 and Cr_2O_3 particles. The Al_2O_3 and TiO_2 powders have distinctive grain sizes, exhibited an irregular morphology and were sharp edged because of the agglomeration of essential particles.The alumina particles are generally nano-sized and the shape of particle is non-spherical. Particle density or true density gives data about the sort of material present in the sample. A particle density higher than 1.0 g/cc is attributed to a high alumina content in the sample rather than the organic matter. The porosity is likewise sensibly high as expected.[13] It demonstrates that the chromium oxide is in pure form and the particles are white colored nano-particles that are almost rhombohedral and isolated.

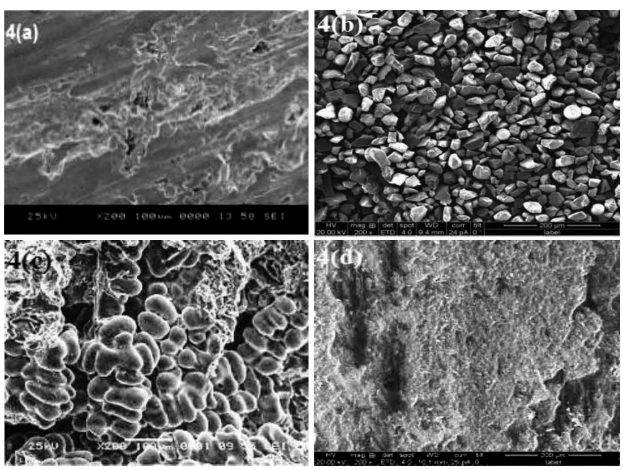

Figure 4: SEM images of steel substrate and ceramic oxides at 200× magnification: a) AISI 1040 forged steel, b) Al_2O_3, c) TiO_2, d) Cr_2O_3

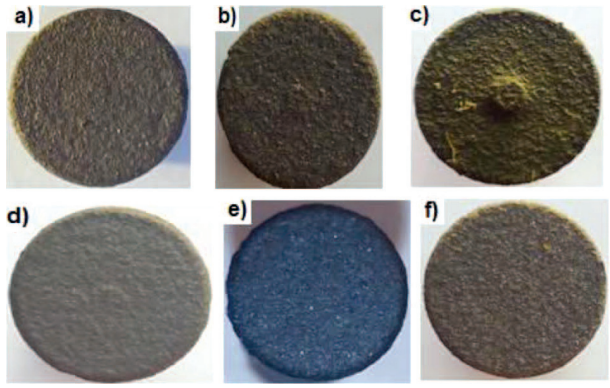

Figure 5: Photographic image of a) Al_2O_3, b)TiO_2, c) Cr_2O_3 d) 45 % Al_2O_3 + 55 % TiO_2, e) 55 % Al_2O_3 + 45 % Cr_2O_3 and f) 45 % TiO_2 + 55% Cr_2O_3

Photographic images of the ceramic oxide coated specimens on AISI 1040 forged steel substrate are shown in **Figure 5**. **Figure 5a** to **5f** show that the Al_2O_3, TiO_2, Cr_2O_3, 45 % Al_2O_3 + 55 % TiO_2, 55 % Al_2O_3 + 45 % Cr_2O_3 and 45 % TiO_2 + 55 % Cr_2O_3 particles are homogenously distributed with less porosity present on the surface of the specimens. An examination of these images revealed that the substrate surface layer and the ceramic coating layer were homogenously fused and there were no pores, cracks, and spaces on the coating area.

3.2 Surface-roughness measurement

The surface roughness (R_a) values were higher for both the coated and uncoated samples before the wear test, whereas the R_a values were lower for both the coated and uncoated samples after the wear test. The recorded values are shown in **Figure 6**. The specimen coated with 55 % Al_2O_3 + 45 % Cr_2O_3 and having a coating thickness of 200 µm is shows a smaller R_a value before the wear test when compared to other values of coated and uncoated specimens.The specimen coated with (99 % of mass fractions) TiO_2 and having a coating thickness of 200 µm shows a lower R_a value after the wear test when compared to the other values of the coated and uncoated specimens after the wear test.

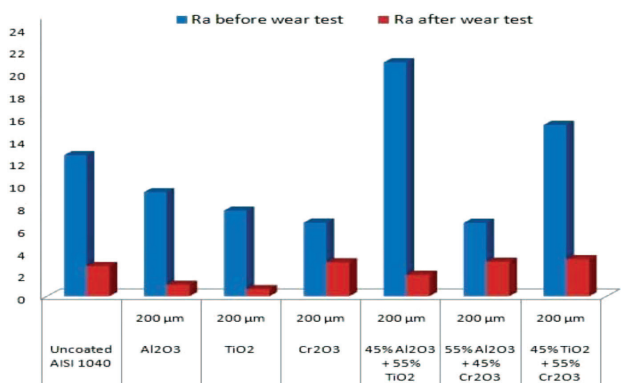

Figure 6: Surface roughness of coated and uncoated specimens

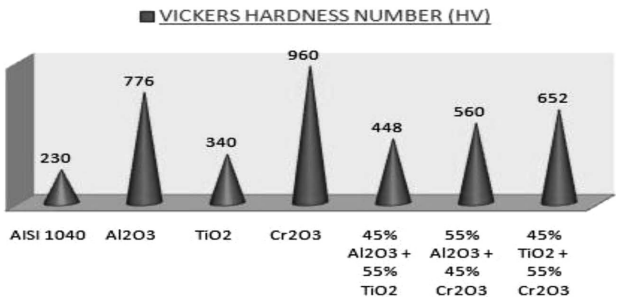

Figure 7: Microhardness of coated specimens and bare AISI 1040 forged steel

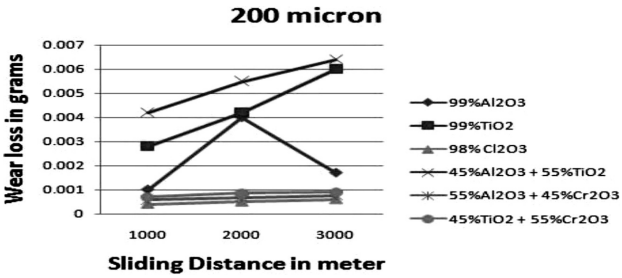

Figure 8: Effect of sliding distance on the wear loss for 200 μm

3.3 Microhardness values of ceramic oxide coating

Figure 7 shows the recorded microhardness values for different ceramic oxide coated and bare specimens. From the recorded values, the 99 % Cr_2O_3 coated specimen has the highest microhardness value when compared to the other coated and uncoated specimens.

3.4 Wear-rate performance of ceramic oxide coated specimens

By using a pin-on-disc apparatus, dry-sliding wear tests were carried out on the ceramic oxide coated and uncoated AISI 1040 specimens according to the ASTM G99-04 standard wear test. The effect of sliding distance in the wear loss of the uncoated and coated specimens at a constant load of 10 N for the different composition coating powder is shown in **Figure 8**.

The specimen coated with 99 % Cr_2O_3 and having a thickness 200 μm has comparatively less wear loss for all the sliding distances rather than the uncoated AISI 1040 forged steel specimen and other combinations of ceramic-oxide-coated specimens. The specimen coated with Al_2O_3-55 % TiO_2 shows a higher wear loss at all the sliding distances when compared to all the other coated specimens. SEM images of ceramic oxide coated specimens and AISI 1040 forged steel after wear test under a constant load of 10 N are shown in **Figures 9**. From **Figure 9a** to **9f** it was observed that the Al_2O_3-55 % TiO_2 coated specimen experienced serious wear condition described by shearing and plastic distortion and the surface of the substrate has turned out to be rough and

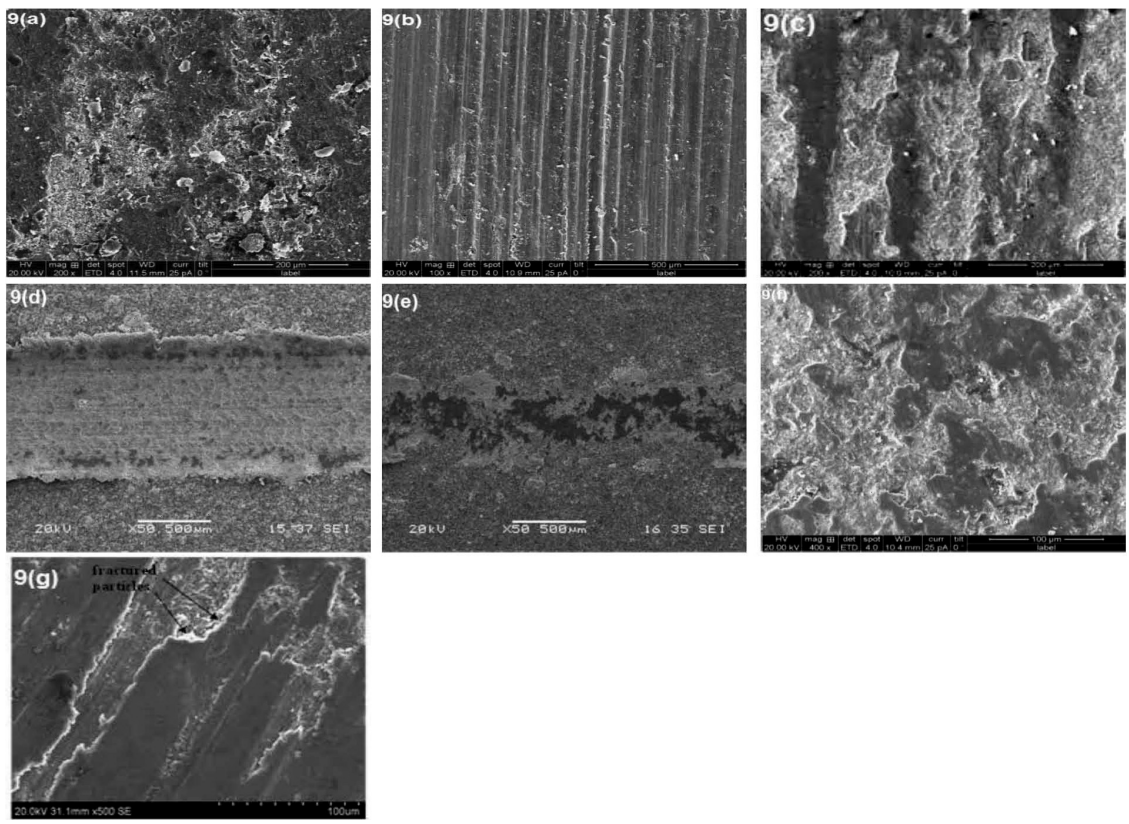

Figure 9: SEM microstructure after wear test of: a) Al_2O_3, b) TiO_2, c) Cr_2O_3, d) 45 Al_2O_3+55 TiO_2, e) 55 Al_2O_3 + 45 Cr_2O_3, f) 45 TiO_2 + 55 Cr_2O_3, g) AISI 1040 forged steel

debris formed because of the wear. The Al_2O_3-coated specimen had a wear mechanism on the surface in the form of flaky micro-cracks. This could be attributed to the high hardness values of the specimens. Micro-cracks occur if a critical value is exceeded in loading and abrasive wear also takes place in relation to the fracture toughness of the abraded material. The TiO_2-coated specimen showed that the wear mechanism on the surface formed micro-cutting of various widths along with plastic deformation because of micro crackings. **Figure 9g** reveals that the transfer of the materials that occurred from the pin to the disc. The debris produced throughout the test was deposited on both sides of the wear track. Over the wear track a few patches of the initial surface are observed, indicating that the transferred steel film was detached as a result of a fatigue process.

4 CONCLUSIONS

The AISI 1040 forged steel substrate was coated with alumina, titania, chromia individually and again with different combinations of ceramic oxides such as 45 % Al_2O_3 + 55 % TiO_2, 55 % Al_2O_3 + 45 % Cr_2O_3, and 45 % TiO_2 + 55 % Cr_2O_3 by using a plasma-spraying process with an intermediate bond coat of NiCr, SEM tests were carried out to determine the surface roughness and adhesion of the coating onto the AISI 1040 substrate.

The specimen coated with 99 % Cr_2O_3 has higher microhardness values among all the ceramic-oxide-coated specimens, which was followed by 99 % Al_2O_3, 45 % TiO_2 + 55 % Cr_2O_3, 55 % Al_2O_3 + 45 % Cr_2O_3. The lowest hardness value was obtained from the ceramic oxide coating surface with a mixture proportion of 45 % Al_2O_3 + 55 % TiO_2.

The chromia-coated specimen showed excellent wear property when compared to other coating materials due to its excellent adhesion to the base metal.

The increase in the weight percentage of TiO_2 in the Al_2O_3 ceramic material affects the microhardness value of the specimens in a decreasing manner.

The microhardness values of the coated specimens influence the wear loss. The specimens having higher microhardness also have a higher wear resistance and cause less wear loss.

If the weight percentage of TiO_2 in Cr_2O_3 ceramic materials increases, this decreases the microhardness value of the specimens.

From the experimental results it can be concluded that the pure 99 % Cr_2O_3 coated AISI 1040 forged steel specimen showed better wear resistance property due to dense, compact, defects free and good adhesion characteristics, while compared to other coating materials. Hence, it is recommended for surface coating on the top mill roll shafts used in sugarcane industries to increase the wear resistance of the shaft.

Acknowledgement

The research work was supported by my father Mr. D. Ponnusamy and my spouse Mrs B. Malathi. Special thanks to Professor Dr. K. K. Ramasamy and Dr. M. Premkumar from Paavai Engineering College, Namakkal, India, for their valuable help.

5 REFERENCES

[1] S.-H. Yao, Comparative study on wear performance of traditional and nano structured Al_2O_3-13 wt.% TiO_2 air plasma spray coatings, J. Ceram. Silikaty, 59 (**2015**) 1, 59–63

[2] Y. Sert, N. Toplan, Tribological behaviour of a plasma – sprayed Al_2O_3-TiO_2-Cr_2O_3 coating, Mater. Technol., 47 (**2013**) 2, 181–183

[3] C. A. Berkath, A. Khan, Dr. Anilkumar, P. M. Suresh, Tribological behaviour of a plasma – sprayed Al_2O_3-TiO_2 coating on Al-6082T6 substrate, Int. J. of Inno. Res. in Sci., Eng. and Techno., 3 (**2014**) 6, 13956–13963

[4] M. H. Korkut, Y. Kucuk, A. C. Karaoglanl, A. Erdogan, Y. Er, M. S. Gok, Effect of the abrasive grit size on the wear behaviour of ceramic coatings during a micro-abrasion test, Mater. Technol., 47 (**2013**) 6, 695–699

[5] S. Islak, S. Buytoz, I. Somunkiran, E. Ersoz, N. Tosun, N. Orhan, J. Stokes, M. Saleem Hashmi, Effect on microstructure of TiO_2 rate in Al_2O_3-TiO_2 composite coating produced using plasma spray method, Optoelectro. Adv. Mater. – Rapid Comm., 6 (**2012**) 9–10, 844–849

[6] S. Salman, R. Kose, L. Urtekin, F. Findik, An investigation of different ceramic coating thermal properties, Mater. Des., 27 (**2006**) 7, 585–590, doi:10.1016/j.matdes.2004.12.010

[7] M. S. Kumar, S. Natarajan, Analysis of tribological factors on dry sliding wear behaviour of thermally sprayed carbide and ceramic coatings by taguchi method, Int. J. of Eng. Sci. Tech., 3 (**2011**) 4, 3336–3347

[8] G. Bolelli, V. Cannillo, L. Lusvarghi, T. Manfredini, Wear behaviour of thermally sprayed ceramic oxide coatings, Wear, 261 (**2006**), 1298–1315, doi:10.1016/j.wear. 2006.03.023

[9] A. Prasad, D. Gupta, M. R. Sankar, A. N. Reddy, Experimental investigations of Ni/La_2O_3 composite micro-cladding on AISI 1040 steel through microwave irradiation, 5th Int. & 26th All India Manufacturing Techno., Des. and Res. Conference, 2014, 55–61

[10] M. S. Gok, The effect of different ceramics on the abrasive wear behavior of coating surface produced by the plasma process, Int. J. of the Phy. Sci., 5 (**2010**) 5, 535–546

[11] P. Gadhari, P. Sahoo, Wear resistance improvement of electroless Ni–P–Al_2O_3 composite coating by optimizing process parameters using taguchi technique, Int. J. of Mater. Chem. and Phy., 1 (**2015**) 1, 1–10, http:// creativecommons.org/ licenses/by-nc/4.0/

[12] M. Yunus, J. F. Rahman, Optimization of usage parameters of ceramic coatings in high temperature applications using taguchi design, Int. J. of Eng. Sci. and Techno., 3 (**2011**) 8, 6364–6371

[13] C. G. Schull, The determination of pore size distribution from gas adsorption data, J. Am. Chem. Soc ., 70 (**1948**) 4,1405–1410

UDK 67.017:620.3:621.74:669.721
Original scientific article/Izvirni znanstveni članek

ISSN 1580-2949
MTAEC9, 51(6)945(2017)

SYNTHESIS AND CHARACTERIZATION OF AN IN-SITU MAGNESIUM-BASED CAST NANO COMPOSITE VIA NANO-SiO_2 ADDITIONS TO THE MELT

SINTEZA IN KARAKTERIZACIJA IN SITU NANOKOMPOZITA NA OSNOVI MAGNEZIJA Z NANO-SiO_2 DODATKOM ZA TALJENJE

Mansour Borouni[1], Behzad Niroumand[2], Ali Maleki[3]

[1]Isfahan University of Technology, Pardis College, Materials Engineering Group, Isfahan 84156-83111, Iran
[2]Isfahan University of Technology, Department of Mechanical Engineering, Isfahan, 84156-83111, Iran
[3]Isfahan University of Technology, Research Institute for Steel, Isfahan, 84156-83111, Iran
m.borouni@pa.iut.ac.ir

Prejem rokopisa – received: 2017-04-01; sprejem za objavo – accepted for publication: 2017-05-12

doi:10.17222/mit.2017.036

In this study, AZ91C magnesium matrix in-situ nano-composites reinforced with oxide particles were produced by the addition of 2 % of mass fractions of silica nanoparticles to the melt using the stir-casting method. For this purpose, nano-silica powder was mixed in molten AZ91C by a special procedure and stirred for 15 min at 750 °C and cast in a preheated die at 720 °C. Control samples were also cast under the same conditions. Improved microstructure, reduced porosity and increased hardness, tensile strength and yield strength of the composite sample were revealed by microstructural and mechanical investigations. The hardness, yield strength and tensile strength values increased from 65 BHN, 82 MPa and 165 MPa for the monolithic samples to 77 BHN, 97 MPa and 175 MPa for the in-situ formed cast composites. Microstructural and EDS analyses suggested the in-situ formation of Al_2O_3, $MgAl_2O_4$ and MgO oxide particles by in-situ reaction of the Al, Mg and SiO_2 in the melt.

Keywords: AZ91C alloy, in-situ cast nano-composite, silica nanoparticles, mechanical properties

V študiji so bili izdelani AZ91C nanokompoziti in situ, na podlagi magnezijeve matrike in ojačani z oksidnimi delci z dodatkom 2 % nanodelcev silicija za topljenje, z uporabo metode litja z mešanjem. Za ta namen je bil nanosilicijev prah zmešan v raztopljen AZ91C s posebno metodo in nato 15 min mešan na 750 °C in lit v predogretem modelu na 720 °C. Preizkušanci so bili ravnotako liti v enakih pogojih. Izboljšana mikrostruktura, zmanjšana poroznost in povečana trdota, napetostna trdnost in napetost vzorcev kompozita so bili odkriti s preiskavami mikrostrukture in z mehanskimi preiskavami. Vrednosti trdote, napetosti tečenja in natezne napetosti so se povečali iz 65 BHN, 82 Mpa in 165 MPa in za monolitne vzorce na 77 BHN, 97 MPa in 175 MPa za in situ formirane lite kompozite. Mikrostrukture in EDS-analize so predlagale in situ formacijo Al_2O_3, $MgAl_2O_4$ in MgO oksidne delce z in situ reakcijo Al, Mg in SiO_2 v topljenem.

Ključne besede: AZ91C zlitina, in situ litje nanokompozitov, nanodelci silicija, mehanske lastnosti

1 INTRODUCTION

Besides extensive applications in automobile and aerospace industries, magnesium and its alloys have had considerable growth in three markets of communications, computer and video and photography cameras. Magnesium is the lightest industrial metal with a density of 1.74 g/cm^3. Magnesium has a high specific strength and therefore it is used extensively as the metal matrix in the manufacturing of composites. Among the alloys of magnesium, Mg-Al-Zn alloys, specifically the AZ91 alloy, have extensive applications in various industries. Corrosion resistance and relatively high strength are the particular properties of the AZ91 alloy compared to other magnesium alloys. The AZ91 alloy is one of the most common magnesium alloys to produce magnesium-matrix composites.[1–5]

For producing magnesium-matrix composites, reinforcing materials with different shapes, sizes and materials are used. Micron-sized ceramic reinforcements including carbides, borides and oxides are the most common.[2,5] Various studies are carried out in the field of magnesium-matrix composites reinforced with ceramic particles. For instance, in 2008, Hassan and Gupta produced a magnesium composite reinforced with Al_2O_3 particles with 0.3-micron sizes using disintegrated melt deposition method and reported improved yield strength, tensile strength and flexibility by 2 % of mass fractions increase of Al_2O_3 particles.[6]

By changing the scale of the reinforcing particles from micrometer to nanometer, their specific surface is increased significantly and the impact of the properties of the surface of the particles become more important. Since one of the mechanisms to increase the properties of the composites is the load transfer in the interface of the matrix and reinforcement particles, using nanoparticles, the surface of the reinforcement which is in contact with the matrix is increased and higher increases in the properties are expected.[7] In a research in 2012, AZ91D-TiB_2 nano-composites were manufactured using ultrasonic mixing and their sub-structure and mechanical properties were studied. For AZ91D nano-composites

with 2.7 % weight percentage of TiB_2 with a mean diameter of 25 nanometers, the yield strength, ultimate tensile strength and plasticity were improved by 21 %, 16 %, and 48 %, respectively.[8]

M. Habibnejad et al.[9] studied producing pure magnesium and AZ31 magnesium alloy composites using Al_2O_3 nano-particles by the stir-casting method. Characterization of the mechanical properties indicated that the yield strength and the tensile strength of pure magnesium and the AZ31 alloy is generally increased with nano-particles; however, the flexibility decreases.

In most of the researches, including the above-mentioned studies, the reinforcing particles are placed in the matrix in an ex-situ procedure. In in-situ composite fabrication methods, the reinforcing phase is formed during the procedure with reactions of different materials. The reaction could take place for a solid powder or in molten compounds.[10]

In the current study, the magnesium-matrix nano-composite AZ91C, reinforced with oxide nano-particles is produced in in-situ form by adding nano-silica particles in the molten form and the stir-casting method and the structural and mechanical properties of the produced composites are studied.

2 MATERIALS AND METHODS

The standard and measured (by the wet-chemistry technique) chemical compound of the alloy used in this study are shown in **Table 1**.[11]

Table 1: The chemical compound of the AZ91C alloy used in this research

% Chemical composition	Standard[11]	Measurement
Al	8.1-9.3	8.63
Zn	0.4-1	0.59
Mn	0.13-0.35	0.17
Si	0.3	0.1
Cu	0.1	0.05
Ni	0.01	-
Mg	Remained	Remained

In this research, silica nano-particles produced from pyrolysis and burning of HTV silicon polymer are used for the in-situ production of oxide reinforcing particles. To produce silica nano-particles, HTV silicon polymer manufactured by the Korean KCC company is used as the raw material and the production procedure is modified as done by M. Senmar et al.[12] In this regard, the required value of the afore-mentioned material is placed inside the resistance furnace. The furnace is warmed with a rate of 20 °C/min to reach 700 °C. Then, the material is maintained at 700 °C to be completely pyrolyzed and burnt. The resulted product is a white powder that was analyzed by X-ray diffraction (XRD), Scanning Electron Microscope (SEM) and Transmission electron microscopy (TEM). **Figure 1**, shows the x-ray

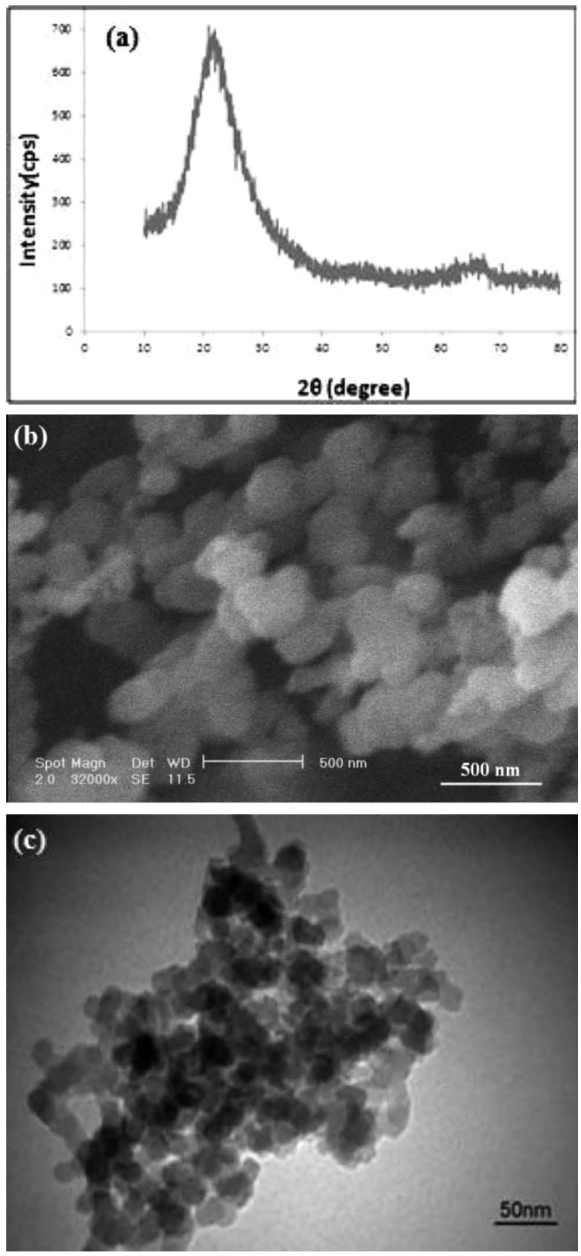

Figure 1: a) XRD pattern[12] b) SEM image, c) TEM image [12] from the powder resulted from pyrolysis and burning of HTV silicon polymer

diffraction pattern and the images of scanning electron and transmission electron microscopy.

To make molten AZ91C, first a burner furnace with natural gas fuel is used for melting the alloy and then a resistance furnace is used to maintain and control the temperature. The reason to select this method for melting the alloy was that the preparation of the molten alloy in the gas furnace is much quicker than in the resistance furnace. Therefore, by decreasing the molten alloy preparation time, one could prevent the oxidation of the molten alloy. As soon as the alloy is melted inside the gas furnace and for accurately controlling the temperature, the crucible of the molten alloy is transferred to the

electric furnace, which is warmed beforehand to reach the intended temperature and was close to the gas furnace. After reaching the desired temperature, the molten alloy is mixed. In **Figure 2**, the schematic picture of the stir casting system is shown.

To manufacture in-situ magnesium-matrix nano-composites AZ91C reinforced with oxide nano-particles, one kilograms of AZ91C magnesium bar and 20 g of nano-silica powder is prepared for each test. Then, holes with a diameter 13 millimeters are drilled into the magnesium bar. SiO_2 nano-powder mixed well with AZ91C alloy filings was put inside the holes and was pounded until the holes were filled with AZ91C filings. Then, the prepared set was put in a graphite crucible inside the furnace.

Unlike aluminum which has a continuous oxide layer and the oxide formation on the surface the molten aluminum prevents the contact between the molten material and air, magnesium oxide is porous and cannot make any protection of the molten material.[3,5] In the casting of magnesium alloy, if the metal and air contact is not cut during and after the melting, all the magnesium is oxidized and nothing but a white powder of magnesium oxide will remain. In stir casting in which the molten material is turbulent and has more contact with air, this issue is much more intense. In this study, to protect the AZ91C molten alloy, a mixture of carbon dioxide and argon with equal fractions is blown on the surface of the molten alloy and to mix it, a stirrer made out of simple carbon steel with three blades with 120° with respect to each other is used according to **Figure 3**. The thickness, width and length of the blades are (2, 15 and 20) mm, respectively. To increase the mixing power and create a more downward flow, blades with angles of 45 degrees were connected with respect to the mixing axis. To keep the molten alloy clean and increase the lifetime of the stirrer, the surface of the stirrer is coated with a nano-ceramic coating. While stirring, the stirrer is inserted into the molten alloy to half the height of the liquid.

After preparing the molten alloy, its temperature is raised to 750 °C and stirring is done for 15 min with a speed of 500 min^{-1} so that the composite slurry is

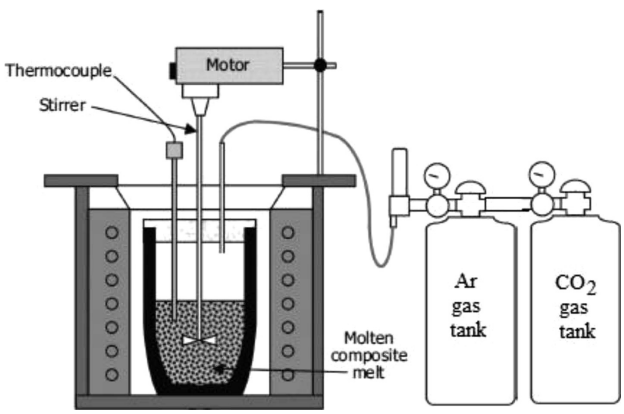

Figure 2: Schematic of the stir-casting system used in this research

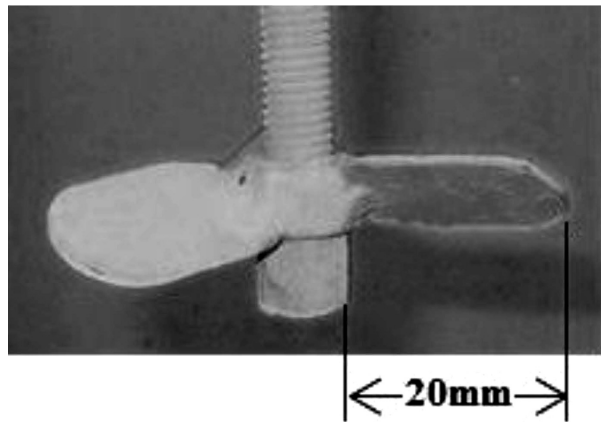

Figure 3: The picture of the stirrer used in this research

formed. Then, the temperature of the slurry was decreased to 720 °C and was poured into steel molds which were pre-warmed to 100 °C. The steel mold used which has four cylindrical holes as well as a cast sample is illustrated in **Figure 4**.

It should be noted that three composite samples consisting of 2 % of mass fractions of nano-silica powder were cast as described above and a non-composite sample made of AZ91C alloy was cast with similar conditions as the control sample. All the samples were lathed as the tensile test sample after cleaning based on ASTM-E8M standard[13] according to **Figure 5** to inves-

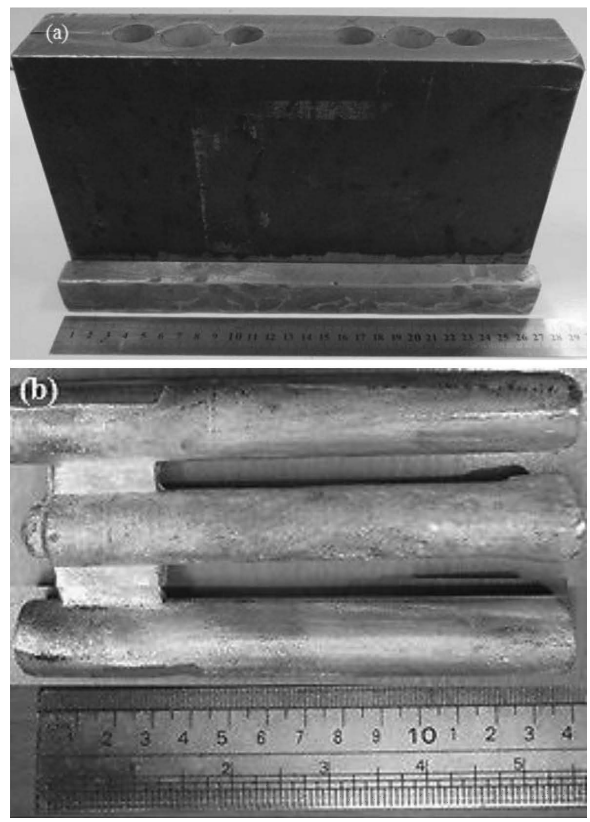

Figure 4: a) Steel mold used in this research, b) A cast sample in the mold

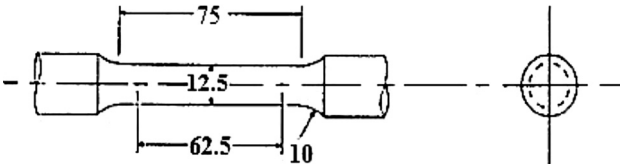

Figure 5: Schematic of the tensile test sample[13]

tigate the tensile properties. Preparing the sample for studying the micro-structures was performed according to the ASTM-E3-01 standard.[14] The surfaces of the samples were prepared in Nital Etch Solution 2 % and their microstructures were studied using a Mec 1042C light microscope.

3 RESULTS AND DISCUSSION

3.1 Microstructural studies

Microstructural non-composite (control) and nano-composites samples are shown in **Figure 6** by optical microscopes. As observed in **Figures 6a** and **6b**, AZ91C alloy microstructures (control sample) consist of continuous intermetallic phase β-$Mg_{17}Al_{12}$ which has surrounded the primary magnesium dendrites a–Mg. β-$Mg_{17}Al_{12}$ phase is mainly distributed along the boundaries of the primary phase a–Mg grains and is in the shape of a long and continuous grid that leads to a reduction of the mechanical properties.

An important point when studying the nano-composite microstructures is to investigate the distribution and the bonds of the reinforcing particles in the matrix. Nevertheless, in **Figures 6c** and **6d** which display the nano-structures of the composite sample consisting of 2 % of mass fractions of nano-silica particles, there is no evidence of reinforcing particles in the matrix. Using nanometric reinforcing materials, when a proper distribution of the particles is achieved in the composite and large lumps of reinforcing material is not present in the structure, identifying and finding the reinforcing particles in the micro-structure is not possible with light microscopy and electronic microscopies are needed to study at higher magnifications. Also, indirect observations and studying the mechanical and physical properties could lead to understanding the presence and distribution of the reinforcements in the matrix.

Figure 7 illustrates the Scanning Electron Microscopy (SEM) images for the composite sample consisting of 2 % of mass fractions SiO_2 reinforcing nano-particles. In this picture, particles with dimensions of tens to

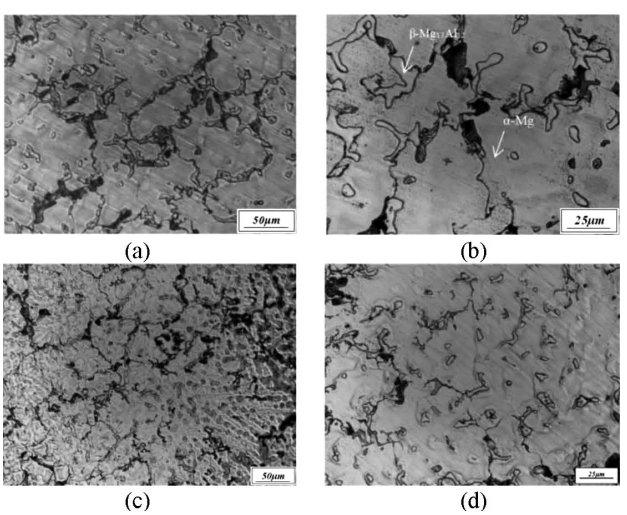

Figure 6: Light microscopic images in two different magnifications, a) and b) non-composite cast sample micro-structure, c) and d) composite cast micro-structure consisting of 2 % of reinforcing SiO_2 nano-particles

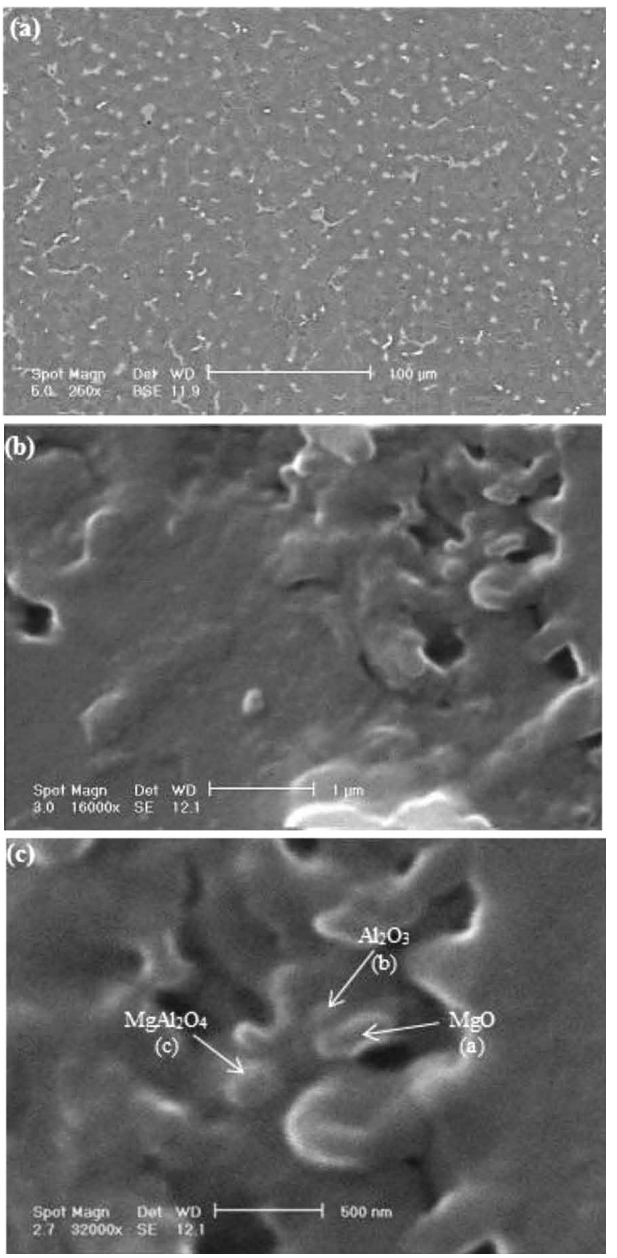

Figure 7: Scanning electron microscopy (SEM) images for the composite sample consisting of 2 % of mass fractions of SiO_2 reinforcing nano-particles

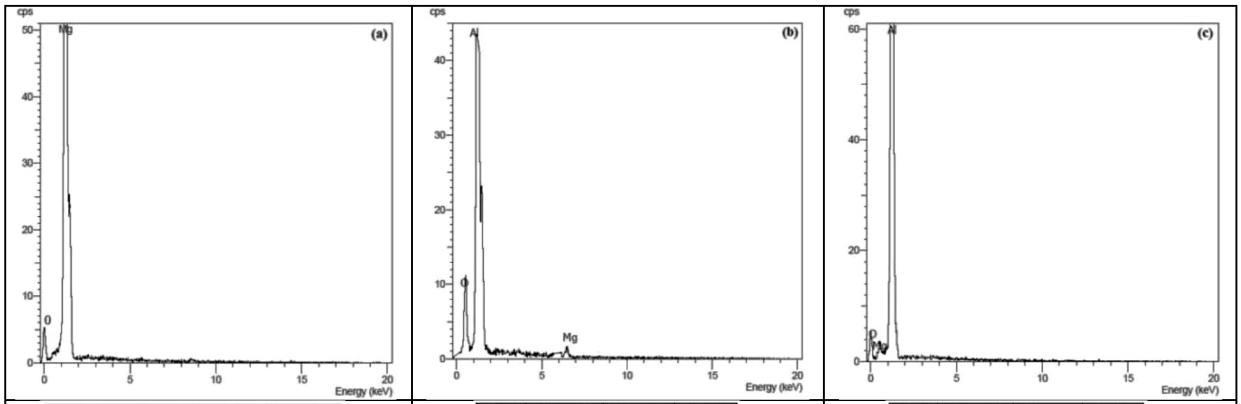

Elt.	Atomic %	Conc	Units
Mg	78.64	76.39	wt.%
O	21.36	23.61	wt.%
	100.00	100.00	wt.%

Elt.	Atomic %	Conc	Units
Mg	4.78	3.65	wt.%
O	36.37	34.61	wt.%
Al	58.85	61.74	wt.%
	100.00	100.00	wt.%

Elt.	Atomic %	Conc	Units
Mg	5.89	4.55	wt.%
Al	81.62	81.31	wt.%
O	12.49	14.14	wt.%
	100.00	100.00	wt.%

Figure 8: EDS elemental analysis from points a, b, and c

hundreds nanometers are observed. **Figure 8** shows the EDS analysis of the three specified phases of **Figure 7c**. According to this analysis, all the observed particles are oxidized and are made of Al_2O_3, MgO and $MgAl_2O_4$ and no sign of added nano-silica particles into the structure is observed. Therefore, it seems that the added nano-silica particles are reduced in the molten alloy and releasing oxygen has led to the in-situ creation of new oxide phases that are studied in what follows.

On the other hand, in **Figures 6c** and **6d**, it is observed that in AZ91C nano-composites, consisting of oxide nano-particles, the dendrites of the main phase α-Mg have become finer and the shape of the initial phase has changed to equiaxed dendritic structure from a coarse dendritic form. It seems that the formed nano-particles in the molten alloy could have led to finer α-Mg phase by creating the condition for better heterogeneous nucleation or effective prevention of the growth of grains, as well as modifying the continuous grids of phase β-$Mg_{17}Al_{12}$.

3.2 Thermodynamic analysis of phase formations in the Mg-SiO_2 system

The chemical compound of the used alloy is presented in **Table 1** in which magnesium is the base metal and aluminum is the main alloying element. Moreover, during the procedure, nano-silica particles with high specific surface areas are added to the molten alloy at 750 °C, which are expected to create a good condition for a reaction with the molten alloy. According Sreekumar et al.,[17] reactions 1 to 5 could occur between the main elements in the molten material and nano-silica particles. The released energy for each reaction at 750 °C (1023 K) is also shown next to each of them in **Table 2**.[15–17]

Since the released energy of all of these reactions is extremely negative at 750 °C, formation of Al_2O_3, $MgAl_2O_4$ and MgO phases, which are shown in **Figure 7c**, are thermodynamically feasible and spontaneous. The $MgAl_2O_4$ phase shows a combination of unique properties such as low electrical conductivity, low thermal expansion coefficient, good thermal shock resistance, low dielectric constant, high electrical resistance, high melting point (2135 °C) and high mechanical strength.[17,18] Moreover, this compound has a good adhesion to metal matrices.[19] Various studies are carried out regarding the formation, interface type and crystallography of the $MgAl_2O_4$ phase with reinforcements used in metal-matrix composites. The oxide reinforcements were used such as Al_2O_3, Saffil, Mullite, Kaowool, $Al_4B_3O_{18}$, MgO, ASZ (Composition Al_2O_3, SiO_2 and ZrO_2 in 3 : 5 : 2 ratio and are amorphous in their as-fabricated state) and glass fibers or non-oxide reinforcements such as graphite, B_4C, AlN and SiC. Studying the reactions with oxide reinforcements has shown that $MgAl_2O_4$ is formed due to the reaction of the oxide reinforcements with aluminum and magnesium in the matrix alloy. Also, the oxidation of the volatile surface of non-oxide reinforcements leads

Table 2: Reactions could occur between the main elements in the molten material and nano-silica particles

(1)	$\Delta G^0_{1023\ K}$ = -348.19 kJ/mol	$4Mg(l)+SiO_2(s) \rightarrow Mg_2Si(s)+2MgO(s)$
(2)	$\Delta G^0_{1023\ K}$ = -268.22 kJ/mol	$SiO_2(s)+2Mg(l) \rightarrow 2MgO(s)+Si(l)$
(3)	$\Delta G^0_{1023\ K}$ = -449.63 kJ/mol	$2SiO_2(s)+Mg(l)+2Al(l) \rightarrow MgAl_2O_4(s)+2Si(l)$
(4)	$\Delta G^0_{1023\ K}$ = -556.44 kJ/mol	$3SiO_2(s)+4Al(l) \rightarrow 2Al_2O_3(s)+3Si(l)$
(5)	$\Delta G^0_{1023\ K}$ = -631.08 kJ/mol	$3SiO_2(s)+2MgO(s)+4Al(l) \rightarrow 2MgAl_2O_4(s)+3Si(l)$

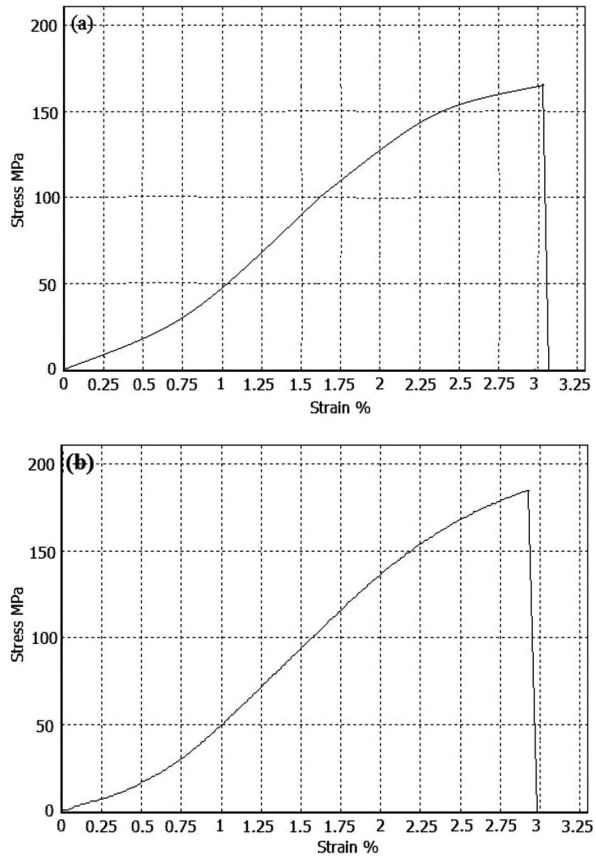

Figure 9: An example of stress-strain curves resulted from tensile test for: a) non-composite samples, b) composite samples

to the formation of a reactive oxide layer, which helps the formation of $MgAl_2O_4$. The formation of SiO_2 on SiC, Al_2O_3 on AlN and B_2O_3 on B_4C are the examples of this mechanism.[17] In some cases it is reported that the absorption of the oxygen on the surface of the reinforcements acts as a source for the formation of $MgAl_2O_4$.[19] Al_2O_3 has rigidity and high strength as well as corrosion resistance and sufficient thermal stability.[20] Magnesium composites reinforced with Al_2O_3 nano-particles show a considerable increase in the microhardness and a slight increase in the elasticity modulus and yield strength.[21] The hardness and tensile strength increase in the AZ91 alloy reinforced with MgO.[22]

3.3 Investigating the mechanical properties

Figure 9 shows an example of stress-strain curves resulting from the tensile test for composite and non-composite samples. The average values of the mechanical properties including hardness, yield strength, ultimate tensile strength and elongation percentage of the non-composite sample and nano-composite samples are shown in **Table 3**.

As observed in **Figure 9** and **Table 3**, hardness, yield strength and ultimate tensile strength of the cast nano-composite samples increased compared to the cast non-composite sample (control sample) and their elongation percentage has slightly decreased.

Different mechanisms are presented for improving the mechanical properties of the metal-matrix composites. Examining the shapes and sizes of the grains and the properties of the composite samples, one could understand the effectiveness of the operation. One of the evidences of the improvement of the properties in the composite samples is that the microstructures of the cast nano-composite samples have finer and more uniform grains compared to the non-composite samples (Hall-Petch effect). Also, the secondary phase β-$Mg_{17}Al_{12}$ is considerably crushed in the grain boundaries of the primary phase, has lost its continuity and is distributed more uniformly in the structure. It seems that the reason for this is the uniform distribution of the reinforcing particles in the structure and their effect on the nucleation of the primary phase and preventing the growth of the grains. Another impact is the formation of oxide nano-particles in the matrix such that they are almost homogeneously distributed in the matrix. As observed in **Figure 6**, the distribution and how the reinforcing nano-particles are put together are not clear in this picture, which shows the relatively proper distribution of the reinforcing particles and the absence of large lumps in the matrix.

A. Sanati Zadeh et al.[23] found the Hall-Petch strengthening effect to be very important for the strength of nano-composites such that it causes up to 50 % of the total strengthening.

As the elasticity modulus of the matrix and reinforcement are completely different, when one-dimensional loading is applied on a composite material, a combined stress distribution is formed. Highly accurate analyses show that shear stresses occur in the boundary of the matrix with the particles, which leads to an increased strength.[24]

As shown in **Figure 8** and **Table 3**, while the strengths of the composite samples are increased, their elongation percentages are somewhat decreased. This is generally observed in composites. In fact, the same

Table 3: Mechanical properties of non-composite and nano-composite samples

% Nano silica	Hardness (BHN)	U.T.S (MPa)	Y.S (MPa)	% El	
0	5±65	3±165	2±82	0.3±3.5	Non-composite sample (control sample)
2	3±77	2±175	3±97	0.2±3	Nano-composite sample (average of three tests)
-	+18.5	+6.1	+18.3	-14.3	Percent change

mechanisms which lead to an increased strength, decrease the deformation of the matrix as well. Moreover, the weak bond between the reinforcing particles and magnesium matrix and defects such as gaseous pores could also be factoring, which leads to a more intense decrease of the flexibility of the composites.

4 CONCLUSION

An AZ91C nano-composite consisting of Al_2O_3, $MgAl_2O_4$ and MgO oxide nano-particles is successfully produced using the stir-casting method. The existence of Al_2O_3, $MgAl_2O_4$ and MgO oxide particles in an AZ91C alloy has a proper reinforcing role and the manufactured nano-composites have finer and more uniform grains compared to the non-composite control sample. Also, the secondary phase β-$Mg_{17}Al_{12}$ is fairly crushed and is distributed in a non-continuous form in the structure. These changes lead to the improvement of the mechanical properties compared to the non-composite control sample so that the hardness, yield strength and tensile strength are increased from 65 BHN, 82 MPa and 165 MPa in the non-composite sample to 77 BHN, 97 MPa and 175 MPa in the composite sample.

Acknowledgements

The authors are grateful for support of this research by Isfahan University of Technology (IUT).

5 REFERENCES

[1] E. F. Horst, L. M. Barry, Magnesium Technology (Metallurgy, Design Data, Applications), Springer, Germany, (2006)

[2] M. Gupta, N. M. L. Sharon, Magnesium, Magnesium Alloys, and Magnesium Composites, John Wiley & Sons, Inc., New Jersey, (2011)

[3] A. W. Brace, F. A. Allen, Magnesium Casting Technology, London, Chapman & Hall; New York, Reinhold Pub. Corp., (1957)

[4] ASM Handbook Committee, Metals Handbook, Vol. 15, casting, ASM International, Ten Edition, (2008)

[5] H. E. Friedrich, B. L. Mordike, Magnesium Technology (Metallurgy, Design Data, Applications), 1st Ed., Springer, Germany, (2006)

[6] S. F. Hassan, M. Gupta, Effect of submicron size Al_2O_3 particulates on microstructural and tensile properties of elemental Mg. Journal of Alloys and Compounds, 457 (**2008**), 244–250, doi:10.1016/j.jallcom.2007.03.058

[7] D. Vollath, Nanomaterials: Nanomaterials: An Introduction to Synthesis, Properties and Applications, 2nd Edition, (2013)

[8] H. Choi, Y. Sun, B. P. Slater, H. Konishi, X. Li, AZ91D-TiB_2 Nanocomposites Fabricated by Solidification Nanoprocessing, Advanced Engineering Materiales, 14 (**2012**) 5, 291–295, doi:10.1002/adem.201100313

[9] M. Habibnejad-Korayem, R. Mahmudi, W. J. Poole, Enhanced properties of Mg-based nanocomposites reinforced with Al_2O_3 nano particles, Materials Science and Engineering A, 519 (**2009**), 198–203, doi:10.1016/j.msea.2009.05.001

[10] K. Kainer, Metal matrix composite, Wiley book, (2006)

[11] International ASTM B 80-05, Standard specification for magnesium –alloy sand casting, (2005)

[12] M. Senemar, A. Maleki, B. Niroumand, A. Allafchian, A Novel And Facile Method For Silica Nanoparticles Synthesis From High Temperature Vulcanization (HTV) Silicone, Association of Metallurgical Engineers of Serbia (AMES), 22 (2016) 1, 1–8, https://metall-mater-eng.com/index.php/home/article/view/134/120

[13] International ASTM B E8/E8M – 09, Standard Test Methods for Tension Testing of Metallic Materials1, (2010)

[14] International ASTM E03-1, Standard Practice for Preparation of Metallographic Specimens, (2007)

[15] D. Huang, Y. Wang, Y. Wang, H. Cui, X. Guo, In situ Mg_2Si reinforced Mg alloy synthesized in Mg-SiO_2 system, Advanced Materials Research, 146–147 (**2011**), 1775–1779, doi:10.4028/www.scientific.net/AMR.146-147.1775

[16] Y. J. Liang, Y. C. Chen, Thermodynamic Data Handbook on Inorganic Substances, Dongbei University Press, China, in Chinese, (1993)

[17] V. M. Sreekumar, R. M. Pillai, B. C. Pai, M. Chakraborty, Evolution of $MgAl_2O_4$ crystals in Al-Mg-SiO_2 composites, Applied Physics A Materials Science & Processing, A 90 (**2008**), 745–752, doi:10.1007/s00339-007-4357-2

[18] C. Pacurariu, I. Lazau, Z. Ecsedi, R. Lazau, P. Barvinschi, G. Marginean, New synthesis methods of $MgAl_2O_4$ spinel, Journal of the European Ceramic Society, 27 (**2007**), 707–710, doi:10.1016/j.jeurceramsoc.2006.04.050

[19] G. Ramani, R. M. Pillai, B. C. Pai, T. R. Ramamohan, Factors affecting the stability of non-wetting dispersed suspensions in metallic melts, Composites, 22 (**1991**) 2, 143–150, doi:10.1016/0010-4361(91)90673-5

[20] A. Kazunori, Y. Hiroyuki, Effects of Particle-Dispersion on the Strength of an Alumina Fiber-Reinforced Aluminum Alloy Matrix Composite, Materials Transactions, 44 (**2003**) 6, 1172–1180, https://www.jim.or.jp/journal/e/pdf3/44/06/1172.pdf

[21] T. S. Srivatsan, C. Godbole, T. Quick, M. Paramsothy, M. Gupta, Mechanical Behavior of a Magnesium Alloy Nanocomposite Under Conditions of Static Tension and Dynamic Fatigue, Journal of Materials Engineering and Performance, 22 (**2013**), 439–453, doi:10.1007/s11665-012-0276-2

[22] Z. Song-li, Z. Yu-tao, C. Gang, In situ (Mg_2Si+MgO)/Mg composites fabricated from AZ91-$Al_2(SiO_3)_3$ with assistance of high-energy ultrasonic field, Transactions of Nonferrous metals Society of china, 20 (**2010**), 2096–2099, doi:10.1016/S1003-6326(09)60424-6

[23] A. Sanaty-Zadeh, P. K. Rohatgi, Comparison between Current Models for the Strength of Particulate Reinforced Metal Matrix Nanocomposites with Emphasis on Consideration of Hall–Petch Effect, Materials Science and Engineering, A 531(**2012**), 112–118, doi:10.1016/j.msea.2011.10.043

[24] G. E. Dieter, Mechanical Metallurgy, MacGraw-Hill Book Company Limited, UK, (1988)

UDK 52-17:62-493-026.775:621.9
Original scientific article/Izvirni znanstveni članek

ISSN 1580-2949
MTAEC9, 51(6)953(2017)

2D NUMERIC SIMULATION OF SERRATED-CHIP FORMATION IN ORTHOGONAL CUTTING OF AISI316H STAINLESS STEEL

NUMERIČNA 2D SIMULACIJA NASTANKA NAZOBČANEGA ODREZKA PRI PRAVOKOTNEM REZANJU AISI316H JEKLA

Arif Gök

Amasya University, Faculty of Technology, Department of Mechanical Engineering, 05100 Amasya, Turkey
arif.gok@amasya.edu.tr

Prejem rokopisa – received: 2017-04-06; sprejem za objavo – accepted for publication: 2017-05-30

doi:10.17222/mit.2017.038

Low thermal conductivity, high strength, high ductility and high work-hardening tendency of austenitic stainless steels are the main factors that make their machinability difficult. This study investigates the influence of material modelling on the serrated-chip formation during the orthogonal cutting of the AISI316H stainless steel using finite-element simulations. Turning tests were carried out at three different cutting speeds and constant depth of cut and feed rate. Predictions were compared with the orthogonal-cutting tests and found to be in agreement.

Keywords: AISI 304 stainless steel, finite-element method, serrated-chip formation, machinability

Nizka toplotna prevodnost, visoka trdnost, velika duktilnost in sposobnost močnega utrjevanja so glavni vzroki za to, da se austenitno nerjavno jeklo težko mehansko obdeluje. V študiji so avtorji modelirali tvorbo nazobčanega ostružka med pravokotnim rezanjem AISI316H nerjavnega jekla. Za modeliranje so uporabili metodo končnih elementov (MKE). Preizkusi struženja so bili izvedeni pri treh različnih rezalnih hitrostih ter pri konstantni globini reza in pomikanja. Rezultate modeliranja so primerjali s praktičnimi preizkusi pravokotnega rezanja (struženja). Ugotovili so, da se praktični rezultati preizkusov dobro ujemajo z rezultati MKE-modeliranja.

Ključne besede: AISI 304 nerjavno jeklo, metoda končnih elementov, tvorba nazobčanih ostružkov, sposobnost strojnega obdelovanja

1 INTRODUCTION

Austenitic stainless steels, characterised by a high work-hardening rate and low thermal conductivity [1], are used to fabricate chemical and food-processing equipment, as well as machinery parts requiring high corrosion resistance.[2] They are generally regarded as more difficult to machine than carbon and low-alloy steels on account of their high strength, high work-hardening tendency and poor thermal conductivity.[3,4] Problems such as poor surface finish and high tool wear are common.[5] Work hardening is recognised to be responsible for the poor machinability of austenitic stainless steels.[6] In addition, they bond very strongly to the cutting tool during cutting and when a chip is broken away, it may bring with it a fragment of the tool, particularly when cutting with cemented carbide tools. When machining this material, cutting-force variation is also much more obvious than in the case of machining unalloyed steel.[1]

Especially, in order to increase the productivity and tool life in the machining of the AISI304 and AISI316 series stainless steel, it is necessary to develop a reliable FE model for different cutting processes. To accurately analyse this process using numerical methods such as the finite-element analysis (FEA), the knowledge of the material constitutive behaviour under these severe loading conditions is a pre-requisite and hence correct work-material flow-stress data need to be used. In fact, the success and reliability of numerical models are heavily dependent upon the work-material-flow stress, friction parameters for the tool and work-material interfaces, the fracture criterion and thermal parameters.[3,7–10]

Many studies on the chip formation have been published by now. Titanium alloys are used in most of these studies. M. Bäker[11] studied the influence of the material law determining the plastic flow on the chip formation of titanium alloys at high cutting speeds, while T. Özel et al.[12] studied constitutive-material models to simulate the serrated-chip formation, including also other materials. In parallel with these investigations, M. Sima and T. Özel[13] investigated the influence of constitutive-material models and elastic/viscoplastic finite-element formulation on a serrated-chip formation for modelling the machining of the Ti–6Al–4V titanium alloy. R. Alvarez et al.[14] analysed the effect of eight constitutive models on the saw-toothed chip formation in Ti6Al4V orthogonal cutting. In another study carried out by G. Chen et al.[15], a Johnson-Cook material model with an energy-based ductile-failure criterion was developed using a titanium-alloy (Ti–6Al–4V) high-speed machining FEA. D. Umbrello[16] presented a finite-element analysis (FEA) of machining TiAl6V4 for both conventional and high-speed cutting regimes. Work to date has shown that little work has been carried on the determination of

the chip formation when machining AISI304 stainless steels. In a study carried out by J. Q. Xie et al.[17], the theory of shear banding was included in the analysis of chip formation and chip instability. They used analytic and experimental methods to study these characteristics. This work aims to investigate the serrated-chip formation in the machining of the AISI304 stainless steel using finite-element simulations.

2 EXPERIMENTAL PART

2.1 Turning process

Turning processes were performed on a CNC turning lathe that has a capacity of 10kW using AISI 1045 samples with dimensions of Ø50 mm × 100 mm. The rake angle was 0° and the clearance angle was 5°. The turning processes were carried out using the turning parameters from **Table 1**. The cutting length for the turning processes was chosen to be 10 mm.

Table 1: Turning parameters

Parameters	Value
Cutting speed – V_c (m/min)	100
Feed rate – f (min^{-1})	0.1
Depth of cut – ap (mm)	0.5

2.2 Numeric analysis

In 2D numeric simulations, the cutting tool and the workpiece consist of a tetrahedral mesh. While the mesh structure of the workpiece consists of 1453 elements and 1547 nodes, the mesh structure of the cutting tool consists of 770 elements and 823 nodes. The mesh structure of the model of the workpiece and cutting tool

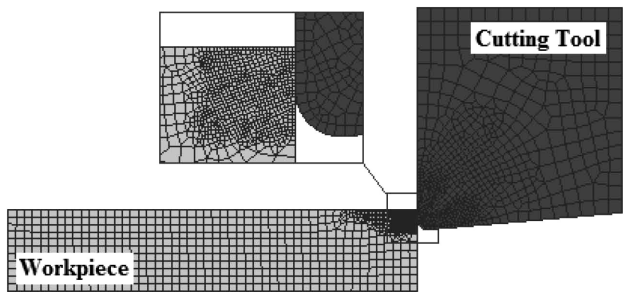

Figure 1: Mesh process

is given in **Figure 1**. However, the workpiece model was constrained by the lateral surfaces and lower surface. The contact algorithm for the interface of the cutting tool and workpiece was defined as the master and slave in the software. As the friction model for these two elements, the Coulomb model of friction was selected because it uses low cutting speeds. The Cockcroft-Latham fracture criterion was selected as the damage criterion. The Cockcroft-Latham criterion is given in Equation (1). According to the Cockcroft-Latham damage criterion, damage occurs when the accumulated stress state D, over the plastic strain, reaches the critical damage value (Dcr). The Dcr was selected to be 90 for all the cutting simulations because it had the most suitable chip form. The friction coefficient for the simulation study was calculated to be 0.41 for the normal machining and 0.60 for the damage criterion. This coefficient of the friction between the tool and the chip in orthogonal cutting was calculated using Equations (2) and (3).[18] F_c and F_t forces were obtained experimentally; F_s, N_s, F and N forces depend on them and can be calculated from **Figure 2**.

$$D = \int_0^{\bar{\varepsilon}_f} \sigma_1 \, d\bar{\varepsilon} \tag{1}$$

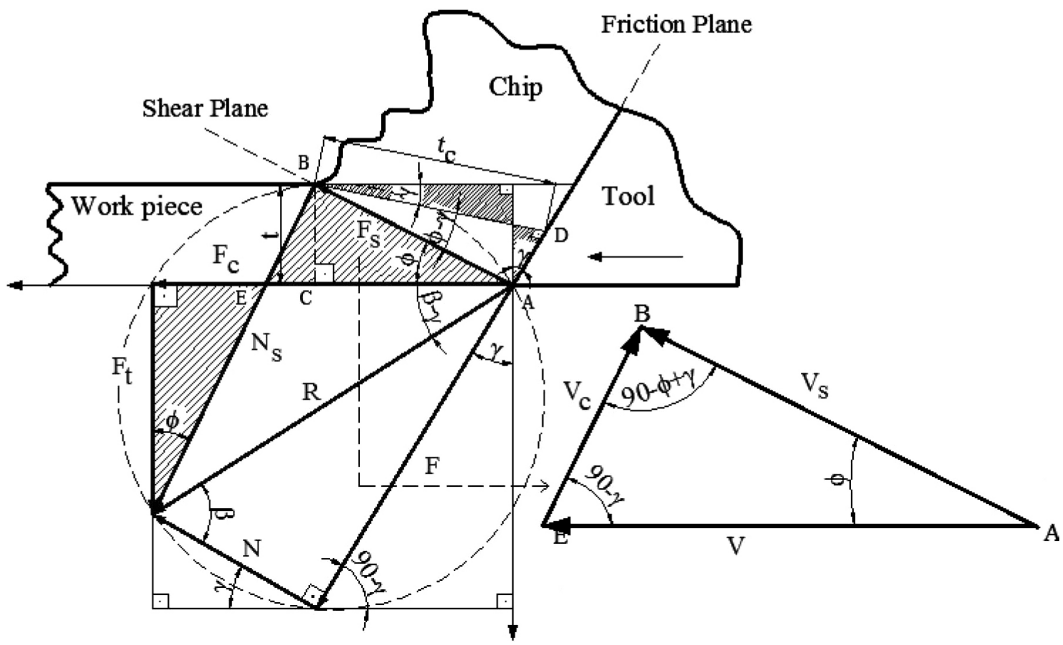

Figure 2: Two-dimensional (2D) force system in turning operations (Merchant's force circle)

$$\mu = \tan\beta = \frac{F}{N} \tag{2}$$

$$\mu = \frac{F_t + F_c \tan\gamma}{F_c - F_t \tan\gamma} \tag{3}$$

2.3 Material model

While the workpiece was selected as AISI 316h, the cutting tool was selected to be tungsten carbide (WC). The mechanical and thermal properties of the WC and AISI 316h are given in **Table 2**.[19] The flow-stress curve of the workpiece-material model was taken from reference[19]. The flow stress was defined as a function of the strain, strain rate and temperature as seen in **Figure 3**. The flow stress ($\overline{\sigma}$) in Equation (4) was selected to exhibit the true material behavior as a function of the effective plastic strain ($\overline{\varepsilon}$), effective strain rate ($\dot{\overline{\varepsilon}}$) and temperature ($T$). The flow-stress curves are very important for high-temperature applications such as metal cutting.

$$\overline{\sigma} = (\overline{\varepsilon}, \dot{\overline{\varepsilon}}, T) \tag{4}$$

Table 2: Mechanical and thermal properties of the drill bit and bone materials[19]

Workpiece-material properties (AISI 316h316H)	
Modulus of elasticity (GPa)	20 °C (210)
Poisson's ratio	0.3
Thermal-expansion coefficient (10^{-6} °C^{-1})	93.33 °C (1.20×10^{-5})
Thermal conductivity(W/mK)	100 °C (17)
Heat capacity (N/mm^2 °C)	93.33 °C (2.78)
Emissivity	0.7
Cutting-tool-material properties (WC)	
Modulus of elasticity (GPa)	650
Poisson's ratio	0.25
Thermal-expansion coefficient (10^{-6} °C^{-1})	5
Thermal conductivity(W/mK)	59
Heat capacity (N/s /mm/°C)	15
Emissivity	0

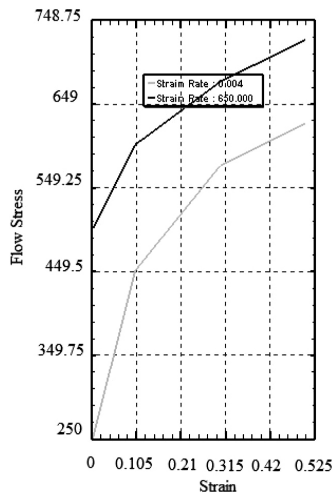

Figure 3: Flow-stress curves for the workpiece material[19]

3 RESULTS

At the end of the study, force variations occurred in the normal machining (NM) and the machining with damage criterion (MWDC) was very different, as seen in **Figure 4**. As seen in **Table 3**, while the MWDC deformed-chip thickness was lower than during the NM, the chip ratio and shear-angle values were higher during the MWDC than during the NM. Good agreement between experimental tests and FEM simulations was found for cutting forces and shear-angle values, as shown in **Figures 5** and **6**.

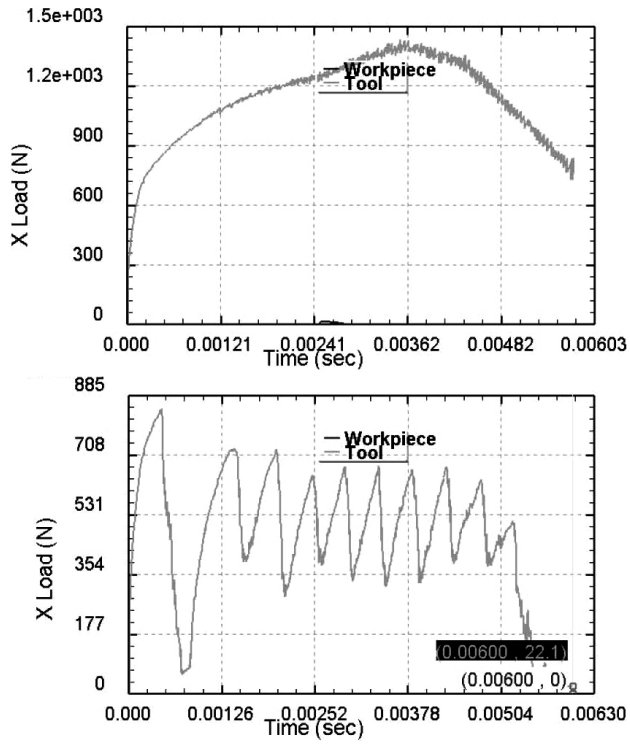

Figure 4: Force variations occurred during NM and MWDC

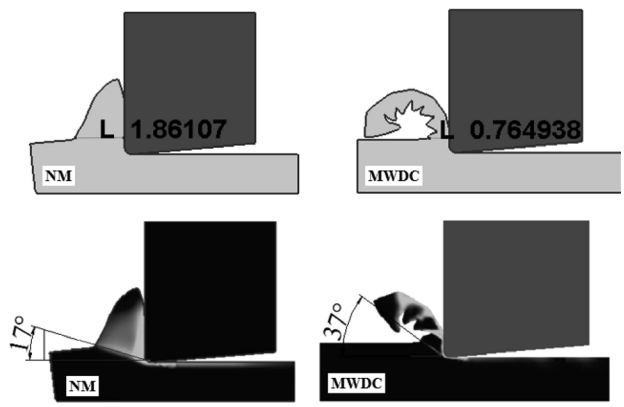

Figure 5: Deformed-chip thickness and shear angles for the NM and MWDC

Table 3: Comparison of NM and MWDC

	Cutting speed (m/min)	Undeformed chip thickness, t (mm)	Deformed chip thickness, t_c (mm)	Chip ratio, r_c	Shear angle, ϕ (with Eg. 17)	Shear angle, ϕ (FEM)
NM	100	0.5	1.85	0.268	15	17
MWDC	100	0.5	0.76	0.657	33.304	37

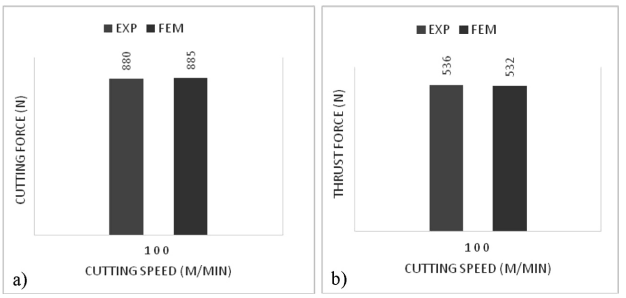

Figure 6: a) Cutting and b) thrust force for MWDC

4 CONCLUSIONS

In this study, a finite-element model was developed to see the effect of a serrated-chip formation in the machining of the AISI304 stainless steel using finite-element simulations. A computer-aided numerical simulation of the turning process was also performed using DEFORM – 2D software. It can be said that the 2D FEM model gives reasonable results compared to the experimental results in view of cutting forces, thrust force and shear angles. This proves the accuracy of the developed 2D FEM model, which can be used for this type of turning simulations.

5 REFERENCES

[1] S. Coromant, Modern metal cutting: a practical handbook, Sandvik Coromant Press, 1st ed., 1994

[2] M. P. Groover, Fundamentals of Modern Manufacturing: Materials, Processes, and Systems, Prentice Hall, Wiley, 1996

[3] E. M. Trent, Metal Cutting, Elsevier Science, Butterworth-Heinemann, 2016

[4] J. Paro, H. Hänninen, V. Kauppinen, Tool wear and machinability of X5 CrMnN 18 18 stainless steels, Journal of Materials Processing Technology, 119 (**2001**), 14–20, doi:10.1016/S0924-0136(01)00877-9

[5] D. O'Sullivan, M. Cotterell, Machinability of austenitic stainless steel SS303, Journal of Materials Processing Technology, 124 (**2002**), 153–159, doi: 10.1016/S0924-0136(02)00197-8

[6] L. Jiang, Å. Roos, P. Liu, The influence of austenite grain size and its distribution on chip deformation and tool life during machining of AISI 304L, Metallurgical and Materials Transactions A, 28 (**1997**), 2415–2422, doi: 10.1007/s11661-997-0198-z

[7] T. H. C. Childs, Material Property Needs in Modeling Metal Machining, Machining Science and Technology, 2 (**1998**), 303–316, doi:10.1080/10940349808945673

[8] M. C. Shaw, Metal Cutting Principles, Oxford University Press, 2005

[9] K. Maekawa, T. Obikawa, Y. Yamane, T. H. C. Childs, Metal Machining: Theory and Applications, Elsevier Science, 2013

[10] V. P. Astakhov, Metal Cutting Mechanics, Taylor & Francis, 1998

[11] M. Bäker, The influence of plastic properties on chip formation, Computational Materials Science, 28 (**2003**), 556–562, doi:10.1016/j.commatsci.2003.08.013

[12] T. Ozel, M. Sima, A. Srivastava, Finite element simulation of high speed machining Ti-6Al-4V alloy using modified material models, Transactions of the NAMRI/SME, 38 (**2010**), 49–56,

[13] M. Sima, T. Özel, Modified material constitutive models for serrated chip formation simulations and experimental validation in machining of titanium alloy Ti–6Al–4V, International Journal of Machine Tools and Manufacture, 50 (**2010**), 943–960, doi:10.1016/j.ijmachtools.2010.08.004

[14] R. Alvarez, R. Domingo, M. A. Sebastian, The formation of saw toothed chip in a titanium alloy: influence of constitutive models, Journal of Mechanical Engineering, 57 (**2011**), 739–749, doi:10.5545/sv-jme.2011.106

[15] G. Chen, C. Ren, X. Yang, X. Jin, T. Guo, Finite element simulation of high-speed machining of titanium alloy (Ti–6Al–4V) based on ductile failure model, The International Journal of Advanced Manufacturing Technology, 56 (**2011**), 1027–1038, doi:10.1007/s00170-011-3233-6

[16] D. Umbrello, Finite element simulation of conventional and high speed machining of Ti6Al4V alloy, Journal of Materials Processing Technology, 196 (**2008**), 79–87, doi:10.1016/j.jmatprotec.2007.05.007

[17] J. Q. Xie, A. E. Bayoumi, H. M. Zbib, Analytical and experimental study of shear localization in chip formation in orthogonal machining, Journal of Materials Engineering and Performance, 4 (**1995**), 32–39, doi: 10.1007/bf02682702

[18] P. J. Arrazola, T. Özel, Investigations on the effects of friction modeling in finite element simulation of machining, International Journal of Mechanical Sciences, 52 (**2010**), 31–42, doi:10.1016/j.ijmecsci.2009.10.001

[19] DEFORM-3D Material Library, http://home.zcu.cz/~sbenesov/Deform2Dlabs.pdf, 12.04.2017

UDK 621.927:621.9.07:621.926.5
Original scientific article/Izvirni znanstveni članek

ISSN 1580-2949
MTAEC9, 51(6)957(2017)

EFFECTS OF CUTTING PARAMETERS AND TOOL-PATH STRATEGIES ON TOOL ACCELERATION IN BALL-END MILLING

UČINKI REZALNIH PARAMETROV IN STRATEGIJA ZA POSPEŠEK ORODJA PRI MEHANSKI OBDELAVI S KROGLIČNIM FREZALOM

Arif Gök[1], Kadir Gök[2], Mehmet Burak Bilgin[1], Mehmet Ali Alkan[3]

[1]Amasya University, Faculty of Technology, Department of Mechnical Engineering, 05100 Amasya, Turkey
[2]Celal Bayar University, Favulty of Technology, Department of Mechanical and Manufacturing Engineering, 45100 Manisa, Turkey
[3]Muğla Sitki Kocman University, Ula Vocational High School, Department of Energy, 48000 Muğla, Turkey
arif.gok@amasya.edu.tr

Prejem rokopisa – received: 2017-04-08; sprejem za objavo – accepted for publication: 2017-06-22

doi:10.17222/mit.2017.039

The determination of the cutting-parameter values that cause increases in vibration values is important to minimize the errors that can occur. Thus, the first aim of this study was to investigate the optimum cutting-parameter values and tool-path strategies in ball-end milling of the EN X40CrMoV5-1 tool steel with three coated cutters using the Taguchi method. The parameters taken into consideration are the cutting speed, feed rate, step over and tool-path strategies. The second aim of the study, a model for the tool acceleration as a function of the cutting parameters, was obtained using the response-surface methodology (RSM). As a result, the most effective parameter within the selected cutting parameters and cutting strategies for both inclined surfaces and different coatings was the step over. In terms of tool coatings, the most deteriorating coating for the tool acceleration on both inclined surfaces was the TiC coating. In addition, the response-surface methodology is employed to predict the tool-vibration values depending on the cutting parameters and tool-path strategy. The model generated gives highly accurate results.

Keywords: inclined surfaces, ball-end milling, tool acceleration, Taguchi method, response-surface methodology, response optimization

Neoptimalni rezalni parametri med mehansko obdelavo lahko povzročijo neželene vibracije in posledično napake. Prvi cilj avtorjev te študije je bil določiti optimalne vrednosti rezalnih parametrov in strategije potovanja orodja med mehansko obdelavo orodnega jekla EN X40CrMoV5-1 s krogličnim frezalom s tremi rezili z različno prevleko (TiC, TiN in TiAlN). Za to so uporabili Taguchi-jevo metodo. Parametri, ki so jih avtorji zajeli v študiji so bili: hitrost rezanja, velikost odvzema, korak odvzema (preskok) in strategija poti orodja. Drugi cilj avtorjev te študije je bil izdelati model pospeševanja orodja v odvisnosti od rezalnih parametrov, z uporabo metodologije odziva površine (angl. RSM). Ugotovili so, da je korak odvzema (angl.: step over) najučinkovitejši parameter med izbranimi rezalnimi parametri in rezalnimi strategijami, tako za oba izbrana nagiba (ukrivljenosti) površine, kot tudi izbrane trde prevleke. Med izbranimi trdimi prevlekami se je v vseh pogojih frezanja kot najslabša izkazala TiC prevleka. RSM metodologija dodatno omogoča napoved vibracij orodja v odvisnosti od rezalnih parametrov in izbrane strategije poti orodja. Izdelani model daje zelo točne rezultate.

Ključne besede: nagib (ukrivljenost) površine, mehanska obdelava s krogličnim frezalom, pospešek orodja, Taguchi metoda, metodologija odgovora površine, optimizacija odgovora

1 INTRODUCTION

Nowadays, machining is one of the most important methods for manufacturing technologies and it remains up-to-date.[1] In the machining of inclined surfaces, tight machining tolerances are generally requested for the processes of finishing and semi-finishing, which are accomplished using indexable insert ball-end mills.[2,3] The forces that occur at high cutting speeds, especially during hard machining, and at high rates of metal removing, cause excessive, irregular vibrations of cutting tools during the machining. These vibrations cause the cutting tools to break, disrupting the process stability and the quality. Therefore, generating the optimum cutting parameters is crucial to obtain high productivity in the manufacturing process of complex geometries and to reach the desired tolerance values.[4,5] The studies carried out in the field commonly focus on:

1) the effect of cutting parameters and cutting strategies of plain-surface milling,
2) analytical tool-acceleration calculations and measurements for end-milling and turning operations.

W. H. Yang and Y. S. Tarng[6] worked on the optimization of the cutting parameters for turning operations so that both optimum cutting parameters were demonstrated and the basic cutting parameters affecting the cutting performance in turning were defined.

M. Kurt et al.[7] worked on the optimization of the cutting parameters for the finish surface and the accuracy of the hole diameter during dry drilling. In this way, optimum cutting conditions were obtained with the process optimization.

C. Gologlu and N. Sakarya[8] investigated the effects of tool-path strategies on the surface roughness for pocket-milling operations using cutting parameters with

different values. It was found that the most influential parameter for one-way and spiral tool-path strategies was the feed rate, and the depth of cut was the most important parameter for back-and-forth tool-path strategies. S. Neseli et al.[9] worked on the optimization of the tool-geometry parameters for turning operations based on the response-surface methodology. In parallel to this study, Asilturk and Neseli[10] worked on the multi-response optimization of CNC turning parameters via a Taguchi-method-based response-surface analysis. M. M. De Aguiar et al.[11] investigated the correlating surface roughness, tool wear and tool vibration in the milling process of hardened steel using long slender tools. In this study, a good workpiece-surface roughness together with a long tool life of long tools with small diameters was achieved. H. Wang et al.[12] worked on an investigation of the influence of the tool-tip vibration on the surface roughness and its representative measurement in ultra-precision diamond turning. This paper is dedicated to a study of the influence of the tool-tip vibration on the surface roughness. A. O. Abouelatta and J. Madl[13] worked on the surface-roughness prediction based on the cutting parameters and tool vibrations in turning operations. S. Orhan et al.[14] worked on the relationship between the vibration and the tool wear during end milling.

The studies given above were concentrated on the determination of the most appropriate parameters for the machining processes involving flat and inclined surfaces. However, the studies confirm that an aggregated effect of the cutting parameters and tool-path styles on the tool acceleration in inclined geometries (convex and concave) were not widely investigated. This study examines the effects of the cutting parameters and tool-path styles on the tool acceleration in the machining of convex and concave surfaces using ball-end mills. By doing so, it aims to keep the tool-acceleration values at a minimum, and to control the unwanted machining results such as poor surface quality and machining errors.

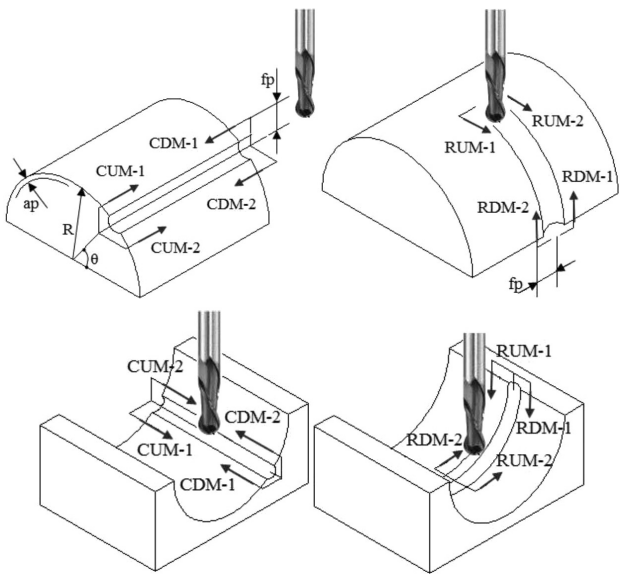

Figure 1: Inclined surfaces and related cutter path styles: CUM-1 (upward step over), CDM-1 (upward step over), CUM-2 (downward step over), CDM-2 (downward step over), RUM-1 (left step over), RDM-1 (left step over), RUM-2 (right step over), RDM-2 (right step over)

1.1 Tool-path strategies and cutting parameters

In the experimental studies, contouring and ramping tool-path styles are used to produce inclined surfaces. These tool-path styles can be established based on up-milling and down-milling strategies by making the movements of ramping and contouring. Ramping and contouring are inevitable choices of the tool-path styles for the implementation of the up-milling and down-milling strategies.[5] In the ramping tool-path styles, the cutter scans an inclined surface following the lines in parallel to the surface radius. On the other hand, in the contouring tool-path styles, the cutter scans an inclined surface following the lines perpendicular to the surface radius.[15–17] In this study, the step-over values are kept constant in both tool-path styles. After each step of the machining, the cutter moves one step sideways to the position, in which it returns back to the staring level of that step and then makes the next step.[15] In the study under these conditions, four tool-path styles were generated: contouring up milling (CUM), contouring down milling (CDM), ramping up milling (RUM) and ramping down milling (RDM). The form radius of workpiece, milling position angle, nominal depth of cut, step over and spindle speed are indicated by R, θ, a_p, f_p, and S, respectively (**Figure 1**).

In addition to the cutter path styles defined, three different variable parameters were used for semi-finishing operations. These were the cutting velocity (V_c), feed rate (V_f) and cutting step over (f_p). The cutting-velocity and feed-rate values were taken from the reference catalogues of the tool manufacturer (Sandvik Company). In order to determine the right cutting-tool values (**Table 1**), a number of experiments for each tool coating was conducted based on the reference values.[5] The cutting-

Table 1: Assignment of the levels to factors

Factors		Level 1	Level 2	Level 3	Level 4
Cutting velocity, V_c (m/min) – A	TiC	70	80	90	100
	TiN	100	110	120	130
	TiAlN	110	120	130	140
Feed rate, V_f (mm/rev) – B	TiC	223	255	286	318
	TiN	318	350	382	414
	TiAlN	350	382	414	445
Step over, f_p (mm) – C		0.8	1	1.5	2
Cutting path styles – D		Contouring up milling (CUM)	Contouring down milling (CDM)	Ramping up milling (RUM)	Ramping down milling (RDM)

tool step-over values directly affect the tracks on the surface made by the cutter, the load on the cutter and processing time.[8] The step-over value was chosen to be 5 % of the tool diameter and this value was set as the lower level of *fp*. The depth of cut was taken as 0.3 mm and fixed as a constant. An orthogonal array of *L*'16 was chosen for the experimental design and four different levels were defined for each cutting parameter (**Table 1**).

2 EXPERIMENTAL PART

The EN X40CrMoV5-1 hot-work tool steel was selected for the study. The material is commonly used in tool-making processes due to the quality characteristics including high durability, high thermal conductivity, high machinability and high cracking resistance.[5] First, experimental samples of (40 × 30) mm islands on a (220 × 135 × 50) mm block were machined. In the experiments, an indexable cutter body of an Ø16 mm cylindrical shank (CoroMill, R216-16A20-045) with a two-fluted 30°-helix-angle end mill was used. The ball-end inserts of TiC, TiN and TiAlN coated with 3-µm R216-16 03 M-M H13A were used. Semi-finishing operations were employed and no coolant was used in the machining. The experiments were carried out on a vertical machining center of a John Ford VMC 550, with 12000 min^{-1} and a 12-kW engine. The experimental set-up is shown in **Figure 2**. The acceleration of the vibration signals generated during the cutting was measured using a piezoelectric accelerometer (VibroTest 60) based on the ISO 2954 standard. The accelerometer was mounted on the workpiece via a magnetization feature.

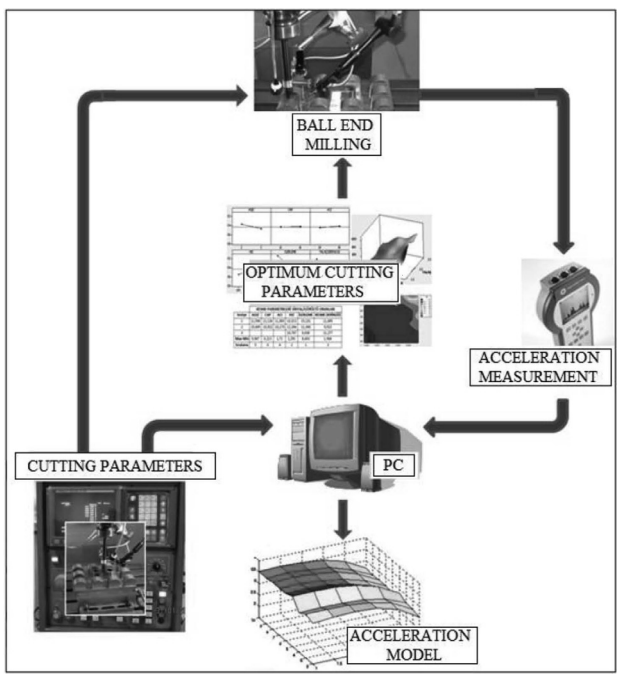

Figure 2: Experimental set-up

2.1 Tool acceleration

Tool acceleration occurs in machining operations due to the interaction between the tool and workpiece structure. Each tooth pass leaves a modulated surface on the workpiece due to the vibrations of the tool and workpiece, causing a variation in the expected chip thickness. Under certain cutting conditions (i.e., feed rate, depth of cut and cutting velocity), significant chip-thickness variations, and hence force and displacement variations, occur and a vibration is present.[18] Vibrations result in a poor surface finish, excessive tool wear, reduced dimensional accuracy and tool damage. For a milling process, conservative cutting conditions are usually selected to avoid vibrations that decrease productivity.[19]

The values of the tool acceleration were experimentally measured during the machining of inclined surfaces (**Table 2**).

Table 2: Measured values of tool acceleration

	Convex inclined surface			Concave inclined surface		
Exp. No.	(m/s^2 peak) (TiC)	(m/s^2 peak) (TiN)	(m/s^2 peak) (TiAlN)	(m/s^2 peak) (TiC)	(m/s^2 peak) (TiN)	(m/s^2 peak) (TiAlN)
1	0.125	0.117	0.103	0.287	0.254	0.241
2	0.197	0.189	0.214	0.428	0.277	0.358
3	0.205	0.216	0.235	0.501	0.411	0.383
4	0.292	0.239	0.286	0.637	0.471	0.465
5	0.137	0.154	0.149	0.356	0.346	0.326
6	0.145	0.167	0.195	0.311	0.265	0.275
7	0.261	0.217	0.277	0.556	0.456	0.411
8	0.253	0.206	0.218	0.477	0.461	0.437
9	0.210	0.196	0.174	0.389	0.379	0.325
10	0.249	0.247	0.219	0.461	0.381	0.375
11	0.174	0.162	0.189	0.292	0.260	0.317
12	0.181	0.187	0.228	0.481	0.398	0.263
13	0.191	0.175	0.182	0.447	0.417	0.445
14	0.131	0.186	0.197	0.345	0.357	0.281
15	0.138	0.135	0.130	0.308	0.293	0.279
16	0.129	0.127	0.128	0.297	0.259	0.254

The orthogonal array chosen was *L*16 (4^4), with 16 rows corresponding to the number of experiments (4 factors with 4 levels each). To obtain the optimum cutting performance, the smaller-the-better quality characteristic for the tool acceleration was adopted. The *S/N* ratio was defined as follows in Equation (1):

$$\frac{S}{N} = -10\lg\frac{1}{N}\sum_{i=1}^{n} Y_i^2 \qquad (1)$$

where Y_i is the observed data at the *i*th experiment and *n* is the number of experiments.

2.2 Response-surface methodology

The response surface methodology (RSM) is a well-known up-to-date approach to the optimization of input-parameter models based on either physical or simulation experiments and experimental observations.

These approximated models need to be assessed statistically for their adequacy, and then they can be utilized for an optimization of the initial model.[10] Response-surface-methodology problems follow a functional relation between responses and independent variables, and this relation can be explained using the second-order polynomial model in Equation (2):[20]

$$\eta = \beta_0 + \sum_{i=1}^{k} \beta_i X_1 + \sum_{i=1}^{k} \beta_{ii} X_i^2 + \sum_i \sum_j \beta_{ii} X_i X_j + \varepsilon \quad (2)$$

where η is the estimated response (the tool acceleration); β_0 is the constant; βi, βii and βij represent the coefficients of linear, quadratic and cross-product terms, respectively. X reveals the coded variables.

3 RESULTS

The *S/N* ratios of the four factors from Equation (1) were calculated for each of the tool coatings, and convex and concave inclined surface types (**Figures 3** to **8**). The largest *S/N* ratios always yield the optimum quality with the minimum variance.[5] Therefore, the level with the largest value determines the optimum level of each factor. From **Figures 3** and **4**, relating to the milling of the TiC-coated convex and concave inclined surfaces, the optimum levels in terms of the tool acceleration can be observed at A4 for V_c (100 m/min), B1 for V_f (223 min^{-1}) and C1 for f_p (0.8 mm). For the tool-path styles, the optimum levels can be observed at D4 (UMC) for the convex inclined surface and D1 (DMR) for the concave inclined surface. From **Figures 5** and **6**, relating to the milling of the TiN-coated convex and concave inclined surfaces, the optimum levels in terms of the tool acceleration can be observed at A4 for V_c (130 m/min), B1 for V_f (318 min^{-1}), C1 for f_p (0.8 mm) and D1 (DMR) for the

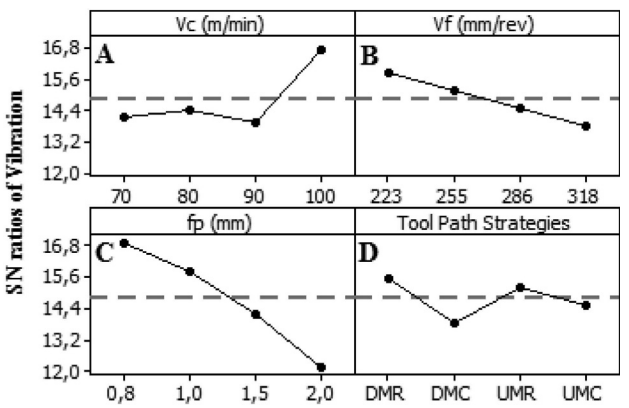

Figure 3: *S/N* ratios for milling a TiC-coated convex inclined surface

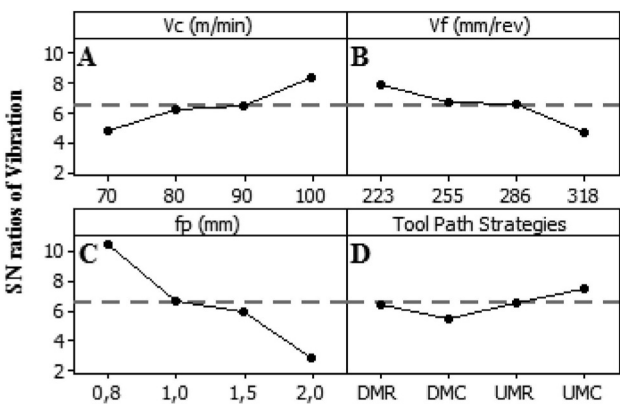

Figure 4: *S/N* ratios for milling a TiC-coated concave inclined surface

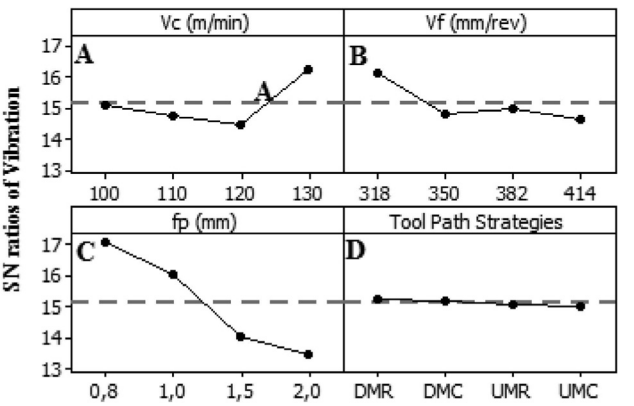

Figure 5: *S/N* ratios for milling a TiN-coated convex inclined surface

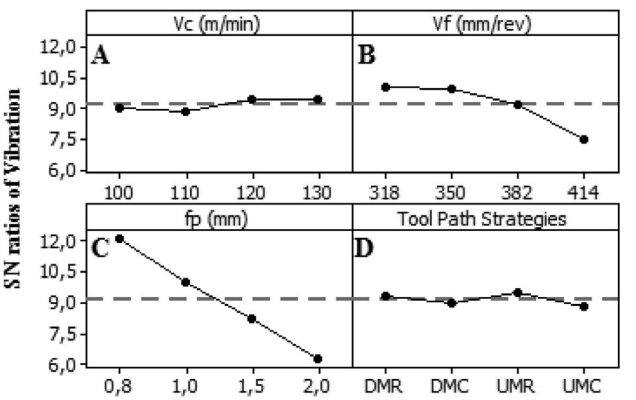

Figure 6: *S/N* ratios for milling a TiN-coated concave inclined surface

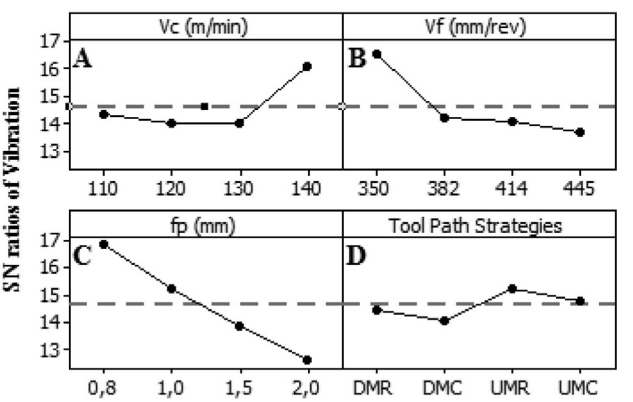

Figure 7: *S/N* ratios for milling convex inclined surfaces with a TiAlN-coated cutter

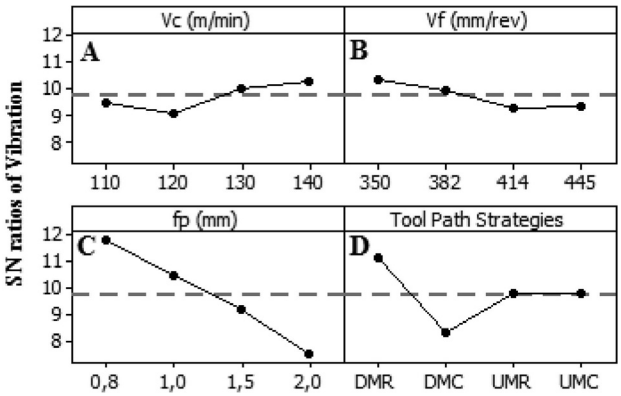

Figure 8: *S/N* ratios for milling a TiAlN-coated concave inclined surface

tool-path style. Likewise, from **Figures 7** and **8**, relating to the milling of the TiAlN-coated convex and concave inclined surfaces, the optimum levels in terms of the tool acceleration can be observed at A4 for V_c (140 m/min), B1 for V_f (358 mm/rev), C1 for f_p (0.8 mm) and D1 (DMR) for the tool-path style.

In the machining of inclined surfaces, as seen in **Figures 3** to **8**, the tool-acceleration values decreased slightly with an increase of V_c, in line with the data from references[4,18,21]. The literature emphasizes that a slight increase in V_c is caused by the following reasons: deformations of the main cutting edge of the cutting tool increase with a decrease in V_c, and this causes an increase in the contact length between the cutting tool and

Table 3: ANOVA of the tool acceleration for inclined surface types

Source of variance	DOF, v	SS	Variance, V	F ratio (α=5 %)	p	PCR (%)
Convex inclined surface (TiC)						
Cutting velocity, V_c (m/min)	3	0.0050203	0.0016734	5.92	0.049	11.70
Feed rate, V_f (m/rev)	3	0.0092032	0.0030677	10.85	0.041	21.50
Step over, f_p (mm)	3	0.0255268	0.0085089	30.09	0.010	59.60
Tool-path style	3	0.0022432	0.0007477	2.64	0.223	5.20
Error, e	3	0.0008483	0.0002828			2.00
Total	15	0.0428417				100.00
Concave inclined surface (TiC)						
Cutting velocity, V_c (m/min)	3	26.015	8.672	1.84	0.050	13.63
Feed rate, V_f (m/rev)	3	21.613	7.204	1.53	0.048	11.32
Step over, f_p (mm)	3	120.608	40.203	8.52	0.036	63.19
Tool-path style	3	8.455	2.818	0.6	0.659	4.43
Error, e	3	14.148	4.716			7.41
Total	15	190.839				100.00
Convex inclined surface (TiN)						
Cutting velocity, V_c (m/min)	3	0.002192	0.0007307	3.54	0.490	10.99
Feed rate, V_f (m/rev)	3	0.002838	0.0009461	4.58	0.042	14.23
Step over, f_p (mm)	3	0.014166	0.0047221	22.88	0.014	71.03
Tool-path style	3	0.000126	0.0000419	0.2	0.888	0.63
Error, e	3	0.000619	0.0002064			3.1
Total	15	0.019941				100.00
Concave inclined surface (TiN)						
Cutting velocity, V_c (m/min)	3	0.006494	0.002165	0.44	0.048	3.22
Feed rate, Vf (m/rev)	3	0.04115	0.013717	2.81	0.040	20.42
Step over, f_p (mm)	3	0.133717	0.044572	9.14	0.021	66.37
Tool-path style	3	0.005465	0.001822	0.37	0.780	2.71
Error, e	3	0.014633	0.004878			7.26
Total	15	0.20146				100.00
Convex inclined surface (TiAlN)						
Cutting velocity, V_c (m/min)	3	0.005747	0.001916	1.42	0.050	15.07
Feed rate, V_f (m/rev)	3	0.009267	0.003089	2.29	0.045	24.3
Step over, f_p (mm)	3	0.017734	0.005911	4.37	0.028	46.51
Tool-path style	3	0.00132	0.00044	0.33	0.809	3.46
Error, e	3	0.004055	0.001352			10.63
Total	15	0.038123				100.00
Concave inclined surface (TiAlN)						
Cutting velocity, V_c (m/min)	3	0.005838	0.001946	5.53	0.047	6.37
Feed rate, V_f (m/rev)	3	0.020738	0.006913	19.63	0.018	22.63
Step over, f_p (mm)	3	0.059669	0.01989	56.49	0.004	65.12
Tool-path style	3	0.004318	0.001439	4.09	0.139	4.71
Error, e	3	0.001056	0.000352			1.15
Total	15	0.091619				100.00

the workpiece. The longer contact length between the cutting tool and the workpiece increases the friction force on the cutting-tool rake face and this leads to an increase in the tool acceleration depending on the cutting forces.[4,21] The chip cross-sectional area generated by f_p and V_f is the most influential factor in determining the tool acceleration. As the f_p and V_f values increase, the tool acceleration increases as seen in **Figures 3** to **8**.

3.1 Analysis of variance

A statistical analysis of variance (ANOVA) was performed to examine, which cutting parameters were statistically significant for the tool acceleration. The p values of ANOVA for all the cutting parameters and tool-path styles are shown at a significance level of 95 % (**Table 3**). Thus, it can be stated that the differences between the measured values meaningfully result from the differences between the levels.[5]

For the response value of the tool acceleration (**Table 4**) of the TiC-coated cutter, the most significant parameters were f_p (p = 0.010), V_f ($_p$ = 0.041) and V_c (p = 0.049) when machining the convex inclined surfaces. Similarly, in the machining of the concave inclined surfaces, f_p, V_f and V_c were again the significant parameters with the $_p$ values of 0.036, 0.048 and 0.05, respectively. For the cutting-force values of the TiN-coated cutter, f_p (p = 0.014), V_f (p = 0.042) and V_c (p = 0.049) were significant parameters when machining the convex inclined surfaces. Likewise, f_p, V_f and V_c were the most significant control factors with the p values of 0.021, 0.04 and 0.048 when machining the concave inclined surfaces. Lastly, for the cutting-force values of the TiAlN-coated cutter, f_p (p = 0.028), V_f (p = 0.045) and V_c (p = 0.05) were the most significant control factors when machining the convex inclined surfaces. Similarly, when machining the concave inclined surfaces with the TiAlN-coated cutter, f_p, V_f and V_c were the most significant control factors with the p values of 0.004, 0.018 and 0.047, respectively. According to the response values of the tool acceleration (**Table 3**), when machining both convex and concave inclined surfaces with the TiC-, TiN- and TiAlN-coated cutters, the most significant control factors were f_p, V_f and V_c. It is worth mentioning that f_p was superior to V_f in all the cases.

3.2 Determination of the optimum machining parameters and confirmation experiments

The optimum parameters in machining convex inclined surfaces were *A*4*B*1*C*1*D*1 for the TiC-coated cutter; *A*4*B*1*C*1*D*1 for the TiN-coated cutter; and *A*4*B*1*C*1*D*3 for the TiAlN-coated cutter. On the other hand, in terms of the tool acceleration, the optimum parameters in machining concave inclined surfaces were *A*4*B*1*C*1*D*4 for the TiC-coated cutter; *A*4*B*1*C*1*D*1 for the TiN-coated cutter; and *A*4*B*1*C*1*D*1 for the TiAlN-coated cutter. By making a prediction considering the parameters, the results can be calculated in advance using Equations (3) to (4) (**Table 4**):[8]

$$\eta_{\text{cal}} = \overline{\eta}_{\text{m}} + \left(\text{Max}\,\frac{S}{N_1} - \overline{\eta}_{\text{m}}\right) + \left(\text{Max}\,\frac{S}{N_2} - \overline{\eta}_{\text{m}}\right) + \left(\text{Max}\,\frac{S}{N_3} - \overline{\eta}_{\text{m}}\right) + \left(\text{Max}\,\frac{S}{N_4} - \overline{\eta}_{\text{m}}\right) \tag{3}$$

where η_{cal} is the calculated *S/N* ratio under the optimum machining conditions; $\overline{\eta}_{\text{m}}$ is the arithmetic mean of the S/N ration of the studied surface form.

$$Acc_{\text{cal}} = 10^{-\frac{\eta_{\text{cal}}}{20}} \tag{4}$$

Acc_{cal} is the calculated base quantity; η_{cal} is the calculated *S/N* ratio.

Table 4: Calculated values for convex and concave inclined surfaces

Coatings	Convex inclined surface		Concave inclined surface	
	η_{cal}(dB)	Acc_{cal} (m/s^2 peak)	η_{cal}(dB)	Acc_{cal} (m/s^2 peak)
TiC	20.727	0.092	20.915	0.090
TiN	19,337	0.108	13.722	0.206
TiAlN	14.991	0.178	14.379	0.191

Two test trails for each coating type at the optimal-control-factor settings were conducted as confirmation experiments. The tests were carried out with new cutters, one for each coating type in order to prevent undesirable effects caused by worn cutting tools.[5] The results of the experiments are presented in **Table 5**, showing the acceleration values (Acc_{mea}) and *S/N* ratios (η_{mea}).

Table 5: Comparison between confirmatory-test results and calculated values for convex and concave inclined surfaces

	Exp. No.	Acceleration (m/s^2 peak)	Acceleration $_{mea}$ (m/s^2 peak)	Acceleration (η_{mea},dB)	Absolute differences (%)*
Convex inclined surface					
TiC	1	0.086	0.090	20.906	0.2
	2	0.094			
TiN	1	0.091	0.101	19.871	0.7
	2	0.111			
TiAlN	1	0.153	0.172	15.236	0.6
	2	0.191			
Concave inclined surface					
TiC	1	0.101	0.103	19.741	1.3
	2	0.105			
TiN	1	0.202	0.203	13.849	0.3
	2	0.204			
TiAlN	1	0.179	0.188	14.506	0.3
	2	0.197			

* $\frac{Acc_{\text{cal}} - Acc_{\text{mea}}}{Acc_{\text{mea}}} \times 100$

3.3 Confidence interval

Estimating the mean is only a point estimate based on the average of the results obtained from the experiment. It gives a 50 % chance of being greater or lower than the mean.[22] Therefore, confidence interval (CI) should be calculated. A confidence interval includes the maximum and minimum value between which the true average should be at some stated percentage of confidence. Confidence interval is used to verify the quality characteristics of confirmation experiments. The following formula is used to verify the predictions:[23]

$$CI = \sqrt{F_{0.05}(1, \upsilon_e) V_e \left(\frac{1}{n_{\text{eff}}} + \frac{1}{r} \right)} \quad (5)$$

Where $F_{0.05}(1,\upsilon_e)$ is the F ratio at a 95 % confidence[24] against degree of freedom 1 and the error of υ_e; V_e is the error variance; n_{eff} is the effective number of replication and is the number of test trials (r = 2).

$$n_{\text{eff}} = \frac{N}{1 + V_T} \quad (6)$$

where N is the total number of experiments; υ_T is the total main factor of degrees of freedom (V_T = 12). The confidence-interval (CI) values for the convex and concave inclined surfaces obtained using Equations (5) and (6) are provided in **Table 6**.

Table 6: CI values

	Tool acceleration (m/s^2 peak)		
	TiC	TiN	TiAlN
Convex inclined surface	0.047	0.023	0.062
Concave inclined surface	2.027	0.120	0.061

The S/N ratio differences between the estimated values obtained using Equations (2) and (3), and the results obtained with the confirmation experiments are shown in **Table 5**. The differences appear to be the smallest at a confidence-interval value of 5 % given in **Table 6**. Therefore, both inclined surfaces and all the coatings used are confirmed as safe, having the optimal control-factor settings.

3.4 Prediction of the tool acceleration

A tool-acceleration prediction model based on the cutting-parameter values was developed using the response-surface methodology (RSM). The RSM is a methodology that uses a combination of statistical and mathematical techniques for the development and optimization of processes. The RSM optimizes (maximizes, minimizes or makes nominal) the response using a polynomial model of the first order or second order.[5] As a result of the machinability experiments conducted, a first-order model and a quadratic polynomial tool-acceleration model depending on the values of V_c, V_f and f_p were obtained as shown in Equation (7):

$$RMS = k_0 + k_1 \cdot V_C + k_2 \cdot V_f + k_3 \cdot f_p \quad (7)$$

$$RMS = k_0 + k_1 \cdot V_C + k_2 \cdot V_f + k_3 \cdot f_p + k_4 \cdot V_C^2 + k_5 \cdot V_f^2 + k_6 \cdot f_p^2 + k_7 \cdot V_C \cdot V_f + k_8 \cdot V_C \cdot f_p + k_9 \cdot V_f \cdot f_p \quad (8)$$

The values of the polynomial and first-order model regression coefficients and the correlation coefficient for the mathematical model of R_a are given in **Tables 7** and **8**.

Table 7: First-order-model coefficients and correlation coefficients

Coefficient	Multiplier	Regression coefficients					
		Convex inclined surface			Concave inclined surface		
		TiC	TiN	TiAlN	TiC	TiN	TiAlN
k_0	Sabit	0.195	0.183	0.197	0.533	0.376	0.344
k_1	V_c	-0.025	-0.011	-0.020	-0.099	-0.025	-0.022
k_2	V_f	0.023	0.013	0.029	0.095	0.059	0.021
k_3	f_p	0.051	0.037	0.042	0.183	0.116	0.078
%		Correlation coefficients					
		89.19	88.80	86.26	85.77	83.48	83.72

Table 8: Polynomial-regression coefficients and correlation coefficients

Coefficient	Multiplier	Regression coefficients					
		Convex inclined surface			Concave inclined surface		
		TiC	TiN	TiAlN	TiC	TiN	TiAlN
k0	Sabit	0.205	0.206	0.217	0.534	0.322	0.333
k1	V_c	-0.037	-0.015	-0.024	-0.166	-0.005	-0.043
k2	V_f	0.016	0.010	0.030	0.132	0.063	0.017
k3	F_p	0.045	0.030	0.025	0.181	0.060	0.037
k4	$V_c \times V_c$	-0.028	-0.020	-0.022	-0.010	0.012	-0.005
k5	$V_f \times V_f$	0.002	-0.009	-0.018	0.023	0.055	0.000
k6	$f_p \times f_p$	0.057	-0.012	0.000	-0.014	0.015	0.014
k7	$V_c \times V_f$	-0.010	-0.012	-0.029	-0.004	-0.096	-0.070
k8	$V_c \times f_p$	-0.008	-0.004	0.002	0.082	0.000	-0.027
k9	$V_f \times f_p$	-0.017	-0.006	-0.006	-0.125	0.031	0.000
%		Correlation coefficients					
		91.79	94.54	90.57	92.13	97.04	85.29

The correlation coefficients for the convex inclined surface were 91.79, 94.54 and 90.57 % for the TiC, TiN, and TiAlN coatings, respectively. On the other hand, the related coefficients for the concave inclined surface were 92.13, 97.04 and 85.29 % for the coatings of TiC, TiN and TiAlN, respectively. The values indicate that the model generated is successful at predicting the tool-acceleration values for both inclined surfaces.

3.5 Optimization of the response

One of the most important aims of the experiments related to manufacturing is to achieve the desired tool acceleration of the optimal cutting parameters.[9] To this end, the response-surface optimization is the ideal technique for determining the tool acceleration in ball-end milling. Here, the goal is to minimize the tool acceleration. The RSM-optimization result for the acceleration parameter for the convex inclined surface and the TiC

Table 9: Response optimization for tool-acceleration-parameter components

Parameter	Goal	Optimum combination			Lower	Target	Upper	Pre. response	Desirability
		V_c (mm/min)	V_f (m/rev)	f_p (mm)					
Convex surface, TiC									
Acceleration (m/s^2 peak)	Min.	100	223	0.8	0.125	0.125	0,292	0.119	1
Convex surface, TiN									
Acceleration (m/s^2 peak)	Min.	130	318	0.8	0.117	0.117	0.239	0.116	1
Convex surface, TiAlN									
Acceleration (m/s^2 peak)	Min.	140	350	0.8	0.103	0.103	0.286	0.112	1
Concave surface, TiC									
Acceleration (m/s^2 peak)	Min.	100	223	0.8	0.287	0.287	0.637	0.249	1
Concave surface, TiN									
Acceleration (m/s^2 peak)	Min.	130	318	0.8	0.254	0.254	0.471	0.226	1
Concave surface, TiAlN									
Acceleration (m/s^2 peak)	Min.	140	350	0.8	0.241	0.241	0.465	0.222	1

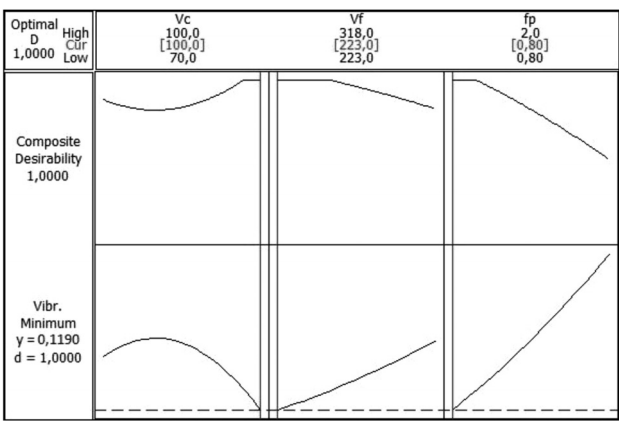

Figure 9: Response-optimization plot for the tool-acceleration-parameter components for the convex surface and TiC coating

coating is shown in **Figure 9**. The optimum cutting parameters obtained for all the surface types and all the coatings are shown in **Table 9**.

4 CONCLUSIONS

The tool acceleration in a ball-end-milling process with cutting parameters and different tool-path strategies was measured, along with the orthogonal array, during the experiments. The results obtained are as follows:

- Both the Taguchi and response-surface statistical analyses indicated that the main effect of the step over is the most significant factor for the tool acceleration.
- According to the confirmation experiments under the optimal conditions, the measured tool-acceleration values for the convex inclined surfaces were found to be smaller than those of the calculated tool-acceleration values. On the other hand, for the concave inclined surfaces, the measured tool-acceleration values were found to be larger than those of the calculated tool-acceleration values. Nevertheless, the absolute difference in the percentile of the measured and calculated values was not more than 3.57 for both inclined surface types.
- The tool-acceleration values obtained for the machining of the convex inclined surfaces were found to be smaller in comparison to the values obtained for the machining of the concave inclined surfaces (**Table 3**). This is because the chip was comfortably removed from the cutting zone of the convex inclined surface. Besides, the cutting tool affects the inner surface and the contacts with the workpiece, resulting in a longer cutting edge during the tool acceleration.
- The tool-acceleration values for the contouring tool-path style were found to be smaller than those for the ramping tool-path style (**Figures 3** to **8**). This is because the contouring tool-path style causes movements parallel to the axis of the inclined surface. Previous studies support the finding that the movements made in parallel to the surface axis are ideal to move the chips away.
- The RSM was found to be effective for the identification and development of the significant relationships between the cutting parameters.
- The highest correlation coefficients were obtained with the tool-acceleration prediction model. The prediction model can be employed in relative studies.
- The optimum combination of the cutting parameters for the response optimization of all surface types includes the values of the largest cutting velocity, the smallest step over and the feed rate.

5 REFERENCES

[1] A. Gok, A new approach to minimization of the surface roughness and cutting force via fuzzy TOPSIS, multi-objective grey design and RSA, Measurement,70 (**2015**), 100–109, doi:10.1016/j.measurement.2015.03.037

[2] A. Gok, C. Gologlu, H. I. Demirci, M. Kurt, Determination of Surface Qualities on Inclined Surface Machining with Acoustic Sound Pressure, *S*trojniški vestnik – Journal of Mechanical Engineering, 58 (**2012**) 10, 587–597, doi:10.5545/sv-jme.2012.352

[3] M. C. Shaw, Metal cutting principles, Oxford Oxford University Press, 2nd Edition ed., 2005

[4] E. M. Trent, Metal Cutting, Elsevier Science, Butterworth-Heinemann, 4th Edition ed., 2016

[5] A. Gok, C. Gologlu, H. I. Demirci, Cutting parameter and tool path style effects on cutting force and tool deflection in machining of convex and concave inclined surfaces, Int J Adv Manuf Technol, 69 (**2013**) 5–8, 1063–1078, doi:10.1007/s00170-013-5075-x

[6] W. H. Yang, Y. S. Tarng, Design optimization of cutting parameters for turning operations based on the Taguchi method, Journal of Materials Processing Technology, 84 (**1998**) 1–3, 122–129, doi:10.1016/S0924-0136(98)00079-X

[7] M. Kurt, E. Bagci, Y. Kaynak, Application of Taguchi methods in the optimization of cutting parameters for surface finish and hole diameter accuracy in dry drilling processes, Int Journal of Adv Manuf Technol. 40 (**2009**) 5–6, 458–469, doi:10.1007/s00170-007-1368-2

[8] C. Gologlu, N. Sakarya, The effects of cutter path strategies on surface roughness of pocket milling of 1.2738 steel based on Taguchi method, Journal of Materials Processing Technology, 206 (**2008**) 1–3, 7–15, doi:10.1016/j.jmatprotec.2007.11.300

[9] S. Neşeli, S. Yaldız, E. Türkeş, Optimization of tool geometry parameters for turning operations based on the response surface methodology, Measurement, 44 (**2011**) 3, 580–587, doi:10.1016/j.measurement.2010.11.018

[10] İ. Asiltürk, S. Neşeli, Multi response optimisation of CNC turning parameters via Taguchi method-based response surface analysis, Measurement, 45 (**2012**) 4, 785-794, doi:10.1016/j.measurement.2011.12.004

[11] M. M. Aguiar, A. E. Diniz, R. Pederiva, Correlating surface roughness, tool wear and tool vibration in the milling process of hardened steel using long slender tools, International Journal of Machine Tools and Manufacture, 68 (**2013**), 1–10, doi:10.1016/j.ijmachtools.2013.01.002

[12] H. Wang, S. To, C. Y. Chan, Investigation on the influence of tool-tip vibration on surface roughness and its representative measurement in ultra-precision diamond turning, International Journal of Machine Tools and Manufacture, 69 (**2013**) 20–29, doi:10.1016/j.ijmachtools.2013.02.006

[13] O. B. Abouelatta, J. Mádl, Surface roughness prediction based on cutting parameters and tool vibrations in turning operations, Journal of Materials Processing Technology, 118 (**2001**) 1–3, 269–277, doi:10.1016/S0924-0136(01)00959-1

[14] S. Orhan, A. O. Er, N. Camuşcu, E. Aslan, Tool wear evaluation by vibration analysis during end milling of AISI D3 cold work tool steel with 35 HRC hardness, NDT & E International, 40 (**2007**) 2, 121–126, doi:10.1016/j.ndteint.2006.09.006

[15] B. W. Ikua, H. Tanaka, F. Obata, S. Sakamoto, Prediction of cutting forces and machining error in ball end milling of curved surfaces -I theoretical analysis, Precision Engineering, 25 (**2001**), 266–273, doi:10.1007/s00170-012-4012-8

[16] B. W. Ikua, H. Tanaka, F. Obata, S. Sakamoto, T. Kishi, T. Ishii, Prediction of cutting forces and machining error in ball end milling of curved surfaces -II experimental verification, Precision Engineering, 26 (**2002**), 69–82, doi:10.1007/s00170-012-4175-3

[17] G. M. Kim, B. H. Kim, C. N. Chu, Estimation of cutter deflection and form error in ball-end milling processes, International Journal of Machine Tools and Manufacture, 43 (**2003**) 9, 917–924, doi:10.1016/S0890-6955(03)00056-7

[18] M. Günay, E. Yücel, Application of Taguchi method for determining optimum surface roughness in turning of high-alloy white cast iron, Measurement, 46 (**2013**) 2, 913–919, doi:10.1016/j.measurement.2012.10.013

[19] R. Landers, A. Ulsoy, Chatter analysis of machining systems with nonlinear force processes, ASME International mechanical engineering congress and exposition, 76 (**1996**), 183–190, doi:10.1016/S0924-0136(01)00877-9

[20] M. C. Kathleen, Y. K. Natalia, R. Jeff, Response surface methodology, center for computational analysis of social and organizational systems (CASOS), CASOS Technical Report, http://www.casos.cs.cmu.edu/publications/papers/CMU-ISR-04-136.pdf, 19.05.2017

[21] M. Sarıkaya, A. Güllü, Taguchi design and response surface methodology based analysis of machining parameters in CNC turning under MQL, Journal of Cleaner Production, 65 (**2014**), 604–616, doi:10.1016/j.jclepro.2013.08.040

[22] D. Montgomery, Design and analysis of experiments, New York: Wiley, 2000

[23] M. Nalbant, H. Gökkaya, G. Sur, Application of Taguchi method in the optimization of cutting parameters for surface roughness in turning, Materials & Design, 28 (**2007**) 4, 1379–1385, doi:10.1016/j.matdes.2006.01.008

[24] T. Ding, S. Zhang, Y. Wang, X. Zhu, Empirical models and optimal cutting parameters for cutting forces and surface roughness in hard milling of AISI H13 steel, Int J Adv Manuf Technol, 51 (**2010**) 1–4, 45–55, doi: 10.1007/s00170-010-2598-2

UDK 67.017:620.3:621.762
Original scientific article/Izvirni znanstveni članek

ISSN 1580-2949
MTAEC9, 51(6)967(2017)

SYNTHESIS AND CHARACTERIZATION OF GRAPHENE NANOSHEETS/MAGNESIUM COMPOSITES PROCESSED THROUGH POWDER METALLURGY

SINTEZA IN KARAKTERIZACIJA MAGNEZIJEVIH KOMPOZITOV, OJAČANIH Z GRAFENSKIMI NANOPLASTMI, IZDELANIH Z METALURGIJO PRAHOV

Xiaoming Du, Kaifeng Zheng, Fengguo Liu

Shenyang Ligong University, School of Materials Science and Engineering, Shenyang 110159, China
du511@163.com

Prejem rokopisa – received: 2017-04-12; sprejem za objavo – accepted for publication: 2017-06-28

doi:10.17222/mit.2017.041

Magnesium-matrix composites reinforced with graphene nanosheets (Mg-Gr) were fabricated using a combination of powder metallurgy and hot rolling. The effects of the graphene-nanosheet content on the microstructures and density of the composites were investigated. It was found that the graphene nanosheets were gradually dispersed in the magnesium matrix with an increasing ball-milling time and a uniform dispersion was achieved after 72 h for the composite with a graphene content of 1.0 % of mass fraction. In addition, no obvious agglomeration of graphene was observed in the as-sintered and as-rolled composites with the graphene contents of up to 1.0 % of mass fraction. A coordinated deformation of multilayer graphene nanosheets occurs with a deformation of the surface grains during the rolling, which may cause a significant reduction in the number of layers of the graphene nanosheets. When increasing the graphene content, the density of the Mg-Gr composites shows an increase.

Keywords: magnesium-matrix composites, graphene nanosheets, powder metallurgy

Kompoziti s kovinsko osnovo, ki so bili ojačani z grafitnimi nanoplastmi (Mg-Gr), so izdelani s kombinacijo postopkov metalurgije prahov in metodami vročega valjanja. Raziskani so bili vpliv vsebnosti grafitnih nanosov na mikrostrukturo in gostoto kompozitov. Ugotovljeno je bilo, da se grafenske nanoplasti postopoma razpršijo v magnezijevo matriko, s povečanjem časa krogličnega mletja. Pri kompozitu z 1,0 % utežnih odstotkov vsebnosti grafena so dobili enakomerno disperzijo po 72 h mletja. Pri obeh, sintranih in valjanih kompozitih niso opazili nobene očitne aglomeracije grafena do vsebnosti 1,0 % utežnih odstotkov grafena. Med valjanjem je istočasno z deformacijo površinskih zrnpotekala usklajena deformacija grafesnkih nanoplasti, kar lahko povzroči znatno zmanjšanje števila grafenskih nanoplasti. Z zviševanjem vsebnosti grafena se je povečevala gostota Mg-Gr kompozitov.

Ključne besede: kovinski kompoziti, ojačani z grafenom; grafitne nanoplasti, metalurgija prahov

1 INTRODUCTION

Owing to a low density, high specific strength, good machinability and easy recycling, magnesium and its alloys have widespread applications in the fields of the automobile, aerospace and electronics industries. However, the usage of magnesium is limited due to its low strength and ductility, as compared to steel and aluminium. Many attempts have been made to improve the mechanical properties of magnesium by developing magnesium-base metal-matrix composites, such as Y_2O_3/Mg, Al_2O_3/Mg, SiCp/Mg and Ti/Mg, during the past decades.[1–5] Recently, the researchers focused on the lighter reinforcements, such as graphene and carbon nanotube (CNT), to enhance the mechanical properties of Mg alloys.[6–7]

Graphene, a single atomic layer of sp^2 hybridized carbon, has extraordinary electrical, thermal, and physical properties. The nanometric nature and high specific surface area allow a great interaction of the reinforcement phase with the matrix even in small concentrations. The modulus of elasticity and intrinsic fracture strength of monolayer graphene are 1 TPa and 125 GPa, respectively.[8–10] Compared to one-dimensional carbon nanotubes, two-dimensional graphene is much easier to be controlled and dispersed in a metal matrix. Furthermore, graphene can be prepared in large quantities using chemical exfoliation of graphite.[11] Therefore, graphene is considered as an ideal reinforcement for metal-matrix composites.

In the past few years, research results for nanoscale graphene-reinforced polymer[12] and ceramic[13] matrix composites were reported. The tensile strength of polyvinyl alcohol (PVA) filled with 0.7 % mass fraction of graphene nanosheets increased by 76 %.[12] The bending strength and breaking strength of an Al_2O_3 ceramic matrix filled with 0.78 % of volume fraction of graphene nanosheets increased by 30.75 % and 27.20 %, respectively.[13] However, the Mg composites reinforced with graphene nanosheets are relatively limited. The existing results in the literature indicate that graphene has incomparable advantages in solving the dispersion and wettabi-

lity conundrums, compared with carbon nanotubes. There is an obvious reinforcement effect and graphene has potential applications as the ideal reinforcement in graphene-reinforced magnesium-matrix composites.[14–16]

In this study, graphene-nanosheet-reinforced magnesium-matrix composites (Mg-Gr) were fabricated using high-energy ball milling, hot-press sintering and hot rolling. The effects of the ball-milling time on the morphologies and structures of the graphene nanosheets in the composites were studied. Meanwhile, the effects of the graphene nanosheets on the microstructure and density of the composites were also investigated.

2 EXPERIMENTAL PART

The graphene nanosheets used in our experiments were prepared with a modified Hummers method as reported previously.[17] The experimental material was natural graphite with a particle size of about 45 um. Natural graphite was reduced at 95 °C for 24 h using hydrazine hydrate. Graphene nanosheets with a thickness of several atomic layers were obtained. The preparation method was similar to that from reference[17]. A magnesium powder with a 99.5 % purity was bought from Hebi Jianglang Metals Co., Ltd., China, with the average particle size of 20 um and it was used as the matrix material. The densities of magnesium powder and graphene nanosheets were 1.74 g/cm^3 and 2.25 g/cm^3, respectively.

Pure magnesium powders were initially mixed with (0.5, 1.0, 1.5, 2.0) % of mass fractions of the as-prepared graphene nanosheets in a conventional rotating ball-milling machine using a stainless jar and balls. Ball milling was carried out in an argon atmosphere at a rotating speed of 90 min^{-1} for 6–72 h with a ball-to-powder weight ratio of 3:1. No process-control agent was used. The milling was paused for 5 min after every 40 min to prevent heating. The above Mg-Gr powders were loaded into a graphite die with a diameter of 50 mm. A sheet of graphite paper was placed between the punch and the powders as well as between the die and the powders for easy removal. The compact Mg-Gr composite billets were vacuum hot pressed at 610 °C for 1.5 h under a pressure of 25 MPa using powder metallurgy. The Mg-Gr composite with 2.0 % mass fraction of graphene nanosheets was rolled at 400 °C with a thickness reduction of 10 % per pass. The rolling-wheel pressure was 40 t, and the rolling-wheel temperature was 25 °C. The as-rolled composites were heat treated at 350 °C for (1, 2 and 3) h, respectively.

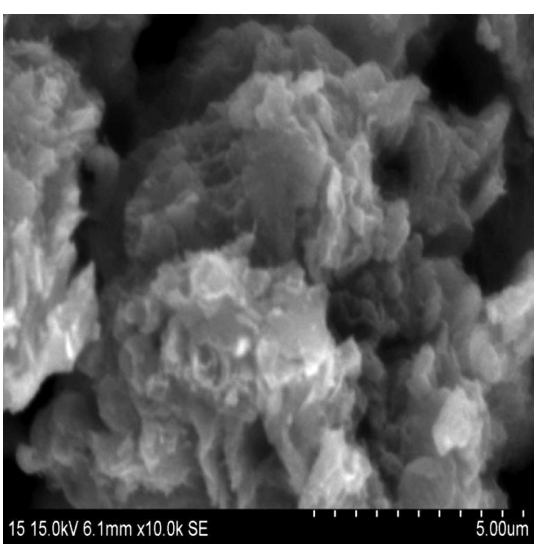

Figure 1: SEM micrograph of graphene nanosheets

The microstructures of the as-sintered composites were observed with an X-ray diffractometer of Rigaku Ultima IV with Cu-K_α radiation at 40 KV and 40 mA, and a scan rate of 0.02 °/s in a 2θ range of 20–90°. The surface morphology was observed with an S-3400N scanning electron microscope (SEM) equipped with an energy-dispersive spectrometer (EDS) and a Carl Zeiss Axioert200MAT optical microscope. The density was measured using Archimedes' method. Theoretical densities of the composites were calculated using rules of mixtures.

3 RESULTS AND DISCUSSION

The typical microstructures of the graphene observed with SEM are shown in **Figure 1**. The graphene nanosheets, having a feather-like, translucent structure, show that their thickness is very thin. The radial size is in the micron order. These nanosheets have the typical characteristics of a folded structure.

The ball-milling time and the graphene content have an important influence over the morphology, powder size, microstructure and physical properties of Mg-Gr composites. **Figures 2** to **4** show a comparative analysis for the sintered composites with different milling times and graphene contents. **Figure 2** shows the effect of the graphene content (taking 0.5, 1 and 2 % as the examples) on its dispersion for the ball-milling time of 6 h. It can be found that the graphene nanosheets are mainly distributed at the magnesium grain boundaries, showing no obvious agglomeration for the graphene content of 0.5 %. However, there is an obvious agglomeration of the graphene nanosheets in the Mg matrix when the content of graphene in the Mg-Gr composites is up to 1.0 %. This is because magnesium grains cannot be completely coated when the content of graphene is less than 1.0 %. The graphene is distributed intermittently at the grain boundaries. When the graphene content is 1.0 %, its presence at the grain boundary can be observed (**Figure 2b**); and when the content of graphene is increased, the graphene nanosheets at the magnesium grain boundaries gradually increase. A serious agglomeration of the graphene nanosheets is observed in the Gr composites containing 2.0 % of mass fractions of Mg, as shown in **Figure 2c**.

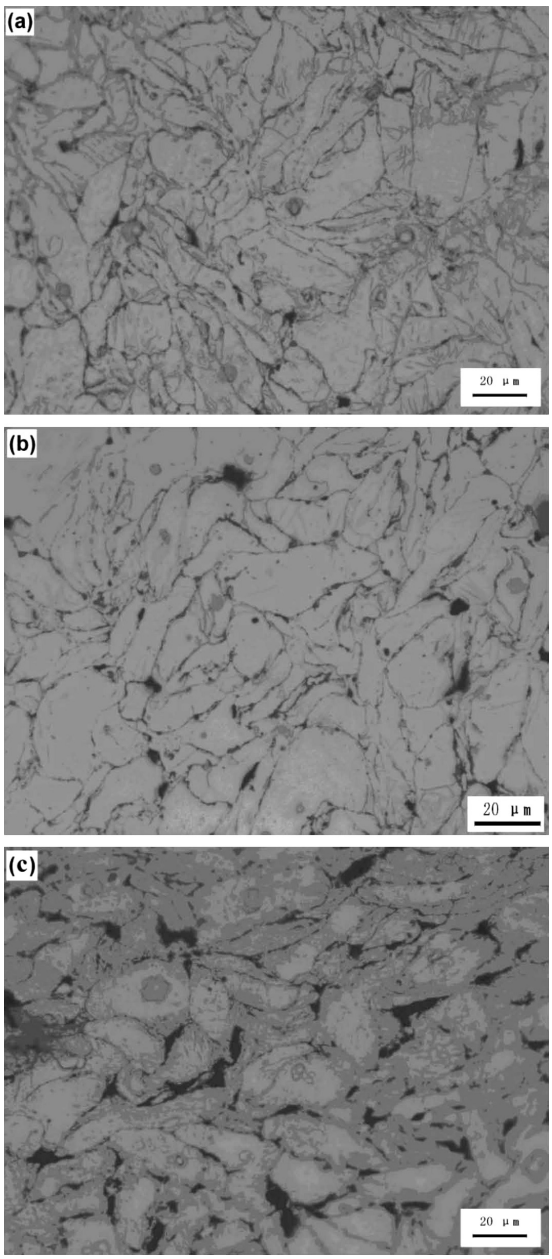

Figure 2: Microstructures of the composites with different graphene contents for the ball-milling time of 6 h: a) 0.5 %, b) 1.0 %, c) 2.0 %

In order to obtain a uniform dispersion of graphene in the magnesium matrix for a higher content of graphene, the milling time was increased to 72 h. We tried to carry out ball-milling tests at 12 h, 24 h and 48 h, respectively. However, the agglomeration was still present in the composites with 1.0 % graphene. Then the milling time was further extended to 72 h. Figure 3 shows the microstructures of the sintered composites with 1.0 % and 2.0 % graphene contents for the ball-milling time of 72 h. It is found that the graphene nanosheets at the magnesium grain boundaries gradually tend to be uniform for the composites with the 1.0 % graphene content. The figure indicates an excellent dispersion of the graphene in the magnesium matrix after the ball-milling period of 72 h.

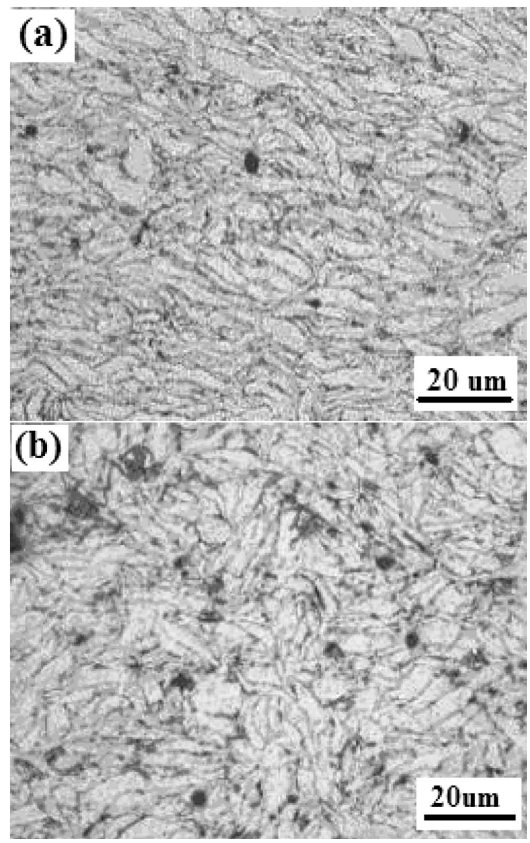

Figure 3: Microstructures of the sintered composites with different graphene contents for the ball-milling time of 72 h: a) 1.0 % of mass fraction, b) 2.0 % of mass fraction

However, clusters of graphene nanosheets are still visible after 72 h in the composites with the 2.0 % graphene content (**Figure 3b**). No experiment with a longer milling time was performed in this study.

In order to eliminate the porosity of the composites, improve the density of the composites and refine the grain size of the composites, hot rolling and heat treatment were successively preformed. Optical micrographs of the Mg-Gr composite with the graphene content of 1.0 % in hot-rolling and heat-treatment conditions are presented in **Figures 4** and **5**, respectively. It is found that the grains of the as-rolled composite are elongated along the rolling direction, as shown in **Figure 4**. The graphene nanosheets are still distributed mainly along the grain boundaries. Compared with **Figure 2b**, it is important to note that a coordinated deformation of the multilayer graphene nanosheets occurs with the deformation of the surface grains, which may cause a significant reduction in the number of layers of the graphene nanosheets. It can be explained that the refinement of the grains on the surface greatly increases the number of grain boundaries, which can cause a reduction of the thickness of the graphene nanosheets. A recovery and recrystallization of the microstructure appear at an aging temperature of 350 °C, as shown in **Figure 5**. The microstructure of the composite tends toward homogenization

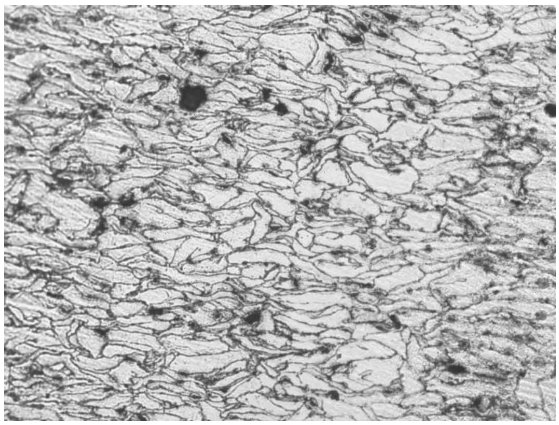

Figure 4: Microstructure of the as-rolled composite with 1.0 % of mass fraction of graphene content

after an aging time of 3 h. This is expected to improve the mechanical properties of the composite. The investigation in this field will be implemented in the future.

The theoretical solid density of magnesium is 1.74 g/cm^3. The density of the sintered sample, ρ_{ac}, was measured using Archimedes' method. The mixture density, ρ_{th}, was calculated with the rule of mixtures, using the theoretical density of 1.74 g/ cm^3 for the pure magnesium powder and 2.25 g/cm^3 for the graphene nanosheets,[18] as follows in Equation (1):

$$\rho_{th} = \frac{100}{\frac{W_{mg}}{\rho_{mg}} + \frac{W_g}{\rho_g}} \quad (1)$$

where ρ_{mg} and ρ_g are the specific weights of the base magnesium powder and graphene nanosheets, respectively; W_{mg} and W_g indicate the weight percentage of the magnesium powder and graphene nanosheets, respectively. The relative density representing the quality of powder metallurgy, ϕ, is defined in Equation (2):

$$\phi = \frac{\rho_{ac}}{\rho_{th}} \times 100\% \quad (2)$$

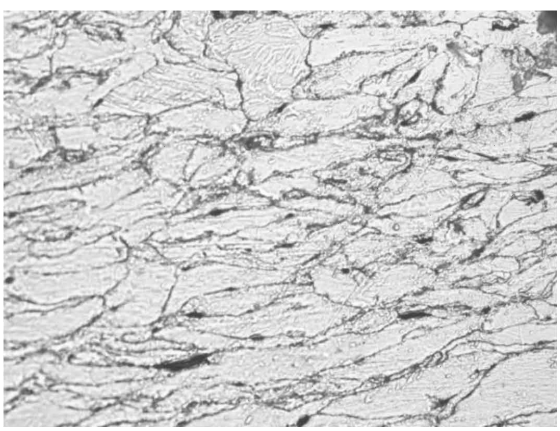

Figure 5: Microstructure of the as-rolled composite with 1.0 % of mass fraction of graphene content after the aging time of 3 h

Based on Equation (1), the densities of the magnesium-based composites reinforced with graphene nanosheets were expected to be increased compared with the density of the pure magnesium powder.

Theoretical, experimental and relative densities of the Mg-Gr composites with different graphene contents are shown in **Figure 6**. It is found that the relative densities of the composites are more than 99.8 %, which shows that the sintered composites are dense. The relative density of the Mg-Gr composites shows a decrease with the increase in the amount of graphene nanosheets in the Mg matrix (**Figure 6a**). This may be attributed to the fact that the dispersion of the graphene nanosheets in a Mg matrix becomes poor and the microvoid increases with the increase in the amount of the graphene nanosheets. The increase in the amount of the graphene nanosheets causes a poor combination of magnesium particles, which results in an increase in the porosity of the composites leading to a poor relative density of the composites. **Figure 6b** shows the variation in the theoretical density and experimental density with the variation in the graphene content in the Mg-Gr composites. The theoretical density follows the rule of mixture, showing a linear increase with the addition of the graphene nanosheets. However, the experimental density is slightly lower than the theoretical density and the difference bet-

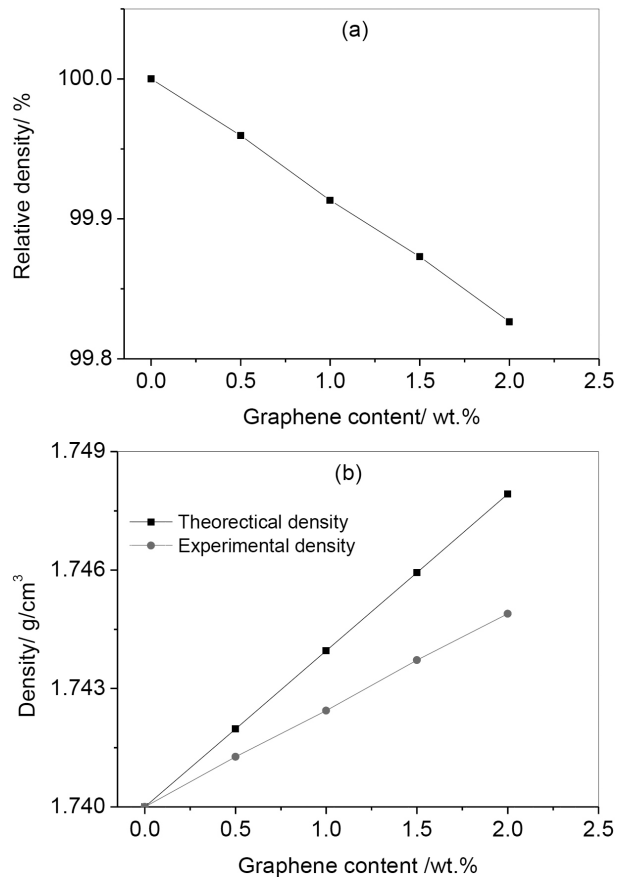

Figure 6: Variation of: a) relative density, b) theoretical density and experimental density of pure Mg and various Mg-Gr composites

ween them becomes large with the increase in the addition of the graphene nanosheets to the Mg matrix. This may lead to a reduction in the mechanical properties.

4 CONCLUSIONS

In this work, Mg-Gr composites were fabricated with ball-milling mixing of a pure magnesium powder and graphene nanosheets, followed by hot pressing, rolling and, finally, heat treatment. The contents of the graphene nanosheets were varied from 0.5 % to 2.0 % mass fraction in the magnesium matrix. The microstructures of the as-sintered and as-rolled composites were analyzed; the densities of the Mg-Gr composites in the as-rolled state were tested. Experimental results revealed that the graphene nanosheets were gradually dispersed in the magnesium matrix by increasing the ball-milling time, and a uniform dispersion was achieved after 72 h. No obvious agglomeration of graphene was observed in the as-sintered and as-rolled composites with the contents of the graphene nanosheets of up to 1.0 % mass fraction. A coordinated deformation of the multilayer graphene nanosheets occurs with the deformation of the surface grains during rolling, which may cause a significant reduction in the number of layers of the graphene nanosheets. By increasing the graphene content, the density of the Mg-Gr composites shows an increase.

Acknowledgment

This work was supported by the Natural Science Foundation of Liaoning (2015602642), Scientific Fund of Liaoning Provincial Education Department and Shenyang Science and Technology Project, Liaoning Province, China.

5 REFERENCES

[1] G. Garcés, M. Rodriguez, P. Pérez, P. Adeva, Effect of volume fraction and particle size on the microstructure and plastic deformation of Mg–Y_2O_3 composites, Mater. Sci. Eng., A 419 (**2006**) 1–2, 357–364, doi:10.1016/j.msea.2006.01.026

[2] B. Nguyen, M. Gupta, Increasing significantly the failure strain and work of fracture of solidification processed AZ31B using nano-Al_2O_3 particulates, J. Alloys Compd., 459 (**2008**) 1–2, 244–250, doi:10.1016/j.jallcom.2007.05.038

[3] G. Huard, R. Angers, M. R. Krishnadev, R. Tremblay, D. Dube, SiCp/Mg composites made by low-energy mechanical processing, Can. Metall. Q., 38 (**1999**) 3, 193–200, doi:10.1179/cmq.1999.38.3.193

[4] S. F. Hassan, M. Gupta, Development of ductile magnesium composite materials using titanium as reinforcement, J. Alloys Compd., 345 (**2002**) 1, 246–251, doi:10.1016/S0925-8388(02)00413-9

[5] P. Pérez, G. Garcés, P. Adeva, Mechanical properties of a Mg–10 (vol.%)Ti composite, Compos. Sci. Technol., 64 (2004) 1, 145–151, doi:10.1016/S0266-3538(03)00215-X

[6] C. S. Goh, J. Wei, L. C. Lee, M. Gupta, Ductility improvement and fatigue studies in Mg-CNT nanocomposites, Compos. Sci. Technol., 68 (**2008**) 6, 1432–1439, doi:10.1016/j.compscitech.2007.10.057

[7] S. C. Tjong, Recent progress in the development and properties of novel metal matrix nanocomposites reinforced with carbon nanotubes and graphene nanosheets, Mater. Sci. Eng. R, 74 (**2013**) 10, 281–350, doi:10.1016/j.mser.2013.08.001

[8] A. A. Balandin, S. Ghosh, W. Bao, I. Calizo, D. Teweldebrhan, F. Miao, C. N. Lau, Superior thermal conductivity of single-layer graphene, Nano Lett., 8 (**2008**) 3, 902–907, doi:10.1021/nl0731872

[9] K. I. Bolotin, K. J. Sikes, Z. Jiang, M. Klima, G. Fudenberg, J. Hone, P. Kim and H. L. Stormer, Ultrahigh electron mobility in suspended graphene, Solid State Commun., 146 (**2008**) 9–10, 351–355, doi:10.1016/j.ssc.2008.02.024

[10] C. Lee, X. Wei, J. W. Kysar, J. Hone, Measurement of the elastic properties and intrinsic strength of monolayer graphene, Science, 321 (**2008**), 385–388, doi:10.1126/science.1157996

[11] D. Chen, H. Feng, J. Li, Graphene oxide: preparation, functionalization, and electrochemical applications, Chem. Rev., 112 (**2012**) 11, 6027–6053, doi:10.1021/cr300115g

[12] J. J. Liang, Y. Huang, L. Zhang, Y. S. Chen, Molecular-Level Dispersion of Graphene into Poly(vinyl alcohol) and Effective Reinforcement of their Nanocomposites, Adv. Funct. Mater., 19 (**2009**) 14, 2297–2302, doi: 10.1002/adfm.200801776

[13] J. Liu, H. X. Yan, K. Jiang, Mechanical properties of graphene platelet-reinforced alumina ceramic composites, Cerm. Int., 39 (**2013**) 6, 6215–6221. doi:10.1016/j.ceramint.2013.01.041

[14] M. Rashad, F. Pan, A. Tang, Y. Lu, M. Asif, S. Hussain, J. She, J. Gou, J. Mao, Effect of graphene nanoplatelets (GNPs) addition on strength and ductility of magnesium-titanium alloys, J. Magn. Alloy, 1 (**2013**) 3, 242–248, doi:10.1016/j.jma.2013.09.004

[15] M. Rashad, F. Pan, J. Zhang, M. Asif, Use of high energy ball milling to study the role of graphene nanoplatelets and carbon nanotubes reinforced magnesium alloy, J. Alloys Compd., 646 (**2015**) 1, 223–232, doi:10.1016/j.jallcom.2015.06.051

[16] M. Rashad, F. Pan, M. Asif, Exploring mechanical behavior of Mg-6Zn alloy reinforced with graphene nanoplatelets, Mater. Sci. Eng., A 649 (**2016**) 4, 263–269, doi:10.1016/j.msea.2015.10.009

[17] W. S. Hummers, R. Offeman, Preparation of graphitic oxide, J. Am. Chem. Soc., 80 (**1958**) 6, 1339–1339, doi: 10.1021/ja01539a017

[18] M. Rashad. F. Pan. A. Tang. M. Asif. J. Gou, Improved strength and ductility of magnesium with addition of aluminum and graphene nanoplatelets (Al+GNPs) using semi powder metallurgy method, Journal of Industrial and Engineering Chemistry, 23 (**2015**), 243–250, doi:10.1016/j.jiec.2014.08.024

UDK 620.17:669.15-194.56:621.74
Original scientific article/Izvirni znanstveni članek

ISSN 1580-2949
MTAEC9, 51(6)973(2017)

DISTRIBUTION OF Al_2O_3 REINFORCEMENT PARTICLES IN AUSTENITIC STAINLESS STEEL DEPENDING ON THEIR SIZE AND CONCENTRATION

PORAZDELITEV DELCEV Al_2O_3 V AVSTENITNEM NERJAVNEM JEKLU V ODVISNOSTI OD VELIKOSTI IN KONCENTRACIJE

Ana Kračun[1,2], Bojan Podgornik[1], Franc Tehovnik[1], Fevzi Kafexhiu[1], Darja Jenko[1]

[1]Institute of Metals and Technology, Lepi pot 11, 1000 Ljubljana, Slovenia
[2]Jožef Stefan International Postgraduate School, Jamova cesta 39, 1000 Ljubljana, Slovenia
ana.kracun@imt.si

Prejem rokopisa – received: 2017-04-13; sprejem za objavo – accepted for publication: 2017-09-22

doi:10.17222/mit.2017.042

Achieving a uniform distribution of reinforcement particles within a matrix is one of the challenges that impacts directly on the properties and quality of a composite material. Therefore, the aim of the present work was to investigate the influence of the reinforcing Al_2O_3 particles' concentration and size on their distribution in reinforced austenite stainless steel. Austenitic stainless steel reinforced with (0.5, 1.0 and 2.5) % of mass fractions of Al_2O_3 particles was produced by a conventional casting route. In this study, an innovative pre-dispersion approach for the addition of particles into a steel melt was designed. The results of this investigation indicate that the concentration and size of the Al_2O_3 particles has an impact on the distribution of the reinforcement within the matrix. When the weight percent increased to 2.5 the concentration ratio of the particles' distribution decreases towards the bottom of the cast ingot. In this case also the size of particles starts to play a role, with the larger particle size leading to an increased degree of incorporating particles into the steel matrix. The larger the particles the more particles are found in the cast ingot.

Keywords: metal matrix composite, reinforced particles, distribution, conventional casting method

Doseganje enakomerne porazdelitve delcev v matrici je eden izmed izzivov, ki direktno vplivajo na lastnosti in kvaliteto kompozitnih materialov. Namen raziskave je bil ugotoviti porazdelitev delcev v mikrostrukturi jekla glede na dodano koncentracijo in velikost. Med procesom konvencionalnega litja avstenitnega nerjavnega jekla so bili dodani delci Al_2O_3 v utežnih procentih (0,5, 1,0 in 2,5). V tej študiji smo uporabili inovativni pristop dispergiranja delcev pred dodajanjem v jekleno talino. Rezultati raziskave kažejo, da je koncentracija in velikost Al_2O_3 delcev vplivala na porazdelitev delcev v matrici. S povečanjem utežnega procenta dodanih delcev na 2,5 se je koncentracijsko razmerje delcev zmanjšalo proti dnu ulitega ingota. V tem primeru ima pomemben vpliv na porazdelitev tudi velikost delcev, večji kot so delci več jih je vključenih v matrico. Večji kot so delci, več se jih nahaja v ulitem ingotu.

Ključne besede: kovinski kompoziti, utrjevalni delci, porazdelitev, metoda konvencionalnega litja

1 INTRODUCTION

The application of metal-matrix composites (MMCs) as structural engineering materials has received increasing attention in recent years.[1–3] Ceramic particulates such as borides, carbides, oxides and nitrides are added to MMCs to improve their elastic modulus, wear resistance, creep and strength.[4–5]

There are different routes by which MMCs can be manufactured, and among all the liquid-stat processes are considered to have the most potential for engineering applications in terms of production capacity and cost efficiency. Casting techniques are economical, easier to apply and more convenient for large parts and mass production with regard to other manufacturing techniques. However, it is extremely difficult to obtain a uniform dispersion of ceramic nanoparticles in liquid metals due to the poor wettability and to the difference in specific gravity between the ceramic particles and the metal matrix.[6–8]

The current work aims at contributing to the knowledge and understanding of the conventional casting route and its possibility for ultrafine particle inoculation in a steel matrix. This production route seems to show potential and offers more cost efficiency in achieving the dispersion of second-phase ultrafine range particles compared to the typically used powder and metallurgical techniques used until now. The aim of the present work is to identify the distribution of particles in the steel matrix that were introduced through a conventional melting and casting method, and above all to determine the influence of the different concentrations, sizes and methods of adding Al_2O_3 particles on the distribution of the latter in reinforced austenite stainless steel. In terms of the methods the focus was on the influence of dispersion medium CaSi (Ca-30 %, Si-70 %) on the distribution homogeneity of the Al_2O_3 particles.

2 EXPERIMENTAL PART

2.1 Material

Austenitic stainless steel has been used for the work, mainly due to its distinctive two-phase microstructure of austenite and ferrite. It also belongs to the most used group of stainless steels. They are paramagnetic, have a face-centred cubic lattice and excel with a good combination of hot and cold workability, mechanical properties and corrosion resistance. The chemical composition of the base alloy is given in **Table 1**.

Table 1: Chemical composition of austenitic stainless steel in weight percent (*w*/%)

Elements	*w*/%
Si	0.33
Mn	1.24
Cr	17.4
Ni	10.1
Cu	0.36
Mo	1.29
V	0.08
C	0.02

As reinforcement particles, commercial Al_2O_3 powder from the company US Research Nanomaterials, Inc. with a mean particle size of 500 nm (**Figure 1**) and 50 nm (**Figure 2**) was used. The Al_2O_3 particles were selected due to their high chemical stability with respect to Fe and high specific gravity. Particularly, it was reported that the wetting angle Θ between Al_2O_3 and molten iron alloy is less than 50°, even at high temperatures and in many different types of atmospheres.[9]

As a dispersion medium CaSi (Ca-30 %, Si-70 %) was used. Ca additions are made during steel making for refining, deoxidation, desulphurization, and control of the shape, size and distribution of oxide and sulphide inclusions. However, elemental Ca is difficult and dangerous to add to liquid steel because it has a high reactivity.[10] Therefore, Ca in the stabilized forms of calcium silicon (CaSi), calcium manganese silicon (CaMnSi), calcium silicon barium (CaSiBa) and calcium silicon barium aluminium (CaSiBaAl) alloys or as calcium carbide (CaC_2) is used. In the present work CaSi was used due to the fact that it is most commonly used as deoxidant element in steelmaking, and does not cause contamination of the steel melt. The aim of the CaSi addition was to control the shape, size and distribution of oxide particles added in the steel melt.

2.2 Specimens preparation

First a weighed quantity (14 kg) of austenitic stainless steel was melted in the open induction furnace (TYP SF 70 sl) with a generator under normal atmospheric conditions. The maximum temperature of the melt production is up to 1750 °C. In the first set of experiments six different batches were prepared using two different particle sizes (500 nm and 50 nm) and three different concentrations (0.5, 1.0 and 2.5) % of mass fractions of Al_2O_3, as shown in **Table 2**. The Al_2O_3 particles powder was wrapped into the aluminium foil, placed into the mould and then the molten metal was poured over it into the mould. During casting the aluminium foil melts and dissolves in the metal.

Table 2: Addition scheme for the first set of experiments – Al_2O_3 particles size and concentration used.

	Al_2O_3 particle size	
	500 nm	50 nm
Concentrations (*w*/%)	0.5	0.5
	1.0	1.0
	2.5	2.5

The second set of experiments comprised four batches where two different Al_2O_3 particle sizes (500 nm and 50 nm) in weight percent of 1.0 were used. In two cases the Al_2O_3 powder was mixed with the same amount of dispersion media – CaSi (Ca 30 %, Si 70 %) and filled into a cast-iron tube. For comparison two additional batches were prepared where only Al_2O_3 powder sealed into a cast iron tube was used, **Table 3**. The cast-iron

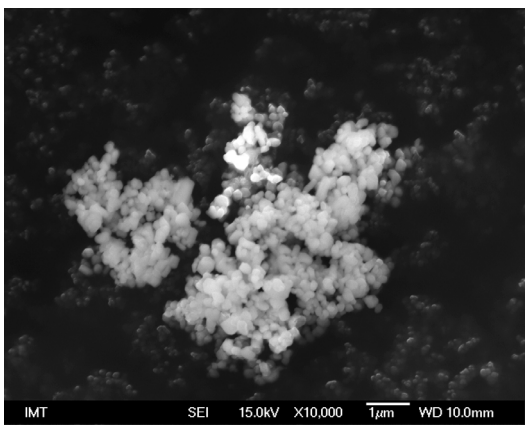

Figure 1: SEI of ultrafine Al_2O_3 powder with a mean particle size of 500 nm

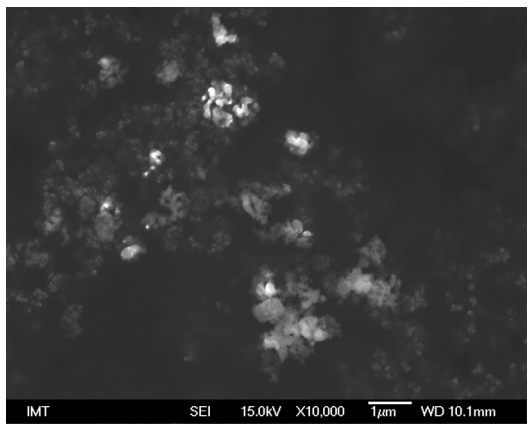

Figure 2: SEI of Al_2O_3 nanopowder with a mean particle size of 50 nm

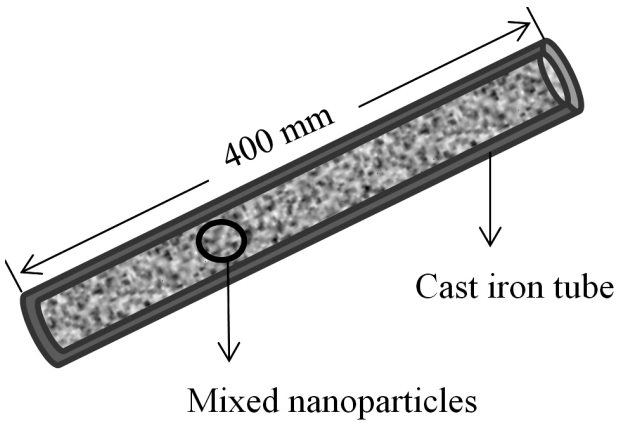

Figure 3: Schematic diagram of a cast-iron tube, filled with nanoparticles

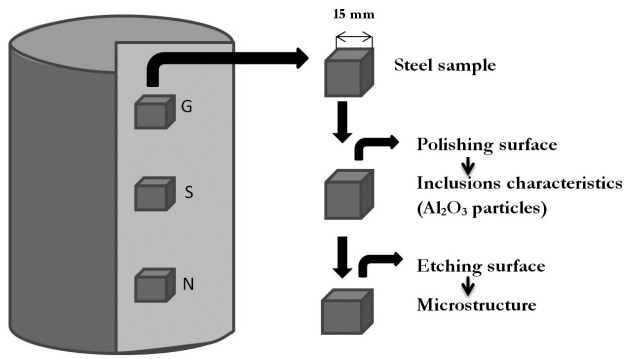

Figure 4: Schematic diagram of subtraction and preparation of metallographic steel samples

tube had a length of 400 mm, outer diameter 12 mm and wall thickness 2 mm, as shown in **Figure 3**. The ends of the tube were sealed with pliers and the molten metal was poured over the iron tube into the mould. The iron tube melts and dissolves in the melt.

Table 3: Addition scheme for the second set of experiments – Al_2O_3 particles mixed with CaSi and dispersion medium.

	Al_2O_3 particle size	
	500 nm (1.0 %)	50 nm (1.0 %)
Dispersion medium (CaSi) (*w*/%)	1	1
	0	0

2.3 Characterization

The microstructural changes and the dispersion of the ceramic particles in the steel matrix were observed and analysed by light microscopy (LM), scanning electron microscopy (SEM), Auger electron spectroscopy (AES) and transmission electron microscopy (TEM). Samples for the microstructure analysis were taken at the bottom, middle and top portions of the cast ingot, **Figure 4**. Metallographic samples were prepared by grinding and polishing, followed by chemical etching and analysed to reveal the particle distribution. In the case of AES ground and polished specimens were ion sputtered and analysed in terms of the elemental composition in the surface region. Samples for TEM were prepared by slicing the specimens into thin 0.5–1.0-mm-thick plates with a length of up to 3 mm. After polishing to a thickness of 100±10 μm, final milling of the specimen was carried out with an ion slicer.

For a representative analysis of the particles' distribution, three specimens located at different positions within the ingot diameter were prepared for each position (top-G, middle-S, bottom-N) and ten images taken with a scanning electron microscope for each sample and position. In order to do particle analysis efficiently, all images were taken at the same magnification (1000×) with similar contrast. Then ImageJ commercial software was used to calculate and determine the particles distribution and their volume fraction.

3 RESULTS AND DISCUSSION

3.1 Light microscopy (LM)

Figure 5 shows a LM image of the microstructure of pure austenitic stainless steel with a distinctive two-phase microstructure of austenite and δ-ferrites obtained. LM micrographs of the microstructure with included ultrafine Al_2O_3 particles; produced by the casting process where the melted austenitic stainless steel was poured over the Al_2O_3 particles wrapped into the Al foil is shown in **Figure 6** and **7**.

It is clear that the distribution of Al_2O_3 particles with a mean particle size of 500 nm is non-homogeneous and concentrated in several isolated areas (**Figure 6**). However, the distribution of Al_2O_3 particles with a mean particle size of 50 nm, shown in **Figure 7**, is more homogeneous with reduced clustering of the particles, as compared to the 500-nm particles size case.

From the light micrographs in **Figures 8** and **9** we can see that the distribution of ultrafine Al_2O_3 particles from the second set of experiments, **Table 3**. Distribution

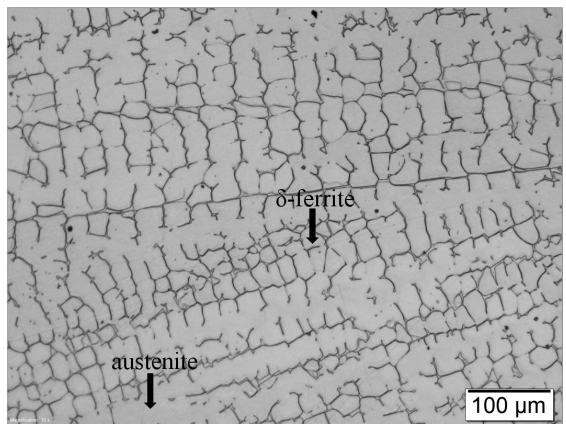

Figure 5: Cast microstructure of austenitic stainless steel with 6 % of δ-ferrite

of Al_2O_3 particles (white arrows) is more homogeneous and not concentrated in certain areas. Furthermore, clustering of the particles is smaller than in the first set of experiments without using the CaSi.

As shown in **Figures 10** and **11**, the microstructure of austenitic stainless steel and the distribution of the incorporated nanosized particles is further modified when using Al_2O_3 particles mixed with CaSi dispersion media, from the second set of experiments, **Table 3**. In this case the distribution of Al_2O_3 particles (white arrows) becomes much more homogeneous and almost equally distributed within the metal matrix. Furthermore, the

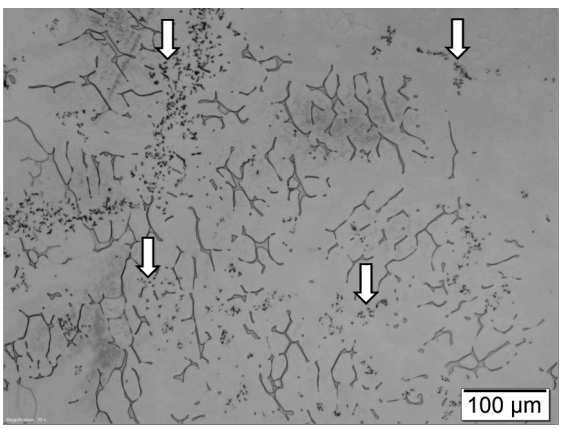

Figure 6: Cast microstructure of austenitic stainless steel with 6 % of δ-ferrite and Al_2O_3 (500 nm, 1.0 %) ultrafine particles (white arrows)

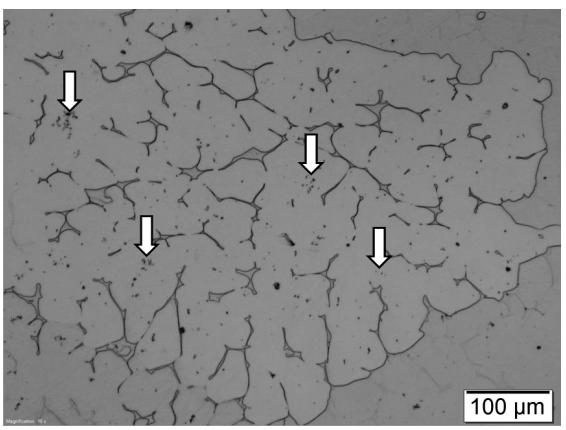

Figure 7: Cast microstructure of austenitic stainless steel with 6 % of δ-ferrite and Al_2O_3 (50 nm, 1.0 %) nanoparticles (white arrows)

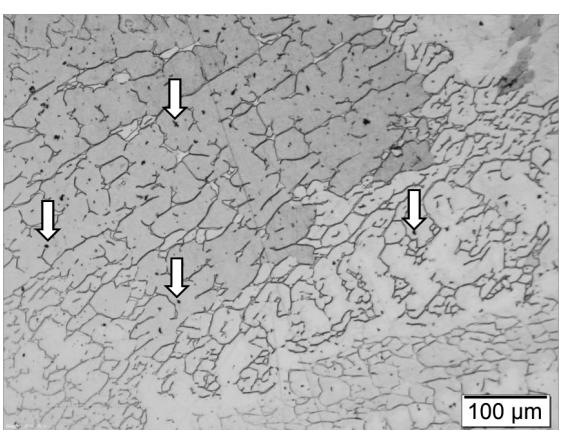

Figure 8: Cast microstructure of austenitic stainless steel with 6 % of δ-ferrite and Al_2O_3 (500 nm, 1.0 %) ultrafine particles (white arrows)

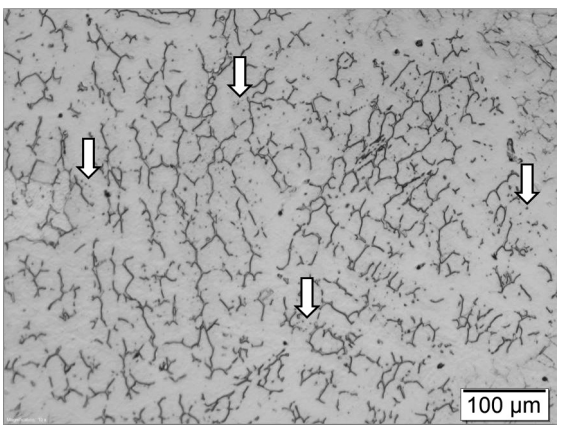

Figure 9: Cast microstructure of austenitic stainless steel with 6 % of δ-ferrite and Al_2O_3 particles (white arrows); ultrafine powder (500 nm, 1.0 %) mixed with CaSi (Ca-30 %, Si-70 %)

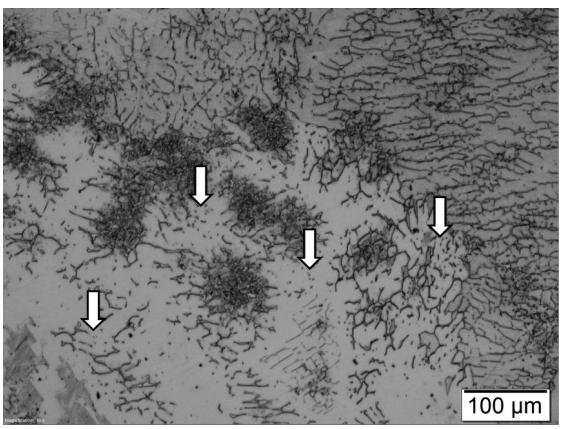

Figure 10: Cast microstructure of austenitic stainless steel with 6 % of δ-ferrite and Al_2O_3 (50 nm, 1.0 %) nanoparticles (white arrows)

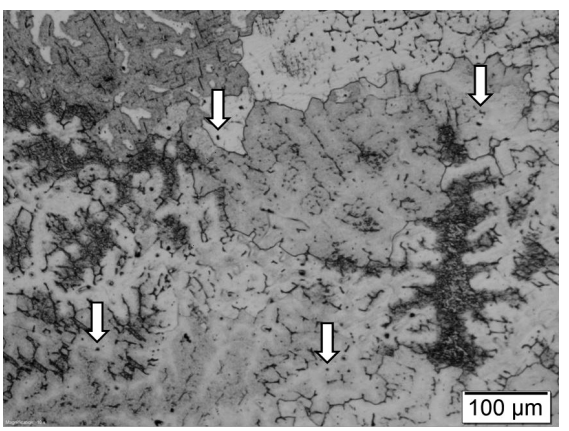

Figure 11: Cast microstructure of austenitic stainless steel with 6 % of δ-ferrite and Al_2O_3 nanoparticles (white arrows); nanoparticles powder (50 nm, 1.0 %) mixed with CaSi (Ca-30 %, Si-70 %)

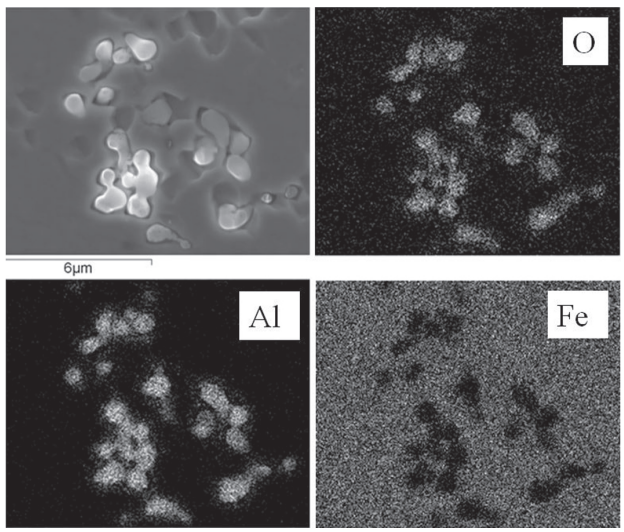

Figure 12: SEM/EDS elemental mapping of Al_2O_3 ultrafine particles (500 nm, 1.0 nm %) in the cast microstructure of austenitic stainless steel, from the first set of experiments, without using the CaSi

clustering of the particles reduced as compared to the first set of experiments, without using the CaSi.

A size-dependent analysis show that Al_2O_3 powder with a mean particle size 50 nm is more homogeneously distributed than the 500 nm powder. In the cases when we added the CaSi to Al_2O_3 the distribution of particles was more homogeneous in all three sampling areas (top-G, middle-S, bottom-N) of the cast ingot; from the top to the bottom of the cast ingot.

3.2 Scanning electron microscopy (SEM)

After the metallographic examination the specimens were subjected to SEM analysis in order to confirm the incorporation/presence of Al_2O_3 ultrafine particles in the microstructure and to analyse the particles clustering. From the SEM/EDS elemental mapping analysis, shown in the **Figure 12**, it was confirmed that the bright, small, spot-like features represent the Al_2O_3 ultrafine particles,

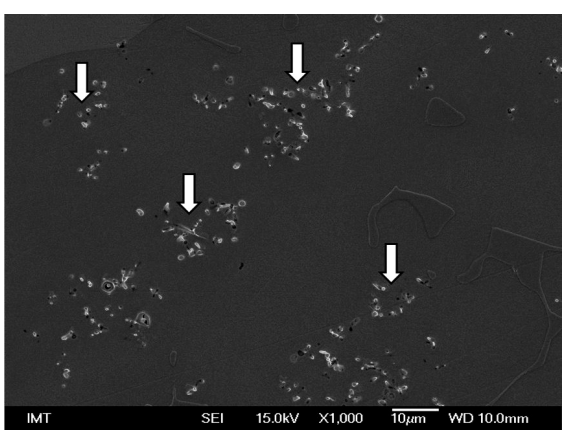

Figure 13: Cast microstructure of austenitic stainless steel with 6 % of δ-ferrite and Al_2O_3 (500 nm, 1.0 %) ultrafine particles (white arrows), without using the CaSi

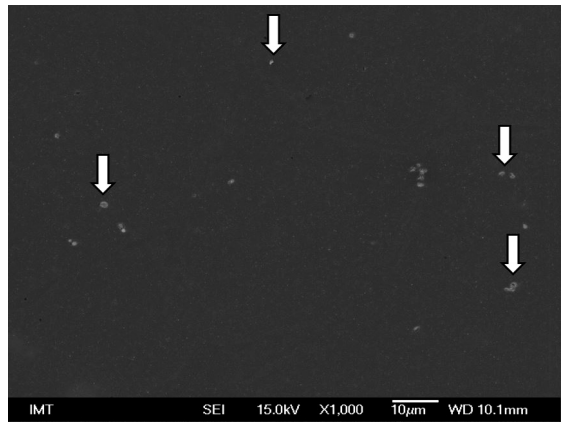

Figure 14: Cast microstructure of austenitic stainless steel with 6% of δ-ferrite and Al_2O_3 particles (white arrows); ultrafine powder (500 nm, 1.0 %) mixed with CaSi (Ca-30%, Si-70%)

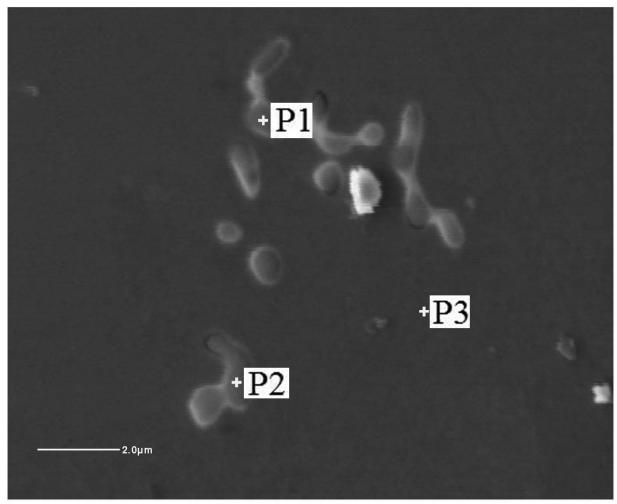

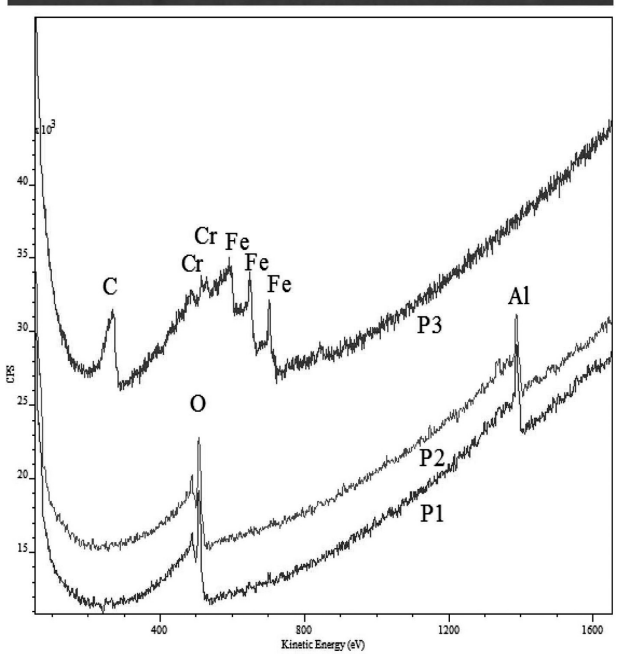

Figure 15: AES spectrum of the Al_2O_3 ultrafine particles (500 nm, 1.0 %) in the cast microstructure of austenitic stainless steel, without using the CaSi

which are incorporated but non-uniformly distributed in the steel matrix. Furthermore, a high degree of particles clustering was observed.

Concentration-dependent analysis shows that at the 0.5 % to 1.0 % of mass fractions of the distribution of particles is more homogeneous throughout the cast ingot than in the case of 2.5 % of mass fractions. Size-dependent analysis show that Al_2O_3 powder with a mean particle size 50 nm is more homogeneously distributed than 500 nm. The addition of CaSi plays an important role in case of distribution and clustering of A_2O_3 particles, as shown in **Figures 13** and **14** where Al_2O_3 particles were mixed with CaSi dispersion media, from the second set of experiments, **Table 3**.

From **Figures 13** and **14** we can see that distribution of Al_2O_3 particles (white arrows) becomes much more homogeneous and quite equally distributed within the metal matrix when using CaSi dispersion media.

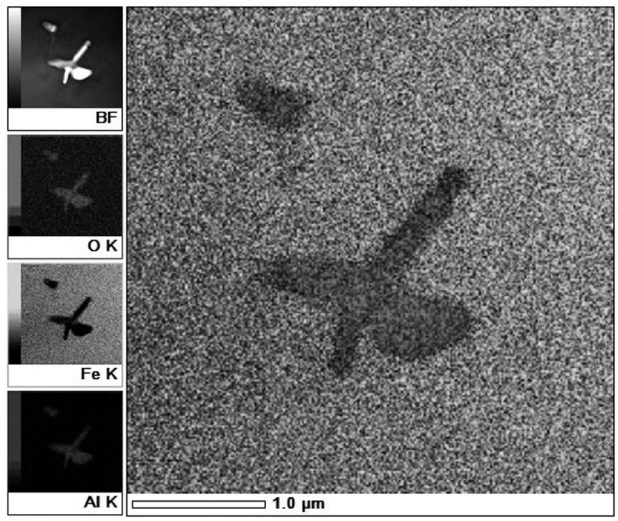

Figure 17: STEM/EDS elemental mapping of Al_2O_3 ultrafine particles (500 nm, 1.0 %) in the cast microstructure of austenitic stainless steel, without using the CaSi

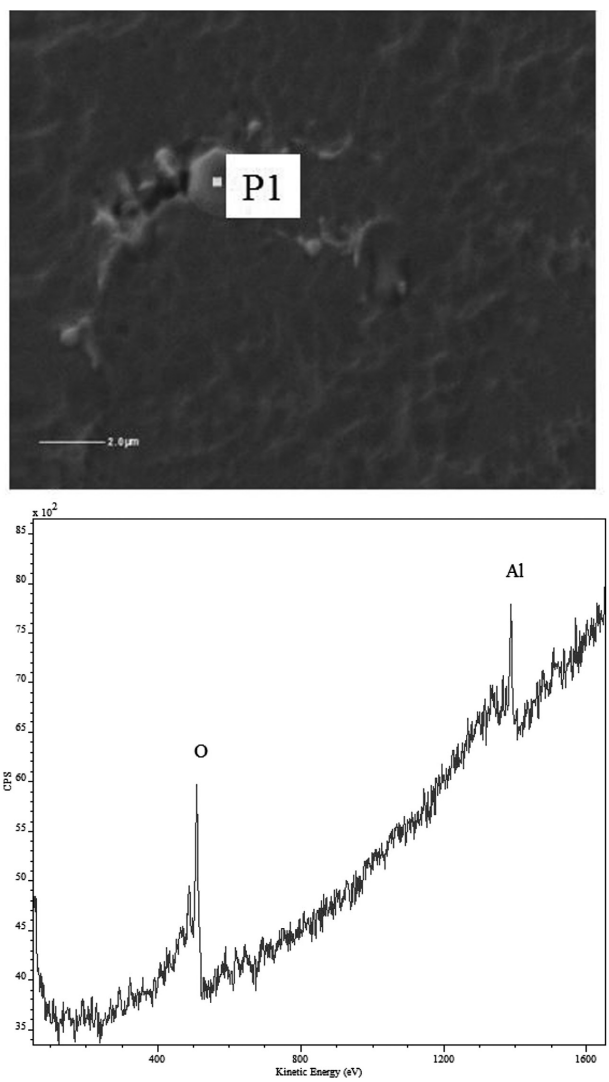

Figure 16: AES spectrum of the Al_2O_3 ultrafine particles (500 nm, 1.0 %) mixed with CaSi (Ca-30%, Si-70%) in the cast microstructure of austenitic stainless steel

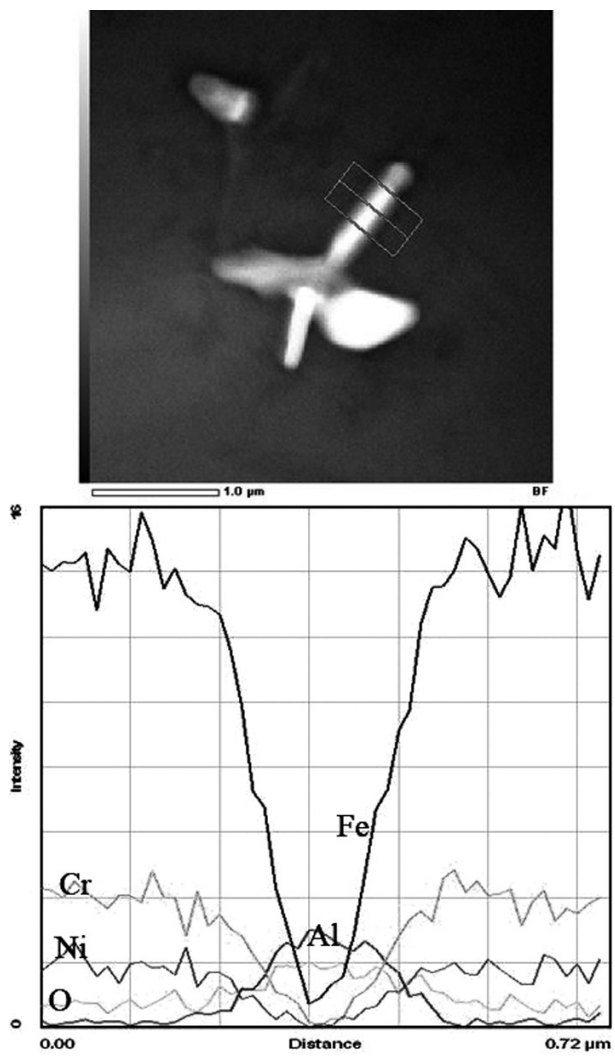

Figure 18: STEM – line profile of Al_2O_3 ultrafine particles (500 nm, 1.0 %) in the cast microstructure of austenitic stainless steel, without using the CaSi

3.3 Auger electron spectroscopy (AES)

In the next step a surface analysis of the sample using Auger electron spectroscopy technique was performed. In **Figure 15** the AES spectrum of the Al_2O_3 ultrafine particles (500 nm, 1.0 %) in the cast microstructure of austenitic stainless steel is shown. The AES spectra of particles (P1 and P2) showing only O and Al peaks and line scans over the particle/matrix interface confirm the successful introduction of Al_2O_3 particles into the steel matrix (P3) without any intermetallic reactions taking place, which is true for all the Al_2O_3 particle sizes and concentrations used. In **Figure 16** the AES spectrum of the Al_2O_3 ultrafine particles (500 nm, 1.0 %) mixed with CaSi (Ca-30%, Si-70%) in the cast microstructure of the austenitic stainless steel is shown. The AES spectrum of particles (P1) shows only O and Al peaks. Also in cases when CaSi was added to Al_2O_3 ultrafine and nano-particles no intermetallic reactions or presence of Ca and Si were observed. However, as already mentioned the distribution of particles was more homogeneous.

3.4 Transmission electron microscopy (TEM)

In the context of the microstructural changes a characterization and analysis of the ceramic particles incorporation in the steel matrix transmission electron microscopy (TEM) was also employed. With STEM/EDS elemental mapping shown in the **Figure 17** and STEM – line profile analysis shown in the **Figure 18** successful incorporation and coherent bonding of the Al_2O_3 nanoparticles in the steel matrix was confirmed. No discontinuities at the particle/matrix interface, modification of metal matrix or formation of intermetallic phases could be observed.

3.5 Particles distribution

The particle distribution analysis performed on the specimens from the first set of experiments revealed that Al_2O_3 particles of 0.5 % to 1.0 % of mass fractions, regardless of the mean particle size of 500 nm or 50 nm, results in a relatively homogeneous distribution of Al_2O_3 particles throughout the volume of the cast ingot. For low particle weight percents of 0.5 % and 1.0 % the distribution of Al_2O_3 particles in the cast ingot was found to be more or less independent on the position, concentration and size of particles, resulting in about 0.01 particles/μm^2. However, as the weight percent increased to 2.5 the particle concentration ratio starts to decrease toward the bottom of the cast ingot (**Figure 19**). Furthermore, with the increased particle mass fraction, also their concentration in cast ingot increased by up to 3 times, with the size of particles starting to play a role. The larger the particles the larger is the volume fraction of the incorporated particles.

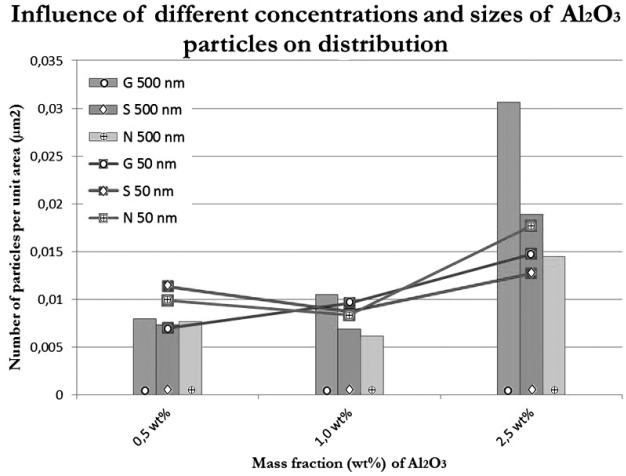

Figure 19: Influence of different concentrations and size of Al_2O_3 particles on their distribution in the cast ingot

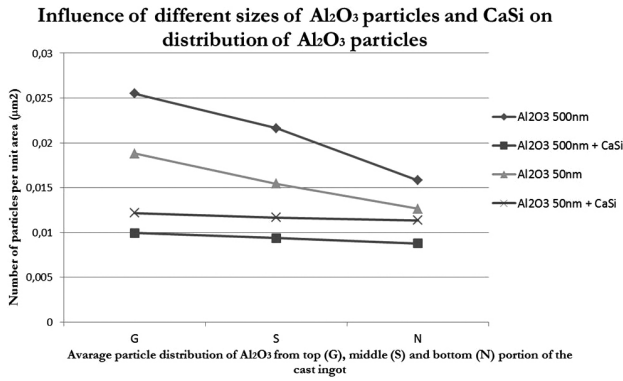

Figure 20: Influence of different sizes of Al_2O_3 particles and CaSi on distribution of Al_2O_3 particles (1 %)

The particles distribution analysis from the second set of experiments (**Figure 20**) shows that the use of dispersion agent reduces the influence of particles size (500 nm or 50 nm) on the particles' distribution in the steel matrix. It results in a difference in the particles' concentration throughout the ingot being reduced from about 0.01 particles/μm^2 to less than 0.002 particles/μm^2.

5 CONCLUSIONS

The results of our investigation indicate that steel reinforced with ceramic ultrafine/nanosized particles can be produced by using a conventional casting route. Ultrafine particles and nanoparticles where successfully incorporated into the steel matrix, being confirmed by different analysing techniques, including light microscopy (LM), scanning electron microscopy (SEM), Auger electron spectroscopy (AES) techniques and transmission electron microscopy (TEM).

By using CaSi as a dispersion media and introducing Al_2O_3/CaSi mixture through a sealed iron tube reduced

particles clustering and more homogeneous distribution of reinforcement nanoparticles in the steel matrix were obtained. It was found that the concentration and the size of particles have an impact on the distribution of the reinforcement within the matrix. When the weight percent is increased above 1.0 it starts to affect the particles' distribution, with the concentration ratio decreasing towards the bottom of the cast ingot. In this case also the size of the particles plays a role: a larger particle size leading to an increased degree of incorporated particles in the steel matrix.

In this study, an innovative pre-dispersion approach for more the effective addition of ultrafine particles and nanoparticles into a steel melt through a conventional casting route was designed. It is based on mixing ultrafine particles and nanoparticles powder with dispersion media.

Acknowledgment

This work was done in the frame of the research programs P2-0050, which are financed by the Slovenian Research Agency. The authors would also like to acknowledge help from Miroslav Pečar, inž., from Institute of Metals and Technology for the AES analysis.

6 REFERENCES

[1] R. Casati, M. Vedani, Metal Matrix Composites Reinforced by Nano-Particles – A Review, Metals (Basel), 4 (**2014**) 1, 65–83, doi:10.3390/met4010065

[2] S. H. Lee, J. J. Park, S. M. Hong, B. S. Han, M. K. Lee, C. K. Rhee, Fabrication of cast carbon steel with ultrafine TiC particles. Trans Nonferrous Met Soc China (English Ed.) 21 (**2011**), 54–57, doi:10.1016/S1003-6326(11)61060-1

[3] Y. Q. Liu, H. T. Cong, W. Wang, C. H. Sun, H. M. Cheng, AlN nanoparticle-reinforced nanocrystalline Al matrix composites: Fabrication and mechanical properties. Met.Sic.Eng.A, 505 (**2009**), 151–156, doi:10.1016/j.msea.2008.12.045

[4] Z. Zhang, L. D. Chen, Consideration of Orowan strengthening effect in particulate-reinforced metal matrix nanocomposites: A model for predicting their yield strength. Scripta Mater., 54 (**2006**), 1321–1326, doi:10.1016/j.scriptamat.2005.12.017

[5] J. Llorca, Fatigue of particle-and whisker reinforced metal-matrix composites. Prog Mater Sci., 47 (**2002**), 283–353, doi:10.1016/S0079-6425(00)00006-2

[6] B. N. Chawla, Y. Shen, Mechanical Behavior of Particle Reinforced Metal Matrix Composites **. Adv Eng Mater., 3 (**2001**) 6, 357–370, doi:10.1002/1527-2648(200106)3:6<357::AID-ADEM357>3.3.CO;2-9

[7] Z. Ni, Y. Sun, F. Xue, J. Bai, Y. Lu, Microstructure and properties of austenitic stainless steel reinforced with in situ TiC particulate,Mater. Des., 32 (**2011**) 3, 1462–1467, doi:10.1016/j.matdes.2010.08.047

[8] F. Akhtar, Ceramic reinforced high modulus steel composites: processing, microstructure and properties,Can. Metall. Q., 53 (**2014**) 3, 253–263, doi: 10.1179/1879139514Y.0000000135

[9] S-Y.Cho, J-H. Lee, Anisotropy of wetting of molten Fe on Al_2O_3 single crystal. Korean J Mater Res., 18 (**2008**) 1, 18–21, doi:10.3740/MRSK.2008.18.1.018

[10] R. V. Väinölä, L. E. K. Holappa, P. H. J. Karvonen, Modern steelmaking technology for special steels, Journal of Materials Processing Technology, 53 (**1995**), 453–465, doi:10.1016/0924-0136(95)02002-4

UDK 62-4-023.7:669.231.6:621.35
Original scientific article/Izvirni znanstveni članek

ISSN 1580-2949
MTAEC9, 51(6)981(2017)

SURFACE CHARACTERIZATION OF PLATINUM STIMULATING ELECTRODES USING AN ELECTROCHEMICAL SCANNING METHOD

KARAKTERIZACIJA POVRŠINE PLATINASTIH STIMULACIJSKIH ELEKTROD S POMOČJO ELEKTROKEMIJSKE VRSTIČNE METODE

Andraž Mehle[1], Janez Rozman[2,3], Martin Šala[4], Samo Ribarič[3], Polona Pečlin[2]

[1]Sensum d. o. o., Tehnološki park 21, 1000 Ljubljana, Slovenia
[2]Centre for Implantable Technology and Sensors, ITIS d. o. o. Ljubljana, Lepi pot 11, 1000 Ljubljana, Slovenia
[3]Institute of Pathophysiology, Medical Faculty, University of Ljubljana, Zaloška 4, 1000 Ljubljana, Slovenia
[4]Analytical Chemistry Laboratory (L04), National Institute of Chemistry, Hajdrihova 19, Ljubljana, Slovenia
janez.rozman@guest.arnes.si

Prejem rokopisa – received: 2017-04-25; sprejem za objavo – accepted for publication: 2017-06-28

doi:10.17222/mit.2017.044

The purpose of this article is to investigate the electrochemical performance of platinum stimulating nerve electrodes (WE1 and WE2) with different surface structures to define which one is able to produce a higher neural activation function during nerve stimulation than that achieved by conventional electrodes. The purpose is also to present a method that enables the electrochemical scanning of stimulating electrode surfaces. The surface of WE1 was modified using rough sand paper, while the surface of WE2 was modified using fine sand paper. The potential at the different roughened surfaces in the sodium phosphate mixture, when excited with specific current pulses, was measured against a Ag/AgCl reference electrode. Voltage transients were recorded to determine the polarization across the electrode-electrolyte interface. The results indicate that the surface of WE1 could deliver more current to the nerve tissue and more activation for a fixed input voltage than WE2. Namely, it is shown that the mean $|Z_{pol}|$ of WE1 was lower than that for WE2 (237.1 Ω vs. 251 Ω). Accordingly, the platinum electrode that was superficially modified using rough sand paper is more suitable for safe and efficient nerve stimulation than the electrode that was superficially modified using fine sand paper.

Keywords: platinum, polarization, interfaces, potential parameters

Namen članka je preiskati elektrokemijske lastnosti platinastih elektrod WE1 in WE2 za stimulacijo živca, ki imata različni površinski strukturi, s ciljem določiti katera od njiju je sposobna povzročiti večjo aktivacijsko funkcijo vlaken med stimulacijo glede na konvencionalno površino. Namen je tudi predstaviti metodo, ki omogoča elektrokemijsko vrstično preiskavo površin stimulacijskih elektrod. Površina WE1 je bila obdelana z grobim brusnim papirjem medtem, ko je bila površina WE2 obdelana s finim brusnim papirjem. Potencial različno grobih površin v fiziološki raztopini pri vzdraženju s specifičnimi stimulacijskimi impulzi je bil merjen glede na Ag/AgCl referenčno elektrodo. Napetostni prehodni pojavi so bili zajeti z namenom določitve polarizacije na prehodu med elektrodo in elektrolitom. Rezultati kažejo, da lahko WE1 dovede na živec več toka in s tem doseže večjo aktivacijo pri konstantni napetosti kot WE2. Izkazuje se namreč, da je polarizacijska upornost $|Z_{pol}|$ pri WE1 manjša kot pri WE2 (237.1 Ω proti 251 Ω). Potemtakem je elektroda, ki je bila brušena z grobim brusnim papirjem, bolj primerna za varno in učinkovito stimulacijo živca, kot elektroda, ki je bila brušena s finim brusnim papirjem.

Ključne besede: platina, polarizacija, prehodi, parametri potenciala

1 INTRODUCTION

In recent decades, considerable scientific and technological efforts have been devoted to understanding and characterizing the interface between a stimulating electrode and its surrounding medium. In this region, a transduction of charge carriers occurs from electrons in the metal electrode to ions in the tissue, which is exceptionally important in determining how the electrodes respond to charge injection. To be specific, characterizing the electrode-tissue interface is crucial to determining safe charge delivery to the nerve.[1–3]

In implantable prosthetic devices, electrodes are the interfaces between the electronic circuitry and nerve tissue and can be used for neural stimulation and/or neural signal recording. In the past few years, implanted electrodes have been used extensively for efficient stimulation of peripheral nervous systems. Although much effort has been made to find optimal anatomical targets for different nerve-stimulation techniques, little work has been done to improve the efficiency of nerve stimulation using analytically driven designs and configurations of the stimulating electrodes.

The electrode geometry itself plays a significant role in controlling the activation of neuron populations.[4] In this connection, the electrode geometry can affect the impedance, spatial distribution of the electric field in the tissue, and consequently the pattern of neural excitation. One approach to enhance the efficiency of neural stimulation is to increase the irregularity of the surface current profile, which can be quantified by defining a metric known as the topological edginess.[5]

In this relation, adequately optimized electrode geometries and surfaces that increase the variation of the current density on the electrode surface also increase the efficiency of the neural stimulation.[5,6] This is in accordance with the suppositions of E. N. Warman et al.[7] and F. Rattay[8]; they showed that electrode-induced neural excitation could be predicted using the driving function of a neuron, which is directly proportional to the second spatial derivative of the extracellular potential and thus, the spatial derivative of the current density in the tissue. Therefore, electrode geometries with a greater roughness and more sharp edges can increase the stimulation efficiency by increasing the spatial derivative of the current density, and therefore the driving function.

However, specific neural stimulation applications sometimes require high electrode charge densities that may lead to high energy transfer and elicit chemical reactions that involve changes in the electrode properties and even corrosion. In this relation, A. Hung et al.[9] described a pulse-clamp technique that could be used to accurately quantify the roughness modification in an electrode used in selective nerve stimulation applications that demand both a large amount of charge injection and a small electrode size. However, to ensure safe and reversible charge injection for stimulation, all applications require low-impedance electrodes. In this relation, the medium surrounding the stimulating electrodes is exceptionally important to determine how they respond to charge injection. Consequently, for the development of chronically implanted multi-electrode devices, an understanding of the electrochemical mechanisms underlying the behavior of neural stimulation electrodes is important.

When platinum is used as the material for stimulating electrodes, it injects charge by both reversible Faradaic reactions and double-layer (DL) charging. However, reversible Faradaic reactions predominate under most stimulating conditions.[10–12] Furthermore, changes in the electrolyte composition adjacent to the electrode and the finite rate of Faradaic reactions can lead to irreversible processes that cause electrode degradation or tissue injury.[13–16]

In most in-vitro experiments, the electrodes were submerged in a certain electrolyte to simulate a specific physiological medium.[17,18] For in-vitro experiments, voltage transient (VT) measurements are used to estimate the charge-injection limit, which defines the quantity of charge that can be injected in a current-controlled stimulation pulse by electrochemical reversible processes only. More precisely, VTs are analyzed to determine the maximum negative polarization (E_{mc}) and maximum positive polarization (E_{ma}) across the electrode-electrolyte interface. These potential extremes are then compared to the established maximum potentials, beyond which it is considered unsafe to polarize the electrode (typically the water electrolysis potential window).[19,20]

Determining the optimum surface roughness for stimulating electrodes is a challenging topic. In recent years, a variety of mechanical adaptations, such as adaptations to the geometry and surface roughness of the electrodes, to contribute to neuro-prostheses designs have been investigated and implemented.[5,6] Namely, the geometry of an electrode significantly affects the shape of the generated electric field, which in turn affects the current density produced by the electrode.

The efficiency of a stimulating electrode is characterized by its ability to activate a certain volume of neural tissue with lower voltage and power requirements.[5,6] Electrode designs involving a greater amount of sharp peaks and edges will have higher current density variations than electrodes with flat or rounded edges (the higher current density variations will increase the stimulation efficiency). Besides, such an electrode activates a significantly larger number of axons with a lower threshold than electrodes with smooth or rounded edges.[21] In this regard, L. Golestanirad et al.[5] demonstrated that the feasibility of increasing the stimulation efficiency using modified fractal geometries is still beyond the levels already reported in the literature. Related experimental studies have shown that neural stimulation can be improved by creating a rougher surface; however, the electrodes are covered with a layer of material with a high porosity.[6,21] Nevertheless, the electrode functionality can also be increased by depositing conducting porous polymers with incorporated cell adhesion peptides, proteins, and anti-inflammatory drugs.[22,23] Most of these improvements could reduce the fibrous tissue encapsulation thickness because of tissue in-growth. However, smooth surfaces would make it more difficult to initiate corrosion.

There is a need to accurately predict the neural activation as a function of the stimulation parameters and electrode design; thus, we evaluate the effects of the electrode surface conditions on the electrochemical performance of the platinum electrode for selective nerve stimulation in vitro.

For this purpose, a method for the in-vitro evaluation of platinum electrodes for use in neural stimulation applications, was developed. The present work focuses on modifying the geometry of the rectangular platinum electrode to produce a higher neural activation function than that achieved by conventional electrodes.[8] In this relation, the aim is to increase the surface current irregularity while maintaining the amount of total current delivered to the tissue. We present the preliminary results for these electrodes with mechanically modified surfaces. Our hypothesis is that such a modified surface could increase the irregularity of the current density profile on the electrode surface, and consequently in the adjacent nerve tissue. For this purpose, a method that enables an in-vitro assessment of the electrochemical performance of stimulating electrodes using modified electrode geo-

metries was developed.[24,25] This article investigates the electrochemical performance of two stimulating electrodes with different surface structures obtained by treating the surface with smooth and rough sand paper.

2 EXPERIMENTAL PART

2.1 Electrochemical cell

The body of the electrochemical cell (**Figure 1**) was machined from bulk polyamide (nylon) using a milling machine. The dimensions and design of the cell were optimized to enable easy manipulation of the electrical connections and three electrodes. For the measurements, a 0.03-mm-thick silicone strip embedding tested electrodes (working electrode number one (WE1) and working electrode number two (WE2)), was adhered onto the top of the cylinder made of polyamide (Novilon) using the medical-grade silicone adhesive. Then, the cylinder was mounted at the bottom of the chamber using a medical-grade silicone adhesive (Med RTV Adhesive, Implant Grade 40064, Applied Silicone Corporation).

In the developed technique, only the working electrode (WE) uncovered face was investigated, while the other surfaces were insulated from the electrolyte. The auxiliary electrode (AE) with a large geometrical area (~600 mm^2) was created by adhering a platinum ribbon to the inner walls of the cell (approximately 20 mm from the WEs and the reference electrode (RE)). The RE was a simple open-ended standard Ag/AgCl glass RE, REF-10 (UNISENSE A/S, Denmark) with an outside tip diameter of 10 µm.

For our measurements, the WE is large enough and the standard glass RE small enough that the surface of the investigated stimulating electrode could be divided into the number of locations where measurements could be performed.

The voltage drop between the RE and WE (actually arising from the series resistance, including the solution resistance between the WE and the RE plus the electrical resistance of the lead wire) was minimized by positioning the RE approximately 0.05 mm from the WE. For this purpose, a 3D micro-manipulator was installed on the chamber.

Prior to experimentation, the WE surface was cleaned by rubbing in a letter-I pattern for a period of 30 s using a polishing cotton tip. Afterwards, the WE surface was rinsed thoroughly with ethanol, then de-ionized with distilled water and air-dried. Finally, the chamber was filled with a phosphate-buffered saline (PBS) solution, as summarized in **Table 1**.

Table 1: PBS solution composition

Component	Mass concentration (g/L)	Molar concentration (mM)	Molar mass (g/mol)
NaCl	7.36	126	58.4425
Na_2HPO_4	11.5	81	141.959
$NaH_2PO4 \cdot H_2O$	3.04	22	137.992
pH = 7.27, T = 21.4 °C			

The measured VT was amplified using one channel of the high-performance differential amplifier (Teledyne LeCroy DA1855A-PR2). However, the voltage drop across the precision serial resistor at the stimulator output (10 Ω) was measured using a custom-designed differential amplifier with the gain (A) set at A = 10. A dual-channel digital oscilloscope (TekScope, Tektronix) was used to monitor both the VT and the drop across the precision serial resistor. The VT measurements between one of the WEs and the AE were performed at room temperature in the PBS solutions (schematically shown in **Figure 2**). The data was collected at 200 kHz using a USB 2.0 interface with a high-performance data-acquisition system (DEWE-43, Dewesoft, Slovenia) and Dewesoft 7.0.2 acquisition software developed by the

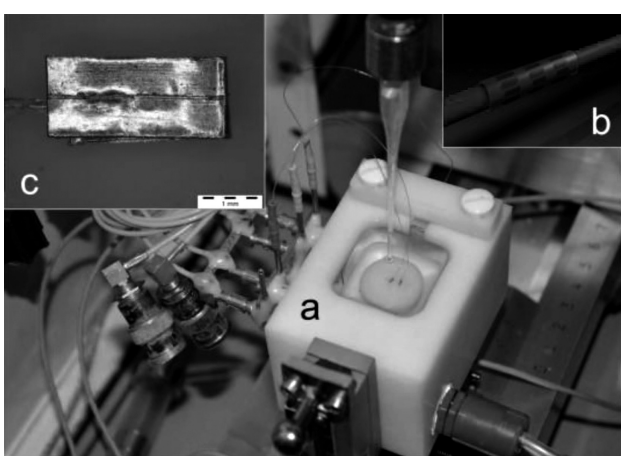

Figure 1: a) Electrochemical cell, b) perspective 3D illustration of the stimulating spiral nerve cuff and c) working electrode

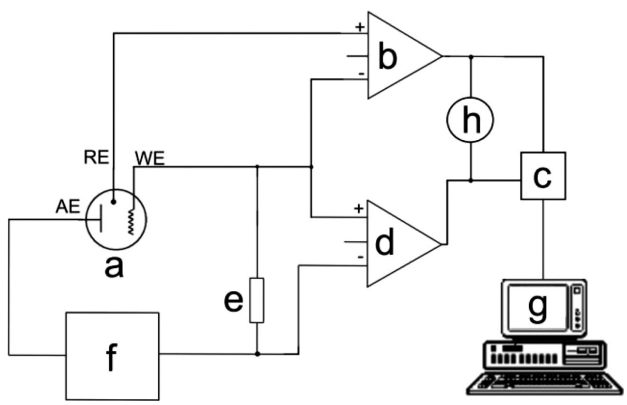

Figure 2: Schematic diagram of the measuring setup comprising the following units: a) electrochemical cell, reference electrode (RE), working electrode (WE), and auxiliary electrode (AE), b) differential amplifier, c) data-acquisition system, d) differential amplifier, e) precision serial resistor (RM), f) precision custom-designed stimulator, g) PC and h) oscilloscope

same company and stored on a portable computer (LenovoT420, China).

2.2 Crafting the working electrodes

Crafting the WEs involved several steps: 1) cutting 0.66-mm-wide strips from the 0.03-mm-thick platinum foil using a sharp blade, 2) cutting two 6-mm-long individual strips, 3) folding the obtained strips into thirds, creating U-shaped forms, and 4) inserting the 2-mm-wide strip made of the silicone sheet between the U-shaped structure to form a sandwich structure. The final dimensions of the electrode surfaces exposed to the PBS were width=0.66 mm, length=3mm, and surface area=2 mm^2.

The interconnection between the WEs and the lead wires was performed using a simple construction custom-designed micro-spot-welder based on a thyristor and powered using a large capacitor discharge by highly experienced and well-trained personnel. An energy of approximately 6 Ws (defined experimentally) provided reproducible results for the proposed application of welding the lead wire (AS 631, Cooner Wire, USA) within the sandwich structure. The welding energy for both electrodes is defined in **Table 2**. This table also provides information for the two different types of sand paper (Waterproof Silica Carbide Paper FEPA P#500 and FEPA P#4000, Struers ApS, Denmark) that were used to increase the real surface of the WEs. Specifically, the surface of WE1 was enlarged using rough sand paper (FEPA P#500) while WE2 was enlarged using fine-grained sand paper (FEPA P#4000). In this relation, each of the WE surfaces was treated by grinding in a letter-I pattern for a period of 10 s using an appointed sand paper and vertical force of approximately 5 N.

In **Figure 1**, WE1 is situated at the right-hand side of the cell and WE2 at the left-hand side of the cell.

Table 2: Welding energy and sand paper used in the experiments

WE	Charging current (A)	Charging voltage (V)	Welding energy (Ws)	Sand paper
1	5	2	6	FEPA P#500
2	5	2	6	FEPA P#4000

2.3 VT measurements

VTs were measured using a biphasic, quasi-trapezoidal current stimulating pulse waveform (pulse) with the intensity of the cathodic phase (i_c), which was previously tested in selective nerve stimulation on an isolated left porcine vagus nerve (not shown in this paper)[26], delivered from the precision custom-designed stimulator between an appointed WE and the AE. The relevant parameters (i_c = -4.0 mA; width of the cathodic phase, t_c = 155 μs; width of the cathodic exponential decay, t_{exp} = 100 μs; time constant of the exponential decay, τ_{exp} = 45 μs; intensity of the anodic phase, i_a = 0.45 mA; width of the anodic phase, t_a = 490 μs; charge density within the cathodic phase, σ_{qc} = -800.00 μC/cm^2; and charge density within the anodic phase, σ_{qa} = 849.00 μC/cm^2) were pre-set by the stimulator. For this pulse, E_{mc} and E_{ma} were measured across the electrode-electrolyte interface. These potentials were then tested to determine whether any of them exceeded the values confining the water electrolysis window, which were defined using cyclic voltammetry (not shown in this paper; [-0.60 V + 0.85 V] measured in PBS).[27–29]

There were several characteristic voltages and potentials that contributed to the entire voltage drop (dV) and were accounted for in the calculations of E_{mc} and E_{ma}: polarization across the electrode-electrolyte interface (dE_p), potential of the WE at the onset of the pulse (E_{ipp}), and access voltage (V_a; drop across the electrolyte resistance plus over-potential terms). E_{mc} is defined by Equation (1):[30]

$$E_{mc} = E_{ipp} + dE_p = E_{ipp} + (dV - V_a) \quad (1)$$

VTs above each of the two WEs were measured from various locations on the surface of the WE while the above-mentioned pulses were applied between the WE and CE. The scanning displacements, transverse according to each of the two WEs, were controlled optically using a precise micrometre dial, while at the same time, they were measured using precise linear potentiometer (20 kΩ) connected to the aforementioned high-performance data-acquisition system. During the scanning, the tip of the RE was situated as close as possible to the WEs using a micrometre enabling precise vertical displacement.

2.4 VT analysis

A set of approximately 160 VTs, each corresponding to a specific location at the investigated WE obtained by the displacement Δx performed by the RE above the WE was measured. Afterwards, each VT in a set was automatically analysed/processed to determine the aforementioned characteristic voltages and potentials that contributed to the entire voltage drop dV. Characteristic voltages and potentials for a certain set (displacement Δx) were then calculated as the mean of all the values in a set. In this regard, the potential of the WE at the onset of the pulse E_{pp} was estimated as the mean value of 50 measured signal samples before the onset of the pulse. The points that determine the voltage V_a and the potential E_{ma} of the VT are located at pulse times where the rate of change of inclination of the signal tangent is high. Thus, the times t_{V_a} and $t_{E_{ma}}$ of those points were estimated by locating local maxima of the second derivative of the voltage response. The second derivative of the signals was estimated by convolving the signals with a digital filter of the form [-1 0 1] twice. The voltage V_a and the potential E_{ma} for voltage transient $V(t)$ are defined as shown in Equations (1) and (3):

$$V_a = \left| E_{ipp} - V(t_{V_a}) \right| \quad (2)$$

$$E_{ma} = V(t_{E_{ma}}) \quad (3)$$

Once we have the estimations for V_a and E_{ma}, the calculation of all the other voltage and potentials shown in Equations (4), (5) and (6), is straightforward:

$$\Delta V = \left| E_{ipp} - \min_t V(t) \right| \quad (4)$$

$$\Delta E_p = \Delta V - V_a \quad (5)$$

$$E_{mc} = \min_t V(t) + V_a \quad (6)$$

Afterwards, the polarization impedance |Zpol| was calculated as dE_p/ic at location x, where the RE was the closest to the WEs, i.e., at the middle of the electrodes.

3 RESULTS AND DISCUSSION

Figure 3 shows the stimulation pulse and elicited VT with the indicated characteristic voltage and potential elements that contributed to dV, i.e., E_{ipp}, V_a, and dE_p in both WEs. These elements were then accounted for in the calculation of E_{mc} and E_{ma} in each of the two WEs.

Figure 3 shows that the onset of i_c elicited the near-instantaneous VT voltage, where V_a could be easily determined at the instant rise. However, when i_c was terminated, the behavior of the potential in the exponential decay region where i_c was exponentially approaching the lowest value prevented an easy determination of V_a. In this regard, the analysis technique described by Cogan[30], which introduced a short interruption of the stimulation current between the cathodic and anodic phase of the pulse, could not be used because of the quasi-trapezoidal stimulation waveform used in the study.

E_{mc} and E_{ma}, scanned over WE1 and WE2, are demonstrated in **Figure 4**. The figure also shows the values for E_{ipp}, dV, V_a, and dE_p.

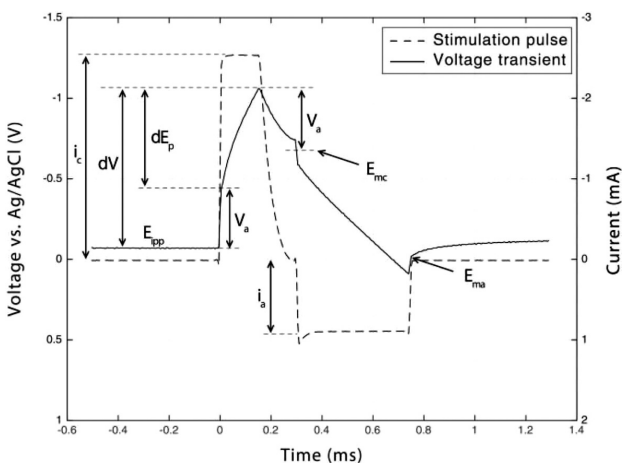

Figure 3: Stimulation pulse and elicited VT in WEs with the indicated elements that contributed to the entire voltage drop, d*V*

3.1 Results for WE1

Figure 4 shows that the average dE_p in WE1 is 0.59 V. The value of V_a is 0.24 V, while the value of E_{ipp} is -0.11 V. It is difficult to accurately measure V_a when i_c is terminated, which is a practical issue when determining E_{mc}, as shown in **Figure 3**. However, E_{ma} was determined with relative ease. As in the VT of the pulse used, E_{mc} and E_{ma} reached values of -0.7 V and -0.01 V, respectively. Accordingly, E_{mc} slightly exceeded the safe potential limits for water electrolysis, while E_{ma} remained slightly negative and did not exceed this limit. **Figure 4** also shows that WE1 was cathodically limited for the pulse waveform used; i.e., E_{mc} reached the cathodic limit before E_{ma} reached the anodic limit of the water electrolysis window. d*V* was 0.83 V across the electrode-electrolyte interface.

3.2 Results for WE2

Figure 4 shows that the average dE_p in WE2 was 0.615 V; the value of V_a was 0.109 V, and the value of E_{ipp} is -0.075 V. Again, the practical issue in determining

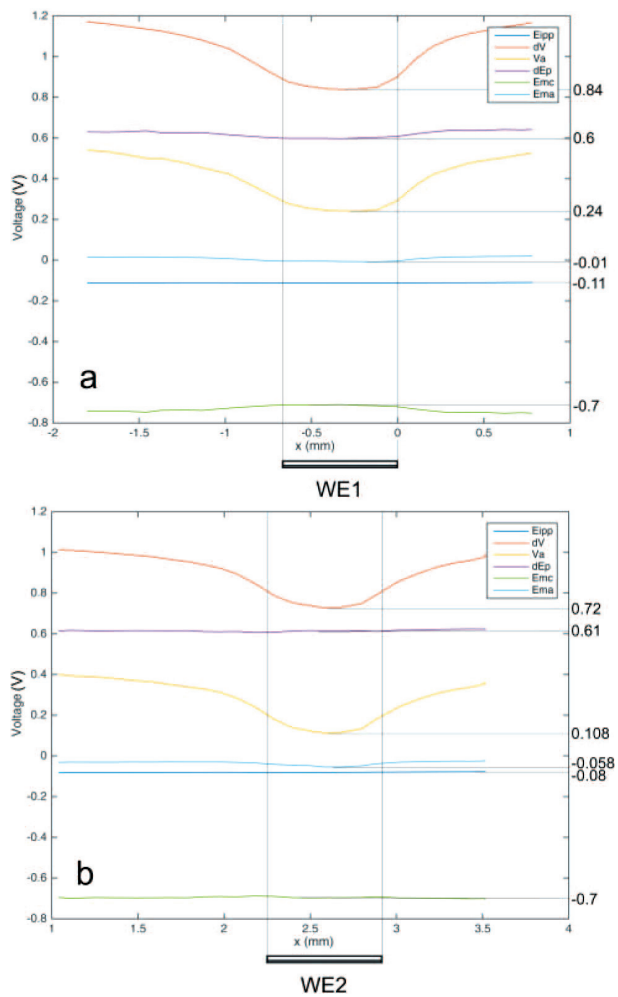

Figure 4: Schematic side-view diagram of the WEs and variables, E_{ipp}, d*V*, V_a, dE_p, E_{mc}, and E_{ma}: a) WE1 and b) WE2

E_{mc} (**Figure 3**) is the difficulty in accurately measuring V_a when i_c is terminated. E_{mc} and E_{ma} reached values of -0.7 V and -0.054 V, respectively as for the VT of the pulse. Accordingly, E_{mc} slightly exceeded the safe potential limits for water electrolysis, while E_{ma} (determined with relative ease) remained slightly negative and did not exceed this limit. **Figure 4** also shows that WE2 was cathodically limited at the pulse waveform that was used; i.e., E_{mc} reached the cathodic limit before E_{ma} reached the anodic limit of the water electrolysis window. dV was 0.72 V across the electrode-electrolyte interface.

Figure 5 shows the voltage changes of the variables dE_p, E_{mc}, and E_{ma} as scanned over WE1 and WE2. The average variability in E_{mc} and E_{ma} were assumed to increase as the number of sharp peaks and edges produced on the surface of WE1 increased.[31] These results support the hypothesis, i.e., that the current density would decrease with a greater number of sharp peaks and edges on WE1. Finally, **Table 3** shows $|Z_{pol}|$ calculated from dE_p/ic at x, where the RE was the closest to the WEs, i.e., at the middle of electrodes.

Table 3: Polarization impedance $|Z_{pol}|$ for WE1 and WE2 derived from two scans

		dEp (V)					
		WE1			WE2		
		First scan	Second scan	Mean value	First scan	Second scan	Mean value
|Zpol| (Ω)	238,8	235,4	237,1	256	246	251	

The results indicate that the surface of WE1 (modified with rough sand paper) delivers more current to the nerve tissue and more activation for a fixed input voltage than WE2 (modified with fine sand paper). Consequently, as the total delivered current is reduced, this activation is obtained at a relatively reduced input power.

Our results are consistent with the results of other investigators.[5] Namely, in the study, the pulse was predefined to retain a near-zero net charge while employing an asymmetry in the current and pulse widths for the cathodic and anodic phases.[30] By doing so, the E_{ipp} of both WEs is maintained within a potential range that avoids WE damage and potential tissue injury. In clinical practice, the latter is generally more of a concern than damage to the WE. The relatively large real area of both WEs obtained by mechanical roughening is largely responsible for accommodating a certain amount of charge on the DL prior to initiating the Faradaic reactions. However, WE1 presumably accommodated larger amounts of charge than WE2. The electrode impedance is strongly related to the surface area at the interface between the electrode and the electrolyte.

Roughening the surface of both the WEs significantly decreases the $|Z_{pol}|$ of the WE-electrolyte interface, while significantly increasing the capacitance of the DL.[32] However, the results show that the $|Z_{pol}|$ of the WE1-electrolyte interface decreased more than that of the WE2-electrolyte interface and the capacitance of the DL was reversed. Both WEs presumably produce a uniform charge density over each WE, which permits maximum utilization of the proprietary WE surface.[33] **Table 3** shows that the mean $|Z_{pol}|$ of WE1 was lower than that for WE2 (237.1 Ω vs. 251 Ω), which confirmed our initial presumption.[34]

One weakness of the developed method is the sensitivity of the VT measurements with respect to the distance between the WEs and RE. Fortunately, this weakness could be minimized using the optical system, enabling precise control of this distance.

The results support our hypothesis that the E_{ipp} of WE1 at the onset of the predefined pulse (-0.83 V) settles at a slightly more negative value at the end of the pulse, indicating that it changes in a negative direction (refer to the measured VT in **Figure 3**). Presumably, E_{mc} slightly breaks the cathodic limit before E_{ma} reaches the anodic limit of the water electrolysis window because of the asymmetric predefined pulse. Consequently, the functionality of WE1 is cathodically limited. This suggests that E_{mc} slightly exceeds the safe potential limits of water electrolysis [-0.65 V to +0.85 V] while the E_{ma} potential does not. Similarly, the E_{ipp} of WE2 at the onset of the predefined pulse of -0.75 V is also settled at a slightly more negative value at the end of the pulse, indicating that it does change less significantly in a negative direction. The functionality of WE2 is also cathodicaly limited.

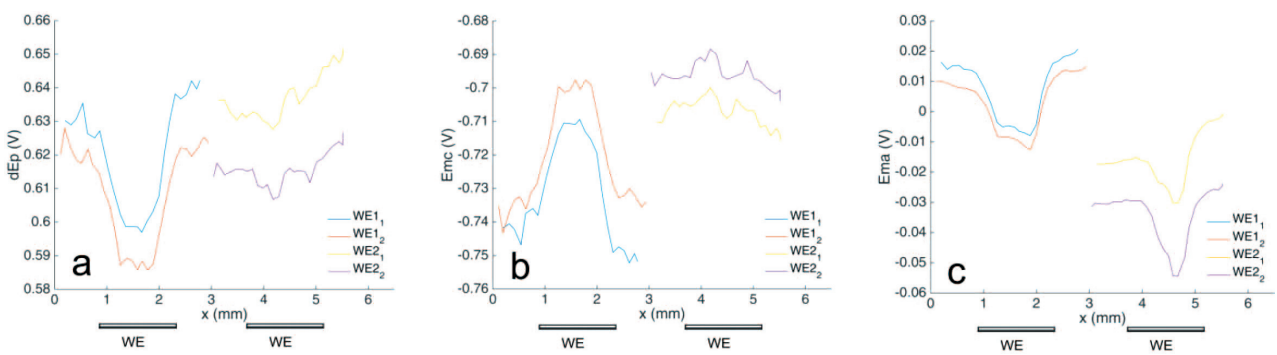

Figure 5: Comparison of dE_p (left), E_{mc} (middle), and E_{ma} (right) with respect to x for WE1 and WE2

In this regard, C. Newbold et al.[22] showed that the WE is polarized until another (possibly irreversible) reaction is recruited to maintain the i_c if i_c exceeds the rate at which the counterions for the intended reversible processes are transported to or from the WE. This can happen in vivo, where the i_c distribution can lead to much larger potentials at the edges of the WEs, resulting in possible WE degradation. Considering these results, the described modification of the surface could potentially require less input power, while maintaining the same level of neural activation in vivo.

4 CONCLUSIONS

Superficially modified WE1 (using rough sand paper) elicited an increased irregularity and decrease of the current density profile on the surface and consequently in the adjacent nerve tissue in vivo using current pulses. Furthermore, superficially modified WE2 (using fine sand paper) elicited a slightly decreased irregularity and corresponding increase of the current density profile on the surface and consequently in the adjacent nerve tissue in vivo under the same conditions. Thus, the impedance of WE1 is lower than that of WE2. Accordingly, WE1 is more suitable for safe stimulation than WE2.

However, these promising observations warrant extensive in-vivo testing. Future investigations should focus on the involvement of VT measurements and an impedance characterization of the platinum WE in the presence of proteins in vitro and acutely in vivo.

These preliminary findings suggest that the development of such scanning electrochemical methods could potentially provide significant advantages in targeting specific neural populations, allowing optimized therapeutic protocols. This study has contributed to the further development of multi-electrode spiral cuffs for the efficient and safe selective stimulation of autonomous peripheral nerves and the simultaneous selective recording of neural responses.

Acknowledgment

This work was financed by research grant P3-0171 from the Slovenian Research Agency (ARRS), Ministry of Education, Science and Sport, Ljubljana, Republic of Slovenia.

5 REFERENCES

[1] C. R. Butson, C. C. McIntyre, Tissue and electrode capacitance reduce neural activation volumes during deep brain stimulation, Clin. Neurophysiol., 116 (**2005**), 2490–2500

[2] S. B. Brummer, M. J. Turner, Electrical stimulation of the nervous system: the principle of safe charge injection with noble metal electrodes, Bioelectrochem. Bioenerg., 2 (**1975**), 13–25

[3] D. R. Merrill, M. Bikson, J. G. R. Jefferys, Electrical stimulation of excitable tissue: design of efficacious and safe protocols, J. Neurosci. Methods, 141 (**2005**), 171–198

[4] X. F. Wei, W. M. Grill, Analysis of high-perimeter planar electrodes for efficient neural stimulation, Front. Neuroeng., 2 (**2009**), 15

[5] L. Golestanirad, B. Elahi, A. Molina, J. R. Mosig, C. Pollo, R. Chen, S. J. Graham, Analysis of fractal electrodes for efficient neural stimulation, Front. Neuroeng., 6 (**2013**), 3

[6] N. Pour Aryan, H. Kaim, A. Rothermel, Electrode Materials: State-of-the-Art and Experiments, in: Stimulation and Recording Electrodes for Neural Prostheses, Springer International Publishing, Cham, 78 (**2015**), 45–64

[7] E. N. Warman, W. M. Grill, D. Durand, Modeling the effects of electric fields on nerve fibers: determination of excitation thresholds, IEEE Trans. Biomed. Eng., 39 (**1992**), 1244–1254

[8] F. Rattay, Analysis of models for extracellular fiber stimulation, IEEE Trans. Biomed. Eng., 36 (**1989**), 676–682

[9] A. Hung, D. Zhou, R. Greenberg, I. B. Goldberg, J. W. Judy, Pulse-clamp technique for characterizing neural-stimulating electrodes, J. Electrochem. Soc., 154 C (**2007**), 479–486

[10] L. S. Robblee, J. McHardy, W. F. Agnew, L. A. Bullara, Electrical stimulation with Pt electrodes. VII. Dissolution of Pt electrodes during electrical stimulation of the cat cerebral cortex, J. Neurosci. Methods, 9 (**1983**), 301–308

[11] L. S. Robblee, J. McHardy, J. M. Marston, S. B. Brummer, Electrical stimulation with Pt electrodes. V. The effect of protein on Pt dissolution, Biomaterials, 1 (**1980**), 135–139

[12] S. B. Brummer, M. J. Turner, Electrochemical considerations for safe electrical stimulation of the nervous system with platinum electrodes, IEEE Trans. Biomed. Eng., 24 (**1977**), 59–63

[13] T. L. Rose, L. S. Robblee, Electrical stimulation with Pt electrodes: VIII. Electrochemically safe charge injection limits with 0.2 ms pulses, IEEE Trans. Biomed. Eng., 37 (**1990**), 1118–1120

[14] D. B. Hibbert, K. Weitzner, B. Tabor, P. Carter, Mass changes and dissolution of platinum during electrical stimulation in artificial perilymph, Biomaterials, 21 (**2000**), 2177–2182

[15] D. B. McCreery, W. F. Agnew, T. G. Yuen, L. Bullara, Charge density and charge per phase as cofactors in neural injury induced by electrical stimulation, IEEE Trans. Biomed. Eng., 37 (**1990**), 996–1001

[16] W. F. Agnew, D. B. McCreery, T. G. H. Yuen, L. A. Bullara, Evolution and resolution of stimulation-induced axonal injury in peripheral nerve, Muscle Nerve, 22 (**1999**), 1393–1402

[17] P. F. Johnson, L. L. Hench, An in vitro model for evaluating neural stimulating electrodes, J. Biomed. Mater Res. 10 (**1976**), 907–928

[18] L. A. Geddes, R. Roeder, Criteria for the selection of materials for implanted electrodes, Ann. Biomed. Eng., 31 (**2003**), 879–890

[19] M. Stevenson, K. Baylor, B. L. Netherton, M. M. Stecker, Electrical stimulation and electrode properties. Part 2: pure metal electrodes, Am. J. Electroneurodiagnostic Technol., 50 (**2010**), 263–296

[20] E. M. Hudak, J.T. Mortimer, H.B. Martin, Platinum for neural stimulation: voltammetry considerations, J. Neural. Eng., 7 (**2010**), 026005

[21] M. M. Benmassaoud, M. V. Meller, S. Kuchibhatla, X. F. Wei, Novel fractal planar electrode design for efficient neural stimulation, Proc. 1st IEEE student EMBS, Orlando, FL, USA, (**2015**), 4 pages

[22] C. Newbold, R. Richardson, R. Millard, C. Huang, D. Milojevic, R. Shepherd, R. Cowan, Changes in biphasic electrode impedance with protein adsorption and cell growth, J. Neural. Eng. 7 (**2010**), 056011

[23] N. K. Guimard, N. Gomez, C. E. Schmidt, Conducting polymers in biomedical engineering, Prog. Polym. Sci., 32 (**2007**), 876–921

[24] T. Ragheb, L. A. Geddes, Electrical properties of metallic electrodes, Med. Biol. Eng. Comput., 28 (**1990**), 182–186

[25] A. Hung, I. B. Goldberg, J, W. Judy, Stimulation electrode materials and electrochemical testing methods, Implantable Neural Prostheses, D. Zhou, E. Greenbaum, 2 (**2010**), 191–216

[26] P. Pečlin, J. Rozman, Alternative paradigm of selective vagus nerve stimulation tested on an isolated porcine vagus nerve, The Scientific World Journal, 1 (**2014**), 310283

[27] P. Pečlin, A. Mehle, B. Karpe, J. Rozman, Electrochemical and electrophysiological performance of platinum electrodes within the ninety-nine-electrode stimulating nerve cuff, Artif. Organs, 39 (**2015**), 886–896

[28] N. de N. Donaldson, P. E. K. Donaldson, When are actively balanced biphasic ('Lilly') stimulating pulses necessary in a neurological prosthesis?: I. Historical background; Pt resting potential; Q studies, Med. Biol. Eng. Comput., 24 (**1986**), 41–49

[29] N.de N. Donaldson, P. E. K. Donaldson, When are actively balanced biphasic ('Lilly') stimulating pulses necessary in a neurological prosthesis?: II. pH changes; noxious products; electrode corrosion; discussion, Med. Biol. Eng. Comput., 24 (**1986**), 50–56

[30] S. F. Cogan, Neural stimulation and recording electrodes, Annu. Rev. Biomed. Eng., 10 (**2008**), 275–309

[31] J.S. Temenoff, A.G. Mikos, Biomaterials: The Intersection of Biology and Materials Science, Pearson/Prentice Hall, Upper Saddle River, NJ, USA, (**2008**), 235–258

[32] B. Onaral, H. P. Schwan, Linear and nonlinear properties of platinum electrode polarisation. Part 1: frequency dependence at very low frequencies, Med. Biol. Eng. Comput., 20 (**1982**), 299–306

[33] D. A. Ksienski, A minimum profile uniform current density electrode, IEEE Trans. Biomed. Eng., 39 (**1992**), 682–692

[34] W. Franks, I. Schenker, P. Schmutz, A. Hierlemann, Impedance characterization and modeling of electrodes for biomedical applications, IEEE Trans. Biomed. Eng., 52 (**2005**), 1295–1302

UDK 621.18.08:621.9.08
Original scientific article/Izvirni znanstveni članek

ISSN 1580-2949
MTAEC9, 51(6)989(2017)

OPTIMIZATION OF MICRO-EDM PARAMETERS USING GREY-BASED FUZZY LOGIC COUPLED WITH THE TAGUCHI METHOD

OPTIMIZACIJA PARAMETROV MIKROELEKTROEROZIJE Z UPORABO MEHKE LOGIKE V POVEZAVI S TAGUCHI METODO

Muthiyalu Shanmugam Vijayanand[1], Mani Ilangkumaran[2]

[1]Paavai Engineering College, Department of Mechanical Engineering, Pachal, 637018 Namakkal, Tamilnadu, India
[2]K.S.R. College of Technology, Department of Mechatronics Engineering, Tiruchengode, 637018 Namakkal, Tamilnadu, India
msvijayanand08@gmail.com

Prejem rokopisa – received: 2017-04-29; sprejem za objavo – accepted for publication: 2017-07-28

doi:10.17222/mit.2017.048

The correct selection of process parameters for the best performance output of a micro-electro-discharge machining (Micro-EDM) process is challenging because the performance measures of micro-EDM are non linear. This work aims to solve and control complex non-linear systems by applying the hybrid grey-based fuzzy logic together with the Taguchi technique in the field of micro-EDM. Input parameters, namely, the discharge current, pulse-off time and pulse-on time were selected to obtain the target responses such as the material-removal rate (*MRR*) and tool-wear rate (*TWR*). Nine experiments were performed based on the Taguchi L_9 orthogonal array. An analysis of variance was performed to find the significant contribution of the intervening process parameter in a single performance characteristic using the grey-based fuzzy-logic expert system. Multi-performance characteristics indexes (MPCIs) were analysed and the results were calculated with good accuracy.

Keywords: ANOVA, fuzzy logic, orthogonal array, grey-based Taguchi technique, electrical-discharge machining, drilling

Pravilna izbira procesnih parametrov za doseganje najboljšega izkoristka procesa mehanske obdelave z mikroelektro erozijo (angl. Micro-EDM) je izziv, ker so procesni parametri mikro-EDM nelinearni. Namen pričujoče raziskave je bil reševanje in nadzor kompleksnih nelinearnih sistemov mikro-EDM mehanske obdelave z uporabo hibridne mehke logike (Grey-based fuzzy logic) v povezavi s Taguchi metodo. Avtorji raziskave so izbrali naslednje vhodne parametre: razelektritveni tok, čas vklopa in čas izklopa impulza. Na njihovi osnovi so dobili odgovore na zastavljeni vprašanji; kakšna je hitrost odstranjevanja materiala in kakšna je hitrost obrabe orodja. Na podlagi Taguchi L9 ortogonalne matrike so izvedli devet praktičnih preizkusov mehanske obdelave z μ-EDM. Izvedli so analizo variance, podprto z ekspertnim sistemom na osnovi mehke logike, da bi ugotovili učinek intervencijskega procesnega parametra pri eni sami spremenljivki. Določili so indekse učinkovitosti (angl. MPCIs) in izračunani rezultati so bili zelo točni.

Ključne besede: analiza variance (ANOVA), mehka logika, ortogonalna matrika, robustna statistična Taguchi metoda, mikro elektroerozija (μ-EDM), vrtanje

1 INTRODUCTION

In recent technological advancements, the products are to be lighter, thinner and smaller. Many advantages arise when a part is miniaturized, such as energy and space savings, accelerating chemical reactions, attractive appearance, and cost-effectiveness.[1] The Monel 400 alloy is considered as the most promising and the most commonly used nickel-based alloy because of its excellent corrosion resistance and toughness over a wide temperature range. The Monel alloy has been extensively used in the chemical industry, food-processing industry, heat-exchanger tubes, nuclear reactors, sub marines and ship propellers.[2] The Monel alloy work hardens rapidly as it undergoes a high strain during machining. This hardening effect decreases further machining of the alloys. Therefore, it is very difficult to machine these alloys using conventional machine tools.[3] Several research works[4–6] have been carried out and reported on machining the nickel-based alloys using different conventional and non-conventional machining methods. Micro-machining is the most fundamental technology used for the production of miniaturized parts and components.[7] Micro-EDM has been known as one of the indispensible micro-machining techniques with obvious advantages of machining complex structures with high aspect ratios, high precision and accuracy irrespective of workpiece material's hardness and toughness.[8] Micro-EDM uses electrical discharge between two electrodes, and the spark from them generates such an extremely high temperature that the material is removed by vapor bubble.[9]

Many studies[1–3] were performed previously on machining nickel-based alloys with EDM and electro-chemical machining. P. Kuppan et al.[10] investigated the effect of various process variables of EDM in deep-hole drilling of Inconel 718. The objective of this study is to investigate the interaction effects of the process variables such as peak current, pulse-on time, duty factor, and electrode speed on machining characteristics. The results reveal that the material-removal rate is more influenced

by the factors such as peak current, pulse-on time and duty factor. H. S. Liu et al[11] investigated the characterization of high-alloy micro-holes using micro-EDM. In this study, it was reported that the discharge current significantly affects the process. To achieve the optimum results, a proper discharge current is required. I. Ayesta et al.[12] investigated the influence of EDM variables on the machining slot in the C1023 aeronautical alloy. The objective of this study is to determine the effects of the parameters related to the discharge process (current, pulse time and voltage) on the machining rate and electrode wear. The results reveal that the discharge current and pulse-on time are the most influencing process parameters. V. Kumar et al.[13] investigated the wire-electrical-discharge machining of the Monel 400 alloy using the response-surface methodology. A high discharge energy increases the extent of the surface damage and results in large diameter craters on the machined surface. A low discharge energy and a high value of the pulse interval leads to minimum defects on the machined surface.

Trim-cut operations were performed to improve the surface integrity at high discharge-energy levels. However, EDM is a multi-input and multi-output process. Some research works were carried out to optimize the EDM process and to select the optimum process parameters for improving the performance of the process. J. Kao et al.[14] explained an experimental approach to determine the EDM-process-parameter optimization of the Ti 6Al 4V alloy using the Taguchi method and grey relational analysis by considering multiple performance characteristics, namely, the electrode-wear ratio, material-removal rate and surface roughness. The pulse duration, discharge current, open voltage and duty factor are the inputs considered. B. Pradhan et al.[15] tried to optimize the micro-EDM process using the response-surface methodology while machining Ti-6Al-4V. The observed results reveal that the pulse-on time was the foremost affecting parameter for the material-removal rate, overcut and taper, whereas the tool-wear rate was mostly affected by the peak current. In this work, we investigated the effects of the process parameters on the material-removal rate and tool-wear rate while producing micro-holes in the Monel 400 alloy using micro-EDM. Three important process parameters were studied and modeled for the material-removal rate and tool-wear rate using the grey-based fuzzy-logic method coupled with the Taguchi technique.

2 MULTI-RESPONSE OPTIMIZATION USING GREY-BASED FUZZY APPROACH

The grey-relational-analysis theory initialized by J. L. Deng[16] makes use of this technique to handle an uncertain systematic problem with only partially known information. The grey relational analysis is a method of measuring the degree of approximation among the sequences according to the grey relational grade. The theories of the grey relational analysis have already attracted the interest of researchers in various manufacturing processes that include electric-discharge machining.[17–20] In this research, the objective is to convert the complex multiple-objective optimization into a single grey-fuzzy reasoning grade. In the grey relational analysis, pre-processing of the experimental data includes the measured values of response attributes that are normalized first. During the normalization, the parameter range is restricted between 0 and 1 because of the use of different units and scales for the attributes. This process is called the grey relational generation. Next, on the basis of the normalized experimental data, the grey relational coefficient is evaluated to represent the deviation between the desired and actual experimental data. Finally, the overall grey relational grade is evaluated by taking the average of the grey relational coefficients corresponding to the selected responses. The optimum parameter combination is then determined, resulting in the highest grey relational grade.[21] The overall performance characteristic of the multiple-response performance characteristics depends on the calculated grey relational grade. The grey relational grade is calculated on the basis of the "lower-the-better", "higher-the-better" or "nominal-the-best" characteristics of each multiple response and hence, there is still some degree of unclearness about the obtained optimal result. The theory of fuzzy logic provides a means for representing the uncertainties associated with vagueness, imprecision and/or lack of information regarding the problem in hand.[22]

The theory of fuzzy logic formulated by L. A. Zadeh[23] is a proven technique and has been useful in dealing with uncertain and vague information. The definition of the objectives contains a certain degree of unclearness with vagueness. Hence, the fuzzy logic is applied to establish the optimal setting of the parameters for multiple objectives. In this way, a complex multi-objective problem is converted into a single-objective optimization problem.

2.1 Proposed methodology

The following are the procedural steps adopted to solve the multi-response optimization problem using the grey-based fuzzy logic for micro-EDM:

1. Identification of the important response parameter and key-process input parameters to be evaluated.
2. Selection of the appropriate orthogonal array to design the plan of experiment.
3. Conducting experiments as per the experimental plan.
4. Evaluation of the output response based on the experimental results.
5. Pre-processing of the raw data that is normalized for the experimental results using Equations from (1) to (3).

6. Computation of the grey-relational coefficient of the machining parameters using Equation (4).
7. Ascertaining the membership function to fuzzify the grey relational coefficient of each response and the generation of the fuzzy rule.
8. Determination of the fuzzy multi-objective outputs with a defuzzification of the output linguistic variables into crisp values representing the grey-fuzzy reasoning grade.

3 EXPERIMENTAL PART

The process parameters, selected for this investigation, were the discharge current, pulse-on time and pulse-off time as they significantly influence the EDM process performances.[10–12] Their influence on the material-removal rate and tool-wear rate was tested through a set of planned experiments based on the L_9 orthogonal array of Taguchi's design of experiments. **Table 1** shows the factors and their levels with coded and actual values. **Figure 1** shows a photographic view of the experimental EDM apparatus. The commercially obtained Monel 400 alloy having a thickness of 5 mm was used as the workpiece material. The chemical composition (mass fractions, *w*/%) of the Monel 400 alloy is as follows: C (0.047 %), Si (0.172 %), Mn (1.03 %), P (0.012 %), S (0.01 %), Cr (0.1 %), Mo (0.1 %), Fe (1.66 %), V (0.029 %), Co (0.103 %), Nb (0.1 %), Ti (0.047 %), Mg (0.031 %) and Ni (67.4 %). A brass electrode (Cu: 61.8 %, Zn: 37.2 % and impurities: 1.0 %) with a diameter 2.0 mm was selected to drill holes in the workpiece. Commercial-grade kerosene was used as the dielectric fluid and side injection of the dielectric fluid was selected.

Figure 1: Electrical-discharge-machine set-up

4 TAGUCHI TECHNIQUE

The Taguchi technique has been widely used in DOE (design of experiment), and it was employed for creating the experimental design.[24] The Taguchi technique provides standardized methods for each of the DOE application steps. It uses a special design of orthogonal arrays to study the entire process-parameter space with only a small number of experiments.[25] The aim of conducting an orthogonal experiment is to find the optimum level for each factor and to ascertain the relative importance of individual factors in terms of their main effects on the response. The experimental data is presented in **Table 2**. The data is then transformed into a signal-to-noise ratio that can be used to measure the quality characteristics. Taguchi projected three classes of objective functions such as the smaller-the-better, larger-the-better and nominal-the-best for optimizing the static problems.

Table 1: Process parameters and their levels

Parameters	Factors	Levels		
		1	2	3
Pulse-off time (μs)	A	2	3	4
Discharge current (A)	B	4	5	6
Pulse-on time (μs)	C	4	5	6

Table 2: Experimental data

Trial Nos	A	B	C	Material-removal rate	Tool-wear rate
1	1	1	1	0.00353	0.01972
2	1	2	2	0.00909	0.05390
3	1	3	3	0.01010	0.07985
4	2	1	2	0.00308	0.02246
5	2	2	3	0.00446	0.03022
6	2	3	1	0.00688	0.05934
7	3	1	3	0.00273	0.02156
8	3	2	1	0.00395	0.03404
9	3	3	2	0.00876	0.05934

5 RESULTS AND DISCUSSION

5.1 Grey-fuzzy analysis

5.1.1 Normalization of the signal-to-noise ratio

In micro-EDM, the response variables are normalized. Depending on the quality characteristics, Equation (1) is for higher-the-better and Equation (2) is for smaller-the-better.

Higher-the-better:

$$X_i(k) = \frac{Y_i(k) - \mathrm{Min}Y_i(k)}{\mathrm{Max}Y_i(k) - \mathrm{Min}Y_i(k)} \quad (1)$$

Smaller-the-better:

$$X_i(k) = \frac{\mathrm{Max}Y_i(k) - Y_i(k)}{\mathrm{Max}Y_i(k) - \mathrm{Min}Y_i(k)} \quad (2)$$

Here: $X_i(k)$ = is the value after the grey relational generation; min $Y_i(k)$ is the smallest value of $Y_i(k)$ for the k^{th} response, and max $Y_i(k)$ is the largest value of $Y_i(k)$ for the k^{th} response.

5.1.2 Computing the grey relational coefficient and grade

On the basis of the normalized experimental data, the grey relational coefficient is evaluated using Equation (3) to represent the deviation between the desired and the actual experimental data. The grey relational coefficient $\xi_i(k)$ can be calculated as:

$$\xi_i(k) = \frac{\Delta_{\min} + \zeta \cdot \Delta_{\max}}{\Delta_{0i}(k) + \zeta \cdot \Delta_{\max}} \quad (3)$$

Here $\Delta_{0i} = \left\| X_0(k) - X_i(k) \right\|$ $\Delta_{0i} = \left\| x_0(k) - x_i(k) \right\|$ the difference between the absolute values of $x_o(k)$ and $x_i(k)$; it is the distinguishing coefficient $0 \leq \Psi \leq 1$:

$\Delta_{\min} = \forall j^{\min} \in i \; \forall k^{\min} \left\| x_0(k) - x_i(k) \right\|$ = the smallest value of Δ_{0i}

$\Delta_{\max} = \forall j^{\max} \in i \; \forall k^{\max} \left\| x_0(k) - x_i(k) \right\|$ = the largest value of Δ_{0i}.

After averaging the grey relational coefficients, the grey relational grade can be computed as:

$$\gamma_i = \frac{1}{n} \sum_{k=1}^{n} \xi_i(k) \quad (4)$$

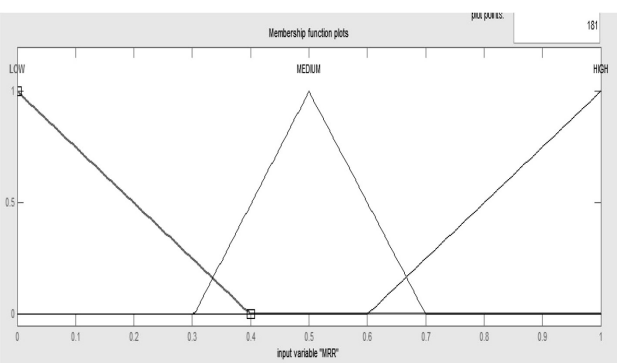

Figure 2: Membership function for the metal-removal rate

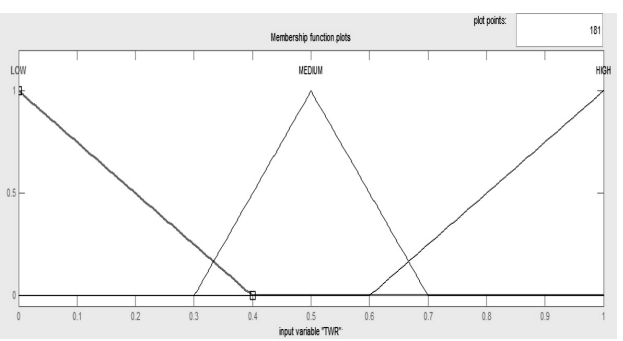

Figure 3: Membership function for the tool-wear rate

Here, n = the total number of process responses. The higher value of the grey relational grade corresponds to the intense relational degree between the reference sequence $X_0(k)$ and the given sequence $X_i(k)$.The reference sequence $X_0(k)$ represents the best process sequence. Therefore, a higher grey relational grade means that the corresponding parameter combination is closer to the optimal value. The calculated grey relational coefficients for the material-removal rate and tool-wear rate are presented in **Table 3**.

5.2 Fuzzy-logic approach

A fuzzy-logic unit comprises a fuzzifier, an interference engine and a defuzzifier. In the fuzzy-logic analysis, the methodology involves the fuzzification of the membership functions into fuzzy subsets, corresponding to linguistic terms, the derivation of fuzzy rules (if-then control rules) on the knowledge base to generate the fuzzy value, and finally, the defuzzification of the fuzzy value into a multi-performance characteristics index (MPCI).

Table 3: Normalized values and grey relational coefficients

Exp. No.	Normalized values of *MRR*	Normalized values of *TWR*	Grey relational coefficients of *MRR*	Grey relational coefficients of *TWR*
1	0.1964	0.0000	0.3828	0.3333
2	0.9194	0.7253	0.8611	0.6454
3	1.0000	1.0000	1.0000	1.0000
4	0.0922	0.0943	0.3551	0.3557
5	0.3751	0.3078	0.4444	0.4193
6	0.7063	0.7930	0.6299	0.7072
7	0.0000	0.0654	0.3333	0.3485
8	0.2823	0.3935	0.4106	0.4518
9	0.8912	0.7935	0.8212	0.7077

5.3 Fuzzification

The proposed model was developed in a MATLAB environment using the fuzzy-logic tool box. The fuzzifier converts the real value of input into fuzzy linguistics terms. Here, the values of individual grey relational coefficients of the material-removal rate and tool-wear rate are used as input variables, and the multi-performance characteristics index (*MPCI*) is considered as an output variable. For each input and output response, a triangular membership function is used. In this model, the triangular membership function is used for describing the inputs, namely, small, medium and large ones as shown in **Figures 2** and **3**. Similarly, five membership functions are mapped and they are indicated as very low, low, medium, high and very high, all being used as fuzzy subsets for the output-response grey-fuzzy reasoning grade (*MPCI*) as shown in **Figure 4**.

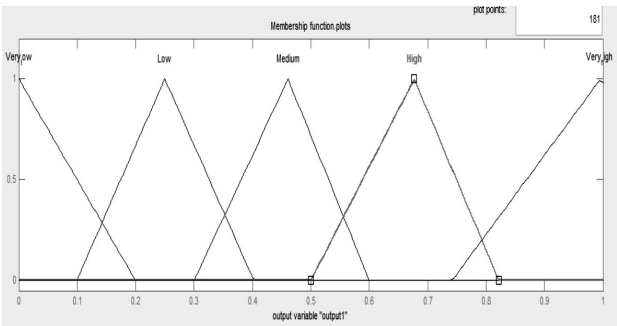

Figure 4: Membership function for the grey-fuzzy reasoning grade

5.4 Fuzzy inferencing

The next stage of the fuzzy-logic system is to derive the if-then rules to represent the relationship between the input and output variables based on linguistics terms.[26] In this study, nine control rules are written using the rule editor for the best fit of the model, which is presented in **Table 4**.

Table 4: Fuzzy rules in the matrix form

Fuzzy rule for grey-fuzzy model		Normalized value of *TWR*		
		Small	Medium	Large
Normalized value of *MRR*	Small	Medium	Low	Very low
	Medium	High	Medium	Low
	Large	Very high	High	Medium

5.5 Defuzzification

The last stage of the fuzzy model is the defuzzification process. Using the defuzzification method, fuzzy values can be combined into one single crisp output value. In this study, the fuzzy output functions are obtained using the center of the gravity method of defuzzification.[26] The formula to find the centroid of the combined outputs, Y_0, is given by:

$$Y_0 = \frac{\sum Y\mu C_0(Y)}{\sum \mu C_0(Y)} \quad (5)$$

where μ is the degree of the membership function. C_0 is the output variable. The yielded value is the final crisp output value obtained from the input variables.

In this research work, the non-fuzzy value Y_0 is called the multi-performance characteristics index (*MPCI*). To determine the optimal process conditions, it is essential to determine the largest multi-performance characteristics index among all the possible combinations of the process parameters. The mean value of the multi-performance characteristics index for each level of the response factors is then calculated as summarized in **Table 5**. As the experiments are conducted based on the Taguchi orthogonal array, it is possible to separate the effect of each machining parameter on the multi-performance characteristics index at different levels. For example, the mean of all the multi-performance characteristics indexes for the pulse-off time at levels 1, 2 and 3 can be found by averaging the fuzzy-reasoning-grade values from 1 to 3, 4 to 6 and 7 to 9, respectively. The mean values of the multi-performance characteristics indexes for the discharge current and pulse-on time are also calculated by adopting the same procedure. The mean fuzzy reasoning grades for the levels of each parameters are presented in Table 6, named the response table, which also contains the mean of the multi-performance characteristics indexes.

The ranges between the maximum and the minimum of the multi-performance characteristics index are ranked and the largest range is ranked as 1. Response factors with a large range of multi-performance-characteristic-index values for their levels have significantly more influences on the micro-EDM process. It is clear that factor B (discharge current) has the strongest effect on the material-removal rate (*MRR*) and tool-wear rate (*TWR*), followed by factor C (pulse-on time) and factor A (pulse-off time). They are regarded as the most important process factors because of their combination directly affecting the thermal-input rate. Therefore, the machining parameter settings of the third experiment are optimal for attaining the desired multiple performances simultaneously with the nine experiments. However, the relative magnitude of the effects of the machining parameters for the multiple performance characteristics still needs to be analyzed so that the optimal combinations of the machining parameter levels can be determined more clearly. The relative magnitude of the effects of the factors can be analyzed through an analysis of variance (ANOVA).

Table 5: Grey-fuzzy reasoning grades and their ranks

Exp. No.	GR grade	Rank
1	0.3333	9
2	0.7154	4
3	1.0000	1
4	0.4081	8
5	0.7280	3
6	0.6436	5
7	0.4100	7
8	0.4539	6
9	0.7586	2

5.6 Analysis of variance (ANOVA)

ANOVA is a statistical technique used to analyze experimental results. It is widely used to identify the performance of a process parameter under investigation.[27] ANOVA was used to investigate the relative effects of the response factors on the MPCIs and, as a result, the optimal combinations of the control factors could be accurately determined. In **Table 7**, the last column shows the percentage contribution of each factor

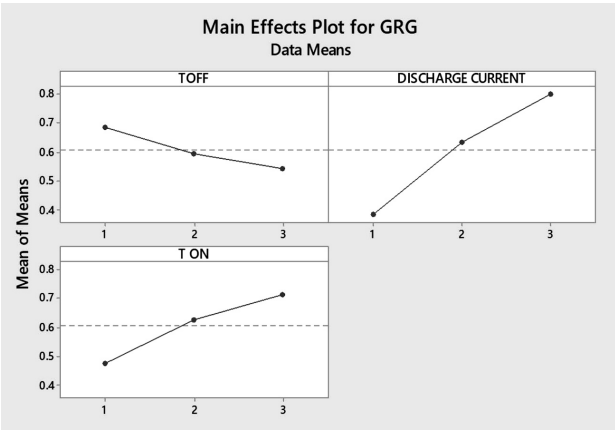

Figure 5: Graph for each level of process parameters

as the total variation, showing its influence on the result. From **Table 7**, it can be seen that the discharge current and pulse-on time are the most significant factors affecting the material-removal rate and tool-wear rate. The pulse-off time has the least effect on the material-removal rate and tool-wear rate. The larger the multi-performance characteristics index is, the better are the performance characteristics.

Table 6: Response table for the grey-fuzzy reasoning grade

Level	Pulse-off time (μs)	Discharge current (A)	Pulse-on time (μs)
1	0.6829	0.3838	0.4769
2	0.5932	0.6324	0.6274
3	0.5408	0.8007	0.7127
Delta	0.1421	0.4169	0.2357
Rank	3	1	2

Table 7: ANOVA table for the grey-fuzzy reasoning grade

Symbol	Process parameter	Degrees of freedom	Sum of squares	Mean squares	*F*-ratio	Percentage contribution
A	Pulse-off time (μs)	2	0.0318	0.01509	16.40	7.421
B	Discharge current (A)	2	0.2639	0.13195	143.42	68.62
C	Pulse-on time (μs)	2	0.0855	0.04279	46.51	21.93
E	Error	2	0.0018	0.00092	-	2.029
Total	8	0.3831	0.19156	-	100	

6 CONCLUSION

The impact of the process parameters and optimum process parameters for a micro-EDM process on multi-response performance characteristics is systematically investigated using the grey relational analysis and fuzzy logic with the Taguchi orthogonal array. The following conclusions can be made:

1. The approach of the Taguchi-based grey-fuzzy-logic analysis is an efficient productive method for optimizing multi-objective problems, predicting the material-removal rate and tool-wear rate in micro-EDM of the Monel 400 alloy.
2. From the ANOVA computations, it is revealed that the discharge current and pulse-on time are the predominant factors that affect the material-removal rate and tool-wear rate. The discharge current (68.62 %) has the main influence on the material-removal rate and tool-wear rate, followed by the pulse-on time (21.93 %) and pulse-off time (7.421 %).
3. The best performance characteristics are obtained with a discharge current of 6 A, pulse-on time of 6 μs and pulse-off time of 2 μs.

7 REFERENCES

[1] Chang-Sheng Lin, Yunn-Shiuan Liao, Yi-Ting Cheng, Yunn-Cheng Lai, Fabrication of micro ball joint by using micro-EDM and electro forming, Microelectronic Engineering, 87 (**2010**) 5, 1475–1478, doi:10.1016/j.mee.2009.11.087

[2] L. E. Shoemaker, G. D. Smith, A Century of Monel Metal: 1906–2006, JOM, 58 (**2006**) 9, 22–26

[3] M. Kalaimathi, G. Venkatachalam, M. Sivakumar, Experimental Investigations on the Electrochemical Machining Characteristics of Monel 400 Alloys and Optimization of Process Parameters, Jordan Journal of Mechanical and Industrial Engineering, 8 (**2014**) 3, 143–151

[4] E. Ezugwu, J. Bonney, D. Fadare, W. Sales, Machining of Nickel-Base, Inconel 718, Alloy with Ceramic Tools under Finishing Conditions with Various Coolant Supply Pressures, Journal of Materials Processing Technology, 162–163 (**2005**), 609–614

[5] H. Krain, A. Sharman, K. Ridgway, Optimization of Tool Life and Productivity when End Milling Inconel 718TM, Journal of Materials Processing Technology, 189 (**2007**) 1, 153–161

[6] M. Antar, S. Soo, D. Aspinwall, D. Jones, R. Perez, Productivity and Workpiece Surface Integrity when WEDM Aerospace Alloys Using Coated Wires, Procedia Engineering, 19 (**2011**), 3–8

[7] T. Masuzawa, H. Tönshoff, Three-Dimensional Micromachining by Machine Tools, CIRP Annals – Manufacturing Technology, 46 (**1997**) 2, 621–628, doi:10.1016/S0007-8506(07)60882-8

[8] U. Maradia, M. Boccadoro, J. Stirnimann, I. Beltrami, F. Kuster, K. Wegener, Die-Sink EDM in Meso-Micro Machining, Procedia CIRP, 1 (**2012**), 166–171, doi:10.1016/j.procir.2012.04.029

[9] S. Son, H. Lim, A. Kumar, M. Rahman, Influences of Pulsed Power Condition on the Machining Properties in Micro EDM, Journal of Materials Processing Technology, 190 (**2007**) 1–3, 73–76, doi:10.1016/j.jmatprotec.2007.03.108

[10] P. Kuppan, A. Rajadurai, S. Narayanan, Influence of EDM Process Parameters in Deep Hole Drilling of Inconel 718, The International Journal of Advanced Manufacturing Technology, 38 (**2008**) 1–2, 74–84, doi:10.1007/s00170-007-1084-y

[11] H. S. Liu, B. H. Yan, F. Y. Huang, K. H. Qiu, A Study on the Characterization of High Nickel Alloy Micro-Holes Using Micro-EDM and their Applications, Journal of Materials Processing Technology, 169 (**2005**) 3, 418–426, doi:10.1016/j.jmatprotec.2005.04.084.

[12] I. Ayesta, B. Izquierdo, J. Sánchez, J. Ramos, S. Plaza, I. Pombo, Influence of EDM Parameters on Slot Machining in C1023 Aeronautical Alloy, Procedia CIR, 6 (**2013**) 129–134, doi:10.1016/j.procir.2013.03.059

[13] V. Kumar, V. Kumar, K. K. Jangra, An Experimental Analysis and Optimization of Machining Rate and Surface Characteristics in WEDM of Monel-400 Using RSM and Desirability Approach, Journal of Industrial Engineering International, 11 (**2015**) 3, 297–307, doi:10.1007/s40092-015-0103-0

[14] J. Kao, C. Tsao, S. Wang, C. Hsu, Optimization of the EDM Parameters on Machining Ti–6Al–4V with Multiple Quality Characteristics, The International Journal of Advanced Manufacturing Technology, 47 (**2010**) 1, 395–402, doi:10.1007/s00170-009-2208-3

[15] B. Pradhan, M. Masanta, B. Sarkar, B. Bhattacharyya, Investigation of Electro-Discharge Micro-Machining of Titanium Super Alloy, The International Journal of Advanced Manufacturing Technology, 41 (**2009**) 11, 1094–1106, doi:10.1007/s00170-008-1561-y

[16] J.L. Deng, Introduction to Grey System Theory, The Journal of Grey System, 1 (**1989**) 1, 1–24

[17] P. N. Singh, K. Raghukandan, B. Pai, Optimization by Grey Relational Analysis of EDM Parameters on Machining Al–10% SiC_P Composites, Journal of Materials Processing Technology, 155 (**2004**), 1658–1661, doi:10.1016/j.jmatprotec.2004.04.322

[18] C. Lin, J. Lin, T. Ko, Optimization of the EDM Process Based on the Orthogonal Array with Fuzzy Logic and Grey Relational Analysis Method, The International Journal of Advanced Manufacturing Technology, 19 (**2002**) 4, 271–277, doi:10.1007/s001700200034

[19] N. Natarajan, R. Arunachalam, Optimization of Micro-EDM with Multiple Performance Characteristics Using Taguchi Method and Grey Relational Analysis, Journal of Scientific and Industrial Research, 70 (**2011**), 500–505, doi:hdl.handle.net/123456789/12065

[20] L. Abhang, M. Hameedullah, Determination of Optimum Parameters for Multi-Performance Characteristics in Turning by Using Grey Relational Analysis, The International Journal of Advanced Manufacturing Technology, 63 (**2012**) 1–4, 13–24, doi:10.1007/s00170-011-3857-6

[21] C. Y. Ho, Z. C. Lin, Analysis and Application of Grey Relation and ANOVA in Chemical–Mechanical Polishing Process Parameters, The International Journal of Advanced Manufacturing Technology, 21 (**2003**) 1, 10–14, doi:10.1007/s001700300001

[22] T. Rajmohan, K. Palanikumar, S. Prakash, Grey-Fuzzy Algorithm to Optimize Machining Parameters in Drilling of Hybrid Metal Matrix Composites, Composites: Part B, Engineering, 50 (**2013**), 297–308, doi:10.1016/j.compositesb.2013.02.030

[23] L. A. Zadeh, The Concept of a Linguistic Variable and its Application to Approximate Reasoning-I, Information Sciences, 8 (**1975**) 3, 199–249, doi:10.1016/0020-0255 (75) 90036-5

[24] P. J. Ross, Taguchi Techniques for Quality Engineering: Loss Function, Orthogonal Experiments, Parameter and Tolerance Design, 1988

[25] T. R. Lin, Optimization Technique for Face Milling Stainless Steel With Multiple Performance Characteristics, International Journal of Advanced Manufacturing Technology, 19 (**2002**) 5, 330–335, doi:10.1007/s001700200021

[26] Y. F. Tzeng, F. C. Chen, Multi-Objective Optimization of High-Speed Electrical Discharge Machining Process Using a Taguchi Fuzzy-Based Approach, Materials & Design, 28 (**2007**) 4, 1159–1168, doi:10.1016/j.matdes.2006.01.028

[27] R. Khanna, A. Kumar, M. P. Garg, A. Singh, N. Sharma, Multiple Performance Characteristics Optimization for Al 7075 on Electric Discharge Drilling by Taguchi Grey Relational Theory, Journal of Industrial Engineering International, 11 (**2015**) 4, 459–472, doi:10.1007/s40092-015-0112-z

UDK 62-761:669.58:67.017
Original scientific article/Izvirni znanstveni članek

ISSN 1580-2949
MTAEC9, 51(6)997(2017)

MECHANISM OF MULTI-LAYER COMPOSITE COATINGS IN THE ZINC PROCESS OF RECYCLING COATED WC-Co CEMENTED-CARBIDE SCRAP

MEHANIZEM VEČPLASTNIH KOMPOZITNIH PREMAZOV V PROCESU CINKANJA ZA RECIKLIRANJE ODPADKOV OPLAŠČENIH WC-Co KARBIDNIH TRDIN

Hai Kuang[1,2], Dunqiang Tan[1], Wen He[1], Xiaoru Wang[1], Jun Zhong[1], Huajian Wang[1], Chenghui Yang[1]

[1]Nanchang University, School of Materials Science and Engineering, Nanchang 330031, China
[2]Jiangxi Science and Technology Normal University, School of Materials and Electromechanics, Nanchang 330038, China
tdunqiang@ncu.edu.cn

Prejem rokopisa – received: 2017-04-30; sprejem za objavo – accepted for publication: 2017-06-16

doi:10.17222/mit.2017.049

The mechanism of a coating is crucial for the zinc-process parameters and zinc-recycled WC powders as well as the subsequent production. The mechanism of a multi-layer composite coating in a zinc process was discussed and the coating with recycled WC powders was studied. The results demonstrated that the coating created a barrier in the zinc process, resulting in a longer recycling time for the coated hard-metal scrap. Furthermore, cracks that appeared due to different thermal-expansion coefficients of the materials were the main reason for the breakdown of the coating, rather than the reaction or the dissolution; and the molten zinc mainly went through cracks. Additionally, the coating elements and fragments were found in the recycled WC powders.

Keywords: zinc process, coated cemented-carbide scrap, recycle, cracks

Način in vrsta oplaščenja WC-Co karbidne trdine je ključnega pomena za procesne parametre cinkanja za s cinkom reciklirane WC-prahove, kot tudi za njihovo nadaljnjo obdelavo. V pričujoči raziskavi so avtorji raziskovali vpliv oplaščenja karbidne trdine na proces cinkanja za reciklažo WC-prahov. Rezultati so pokazali, da večslojna prevleka ustvari oviro v procesu cinkanja, kar posledično podaljša čas recikliranja oplaščenih karbidnih trdin. Poleg tega so glavni razlog za pokanje prevlek različni koeficienti toplotnega raztezanja materialov in namesto njihovega raztapljanja poteka infiltracija raztaljenega cinka skozi razpoke do karbidne trdine. Tako so v recikliranem WC prahu našli tudi elemente in delce trdih prevlek.

Ključne besede: cinkanje, odpadki oplaščenih karbidnih trdin, recikliranje, razpoke

1 INTRODUCTION

The coated WC-Co cemented-carbide is winning an increasing market share for its good performance.[1–4] Accordingly, the quantity of coated WC-Co hard-metal scrap is also increasing. However, Tungsten, its main component, has very limited resources worldwide and encounters a supply risk.[5,6] Therefore, the recycling of WC from coated cemented-carbide scrap is imperative for stringent environmental controls and resource-conservation policies.

In recent years, the recycling of the coated WC-Co cemented-carbide scrap has attracted more and more attention. To our knowledge, only a few articles reported it and they mainly focused on the process of recycling. WC-Co hard-metal scrap was reported to be treated directly in sulphuric acid or after removing the coatings by oxidation.[7,8] However, both of the above would cause serious health and environmental problems. In research, recycled WC powders were obtained with a treatment at a high temperature and a crushing procedure, but the performance was not as good as for virgin powders and needed to be improved.[9,10] In our previous studies, removing the coating with a chemical method was researched,[11] but it was difficult to remove the coating completely. Therefore, it is essential to promote a high-efficiency procedure for recycling the WC powders from the coated WC-Co cemented-carbide scrap.

The zinc process, which is one of the most extensively used methods for recovering WC powders, was proved to be efficient and economical.[12–14] In the zinc process, the molten zinc reacts with Co, and subsequently the bond between the binder and the tungsten carbide grains is broken. As a result, the produced porous tungsten carbide product can be easily mechanically broken. K. Stjernberg[15] thought that the coating was a hazard for recycling the coated WC-Co cemented-carbide scrap in the zinc process, as it created a barrier to the reaction. Moreover, the mechanism of coating in the zinc process was not clarified. To our knowledge, no scientific literature reported on the mechanism of coatings, the reason for the breakdown of the coated hard metal in the zinc process, and the place where the coating element leaves at the end. All of the three areas

mentioned are crucial to the quality of the recycled WC powders and the process parameters include the recycling time, zinc content and temperature, even in the industrial production of subsequently recycled powders. Therefore, an investigation of the mechanism of the coating in a zinc process becomes significant for tungsten recycling and environmental protection.

In this research, the zinc process was adopted to recycle multi-layer, composite, coated WC-Co hard-metal tool-tip scraps, aiming to provide an understanding of the mechanism of the coatings. The microstructure and mechanism of the coatings were studied; the material interactions among the coatings, zinc and Co were analyzed, and the failure mechanism was also discussed. This work intended to provide valuable information about an efficient zinc process for recycling coated WC-Co cemented-carbide scrap.

2 EXPERIMENTAL PART

2.1 Materials

The multi-layer composite coated WC-Co cemented-carbide scrap employed for this study was a turning insert after sufficient usage, purchased from a scrap merchant. The dimensions of the sample were 12 mm × 12 mm × 5 mm and its weigh was about 9 g. The chemical composition of the sample mainly included WC and the Co binder (7.41 % mass fraction) and also some other rare elements such as Ta, Nb and Ti. Four flanks of the sample were coated with titanium carbonitride (TiCN)/aluminum oxide (Al_2O_3)/titanium nitride (TiN) through the chemical-vapor-deposition (CVD) method, while the other two faces were covered with TiCN (dark grey)/Al_2O_3 (light grey), as shown in **Figure 1a**. The top coating, TiN, was removed to reduce the stress. Zinc blocks were cut from zinc ingots with a purity of 99.95 % in order to be conveniently placed in graphite crucibles.

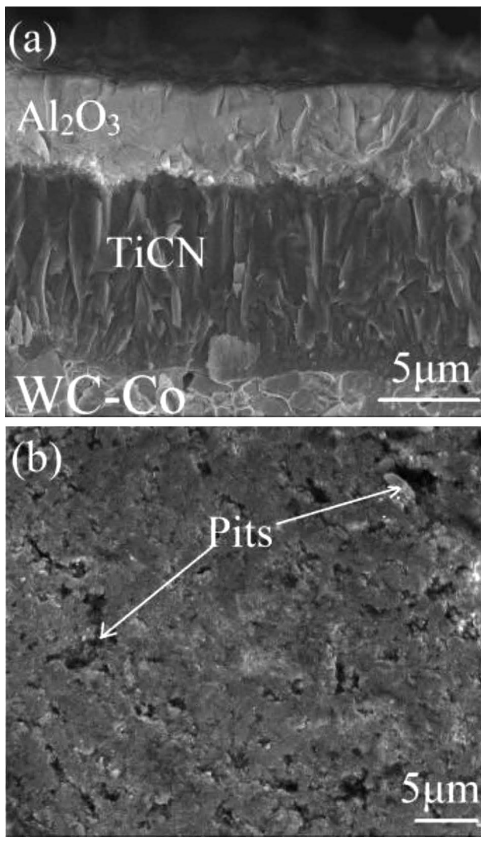

Figure 1: SEM images of multi-layer composite coated WC-Co cemented-carbide scrap: a) cross-section, b) surface

2.2 Experiment procedure

The multi-layer, composite, coated WC-Co cemented-carbide scrap was first treated with an ultrasonic cleaner using acetone and ethanol, and the sample was then packed into high-purity graphite crucibles along with pure zinc blocks. The crucible was a hollow cylinder with a 5-mm inner diameter and 40-mm height. The weight of zinc blocks depends on the Co content in the industry and the preferred weight ratio of zinc to cobalt is usually within a range of about 20:1 to 15:1.[16] In our study, the weight ratio of zinc to cobalt was about 50:1. The excessive weight of zinc aimed to research the corrosion behavior in detail. Lids were put on crucibles, and these were then placed in an electric furnace (Yifeng, SX2-4-10). A standard thermocouple was used to check the temperature of the furnace, which was heated from room temperature to 880 °C. A sample and zinc ingots were isothermally maintained at 880 °C. The tips were immersed into molten zinc since the zinc blocks melted at 419.5 °C. The coated hard-metals were treated for (2, 6, 9 and 15) h, while the uncoated samples were treated for (2, 6 and 9) h during the zinc process. Subsequently, the sample was naturally cooled down to room temperature and then cut using wire-electrode cutting to conveniently examine the interface. In addition, the samples treated with the zinc process for 15 h were placed in a baker containing a 2 mol/L hydrochloric acid aqueous solution. Zn and Co were dissolved in the solution, while WC was deposited on the bottom as a solid. After being washed with water, the solution was filtrated and dried to obtain the WC powder.

The WC-Co cemented-carbide scrap in the zinc process from the photographs was examined using an optical microscope. The micromorphologies were investigated with a field-emission scanning electron microscope (FESEM), whilst the element compositions of the samples were characterized using energy-dispersive X-ray spectroscopy (EDS). The inductively-coupled-plasma method (ICP, optima 5300DV) was employed to test the element content of the recycled powder. Recycled products of the WC–Co scrap samples were identified using an X-ray diffractometer (XRD; PANalytical, EMPYREAN).

3 RESULTS AND DISCUSSION

3.1 Multi-layer composite coated WC-Co cemented-carbide scrap in the zinc process

The macrostructures of the multi-layer, composite, coated WC-Co cemented-carbide scrap treated with the zinc process were characterized. **Figure 2** includes cross-section images of the WC-Co cemented carbides in the zinc process after cooling down and solidification. Obvious changes can be observed. As shown in **Figure 2a**, a few cracks could be clearly observed in the sample having been treated at 880 °C for 2 h. Zinc got into the samples mainly through the cracks. The volume of scrap expanded and more cracks were found after having been treated for 9 h (as shown in **Figure 2b**). As shown in **Figure 2c**, the substrate was dispersed in zinc after a treatment for 15 h. **Figures 2d** and **2e** show the uncoated WC-Co cemented-carbides scrap. It can be found that the samples could not even maintain the square shape after the 2-h treatment and the WC particles were distributed in zinc only after the 9-h treatment. The results demonstrated that the coating was a barrier in the zinc process. More time was required to recover the WC powders from the coated WC-Co cemented-carbide scrap.

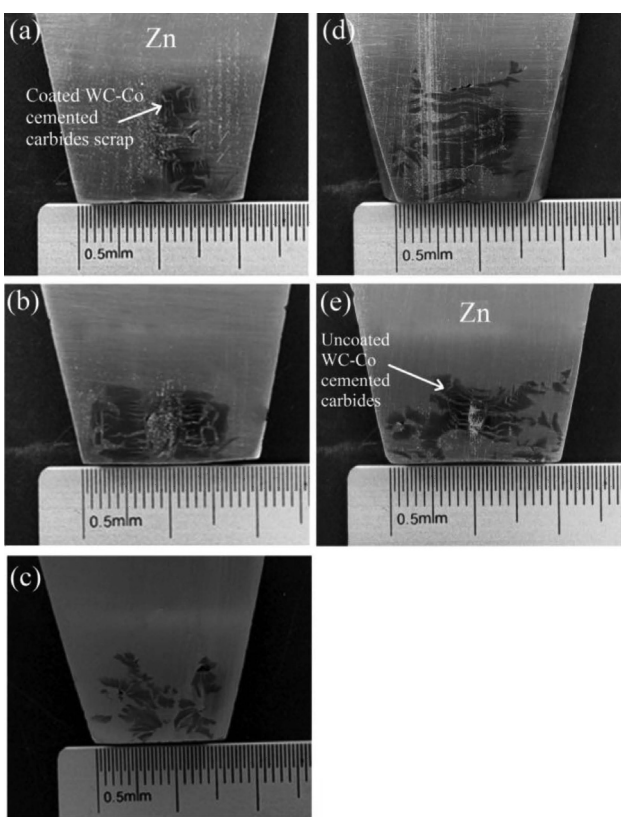

Figure 2: Photographs of coated and uncoated WC-Co cemented-carbide scraps in the zinc process: a) coated sample treated for 2 h, b) coated sample treated for 9 h, c) coated sample treated for 15 h, d) uncoated sample treated for 2 h, e) uncoated sample treated for 9 h

3.2 Characterization of the recycled powders

Figure 3 shows the results for the recycled WC particles. The substrate of the coated sample treated with the zinc process for 15 h was characterized for comparison. As seen in **Figure 3b**, the substrate (WC) was dispersed in zinc, revealing that the coating was broken and Zn completely reacted with Co. It can be observed that the substrate was porous and loose, and can be easily broken down mechanically.[17] So, recycling the coated WC-Co cemented-carbide scrap during the zinc process was feasible, though the coating created a barrier to the reaction. The recycled WC powders obtained in the present study can be seen in **Figure 3**. It can be seen that the coating was found among the WC particles. EDS results show the Al element is in the powders recycled from the coated scrap; but this element could not be found in the powders obtained from the uncoated samples, as shown in **Figure 3d**. However, only WC was found with the XRD (**Figure 3f**). The amount of Al in the recycled powders was only 78 mg/kg, which was difficult to detect with the XRD analysis.

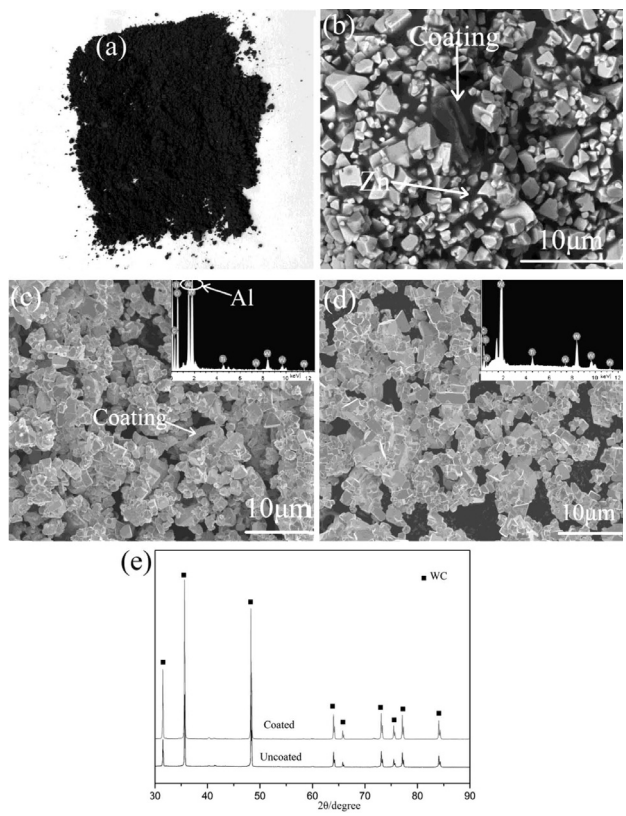

Figure 3: Results for recycled WC powders: a) photograph of recycled WC powders from coated samples, b) cross-section of WC particles in the substrate of the coated sample in the zinc process for 15 h, c) SEM image and EDS result for the recycled WC powders of coated samples, d) SEM image and EDS result for the recycled WC powders of uncoated samples, e) XRD result

3.3 Material interactions

3.3.1 Chemical reactions among the coatings, Zn and Co

When the molten zinc is in contact with TiCN /Al_2O_3, these are possible reactions:

$$3Zn+Al_2O_3 \rightarrow 2Al+3ZnO \quad (1)$$

$$Zn+TiCN \rightarrow TiC +ZnN \quad (2)$$

$$9Co +4Al_2O_3 \rightarrow 3Co_3O_4+8Al \quad (3)$$

$$TiCN+Co \rightarrow Co_3N+TiC \quad (4)$$

The thermodynamic parameters are calculated and the standard free-energy change of the equations above are all over zero ($\Delta G>0$). According to the analysis of the thermodynamics, Al_2O_3 and TiCN could not react with Zn or Co on this condition. This is consistent with the fact that Al_2O_3 is usually used to be the anti-corrosion material for the zinc corrosion.[18] The chemical reaction is not the main factor for the failure of the coated WC-Co cemented-carbide scrap in the zinc process.

3.3.2 Dissolution and diffusion

The molten-zinc corrosion occurs together with the physical effect, not a general chemical reaction, and the physical effect leads to the failure of the material. The most important ways are dissolution and diffusion.[19–21] For a better understanding of the mechanism, the element mapping of the sample in the zinc process was further studied, as shown in **Figure 4**. It can be seen that Co was distributed in the zinc-enrichment area due to the fact that Zn reacts with Co. But only some Co could be found at the position of the coatings. Moreover, most coating elements, like Al and Ti, were distributed along the coating location, revealing that coatings Al_2O_3 and TiCN could not dissolve or diffuse much in the molten zinc and Co. Therefore, the physical effect of dissolution and diffusion was not the main reason for the breaking down of the multilayer, composite, coated WC-Co cemented-carbide scrap in the zinc process. Near the WC particles, it can be seen that there are a few Ti particles, which were contained in the substrate of the tip.

3.3.3 Pits and cracks

Figures 5 and **6** show the surface and cross-section images of the multilayer, composite, coated WC-Co cemented-carbide scrap in the zinc process for different times. As seen in **Figure 5a**, the zinc residue on the surface of the coating was in the shape of a sphere, demonstrating that Al_2O_3 is not well wetted by zinc, which can delay the penetration of molten zinc into the substrate.[22] Previous researches[19,23] revealed that the corrosion of the materials poorly wetted by zinc was caused by surface defects, usually pits and cracks. They could provide preferential paths for transporting the molten zinc to the coatings and the substrate. Therefore, defects are vulnerable to molten zinc.

In the present study, the multi-layer, composite, coated WC-Co cemented-carbide scrap was worn out. As seen in **Figure 1**, the localized areas of the coating began to disintegrate, especially at the corners and flanks.[24,25] A number of defects were observed on the surfaces of the samples. Pits could be generated during the deposition of coatings or appear during the cutting of alloys.[23] Most pits were concentrated on damaged local edges and corners. In this study, the pits provided the paths for transporting the molten zinc. The molten zinc could penetrate inwards via intergranular boundaries of the coatings (**Figure 5a**). Therefore, the pits were the reason for the failure of the coatings. Pits in coatings are inversely proportional to the coating resistance, i.e., a lot of pits with a larger size lead to an easier coating breakdown.[26] It can be seen from **Figures 5** and **6** that not much zinc

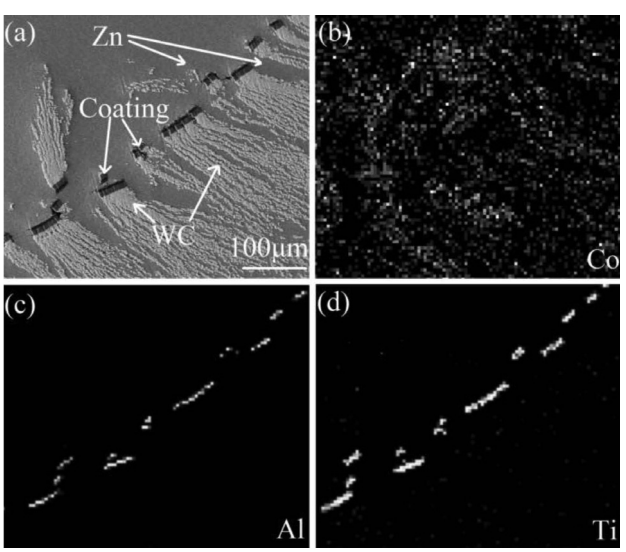

Figure 4: Element mapping for multilayer, composite, coated, WC-Co cemented-carbide scrap in zinc process

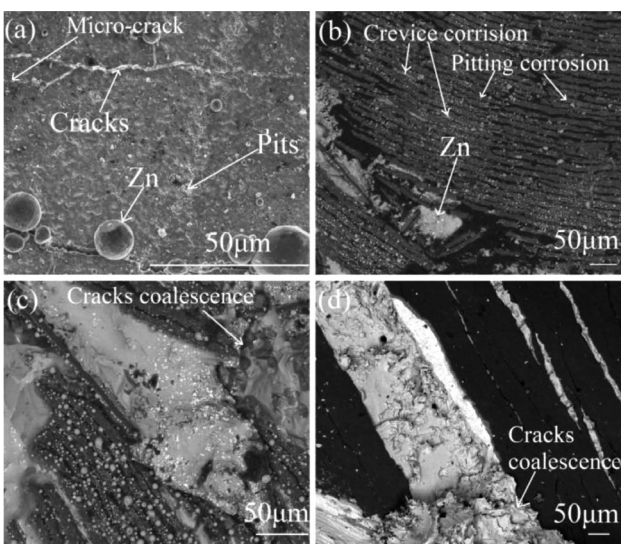

Figure 5: Surface SEM images of multi-layer, composite, coated WC-Co cemented-carbide scrap in zinc process for different times: a) 2 h, b) 6 h, c) 9 h, d) 15 h

got into the samples through the pits as the coating created a barrier.

Most of zinc got into the samples through cracks, as shown in **Figures 5** and **6**. When coatings are deposited, cracks are created due to the lattice mismatch. As shown in **Figures 6a** to **6d**, the molten zinc reached the substrate mainly by penetrating the cracks. At the early stage, pits also lead to the formation of microcracks with the increasing treating time. Most of these cracks were generated during the cutting or heating of the metals due to a difference between the thermal-expansion coefficients of the substrate and coating materials (**Table 1).**[27] Stress was the main reason for an increased number of larger cracks.[28] Furthermore, the exfoliation of the coatings contributed to an increased crack coalescence.[29]

Table 1: Thermal-expansion coefficients of materials

Material	TiN	Al_2O_3	TiCN	WC	Zn
Thermal-expansion coefficient (10^{-6}K)	9.35	9.0	7.8	4.3	30.2

Zinc went through pits and microcracks at the early stage (**Figures 5a** and **6a**). Then the number of pits increased and they became deeper and larger with the increasing treatment time; the cracks also increased due to the expansion. The converging of microcracks also led to wide cracks. It can be seen that at the early stage, a crack (**Figure 5a**) has a width of less than 5 μm, and at the last stage, a wide crack (**Figure 5d**) has a width of more than 230 μm. This led to a localized breakdown of a coating. Several coatings even became detached from the substrate with the increasing treating time, as shown in **Figures 6e** and **6f**. During the last stage, the samples were dispersed. Most WC particles were separated in zinc due to the dissolution of the Co binder. Localized breakdowns of the coatings and substrates can be observed. Some coatings were torn into pieces and deviated from the original position. Several coating elements can be found among the WC particles (**Figure 6e**) or in the zinc-enriched region (**Figure 6f**). This indicates that the molten zinc mainly got in through the cracks, and it was the main mechanism of the failure coatings, which is also demonstrated with the element mapping in **Figure 4**. The result is consistent with the conclusion that the formation and extension of cracks is the main reason for the breakdown of coated carbide tools in the zinc process.[30]

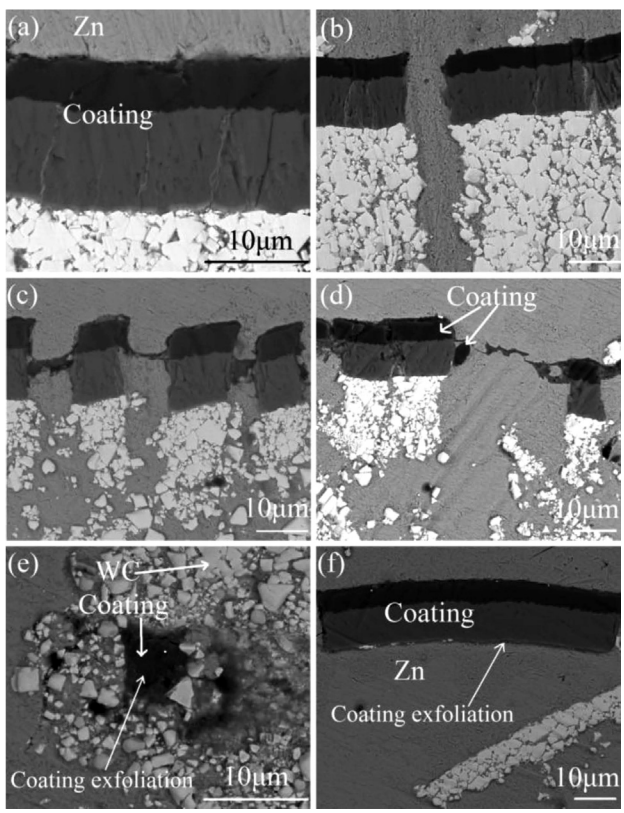

Figure 6: Cross-section SEM images of multi-layer, composite, coated WC-Co cemented-carbide scrap in zinc process for different times: a) 2 h, b) 6 h, c) 9 h, d) 15 h, e) coatings distributed among WC particles in the zinc process of 15 h, f) coatings distributed in the zinc-enriched area in the zinc process of 15 h

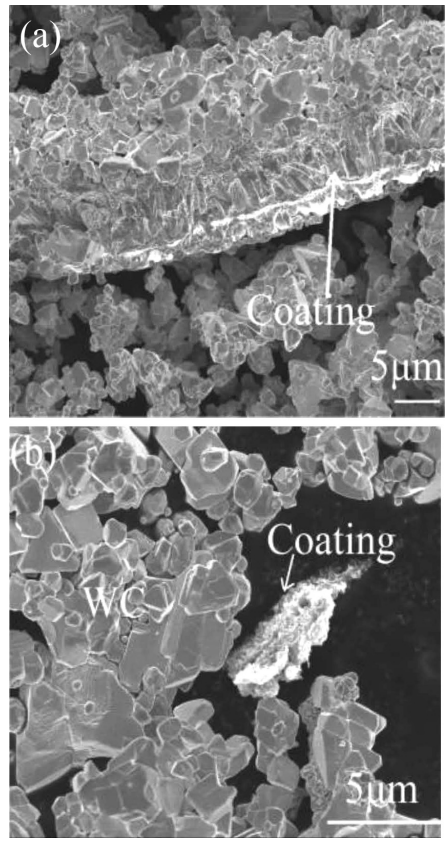

Figure 7: SEM images of the coatings in recycled WC powders

In order to further study the corrosion behavior of the multi-layer, composite coating, recycled WC powders were characterized with SEM as shown in **Figure 7**. Coating fragments flaking off were found. Some were tightly bound with the WC particles (**Figure 7a**) and others were on their own among the WC particles. That is in good agreement with the result from **Figure 6**.

4 CONCLUSIONS

The mechanism of a coating in a zinc process influences the properties of the recycled powders, the recycling process and thus the subsequent industrial production. In this study, the breakdown of a multi-layer composite coating was investigated. The results show that the coating delayed the reaction of Zn and Co in the zinc process; therefore, a longer time was needed for recycling coated hard-metal scraps. Both the pits and cracks were the reason for the failure of the coatings in the zinc process and zinc got into the samples mainly through the cracks, most of which appeared due to different thermal-expansion coefficients of the materials. After the treatment in the zinc process for 15 h, the substrate became porous and loose. WC powders were successfully obtained from the multi-layer, composite, coated WC-Co cemented-carbide scrap with the zinc process, and stripped coatings were found in the recycled WC powders. This investigation can provide some fundamental information needed to develop an efficient recycling method for multi-layer, composite, coated WC-Co cemented-carbide scrap.

Acknowledgement

This work was supported by the National Natural Science Foundation of China (51564036 and 50904035), the National High-Tech R&D Program of China (2012AA061902) and the National Key Technology R&D Program of China (2011BAC10B04).

5 REFERENCES

[1] L. Y. Zhou, J. T. Ni, Q. H, Study on failure mechanism of the coated carbide tool, International Journal of Refractory Metals and Hard Materials, 25 (**2007**) 1, 1–5, doi:10.1016/j.ijrmhm.2005.10.002

[2] G. J. Ma, L. L. Wang, H. X. Gao, J. Zhang, T. Reddyhoff, The friction coefficient evolution of a TiN coated contact during sliding wear, Applied Surface Science, 345 (**2015**), 109–115, doi:10.1016/j.apsusc.2015.03.156

[3] Q. Z. Wang, F. Zhou, X. N. Wang, K. M. Chen, M. L. Wang, T. Qian, Y. X. Li, Comparison of tribological properties of CrN, TiCN and TiAlN coatings sliding against SiC balls in water, Applied Surface Science, 25 (**2011**), 7813–7820, doi:10.1016/j.apsusc.2011.04.035

[4] K. J. Brookes, Hardmetals group studies coatings, Metal Powder Report, 69 (**2014**) 2, 22–27, doi:10.1016/S0026-0657(14)70080-3

[5] T. Yamaguchi, H. Hagino, Y. Michiyama, Sliding Wear Properties of Ti/TiC Surface Composite Layer Formed by Laser Alloying, Materials Transactions, 56 (**2015**) 3, 361–366, doi:10.2320/matertrans.m2014330

[6] T. Ishlda, T. Itakura, H. Morlguchl, A. Ikegaya, Development of technologies for recycling cemented carbide scrap and reducing tungsten use in cemented carbide tools, Sei Technical Review, 75 (**2012**) 75, 38–46

[7] W. H. Gu, Y. S. Jeong, K. Kim, J. C. Kim, S. H. Son, S. Kim, Thermal oxidation behavior of WC-Co hard metal machining tool tip scraps, Journal of Materials Processing Technology, 212 (**2012**) 6, 1250–1256, doi:10.1016/j.jmatprotec.2012.01.009

[8] C. D. Vanderpeel, R. A. Seheithauer, R. G. Warmington, Recovery of refractory metal values from scrap cemented carbide, US Patent, 4432950 (**1984**)

[9] Z. J. Wu, P. Zhang, J. S. Zeng, Z. Y. Deng, The process of producing cemented carbide by recycled WC powders, Cemented Carbide, 22 (**2005**) 3, 170–172, doi:10.3969/j.issn.1003-7292.2005.03.010

[10] Z. J. Wu, J. Liu, Research on removing of the coating from the coated cemented carbide, Non-ferrous metals recycling and utilization, 7 (**2005**) 2, 19–20

[11] Y. Liu, D. Q. Tan, D. P. Lu, L. Lei, J. Long, Corrosion behavior in process of removing TiN coating of waste cemented carbide by chemical method, Materials Science and Engineering of Powder Metallurgy, 18 (**2013**) 1, 20–25, doi:10.3969/j.issn.1673-0224.2013.01.006

[12] K. J. Brookes, Hardmetals recycling and the environment, Metal Powder Report, 69 (**2014**) 5, 24–30, doi:10.1016/S0026-0657(14)70225-5

[13] C. S. Freemantle, N. Sacks, M. Topic, C. A. Pineda-Vargas, PIXE as a characterization technique in the cutting tool industry, Nuclear Instruments and Methods in Physics Research Section B: Beam Interactions with Materials and Atoms, 318 (**2014**) 1, 168–172, doi:10.1016/j.nimb.2013.06.044

[14] E. Altuncu, F. Ustel, A. Turk, S. Ozturk, G. Erdogan, Cutting-tool recycling process with the zinc-melt method for obtaining thermal-spray feedstock powder (WC-Co), Materiali in Tehnologije, 47 (**2013**) 1, 115–118

[15] K. Stjernberg, J. Johnson, Recycling of cemented carbides, Metal Powder Report, 53 (**1998**) 12, 40, doi:10.1016/s0026-0657(99)80135-0

[16] P. G. Barnard, A. G. Starliper, H. Kenworthy, Reclamation of refractory carbides from carbide materials, US Patent 3595484 (**1971**)

[17] J. C. Liu, S. W. Park, S. Nagao, M. Nogi, H. Koga, J. S. Ma, G. Zhang, K. Suganuma, The role of Zn precipitates and Cl-anions in pitting corrosion of Sn–Zn solder alloys, Corrosion Science, 92 (**2015**), 263–271, doi:10.1016/j.corsci.2014.12.014

[18] Y. H. Lv, X. S. Wu, Y. F. Liu, Z. J. Wu, Preparation of Al_2O_3-TiB_2 composite ceramic coating and corrosion-resistant property to molten zinc, China surface engineering, 24 (**2011**) 4, 30–33, doi:10.3969/j.issn.1007-9289.2011.04.006

[19] X. J. Ren, X. Z. Mei, J. She, J. H. Ma, Materials resistance to liquid zinc corrosion on surface of sink roll, Journal of Iron and Steel Research, International, 14 (**2007**) 5, 130, doi:10.1016/S1006-706X(08)60066-7

[20] M. P. Taylor, J. R. P. Smith, H. E. Evans, Modelling of the interdiffusion and oxidation of a multilayered chromia forming thermal barrier coating, Materials and Corrosion, 68 (**2016**) 2, 215–219, doi:10.1002/maco.201508778

[21] X. D. Tian, X. P. Guo, Z. P. Sun, J. L. Qu , L. J. Wang, Oxidation resistance comparison of MoSi2 and B-modified MoSi2 coatings on pure Mo prepared through pack cementation, Materials and Corrosion, 66 (**2014**) 7, 681–687, doi:10.1002/maco.201407631

[22] J. F. Zhang, C. M. Deng, J. B. Song, C. G. Deng, M. Liu, K. S. Zhou, MoB-CoCr as alternatives to WC-12Co for stainless steel protective coating and its corrosion behavior in molten zinc, Surface and Coatings Technology, 235 (**2013**), 811–818, doi:10.1016/j.surfcoat.2013.08.052

[23] A. A. Matei, I. Pencea, M. Branzei, D. E. Tranca, G. Tepes, C. E. Sfat, E. Ciovica, A. I. Gherghilescu, G. A. Stanciu, Corrosion resistance appraisal of TiN, TiCN and TiAlN coatings deposited by CAE-PVD method on WC–Co cutting tools exposed to artificial sea water, Applied Surface Science, 358 (**2015**), 572–578, doi:10.1016/j.apsusc.2015.08.041

[24] J. D. Brassard, D. K. Sarkar, J. Perron, A. Audibert-Hayet, D. Melot, Nano-micro structured superhydrophobic zinc coating on steel for prevention of corrosion and ice adhesion, Journal of Colloid and Interface Science, 447 (**2015**), 240–247, doi:10.1016/j.jcis.2014.11.076

[25] D. Zhang, B. Shen, F. Sun, Study on tribological behavior and cutting performance of CVD diamond and DLC films on Co-cemented tungsten carbide substrates, Applied Surface Science, 256 (**2010**) 8, 2479–2489, doi:10.1016/j.apsusc.2009.10.092

[26] M. Karbasi, M. R. Zamanzad Ghavidel, A. Nekahi, Corrosion behavior of HVOF sprayed coatings of Ni TiC and Ni (Ti,W)C SHS produced composite powders and Ni + TiC mixed powder, Materials and Corrosion, 65 (**2012**) 5, 485–492, doi:10.1002/maco.201206536

[27] A. Matthews, Handbook of hard coatings, Edited by Rointan E. Bunshah, (**2001**), 203–205

[28] C. Lee, H. Park, J. Yoo, C. Lee, W. C. Woo, S. Park, Residual stress and crack initiation in laser clad composite layer with Co-based alloy and WC+NiCr, Applied Surface Science, 345 (**2015**), 286–294, doi:10.1016/j.apsusc.2015.03.168

[29] H. B. Wang, X. Z. Wang, X. Y. Song, X. M. Liu, X. W. Liu, Sliding wear behavior of nanostructured WC-Co-Cr coatings, Applied Surface Science, 355 (**2015**), 453–460, doi:10.1016/j.apsusc.2015.07.144

[30] Y. J. Zheng, Y. X. Leng, X. Xin, Z. Y. Xu, F. Q. Jiang, R. H. Wei, N. Huang, Evaluation of mechanical properties of Ti(Cr)SiC(O)N coated cemented carbide tools, Vacuum, 90 (**2013**) 2, 50–58, doi:10.1016/j.vacuum.2012.10.002

UDK 67.017:666.762.1:661.34
Original scientific article/Izvirni znanstveni članek

ISSN 1580-2949
MTAEC9, 51(6)1005(2017)

BASIC PHYSICAL, MECHANICAL AND ELECTRICAL PROPERTIES OF ELECTRICALLY ENHANCED ALKALI-ACTIVATED ALUMINOSILICATES

OSNOVNE FIZIKALNE, MEHANSKE IN ELEKTRIČNE LASTNOSTI ELEKTRIČNO IZBOLJŠANIH, Z ALKALIJAMI AKTIVIRANIH ALUMINOSILIKATOV

Lukáš Fiala[1], Miloš Jerman[1], Pavel Rovnaník[2], Robert Černý[1]

[1]Czech Technical University, Faculty of Civil Engineering, Department of Materials Engineering and Chemistry, Thákurova 7, 166 29 Prague 6, Czech Republic
[2]Brno University of Technology, Institute of Chemistry, Faculty of Civil Engineering, Žižkova 17, 602 00 Brno, Czech Republic
fialal@fsv.cvut.cz

Prejem rokopisa – received: 2017-05-04; sprejem za objavo – accepted for publication: 2017-07-28

doi:10.17222/mit.2017.051

Alkali-activated aluminosilicates (AAAs) with electrically conductive admixtures are promising competitors to the cement-based materials enhanced in the same way. The electrical conductivity of these materials dramatically increases with a sufficient amount of admixtures, which broaden their possible applicability. Electrically optimized materials are typically used in self-heating, self-sensing or magnetic-shielding systems. However, an increase in the amount of admixtures can negatively affect the compressive or flexural strength and can lead to an increase in the porosity. Therefore, it is crucial to experimentally determine the mechanical properties in order to decide whether an electrically enhanced material is applicable in the building industry. In this research, basic physical, mechanical and electrical properties of AAAs with three types of electrically conductive admixtures in different dosages are studied. Typical representatives of spherical inclusions, carbon black (CB), graphite powder (GP) and carbon fibers (CF) as fibrous fillers, are tested. The experimental results reveal that AAAs with CB dosages higher than 4 % are promising materials that could be utilized in self-heating systems due to their sufficiently high electrical conductivity.

Keywords: alkali-activated aluminosilicates, electrically conductive admixtures, compressive strength, flexural strength, electrical conductivity

Z alkalijami aktivirani aluminosilikati (AAA) z električno prevodnimi dodatki so obetavni konkurenti materialov, ki izboljšani na enak način, temeljijo na cementu. Električna prevodnost teh materialov se drastično povečuje z zadostno količino takšnih dodatkov, ki razširjajo njihovo možno uporabnost. Tipična praktična uporaba električno optimiranih materialov je v samoogrevanju, samozaznavanju ali magnetno-zaščitnih sistemih. Vendar lahko povečanje količine dodatkov negativno vpliva na tlačno ali upogibno trdnost in lahko povzroči povečanje poroznosti. Zato je ključnega pomena, da določimo eksperimentalno mehanske lastnosti, da bi se odločili, ali se naj električno ojačan material uporablja v gradbeništvu. V tem prispevku so preučevane osnovne fizikalne, mehanske in električne lastnosti AAA s tremi vrstami električno prevodnih dodatkov v različnih doziranjih. Eksperimentalni rezultati kažejo na dejstvo, da so AAA z odmerki CB, višjimi od 4 %, obetavni materiali, ki bi jih lahko uporabili v sistemih za samoogrevanje zaradi dovolj visoke lastne električne prevodnosti.

Ključne besede: aluminosilikati, aktivirani z alkalijami; električno prevodne dodajne mešanice, tlačna trdnost, upogibna trdnost, električna prevodnost

1 INTRODUCTION

Alkali-activated aluminosilicates (AAAs, often also denoted as geopolymers) are promising competitors to the cement-based materials due to their good mechanical properties, chemical resistance and enhanced fire resistance.[1,2] Moreover, other AAA benefits that cannot be overlooked are economic aspects and their environmentally friendly nature.[3,4]

Alkaline activators as components of cementing materials date back to 1930, when Kuhl investigated the setting behavior of mixtures of ground slag powder and caustic potash solution. The first extensive laboratory study on clinkerless cements consisting of slag and sodium hydroxide was performed in 1940s by A. O. Purdon.[5] Further detailed observations of AAAs were performed by V. D. Glukhovsky[6] who aimed at investigating the binders used in ancient Roman and Egyptian constructions and concluded that they were composed of calcium aluminosilicate hydrates similar to the ones of Portland cement, which explained their durability. Based on these observations, Glukhovsky developed a new type of binders, the so-called soil cement, which consists of aluminosilicates mixed with alkalis-rich industrial wastes. Another study carried out by R. Malinowski[7] revealed the fact that the restoration of ancient constructions with the materials based on Portland cement leads to their disintegration after 10 years, which is much lower compared to the durability of the original material.

A further qualitative enhancement of AAAs represented by an increased electrical conductivity can be achieved with an addition of electrically conductive

admixtures, which was already observed for the cement-based materials.[8–10] With an appropriate amount of such admixtures, at around the percolation threshold, an electrically conductive network is built up in the solid matrix. Therefore, the electrical conductivity significantly increases and naturally electrically non-conductive materials become electrically conductive, which broadens their practical utilization. Such materials can then be used in many practical ways, e.g., in self-heating[11] or self-sensing[12] systems.

In the past, various electrically conductive admixtures based on metallic particles or fibers, such as nickel powder (NP) and steel fibers (SF), or on carbon-based materials, such as carbon black (CB), carbon fibers (CF), carbon nanotubes (CNT) or graphite powder (GP) were studied. A comprehensive review of widely used admixtures suitable for self-sensing concrete was given by B. Han et al.[13]

In this paper, the basic physical, mechanical and electrical properties of reference AAAs and several types of electrically enhanced AAAs with different dosages of conductive admixtures, namely, carbon black (CB), carbon fibers (CF) and graphite powder (GP) are studied. The main aim is to determine the relation of the amount of electrically conductive admixtures with the electrical conductivity, the compressive strength and the flexural strength and to identify the most appropriate AAA mixes that allow satisfactory electrical and mechanical parameters.

2 EXPERIMENTAL PART

The studied AAA materials were based on SMŠ 380 produced by Kotouč Štramberk s.r.o. It is a dry, granulated blast-furnace slag with a fineness of 380 $m^2\ kg^{-1}$ fulfilling the requirements of ČSN EN 197-1. The second component, the Britesil C205 waterglass with the SiO_2/Na_2O molar ratio equal to 2.07, was used for the alkali activation. The filler was represented by three normalized CEN fractions of the quartz sand (PG1, PG2, PG3) produced by Filtrační písky, Ltd., Czech Republic, which complies with ČSN EN 196-1. The particle size distribution of the used sand is given in **Figure 1**.

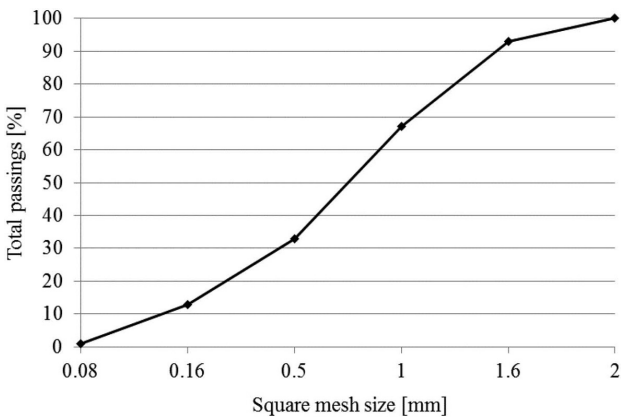

Figure 1: Particle size distribution of the Chlumský reference sand

Within the study, fifteen different types of AAA samples were prepared: the reference sample without any conductive admixture, samples with CB in amounts of (0.89, 2.22, 4.44, 6.67 and 8.89) % of mass fractions, samples with CF in amounts of (0.56, 1.11, 1.67 and 2.22) % of mass fractions, and samples with GP in amounts of (1.78, 3.33, 4.44, 6.67 and 8.89) % of mass fractions. The compositions of the analyzed AAA mixes are given in **Tables 1–3**.

The samples were prepared as follows: Firstly, waterglass was mixed with water. The solution was then mixed with the suspension of an electrically conductive admixture. CB was incorporated into the mixture in the form of a 20 % mass-fraction homogenized suspension (relative to the slag mass), GP in the form of 10 % mass-fraction and 20 % mass-fraction suspensions and CF in the form of a 5 % mass-fraction suspension. Optionally, additional water was added to ensure good workability of the mix. Other components were added in the following order: slag, a fine fraction of sand (PG1), a medium-coarse fraction of sand (PG2), a coarse fraction of sand (PG3). The final mixture was put into 40 mm × 40 mm × 160 mm molds and vibrated. The samples were demolded after 24 h, cured in water for additional 28 d and dried in an oven.

Table 1: Compositions of the reference AAA mixture and AAA mixtures with CB

Component/ Admixture	Reference	CB 0.89 %	CB 2.22 %	CB 4.44 %	CB 6.67 %	CB 8.89 %
Slag (g)	450	450	450	450	450	450
Waterglass (g)	90	90	90	90	90	90
Sand PG1 (g)	450	450	450	450	450	450
Sand PG2 (g)	450	450	450	450	450	450
Sand PG3 (g)	450	450	450	450	450	450
Admixture suspense (%)	0	20	20	20	20	20
Amount of suspense (g)	0	20	50	100	150	200
Additional water (g)	0	190	170	130	90	105

Table 2: Compositions of the AAA mixtures with CF

Component/ Admixture	CF 0.56 %	CF 1.11 %	CF 1.67 %	CF 2.22 %
Slag (g)	450	450	450	450
Waterglass (g)	90	90	90	90
Sand PG1 (g)	450	450	450	450
Sand PG2 (g)	450	450	450	450
Sand PG3 (g)	450	450	450	450
Admixture suspense (%)	5	5	5	5
Amount of suspense (g)	50	100	150	200
Additional water (g)	150	100	50	0

Table 3: Compositions of the AAA mixtures with GP

Component/ Admixture	GP 1.78 %	GP 3.33 %	GP 4.44 %	GP 6.67 %	GP 8.89 %
Slag (g)	450	450	450	450	450
Waterglass (g)	90	90	90	90	90
Sand PG1 (g)	450	450	450	450	450
Sand PG2 (g)	450	450	450	450	450
Sand PG3 (g)	450	450	450	450	450
Admixture suspense (%)	10	10	20	20	20
Amount of suspense (g)	80	150	100	150	200
Additional water (g)	140	70	130	90	50

As the fundamental physical material characteristics, the bulk density ρ_v (kg m^{-3}), the open porosity Ψ (–) and the matrix density ρ_{mat} (kg m^{-3}) were measured using the water-vacuum-saturation method. In the first step, the samples were dried in a drier to remove the majority of the physically bound water. Subsequently, the samples were placed into a desiccator. In three hours, the air was evacuated with a vacuum pump from the desiccator. The samples were then kept under water for 24 h. From the mass of water-saturated sample m_w (kg) and the mass of immersed water-saturated sample m_a (kg), volume V of the sample was determined, and the basic physical properties were calculated.

Mechanical properties were measured on three samples with dimensions of 40 mm × 40 mm × 160 mm according to the Czech Standard ČSN EN 196-1 (**Figure 2**). At first, three samples of each mixture were cured in a water bath for 28 d. Then the flexural strength was determined with the three-point-bending test. The span length between supports was 100 mm, and the loading rate was 0.15 mm/min. The compressive strength was then determined on six halves of the prisms from the previous flexural-strength tests.

Electrical properties were determined on samples with dimensions of 40 mm × 40 mm ×10 mm cut from 40 mm × 40 mm × 160 mm prisms. In order to achieve good contact of the tested materials with the measuring apparatus, two lateral sides (40 mm × 40 mm) playing the role of electrodes were painted with a conductive-carbon paint produced by SPI Supplies, together with a copper adhesive tape that was connected to the conductors. The samples dried in an oven were put into the dessicator for a couple of days in order to achieve dry state with no residual water. Finally, the electrical resistance was determined with a Fluke 8846A 6-1/2 digit precision multimeter in a 4-electrode configuration (**Figure 3**) and the electrical conductivity was calculated with respect to the shape ratio of the samples.

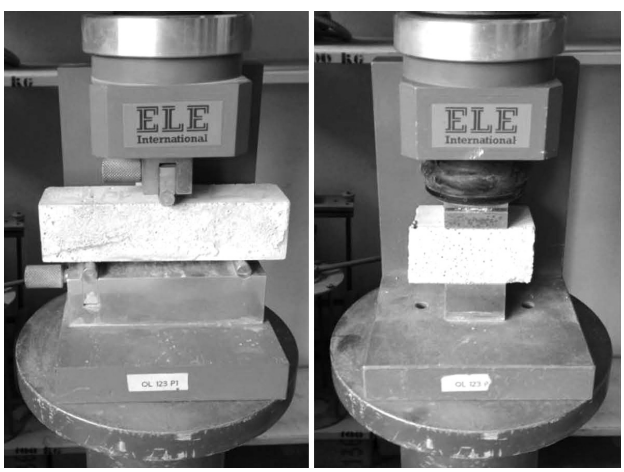

Figure 2: Three-point bending and compressive-strength experiment

Figure 3: Electrical-resistivity measurements

3 RESULTS AND DISCUSSION

The basic physical properties are presented in **Figures 4** to **6**. The bulk density of the reference material (**Figure 4**) was 2164 kg m^{-3}. It decreased with the increasing amount of all the tested electrically conductive admixtures. In the case of CB, the decrease was in a range of 3.3–8.7 % compared to the reference material. The highest decrease of 8.7 % was observed for the AAAs with 8.89 % of CB. Concerning the AAA samples with CF and GP, the decrease in the bulk density was in ranges of 3.1–4.9 % and 2.9–4.5 %, respectively.

The matrix density (**Figure 5**) was highest for the reference material (2673 kg m^{-3}). Concerning the AAA

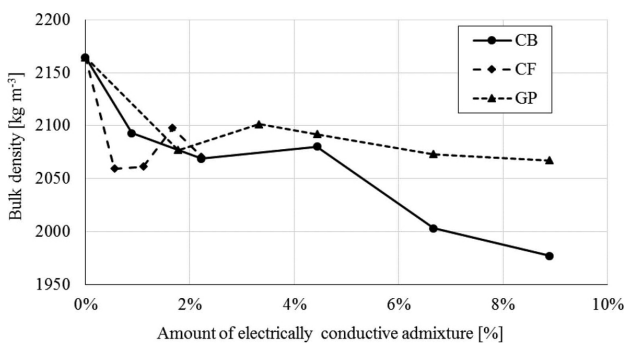

Figure 4: Bulk density of electrically enhanced AAAs

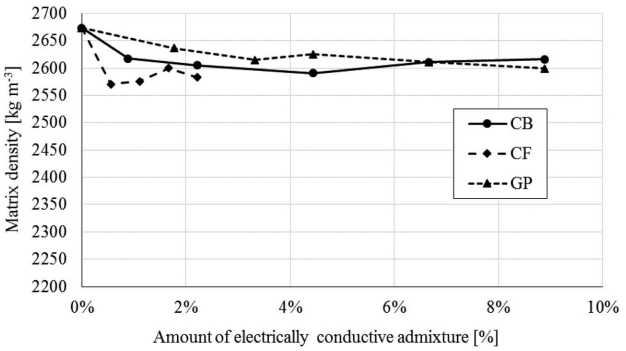

Figure 5: Matrix density of electrically enhanced AAAs

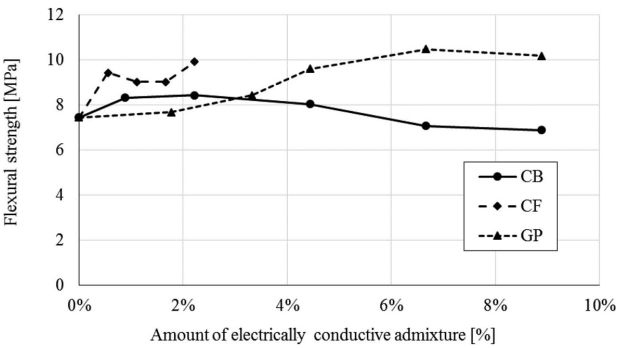

Figure 7: Flexural strength of electrically enhanced AAAs

mixtures with electrically conductive fillers, the samples with a GP admixture exhibited a higher matrix density (2599–2636 kg m^{-3}) compared to the samples with CF and CB. In the case of the samples with CB, the matrix density ranged between 2590–2618 kg m^{-3}. In the case of CF, the decrease was higher than for the reference material and the matrix density ranged between 2570–2600 kg m^{-3}. The maximum decrease (3.9 %) was observed for the samples with 0.56 % of CF admixture.

The total open porosity of the mixtures ranged between 0.193–0.244 % (**Figure 6**). A significant increase in the porosity was observed for the AAA mixtures with 6.67 % of CB and 8.89 % of CB.

The dependence of the flexural strength on the amount of electrically conductive admixtures is presented in **Figure 7**. The flexural strength of the reference AAAs was 7.43 MPa and it slightly increased up to 8.03 MPa for the 4.44 % CB dosage for the materials with a CB admixture (an 8 % increase compared to the reference AAAs). For higher dosages of the CB filler, the flexural strength decreased to 6.88 MPa (a 7.4 % decrease compared to the reference AAAs). In the case of the CF admixture, the flexural strength was higher than that of the reference AAAs, which was due to the fibrous nature of such an admixture. The increase to the maximum of 9.9 MPa (a 33.2 % increase compared to the reference AAAs) was observed for the mixture with CF in the amount of 2.22 %. GP exhibited a systematic increase in the flexural strength of up to 10.47 MPa (40.9 % compared to the reference AAAs) for 6.67 % of GP and then a slight decrease to 10.17 MPa (a 36.9 % increase compared to the reference AAAs) was observed for GP in the amount of 8.89 %.

The dependence of the compressive strength on the amount of electrically conductive admixtures is presented in **Figure 8**. The highest compressive strength equal to 66.38 MPa was observed for the reference AAAs. With the increase in the amount of electrically conductive admixtures, a decrease in the compressive strength was observed. The electrically conductive admixtures reduced the workability of the mixes and therefore a higher amount of the mixing water led to a higher total open porosity, which negatively affected the above mechanical property. Comparing the types of admixture, CF exhibited the lowest maximum decrease of 58.67 MPa for the samples with CF in the amount of 1.11 % (an 11.6 % decrease compared to the reference AAAs), 24.77 MPa for the samples with CB in the amount of 6.67 % (a 62.7 % decrease compared to the reference AAAs) and 37.34 MPa for the samples with GP in the amount of 6.67 % (a 43.7 % decrease compared to the reference AAAs).

The electrical conductivity of the reference AAA material was 1.27×10^{-6} S m^{-1}. Such a material is practically electrically non-conductive. The electrical conductivity of the samples with any type of the studied electrically conductive admixtures increased compared to the reference material (**Figure 9**). However, the increase was by just about one order of magnitude (10^{-5}) and remained constant for all the dosages of the CF and GP admixtures. In the case of CB, the electrical conductivity increased significantly by about three and half

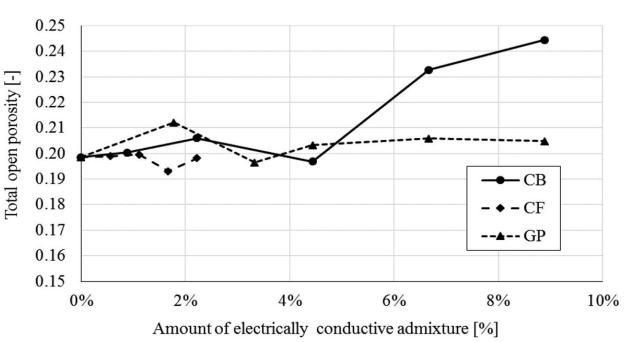

Figure 6: Total open porosity of electrically enhanced AAAs

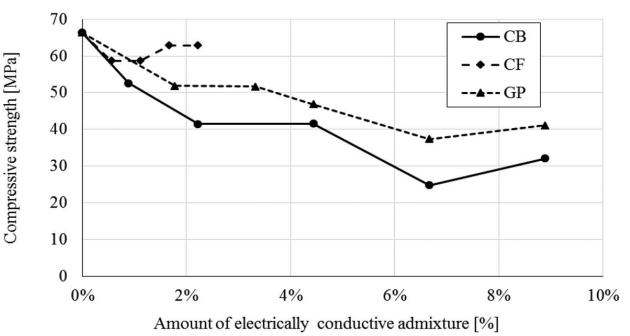

Figure 8: Compressive strength of electrically enhanced AAAs

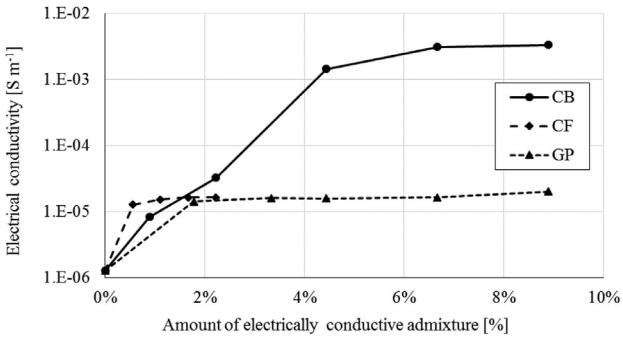

Figure 9: Electrical conductivity of electrically enhanced AAAs

orders of magnitude with the percolation threshold close to 4 % of CB.

4 CONCLUSIONS

Fifteen different AAAs were analyzed in the study, namely the reference AAAs and the AAAs with CB, CF and GP admixtures in different dosages. Basic physical properties represented by the bulk and the matrix density were determined by means of the water-saturation method. The total open porosity was then calculated with respect to the determined basic physical properties. Mechanical properties were measured according to the Czech Standard ČSN EN 196-1 on different types of samples (reference samples and the samples with a given dosage of electrically conductive admixture). Electric properties represented by the electrical conductivity were determined by measuring the electrical resistance in a 4-electrode set-up and calculating the electrical conductivity with respect to the shape ratio of the samples.

The highest increase in the electrical conductivity of about three and half orders of magnitude was observed for the samples with the CB admixture in an amount higher than 4 %, which is promising in terms of possible applications in self-heating systems. The total open porosity of the AAA samples with 4.44 % of CB remained at the same level as for the reference sample. The total open-porosity increase of about 17 % and 22.6 %, respectively, was observed in the case of the AAA samples with 6.67 % and 8.89 % of CB. The increased total open porosity negatively influenced the flexural and compressive strength of the AAAs with a 6.67 % dosage of CB; a decrease in the flexural strength of about 4.8 %, to 7.07 MPa, and a decrease in the compressive strength of about 62.7 %, to 24.77 MPa, were observed. For the AAAs with an 8.89 % dosage of CB, the strengths decreased by 7.4 %, to 6.88 MPa, and 51.7 %, to 32.03 MPa. The decrease in the compressive strength of these materials is particularly significant. However, with respect to the enhancement of electrical properties and the fact that CB is a waste product, such a material can find applications in building practice. In the case of the AAAs with CF and GP admixtures, electrical properties were not enhanced significantly, and the electrical conductivity increased by just about one order of magnitude. However, the AAAs with a CF admixture exhibited an increased flexural strength and only a low decrease in the compressive strength when compared to the reference AAAs.

Based on the results presented in this paper, the AAAs with a CB admixture exhibited the best electrical properties. Therefore, they are promising candidates in the field of smart materials. These materials will be subjected to a deeper investigation in terms of their applicability for self-heating elements.

Acknowledgment

This research was supported by the Czech Science Foundation, under project No. 16-00567S.

5 REFERENCES

[1] J. Davidovits, Geopolymers and geopolymeric materials, Journal of Thermal Analysis, 35 (**1989**) 2, 429–441, doi:10.1007/BF01904446

[2] J. Davidovits, Geopolymers – inorganic polymeric new materials, Journal of Thermal Analysis, 37 (**1991**) 8, 1633–1656, doi:10.1007/BF01912193

[3] P. Marc, I. Costescu, Industrial wastes used in pavement layers, Journal of Environmental Protection and Ecology, 14 (**2013**) 1, 187–195

[4] T. Kim, S. Tae, C. U. Chae, K. Lee, Proposal for the Evaluation of Eco-Efficient Concrete, Sustainability, 8 (**2016**) 8, 705–724, doi:10.3390/su8080705

[5] A. O. Purdon, The action of alkalis on blast furnace slag, Journal of the Society of Chemical Industry, 59 (**1940**), 191–202

[6] V. D. Glukhovsky, Soil Silicates, Gostroyizdat Ukrainy Publishing, Kiev, USSR, 1959

[7] R. Malinowski, Concretes and mortars in ancient aqueducts, Concrete International, 1 (**1979**) 1, 66–76

[8] P. Xie, P. Gu, J. J. Beaudoin, Electrical percolation phenomena in cement composites containing conductive fibers, Journal of Materials Science, 31 (**1996**) 15, 4093–4097, doi:10.1007/BF00352673

[9] M. Chiarello, R. Zinno, Electrical conductivity of self-monitoring CFRC, Cement & Concrete Composites, 27 (**2005**) 4, 463–469, doi:10.1016/j.cemconcomp.2004.09.001

[10] J. Song, D. L. Nguyen, C. Manathamsombat, D. J. Kim, Effect of fiber volume content on electromechanical behavior of strain-hardening steel-fiber-reinforced cementitious composites, Journal of Composite Materials, 49 (**2015**) 29, 3621–3634, doi:10.1177/0021998314568169

[11] J. P. Won, C. Kim, S. Lee, J. Lee, R. Kim, Thermal characteristics of a conductive cement-based composite for a snow-melting heated pavement system, Composite Structures, 118 (**2014**), 106–111, doi:10.1016/j.compstruct.2014.07.021

[12] F. Azhari, N. Banthia, Cement-based sensors with carbon fibers and carbon nanotubes for piezoresistive sensing, Cement & Concrete Composites, 34 (**2012**) 7, 866–873, doi:10.1016/j.cemconcomp.2012.04.007

[13] B. Han, S. Ding, X. Yu, Intrinsic self-sensing concrete and structures: A review, Measurement, 59 (**2015**), 110–128, doi:10.1016/j.measurement.2014.09.048

UDK 669-14:621.7.073:669.715
Original scientific article/Izvirni znanstveni članek

ISSN 1580-2949
MTAEC9, 51(6)1011(2017)

MODELING OF WATER REMOVAL IN DIRECT-CHILL CASTING OF ALUMINUM-ALLOY BILLETS

MODELIRANJE OMEJEVANJA NEPOSREDNEGA HLAJENJA Z VODO MED VERTIKALNIMI KONTI LITJEM GREDIC IZ Al-ZLITIN

Amirhossein Meysami[1], Shahin Mahmoudi[2], Mahmoud Hajisafari[2]

[1]Golpayegan University of Technology (GUT), Metallurgy and Materials Engineering Department, Golpayegan, Iran
[2]Islamic Azad University, Yazd Branch, Department of Metallurgy and Materials Engineering, Yazd, Iran
meysami@gut.ac.ir

Prejem rokopisa – received: 2017-05-13; sprejem za objavo – accepted for publication: 2017-07-28

doi:10.17222/mit.2017.054

Water removal is one of the methods for preventing hot tears in the production of defect-free aluminum billets. Using this method, the cooling rate near the bottom of the sump is reduced, and as a result, the possibility of creating hot tears at the final stages of solidification can be minimized. The temperature of the solid crust can be increased and the residual stresses in a casting can be minimized. A system of direct-chill casting was simulated and the influence of effective parameters, like the casting speed, was investigated. The casting speed and the position of water removal were the most effective parameters. Their optimum amounts for various diameters of the aluminum alloy were critical for the accumulated residual stresses and casting condition. The optimum conditions such as the minimum sump depth, mushy-zone thickness, minimum radial thermal gradient and strain rate near the bottom of the sump were predicted by this simulation.

Keywords: casting, aluminum alloy, hot crack

V pričujočem članku avtorji obravnavajo vertikalno kontinuirno (konti) litje gredic na osnovi Al zlitin z direktnim vodnim hlajenjem (*angl.*: Direct-Chill casting; DC). Primerna kontrola ohlajanja oz. omejevanje pretoka vode je ena izmed metod, ki preprečuje nastanek vročih razpok in drugih livarskih napak med konti litjem gredic. Pri tej metodi zmanjšamo hitrost pretoka vode oz. ohlajanja na dnu zbiralnika in posledično zmanjšamo na minimum tudi možnost tvorbe vročih razpok v zadnji fazi strjevanja. Na ta način je temperatura strjenega dela ingota (gredice) oz. trdne skorje višja in zaostale napetosti v gredici, nastale med litjem so manjše. Avtorji prispevka so izvedli simulacijo procesa DC litja in ugotavljali vpliv posameznih procesnih parametrov. Na proces litja sta najbolj vplivala hitrost litja in mesto odstranjevanja vode. Optimalne vrednosti teh dveh parametrov pri litju gredic različnih premerov so odoločilno vplivale na velikost zaostalih napetosti in ostale pogoje litja Al zlitin. S to simulacijo so avtorji določili optimalne pogoje litja, kot so minimalna globina vodnega zbiralnika, debelina testaste (kašaste) cone, najmanjši radialni termični gradient in hitrost deformacije blizu dna zbiralnika.

Ključne besede: konti litje gredic, aluminijeve zlitine, vroče razpoke

1 INTRODUCTION

One of the major defects in the production of high-strength aluminum (Al) billets are hot tears in the center of a billet. Several efforts have been made to eliminate these drawbacks and different methods have been used. One of the most important ways of producing high-strength aluminum billets with large diameters in different industrial plants is the control of the ingot cooling rate, based on the removal of the water from the ingot surface, achieved by applying the water removal below the mold bottom. Using this method, the cooling rate during the final stages of the solidification in the billet center is decreased and the possibility of hot tearing during the final stages is significantly reduced. Moreover, due to the latent heat released during the solidification, the temperature of the formed solid crust is increased, also causing the removal of the residual stresses from the billet.

Considering this approach, P. P. Zeigler[1] presented a plan, with which full cooling of a billet with water during the secondary cooling could be prevented. With this method, the water streaming on a billet surface will be removed using an air jet in the opposite direction. The air-jet distance changes with a change in the chemical composition of a billet, the cooling rate in the secondary zone of the billet and the casting velocity. The amount of the heating output from the surface of a billet should be controlled so that the temperature of the billet surface after the water removal should not be less than 150 °C and it is preferably between 200 °C and 340 °C. It should be noted that the billets produced with this process have large diameters and need the annealing process to be used during the other stages; the desired temperature of annealing is about 315–430 °C. If the water from the surface of a billet is removed, due to an increase in the temperature of the solid layer, the annealing processes are largely completed and the common annealing heat-treatment process can be greatly reduced.

There are also other researchers who used this method; with the T. C. Zinniger method[2], water removal is done using a rubber ring, placed at a certain distance

from the mold bottom. Another method was proposed by E. W. Reeves et al.[3]; they used a water jet in the direction opposite to the water flow on the surface, at a certain angle and velocity, causing the removal of the streaming water from the surface. E. Gervais et al.[4] provided another method for water removal. In their method, the water is removed from the surface of a billet with a tool called Waiper.

C. Devadas and J. F. Grandfield[5] carried out a general review of modeling a DC aluminum casting. In addition, D. G. Eskin[6] reviewed and fully discussed the metallurgy of the direct-chill-casting process. V. Schneider and E. K. Jensen[7] considered the cracking at the start of billet casting and recognized the depth of the sump as the criterion for hot tearing. According to this criterion, the possibility of hot tearing is increased due to the increasing sump depth, and this assumption is similar to the new theories of hot tearing.[8,9] By increasing the sump depth, the thickness of the mushy zone in the center of a billet will also increase. As a result, the possibility of melt feeding is reduced and the probability of hot cracking is increased.

In the past decades, several methods were employed to produce all the aluminum alloys using the process of DC casting. However, in the production of series 2xxx and 7xxx of aluminum alloys, having a large solidification range, there are both hot and cold cracks.[9] Hot tearing occurs as long as there is a lack of feeding during the solidification. Several studies suggested that by increasing the casting velocity, the possibility of hot tearing will also increase and this defect occurs mostly in the center of a billet.[10–11] M. Lalpoor et al.[12] showed that in steady-state conditions, large compressive stresses are formed close to the surface of a billet in the circumferential direction, while in the center, tensile stresses act in all directions. In a research carried out by Y. Wang,[13] the removal of water from slabs made of the 7075 aluminum was studied.

In this research, the temperature distribution for 7075 Al ingots was calculated and the optimum condition for a water-restricted panel and the casting velocity was determined. This is a new method and no research has recently been done in this field.

2 MATERIALS AND METHODS

One important factor in the process of modeling is to determine the exact geometry of the flow field or, in other words, the range of the melt flow. A schematic design of a DC-casting system including different parts and dimensions of a 254 mm billet is shown in **Figure 1**. In **Figure 2**, a computational grid used in the domain of casting is shown for a 762 mm billet. Physical and thermal properties used for modeling the DC casting of 2024 aluminum-alloy billets vary with the temperature as shown in **Table 1**.

Table 1: Thermophysical properties of 2024 aluminum alloy used for the modeling

Viscosity (mPa s)	Density kg/m^3)	Heat capacity (J/kg)	Enthalpy (J/g)	Conductivity (W/m^2 K)	Temperature (°C)
–	2785	0.85	0	175	25
–	2779	0.9	66	185	100
–	2750	0.95	159	193	200

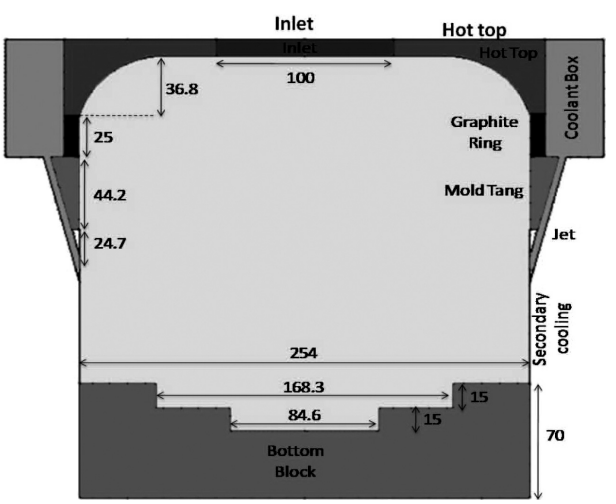

Figure 1: Schematic of DC-casting mold system used in this study for a 254 mm billet

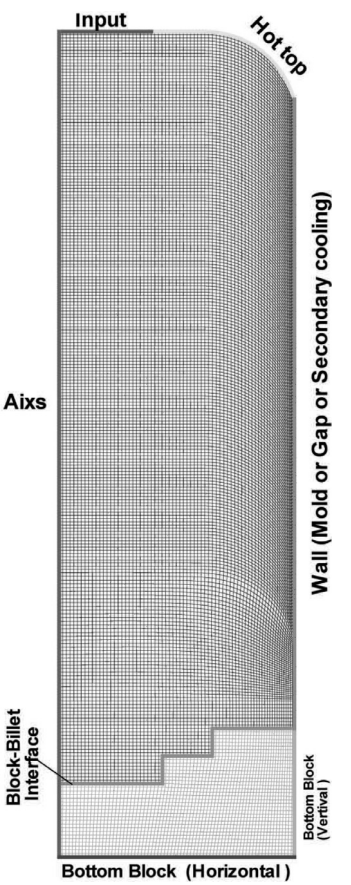

Figure 2: Computational grid used for modeling a 762 mm billet

–	2730	0.97	255	193	300
–	2707	0.10	353	190	400
–	2683	0.18	457	188	500
–	2674	1.10	566	188	538
1.3	2500	1.14	970	85	632
1.2	2480	1.14	1048	84	700
1.1	2452	1.14	1162	175	800

3 GOVERNING EQUATIONS AND BOUNDARY CONDITIONS

In order to determine the velocity vectors of this model, the continuity and momentum equations for an incompressible Newtonian fluid in two-dimensional cylindrical coordinates were employed. In order to predict the temperature distribution, by considering the solidification, the energy equation was solved.

Continuity equation (1):

$$\frac{1}{r}\frac{\partial}{\partial r}=(rv_{\mathrm{r}}+\frac{\partial}{\partial z}(v_z)=0 \tag{1}$$

Momentum equation (2) in the z direction:

$$\rho\left(\frac{\partial v_z}{\partial t}+v_r\frac{\partial v_z}{\partial r}+v_z\frac{\partial v_z}{\partial z}\right)= \\ =\left[\frac{1}{r}\frac{\partial}{\partial r}\left(r\mu\frac{\partial v_r}{\partial r}\right)+\frac{\partial}{\partial z}\left(\mu\frac{\partial v_z}{\partial z}\right)\right]-\frac{\partial P}{\partial z}+\alpha(T-T_0)\rho g_r+Sc \tag{2}$$

Momentum equation (3) in the r direction:

$$\rho\left(\frac{\partial v_r}{\partial t}+v_r\frac{\partial v_r}{\partial r}+v_z\frac{\partial v_r}{\partial z}\right)= \\ =\left[\frac{\partial}{\partial r}\left(\frac{1}{r}\mu\frac{\partial}{\partial r}(rv_r)\right)+\frac{\partial}{\partial z}\left(\mu\frac{\partial v_r}{\partial z}\right)\right]-\frac{\partial P}{\partial r}+\rho g_r+S \tag{3}$$

Energy equation (4):

$$\rho\left(\frac{\partial H}{\partial t}+\frac{\partial(\rho v_z H)}{\partial z}+\frac{1}{r}\frac{\partial(rv_r H)}{\partial r}\right)= \\ =\frac{1}{r}\frac{\partial}{\partial r}\left(kr\frac{\partial T}{\partial r}\right)+\frac{\partial}{\partial z}\left(k\frac{\partial T}{\partial z}\right) \tag{4}$$

In the above equations, α is the coefficient of the thermal expansion, which is the driving force of the thermal buoyancy in the liquid-pool area and Darcy's law is also used to model the flow in the mushy zone:[14]

$$u=\frac{1}{K_{\mathrm{D}}}\left(\frac{\partial P}{\partial z}+\rho g_z\right) \tag{5}$$

In equation (5), K_{D} in the mushy zone is the function of the molten volume fraction.

In the present model, it is assumed that the velocity on all solid surfaces is equal to the casting velocity. For the output (solidified ingots), the velocity is equal to the casting velocity and it is assumed that the molten material enters at a uniform velocity from the top of the computational domain (the flow inlet).

In the DC-casting process, the molten thermal energy is extracted in two regions, primary cooling and secondary cooling. Primary cooling occurs inside the mold zone and below the mold. Secondary cooling is initiated by the water flow on the surface of the billet, and it also has two impingement and streaming zones where the impingement zone is the location of the first water contact, at which the cooling rate is higher than in the streaming zone because the kinetic energy of the inlet water is removed and water moves based on the gravitational force. The boundary condition of the energy equation for the surface of the billet can be summarized as shown in **Table 2**.

Equations (1) to (4) were discretized with the finite volume method (FVM) in a cylindrical coordination. A first-order, upwind, differencing, implicit approach was used and the discretized equations were solved with the TDMA algorithm using an iterative method. **Figure 3** shows the finite volume meshing on the Cartesian coordinates. The program was solved with the Ansys Fluent V12 software.

Table 2: Heat-transfer coefficient of primary and secondary cooling zones in the model of a DC-cast billet

Cooling region	H_{cooling}	T_{cooling} (K)
Hot top	0	-
Mold (primary cooling)		
Melt contact	2000	320
Air gap	50	320
Secondary cooling		
Air gap	50	320
Impingement zone	20000	320
Streaming zone	10000	320

4 RESULTS AND DISCUSSION

4.1 Model validation

Before providing the results of the present study, the results of the current-model validation needed to be provided to ensure a proper performance of this computational model. The validation of the present model was compared with the results of C. J. Vreeman et al.[15] A pool profile was obtained by C. J. Vreeman using a sudden addition of a molten material with a grain refiner to the hot top of the caster during the steady-state casting of a 450 mm billet. **Figure 3b** shows a macrograph of the pool in a grain-refined billet. In this macrograph, the etched lines represent the solidus interface and the transition between the rigid, packed solid and the slurry. **Figure 3a** shows the results of the simulation presenting a computational model with the work of Vreeman[15] (alloy Al-6wt%Cu with a casting velocity of 6 cm/min) including liquid fraction contours and velocity vectors. The profile of the pool obtained with an etched macrograph (**Figure 3b**) of the grain-refined billet was compared with the predictions (**Figure 4a**), with the current calculation and Vreeman's computational model.[15] As

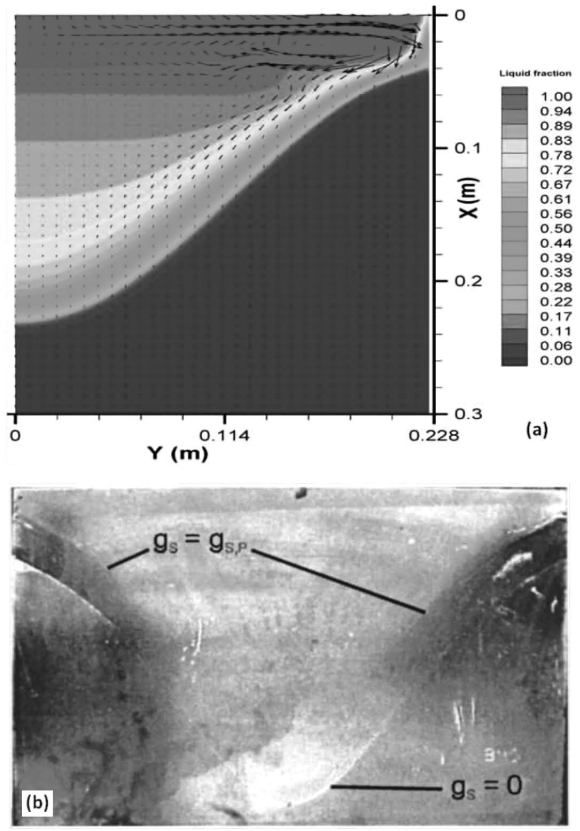

Figure 3: a) Fluid fraction contours with velocity vectors resulting from the current computational model of a casting system is validated, b) macrograph of the pool profile in a grain-refined billet[15]

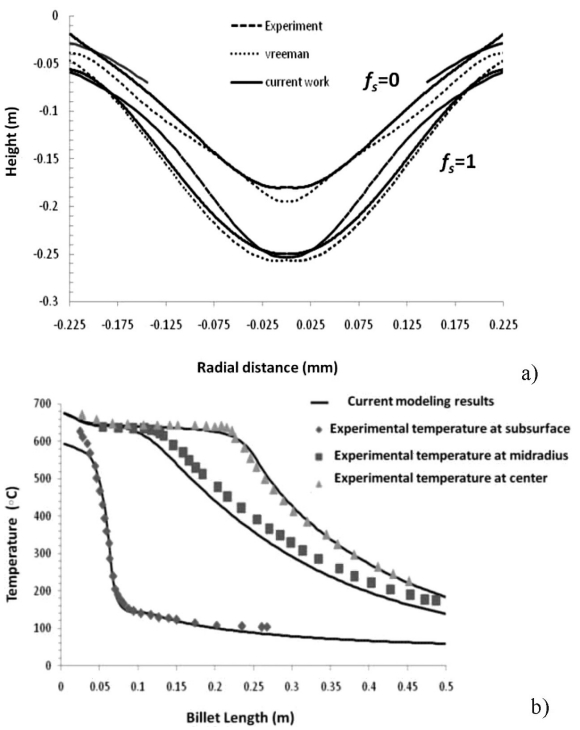

Figure 4: Comparing the results of prediction: a) profile of the pool, b) profile of the temperature variation at three points: surface, middle part and center of a billet[15]

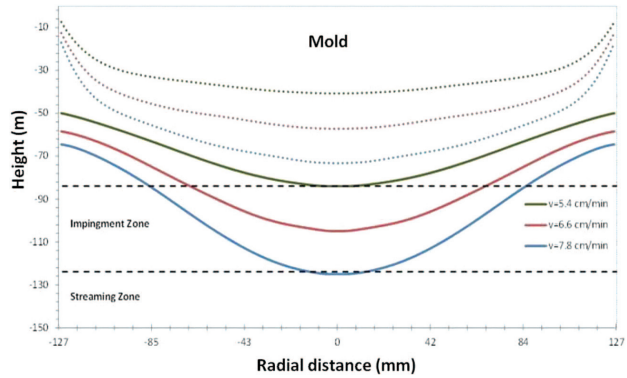

Figure 5: Prediction of the pool profile in the steady-state condition for a 254 mm billet at three casting velocities (5.4, 6.6 and 7.8) cm/min so that dotted lines indicate fluid fraction 0.7 (start of mushy zone) and bold lines are the zero fluid fraction (pool profile)

shown, both models are in good agreement with the results of the measurement done when predicting the pool depth. A comparison of the vertical temperature profiles from the experiments by Vreeman and the current computational model is shown in **Figure 4b**. At all three radial positions (surface, middle part and center), the temperature decreases as a result of the conduction toward the chill, and in the middle part and the center of the solidification range, the steep temperature variation is reduced. As shown in this case, in the three points, especially in the center, there is good agreement between the experiment and the modeling result.

4.2 Computational model results

In the DC-casting process, one of the issues that represents the criterion for the quality of a billet and prevents hot tearing is the pool depth. In **Figure 5**, the pool and mushy profiles are shown for three casting velocities of (5.4, 6.6 and 7.8) cm/min for the 254 mm 2024 billet. As shown, if the casting velocity increases, the pool depth is uniformly increased. On the other hand, by increasing the casting velocity, the starting place of the solid crust (at the mold wall) and the pool bottom (at

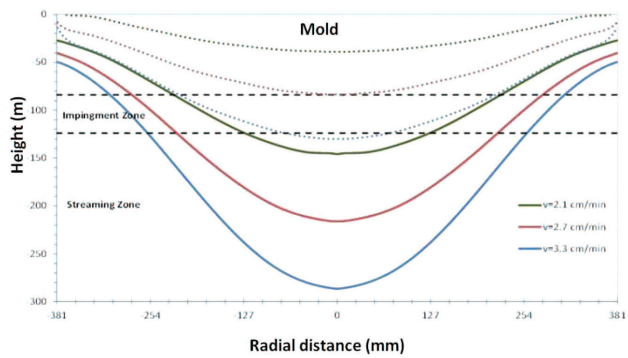

Figure 6: Prediction of the pool profile in the steady-state condition for a 762 mm billet at three casting velocities (2.1, 2.7 and 3.3) cm/min so that dotted lines indicate fluid fraction 0.7 (start of mushy zone) and bold lines are the zero fluid fraction (pool profile)

the center) are transferred to the lower places of the mold that allow more movement. Another parameter that can increase the pool depth is an increase in the cooling in the secondary zone. **Figure 6** shows the pool and mushy profiles at three casting velocities for the 762 mm 2024 billet. As shown, there is a similarity with the 254 mm billet: if the casting velocity increases, the pool depth will be increased. In this billet, the diameter of the pool depth and the mushy thickness are significantly larger than those of the 254 mm billet, which makes it more sensitive to hot tearing. In order to prevent hot tearing, the pool depth and strain rate should be kept at minimum and optimum amounts.

4.3 Water removal

In this section, the method of water removal based on the temperature distribution of the 2024 billet is investigated. In order to have a more accurate and quantitative evaluation of the pool depth by the water-removal panel, **Figure 7** is provided. In this figure, the changes in the pool depth and the thickness of the mushy zone are plotted for the locations of the water-removal panel. In this figure, guidelines of 0.5 *R*, 0.6 *R* and 0.7 *R* (*R* is the radius of the billet) are used. The purpose of drawing these guidelines is to present the condition, under which the billet can be cast without any risk of hot tearing.

According to F. Grandfield's research,[16] the 0.7 *R* criterion is obtained with this experiment and this diagram. It is considered that if the 0.5 *R* criterion can be used for the pool depth of the 762 mm billet for more safety, then the casting velocity of 2.4 cm/min would not be suitable and it is better to use the casting velocity of 2.1 or 1.8 cm/min. At the casting velocity of 2.1 cm/min, with the panel distance being longer than 10 cm (from the bottom of the mold), the pool depth is good; at the casting velocity of 1.8 cm/min, with the panel distance being longer than 6 cm, the pool depth is suitable. If the casting velocity of 2.1 cm/min and the panel distance of 10 cm are selected as a suitable condition, then this distance can also be chosen for the velocity of 1.8 cm/min, with the removal place of 7 cm, to decrease the mushy thickness in the pool depth. This velocity is better than

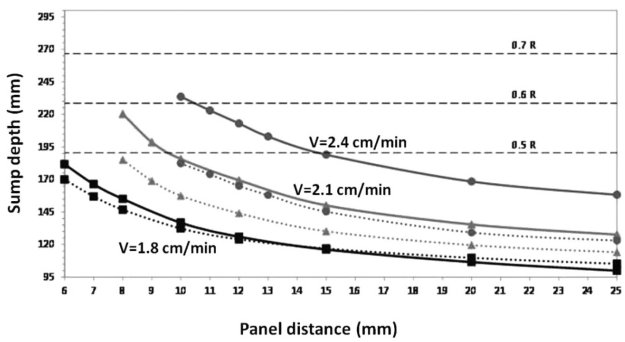

Figure 7: Variations in the pool depth and mushy thickness for the panel place of the 762 mm billet at various casting velocities

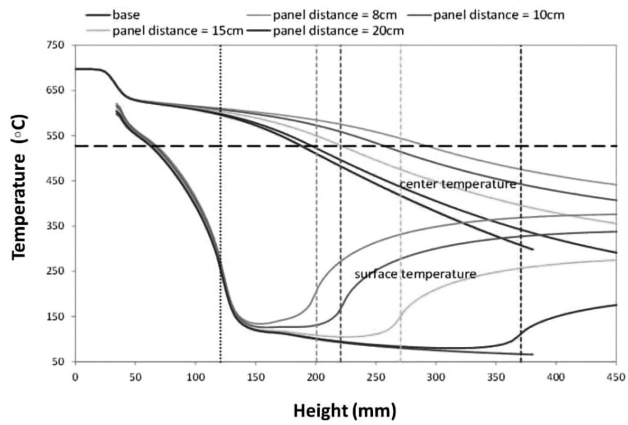

Figure 8: Temperature changes for the surface and center of the billet for different places of the panel of the 762 mm billet at the casting velocity of 2.1 cm/min

the velocity of 2.1 cm/min. Similar studies carried out for the billets with a diameter of 508 mm reveal that if we want to keep the pool depth below 0.5 *R*, the casting velocities of 2.4 cm/min or 3.0 cm/min are suitable and the panel distances should be at least 7 cm and 5 cm from the bottom of the mold. For the billets with a diameter of 254 mm, the suitable casting velocity is less than 6.0 cm/min and the panel distance is 5 cm.

The next parameter for removing the water is the temperature distribution after the water removal from the surface of the billet. The results for the casting velocity of 2.1 cm/min and the 762 mm billet are presented in **Figure 8**. As a result of the reduction in the cooling rate for the surface of the billet, the surface temperature is increased if the water is removed from the surface of the billet. The temperature difference between the surface and the center is reduced and this difference is lower than in the case when there is no water removal. On the other hand, when a water removal occurs, the surface temperature at the location of the panel is not reduced, but it even increases. The trend of the changes in the temperatures of the surface and the center of the billet is such that the overall temperature gradient between the surface and the center decreases. This can greatly reduce the stress exerted on the billet center that can cause hot tearing.

To obtain more accurate observations of the effect of the water removal on the temperature gradient at the bottom of the pool, the plots in **Figure 9** were drawn. In these plots, the temperature distribution in the radial direction is shown at the bottom of the pool. As seen in all the cases, the temperature in the center is equal to the solidus temperature and by increasing the panel distance, the surface temperature decreases and this temperature is similar to the situation of no water removal.

A large-freezing-range alloy promotes hot tearing given that such an alloy is for a longer time in a vulnerable state, in which thin liquid films form between the dendrites. At the final stage of the solidification (f_S >

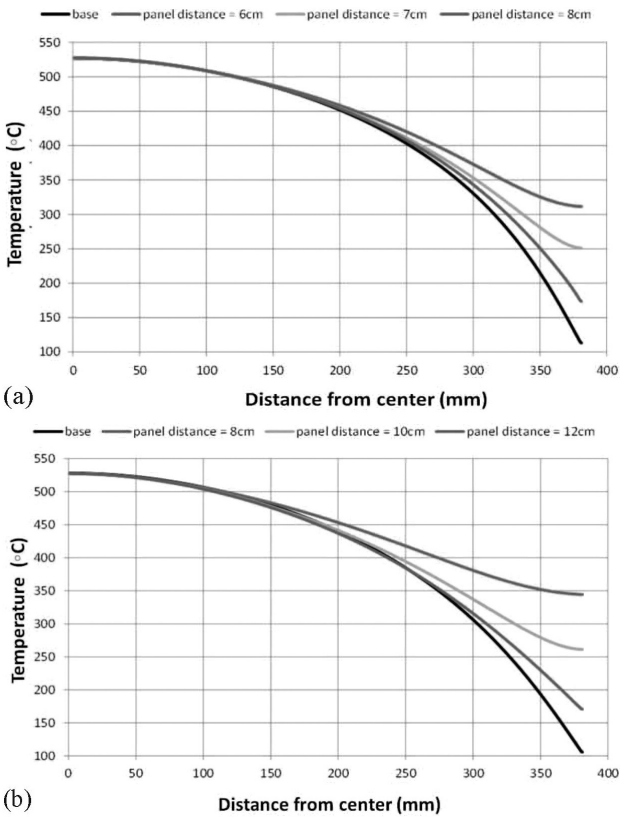

Figure 9: Temperature changes from the billet surface to the center at the end of the melt laver for different places of removing the water from the surface of the 762 mm billet at casting velocities of: a) 2/1 cm/min and b) 1/8 cm/min

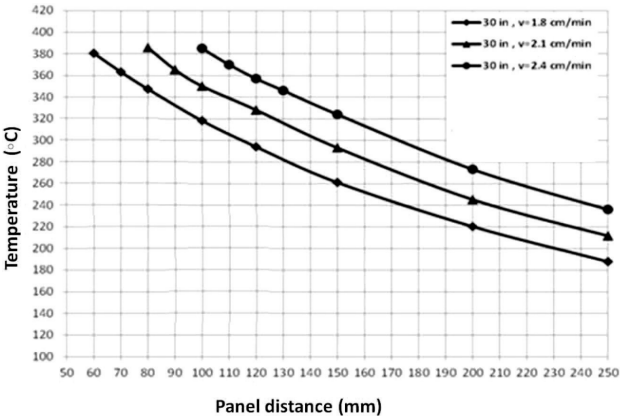

Figure 10: Differences in the temperature average of 762 mm billet in different casting velocities based on different places of removing water from the surface of the billet

0.9), only the solid-state creep can compensate for the solidification shrinkage and thermal stresses[10]. The strains and strain rates in the mushy zone increase if the cooling rate increases at the solid fraction equal to 0.95 in the center of the billet, which is plotted for three casting velocities and for different panel positions. In addition, by increasing the casting velocity, the panel-position (from the bottom of the mold) cooling rate increases and the use of the panel has a remarkable effect on the magnitude of the cooling rate in the critical solid fraction.

An additional reduction in the range of water cooling appears for the temperature gradient and cooling rate at the bottom of the pool. However, this position causes an increase in the pool depth and the mushy-zone thickness, so the place of the panel should be an optimized position. In this respect, the removal places of 7 cm and 10 cm are detected as suitable for 2.1 cm/min and 1.8 cm/min, respectively, for the 762 mm billets as they cause minimum thermal gradients between the bottom of the pool and the surface. With the same calculation for the 508 mm billets, the places of the water removal of 5 cm and 7 cm can also be obtained for the casting velocities of 2.4 cm/min and 3.0 cm/min, respectively. Finally, for the 254 mm billets, the place of the water removal of 5 cm was calculated for a casting velocity between 4.8 cm/min and 5.4 cm/min.

It is necessary to remove the residual stresses from the heat treatment so as to produce an aluminum cast part at a temperature of 343 °C; this temperature is 404 °C for alloy 2024 DC cast in this research and the time for the heat treatment is 2–3 h, as shown in **Figure 10**. With the increasing casting velocities, the billets do not have enough time for cooling and the average temperature difference increases at different casting velocities. These results were obtained to optimize the conditions for 10 mm and 762 mm billets. The average temperature of the surface and the center is between 320–380 °C, which is less than the preferred temperature for alloy 2024. However, at this temperature, it is possible to remove the residual stresses and reduce the overall heat-treatment time.

5 CONCLUSION

In this survey, the modeling results of the water-removal method involving DC-cast billets of the 2024 alloy were investigated and compared with the results obtained with a simulation. Given that water removal causes an increase in the pool depth and expands the mushy zone, it is better to use a low casting velocity, at which the pool depth and mushy-zone thickness are small. On the other hand, as the important tasks of water removal are, firstly, to decrease the temperature gradient and the cooling rate or the strain rate at the bottom of the pool and, secondly, increase the temperature in the billet, it is necessary to decrease the water-cooling zone in order to be close to the above aims. Therefore, the water-cooling zone should be reduced, which causes an increase in the pool depth and the thickness of the mushy zone. Then, according to the points discussed, an optimized middle status should be selected. In this status, the casting velocities of 1.8 cm/min or 2.1 cm/min for the water-removal place of 7 cm and 10 cm, respectively,

are used for casting 762 mm billets. For 508 mm billets, the casting velocity is 2.4 cm/min and 3.0 cm/min and the water-removal place is 7 cm and 5 cm, respectively. For 254 mm billets, the casting velocity of 4.8 cm/min and 6 cm/min and the water-removal place of 5 cm are recognized as suitable casting conditions.

Using the parameters mentioned in the paragraph above, the highest surface temperature is about 320–380 °C, which is lower than the heat required for removing the residual stresses from alloy 2024 (404 °C); but it seems that in the temperature range above, we can remove a considerable amount of residual stresses. Using another strategy, we can position the induction coils during the passing of the billet to bring them to the desired temperature, thereby saving enormous energy and removing the residual stresses that can lead to a distortion in the billet.

Acknowledgment

This work was supported by the Golpayegan University of Technology as an internal research project of 2017.

Nomenclature

Specific heat at constant pressure	c_p
Gravity	g
Enthalpy	H
Kelvin	K
Pressure	P
Source term	S
Time	t
Temperature	T
Ref. temperature	T_0
Radial speed	v_r
Axial speed	v_z
Watt	W
Viscosity	μ
Density	ρ
Coefficient of thermal expansion	α

6 REFERENCES

[1] P. P. Zeigler, Method of Continuous Casting, US patent, 2705335, 1955

[2] T. C. Zinniger, Direct Chill Casting Method with Coolant Removal, US patent, 4237961, 1980

[3] E. W. Reeves, R. Womack, W. J. Fenton, J. Mcdermott, J. Boorman, Method and Apparatus for Removal of Cooling Water from Ingots by Means of Water Jets, US patent, 2009/0301683, 2009

[4] E. Gervais, H. Levert, P. Chollet, Method for the Continuous Casting of Metal Ingots or Strips, US patent, 3891024, 1975

[5] C. Devadas, J. F. Grandfield, Experiences with Modelling DC Casting of Aluminum, in Proceedings of the 120th TMS Annual Meeting Light Metals, TMS Annual Meeting: TMS (The Minerals, Metals & Materials Society), 1990, 883–892

[6] D. G. Eskin, Physical Metallurgy of Direct Chill Casting of Aluminum Alloys, CRC Press, FL, 2008, 63

[7] W. Schneider, E. K. Jensen, Investigations about Starting Cracks in DC Casting of 6063 Type Billets, Part I: Experimental Results, Essential Readings in Light Metals, The Minerals, Metals & Materials Society (TMS), 3 (**1990**), 743–748, doi:10.1002/9781118647783.ch94

[8] M. Rappaz, J. M. Drezet, M. Gremaud, A New Hot Tearing Criterion, Metall. Mater. Trans. A, 30 (**1999**) 1, 449–455, doi:10.1007/s11661-999-0334-z

[9] P. Barral, P. A. Quintela, Numerical method for simulation of thermal stresses during casting of aluminum slabs, Comput. Methods Appl. Mech. Engrg., 178 (**1999**) 1, 69–88, doi:10.1016/S0045-7825(99)00005-5

[10] W. H. Suyitno, L. Kool, Hot tearing criteria evaluation for direct chill casting of an Al-4.5pct Cu alloy, Metall. Mater. Trans. A, 36 (**2005**) 1, 1537–1546, doi:10.1007/s11661-005-0245-6

[11] N. Hatami, R. Babaei, M. Dadashzadeh, Modeling of hot tearing formation during solidification, J. Mater. Process. Technol., 205 (**2007**) 1, 506–513, doi:10.1016/j.jmatprotec.2007.11.260

[12] M. Lalpoor, D. G. Eskin, L. Katgerman, Cold-cracking assessment in AA7050 billets during direct-chill casting by thermomechanical simulation of residual thermal stresses and application of fracture mechanics, Metall. Mater. Trans. A, 403 (**2009**)1, 304–313, doi:10.1007/s11661-009-0031-y

[13] Y. Xu, J. C. Wang, S. J. Guo, X. T. Li, G. X. Xue, Effects of Water-Restricted Panel on the Casting Process of High Strength Aluminum Alloy Ingots, Journal of Materials Processing Technology, 211 (**2011**) 1, 78–83, doi:10.1007/s11831-014-9100-5

[14] V. R. Voller, C. A. Prakash, Fixed grid numerical modeling methodology for convection-diffusion mushy region phase change problems, Int. J. Heat Mass Transfer, 30 (**1978**) 1, 1709–1719

[15] C. J. Vreeman, J. D. Schloz, M. J. M. Krane, Direct Chill Casting of Aluminum Alloys, Modeling and Experiments on Industrial Scale Ingots, Journal of Heat Transfer, Transactions of the ASME, 124 (**2002**) 5, 947–953, doi:10.1115/1.1482089

[16] F. Grandfield, L. Wang, Application of mathematical models to optimization of cast start practice for DC cast extrusion billets, Light Metals 2004, 1st ed., Metals & Materials Society (TMS), 2004, 685–690

UDK 67.017:620.1:62-42:669.721.5
Original scientific article/Izvirni znanstveni članek

ISSN 1580-2949
MTAEC9, 51(6)1019(2017)

IMPROVING THE MICROSTRUCTURE AND MECHANICAL PROPERTIES OF MAGNESIUM-ALLOY SHEETS WITH A NEW EXTRUSION METHOD

IZBOLJŠANJE MIKROSTRUKTURE IN MEHANSKIH LASTNOSTI PLOČEVINE IZ Mg-ZLITINE Z NOVO METODO IZTISKAVANJA

Liwei Lu[1], Zhenru Yin[1], Yanfeng Liu[1], Dandan Chen[1], Chuming Liu[2], Zhiqiang Wu[1]

[1]Hunan University of Science and Technology, Hunan Provincial Key Laboratory of High Efficiency and Precision Machining of Difficult-to-Cut Material, Xiangtan, Hunan 411201, China
[2]Central South University, School of Materials Science and Engineering, Changsha 410083, Hunan, China
cqullw@163.com, wuzq2009@163.com

Prejem rokopisa – received: 2017-05-19; sprejem za objavo – accepted for publication: 2017-06-22

doi:10.17222/mit.2017.059

A new effective extrusion technique, including integrated direct extrusion and bending-shear deformation, was proposed to fabricate AZ31-magnesium-alloy sheets with high performance, and the grain refinement, texture and mechanical properties were further investigated. The results show that the new extrusion technique can noticeably refine the grain size from 240 μm to 3.2 μm at 563 K, and the basal texture is also dramatically weakened, which can be attributed to a fully dynamic recrystallization triggered by a large shearing strain accumulated due to a bar-sheet deformation and continuous bending-shear deformation. Consequently, the ductility significantly increases from 11.67 % to 27.7 %, and the ultimate tensile stress can still keep a high value of 290 MPa, rendering this new technique an effective processing method for further tailoring of the microstructure and properties of Mg-based alloys for a wide range of engineering applications.

Keywords: AZ31-Mg alloy, hot extrusion, microstructure, mechanical properties

Avtorji prispevka so raziskovali vpliv nove učinkovite tehnike iztiskavanja (ekstrudiranja) na lastnosti pločevine iz Mg zlitine AZ31. Pri tej tehniki sta združena postopka direktnega iztiskanja in upogibanja s strižno deformacijo (*angl.*: Direct Extrusion and Bending Shear; DEBS). Avtorji ugotavljajo, da je prišlo do udrobljenja mikrostrukture, raziskali pa so tudi teksturo in določili mehanske lastnosti tako izdelane pločevine. Rezultati raziskave so pokazali, da je nova tehnika ekstrudiranja opazno zmanjšala velikost kristalnih zrn iz 240 μm na 3,2 μm pri 563 K (290 °C), prav tako je občutno oslabela bazala tekstura, kar je pripisati popolni dinamični rekristalizaciji zaradi velike strižne deformacije nakopičene med preoblikovanjem okroglice v pločevino in neprekinjene upogibno-strižne deformacije. Posledično se je občutno povišala duktilnost iz 11, 67 % na 27, 7 % in natezna trdnost je še vedno ostala na visokem nivoju 290 MPa. Zato ta nova tehnika iztiskavanja lahko postane učinkovita procesna tehnologija za nadaljnje prilagajanje mikrostrukture in lastnosti Mg zlitin široki paleti inženirskih aplikacij.

Ključne besede: AZ31 magnezijeva zlitina, vroče ekstrudiranje, mikrostruktura, mehanske lastnosti

1 INTRODUCTION

The efforts to improve energy efficiency and develop low-density and high-specific-strength magnesium alloys for various structural applications in transportation vehicles are strongly driven by the development of light-weight construction. However, its application is still limited due to the hexagonal close-packed structure with poor slip systems at room temperature.[1–3] To overcome this problem, many scholars paid more attention to the grain refinement using severe plastic-deformation (SPD) techniques.[4,5] Nowadays, the most attractive SPD procedures are equal-channel angular pressing (ECAP),[6,7] cyclic extrusion compression (CEC),[8,9] high-pressure torsion (HPT)[10,11] and accumulative roll bonding (ARB).[12,13] A. Muralidhar et al.[14] adopted four passes of ECAP via the B_c route for a magnesium alloy at a temperature of 573 K. The average grain size was reduced from 31.8 μm to 8 μm. J. B. Lin et al.[15] used CEC to extrude the GW102 K alloy at 623 K with 8 passes. The elongation to failure was dramatically increased by 162.5 %, and the yield strength (YS) and ultimate tensile strength (UTS) increased by 41.3 % and 16.1 %, respectively. It should be noted that these techniques commonly require several passes before fine grains and a homogeneous strain can be obtained. Therefore, it is urgent to decrease the SPD passes to reduce the cost and increase the efficiency of practical processing of Mg alloys.

In the current study, AZ31-magnesium-alloy sheets are fabricated using a new extrusion method, integrating direct extrusion and bending shear (DEBS), which adds a successive bending-shear deformation to the conventional extrusion for further improving the microstructure and the basal texture. This deformation process can accumulate a large and homogeneous strain in the materials in a single pass, and the grains and basal texture of the AZ31-Mg-alloy sheets are prominently refined and weakened, respectively. Moreover, DEBS is proved

to be a promising way to produce high-performance Mg-alloy sheets.

2 EXPERIMENTAL PART

A schematic diagram of the DEBS process is in **Figure 1**, which shows the configuration of a designed and manufactured DEBS die. For the sake of clarity, the characteristic zones of the extrusion deformation were divided into stages I, II, III, IV and V, representing the conical part, the forward-extrusion bar sheet, the first bending-shear zone, the second bending-shear zone, and the eventual forming stage, respectively. As for zone I, the forward-extrusion ratio and conical angle were 7.08° and 60°, respectively, and the sample shape was transformed from a bar with a Ø25 mm diameter into a sheet with a width and thickness of 25 mm and 3 mm, respectively. The bending radii R_1, R_2, the bending angles β and ψ were set to be 6 mm, 3 mm, 140° and 100°, respectively.

In the present work, the AZ31-magnesium alloy with a composition of 3 % mass fraction of Al, 1 % mass fraction of Zn, 0.3 % mass fraction of Mn, and the Mg balance was employed. A graphite + engine oil lubrication containing a mass fraction of 70 % of cylinder oil (74#) and 30 % of graphite (400 mesh) was sprayed on the specimens with a 25-mm diameter and 30-mm length, made from as-cast ingots and dies, to reduce the friction. Subsequently, the billet and die were heated to the target temperature for 10 min, and the heated billet was promptly installed into the die to conduct the extrusion process for fabricating AZ31-magnesium-alloy sheets at 563 K and 643 K.

The extrusion products were cut into a rectangle shape with dimensions of 6 mm × 3 mm × 8 mm along the longitudinal plane, as shown in **Figure 1**. The microstructures of the DEBS-ed sheets were examined from the extrusion-direction (ED), transverse-direction (TD) and normal-direction (ND) planes by means of optical microscopy, and the average grain size was measured using the linear intercept process. The central region of an extrusion product was chosen for an X-ray diffraction (XRD) analysis using a Bruker Discover equipment with Cu-K_α radiation operated at 40 kV and 40 mA, and parameters α and β were measured from 0° to 75° and 360°, respectively. Tensile tests were carried out using specimens with a gauge section of 25 mm × 3 mm × 10 mm from the extruded sheets along the ED at room temperature and a constant velocity of 2 mm/min. Finally, the tensile-fracture surface was further analyzed with a scanning electron microscope. Besides, the microstructure and properties of the as-cast specimen were also tested for comparison.

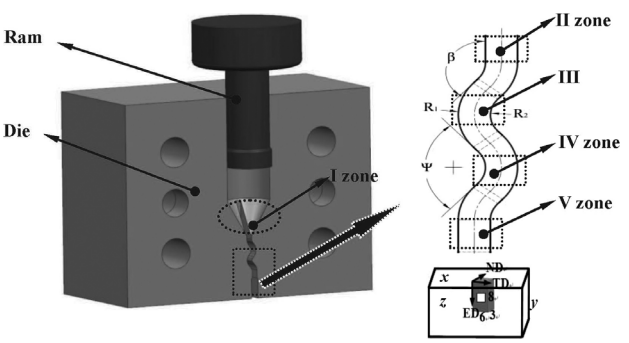

Figure 1: Sketch of the DEBS die and definition of external orientations; ED, TD, and ND denote the extrusion, transverse and normal directions

3 RESULTS AND DISCUSSION

3.1 Microstructure

To examine the microstructure-refinement effect, the optical microstructures of the AZ31-Mg alloy before and after the extrusion are shown in **Figures 2** and **3**. The grains of the as-cast billet are coarse and the average grain size is calculated to be about 240 μm (**Figure 2a**). Significantly, the DEBS-ed AZ31-magnesium-alloy sheet extruded at 563 K shows a prominent grain-refinement effect, and the average grain sizes obtained from the *x*, *y* and *z* planes are about 7.2 μm, 4.5 μm and 3.2 μm, respectively, as presented in **Figures 2b** to **2d**. After one pass, the originally coarse grains are refined markedly during the DEBS process, which is mainly attributed to the occurrence of DRX, triggered by a large accumulated strain during the extrusion process. In **Figure 2b**, the microstructure consists of some coarse grains (8 μm) in the local area, being surrounded by much finer grains (2–4 μm). Even so, from an overall perspective, the grains are relatively homogeneously distributed and refined. It is obvious that the average grain size of the AZ31-magnesium alloy can be only reduced from 31.8 μm to 8 μm after four ECAP passes at 573 K for rout B_c.[14] In contrast, the DEBS process has a unique advantage and a potential for a grain refinement.

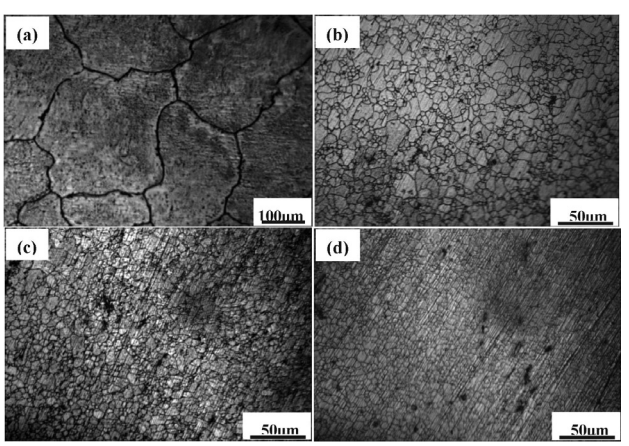

Figure 2: Optical microstructures of AZ31-Mg alloy before and after the DEBS process at 563 K: a) as-cast, b) to d) *x*, *y* and *z* planes of the extruded sample

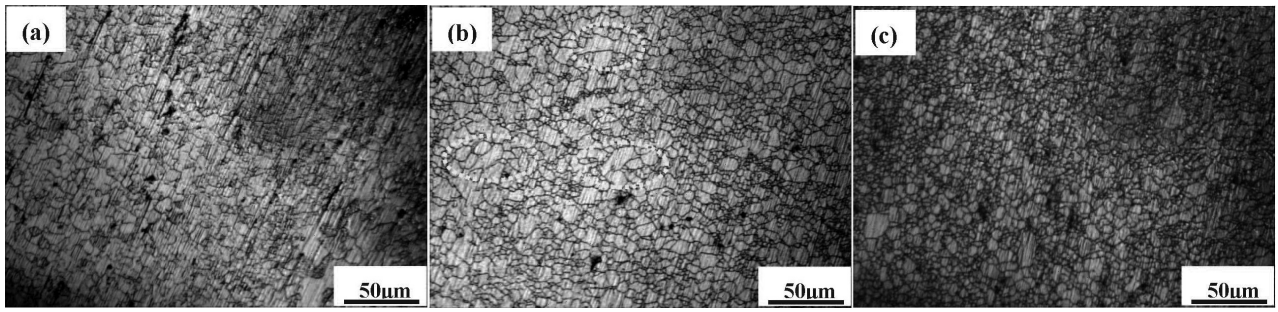

Figure 3: Light microstructures of DEBS-ed AZ31-Mg alloy at 643K: a)–c) *x*, *y* and *z* planes of the extruded sample

With an increase in the extrusion temperature (643 K), many tiny grains emerge (**Figures 3a** to **3c**). However, as there are still some inhomogeneously distorted grains in the local area, marked by ellipses (**Figure 3b**), there is not enough energy stored to fully complete DRX during the DEBS process, demonstrating that the extrusion temperature plays a significant role in the formation of distorted grains affected by the dislocation density, the evolution of dislocation cells and sub-structures. The aforementioned result is consistent with an earlier research result reported by J. F. Jiang et al.[16] They also found that the mean grain size of 27.67 μm can be obtained with ECAP at 623 K, which is much larger than that obtained at 643 K using DEBS.

3.2 Textural evolution

Figure 4 shows the {0002} and {10$\bar{1}$0} pole figures of the DEBS-ed sheets at different temperatures, exhibiting a typical {0002} fiber texture after the DEBS process. However, in comparison with the conventional extrusion (17.55)[17], the texture intensity of the DEBS-ed sheets is significantly weakened (**Figures 4a** and **4b**) and the texture component becomes more dispersive along the ED, which can induce a good deformation capability due to the <11$\bar{2}$0> direction in fewer grains orientated parallel to the ED.

A closer observation reveals that the {0002} pole figure forms a double-peaked basal texture characterized by a pronounced {0002} basal plane tilted towards the ED at about 30° and 13° (**Figure 4a**), respectively, which may be a result of a larger shear strain accumulated by the bar-sheet deformation and continuous bending-shear deformation, activating more <c+a> slip systems. These phenomena were previously reported for compressive shock loading and ARB processes by H. Asgari[18] and H. Chang[19], respectively. When the extrusion temperature increases to 643 K, the {0002} texture intensity decreases to 9.54, as shown in **Figure 4b**, and the {0002} basal plane tilts towards the ED at an angle of 10°, which is smaller than the one at 563 K. The decrease in the basal texture intensity may be attributed to an increased activation of the non-basal slip at the higher temperature during the DEBS process.

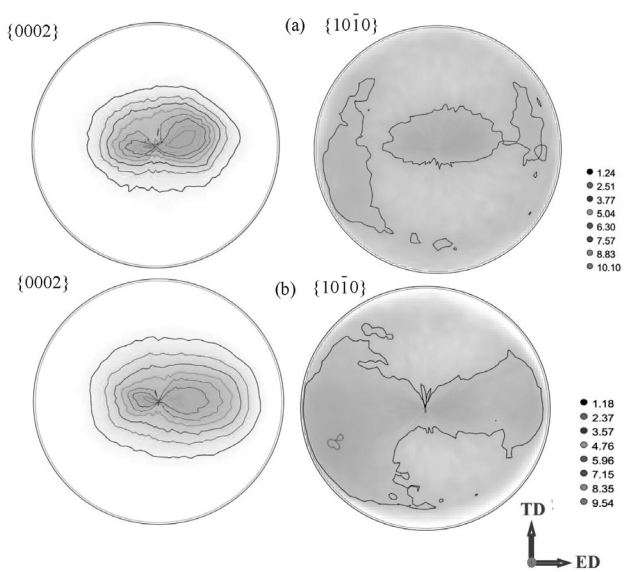

Figure 4: {0002} and {10$\bar{1}$0} pole figures for the DEBS-processed AZ31 alloys at different temperatures: a) 563 K, b) 643 K

3.3 Mechanical properties

To shed light on how the grain refinement and texture evolution affect the mechanical properties, tensile tests of the as-cast and DEBS-ed AZ31-Mg alloys are carried out at room temperature, and the tensile stress-strain pro-

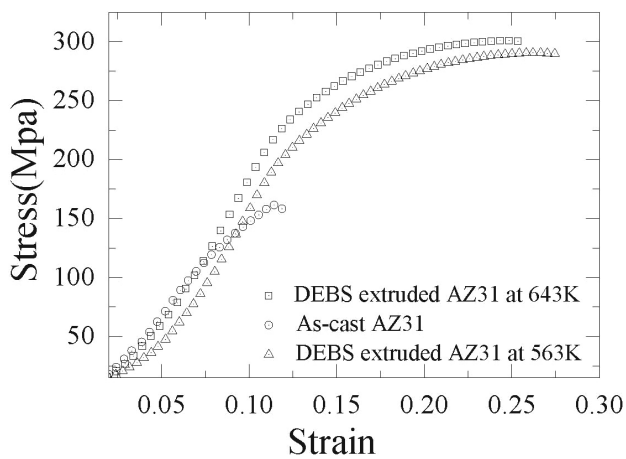

Figure 5: Tensile stress-strain curves at room temperature for the AZ31 samples processed with DEBS at 563 K and 643 K

perties are shown in **Figure 5**. The yield strength (YS), ultimate tensile strength (UTS) and elongation of the as-cast AZ31-Mg alloy are 103.3 MPa, 163.6 MPa and 11.67 %, respectively, and they are mainly caused by the original coarse grains and casting defects.[20] However, the mechanical properties are enormously enhanced with the DEBS process. As for the extrusion sheet at 563 K, the YS and UTS are about 203 MPa and 290 MPa, respectively. It should be noted that the elongation (27.7 %) is two times higher than that of the as-cast sample, which can be attributed to the combined effect of the weak basal texture and fine-grain size. It is well known that the weaker-texture intensity can lead to a larger Schmid factor of the <a> basal slip, which can improve its ductility.[21] When the processing temperature increases from 563 K to 643 K, the YS and UTS are inversely increased to 220 MPa and 300 MPa, respectively. There are some distorted grains with a high density of dislocation in the 643 K sample, which play an important role in improving the strength. However, the elongation decreases from 27.7 %to 25.7 %, indicating that the grain refinement plays a dominant role in the enhancement of ductility. On the other hand, the tilt angle of the basal texture at 563 K is larger than that at 643 K, as shown in **Figures 4a** and **4b**. Besides, the high density of dislocation and stress in the 643 K sample due to the accumulated distorted grains can also decrease its elongation.

The tensile fracture surface of an AZ31-alloy sheet before and after the DEBS process is presented in **Figure 6**. There are a large amount of cleavage planes, some shallow dimples and a few cracks in the fracture surface of the as-cast AZ31-Mg alloy (**Figure 6a**), which are typical characteristics of a quasi-cleavage fracture. By comparison, many dimples emerge and become much deeper in the DEBS-ed AZ31-alloy sheet (**Figure 6b**), but when the extrusion temperature increases to 643 K, the depth and number of dimples become shallower and fewer again (**Figure 6d**), indicating that the extrusion temperature plays an important role in tailoring the ductility.

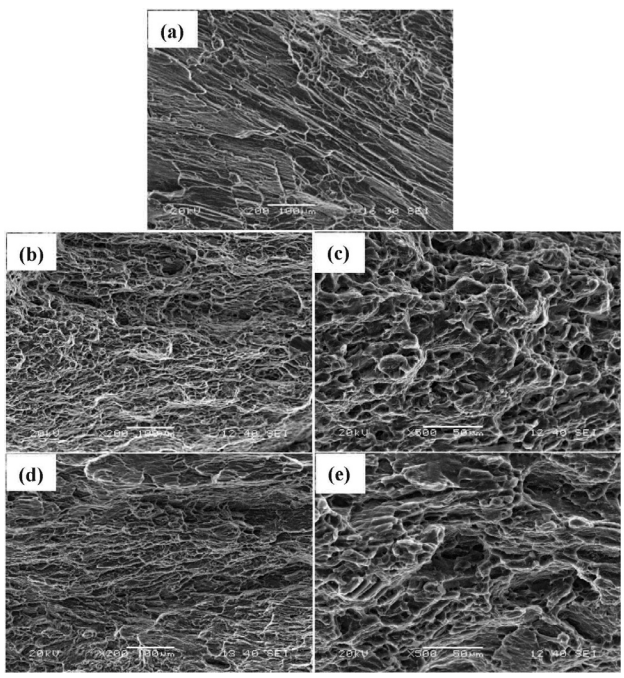

Figure 6: SEM images of the fracture surfaces of AZ31-Mg alloys before and after the DEBS process: a) as-cast, 200×, b) and d) extruded at 563 K and 643 K, 200×, c) and e) extruded at 563 K and 643 K, 500×

Anyhow, the DEBS process can dramatically improve the plasticity and produce typical characteristics of a ductile fracture, which is mainly attributed to the tilted weak texture and grain refinement. A small-scale view of the tensile fracture surface can be seen in **Figures 6c** and **6e**. There is almost no cleavage plane in **Figure 6c**; however, some noticeable cleavage traces and inhomogeneous dimples are shown in **Figure 6e**, caused by some large local and inhomogeneously distributed grains. Therefore, to obtain refined and homogeneous microstructures and a titled weak basal texture, an advanced processing technology can be used as one of the most effective ways of modifying the plasticity of the Mg alloys important for engineering.

4 CONCLUSION

In summary, the DEBS technique was applied to fabricate an AZ31-magnesium-alloy sheet with high performance and we systematically investigated the grain refinement, texture evolution and mechanical properties of the processed alloy. We find that the average grain size of the as-cast AZ31 alloy is successfully refined from 240 μm to 3.2 μm at 563 K; a crystallographic rotation and a weak texture are yielded after the DEBS process. Due to the combined effect of the grain refinement and texture weakening, both the plasticity and strength are dramatically improved. It is demonstrated that DEBS is a simple and highly efficient way of producing AZ31-alloy sheets with high performance.

Acknowledgments

This work was supported by the National Natural Science Foundation of China (Grant No. 51505143), the Scientific Research Fund of Hunan Provincial Education Department (Grant No. 17B089) and the China Postdoctoral Science Foundation (Grant No. 2016T90759 & 2014M562128).

5 REFERENCES

[1] N. El Mahallawy, A. Ahmed Diaa, M. Akdesir, H. Palkowski, Effect of Zn addition on the microstructure and mechanical properties of cast, rolled and extruded Mg-6Sn-xZn alloys, Mater. Sci. Eng. A, 680 (**2017**), 47–53, doi:10.1016/j.msea.2016.10.075

[2] X. Xie, J. Shen, F. B. Gong, D. Wu, T. Zhang, X. Luo, Y. Li, Effects of dwell time on the microstructures and mechanical properties of water bath friction stir spot-welded AZ31 magnesium alloy joints,

Int. J. Adv. Manuf. Technol., 82 (**2016**), 75–83, doi:10.1007/s00170-015-7361-2

[3] H. F. Sun, C. J. Li, W. B. Fang, Evolution of microstructure and mechanical properties of Mg-3.0Zn-0.2Ca-0.5Y alloy by extrusion at various temperatures, J. Mater. Process. Tech., 229 (**2016**), 633–640, doi:10.1016/j.jmatprotec.2015.10.021

[4] L. C. Tang, C. M. Liu, Z. Y. Chen, D. W. Ji, H. C. Xiao, Microstructures and tensile properties of Mg–Gd–Y–Zr alloy during multidirectional forging at 773 K, Mater. Des., 50 (**2013**), 587–596, doi:10.1016/j.matdes.2013.03.054

[5] F. Akbaripanah, F. Fereshteh-Saniee, R. Mahmudi, H. K. Kim, Microstructural homogeneity, texture, tensile and shear behavior of AM60 magnesium alloy produced by extrusion and equal channel angular pressing, Mater. Des., 43 (**2013**), 31–39, doi:10.1016/j.matdes.2012.06.051

[6] L. L. Tang, Y. H. Zhao, R. K. Islamgaliev, C. Y. A. Tsao, R. Z. Valiev, E. J. Lavernia, Y. T. Zhu, Enhanced strength and ductility of AZ80 Mg alloys by spray forming and ECAP, Mater. Sci. Eng. A, 670 (**2016**), 280–291, doi:10.1016/j.msea.2016.06.031

[7] J. Suh, J. Victoria-Hernández, D. Letzig, R. Golle, W. Volk, Effect of processing route on texture and cold formability of AZ31 Mg alloy sheets processed by ECAP, Mater. Sci. Eng. A, 669 (**2016**), 59–170, doi:10.1016/j.msea.2016.05.027

[8] W. Guo, Q. D. Wang, B. Ye, X. C. Li, X. C. Liu, H Zhou, Microstructural refinement and homogenization of Mg-SiC nanocomposites by cyclic extrusion compression, Mater. Sci. Eng. A, 556 (**2012**), 267–270, doi:10.1016/j.msea.2012.06.086

[9] W. P. Yang, X. F. Guo, K. J. Yang, Low temperature quasi-superplasticity of ZK60 alloy prepared by reciprocating extrusion, Trans. Nonferrous Met. Soc. China, 22 (**2012**), 255–261, doi:10.1016/S1003-6326(11)61168-0

[10] P. M. Bhovi, D. C. Patil, S. A. Kori, K. Venkateswarlud, Y. Huange, T. G. Langdon, A comparison of repetitive corrugation and straightening and high-pressure torsion using an Al-Mg-Sc alloy, J. Mater. Res. Technol., 5 (**2016**), 353–359, doi:10.1016/j.jmrt.2016.03.009

[11] M. P. Liu, H. J. Roven, X. T. Liu, M. Murashkin, R. Z. Valiev, T. Ungar, L Balogh, Grain refinement in nanostructured Al-Mg alloys subjected to high pressure torsion, J. Mater. Sci., 45 (**2010**), 4659-4664, doi:10.1007/s10853-010-4604-3

[12] M. H. Maghsoudi, A. Zarei-Hanzaki, H. R. Abedi, Modification of the grain structure, γ phase morphology and texture in AZ81 Mg alloy through accumulative back extrusion, Mater. Sci. Eng. A, 595 (**2014**), 99–108, doi:10.1016/j.msea.2013.11.095

[13] G. Faraji, M. M. Mashhadi, H. S. Kim, Microstructure inhomogeneity in ultra-fine grained bulk AZ91 produced by accumulative back extrusion (ABE), Mater. Sci. Eng. A, 528 (**2011**), 4312–4317, doi:10.1016/j.msea.2011.02.075

[14] A. Muralidhar, S. Narendranath, H. Shivananda Nayaka, Effect of equal channel angular pressing on AZ31 wrought magnesium alloys, J. Magnesium Alloys, 1 (**2013**), 336–340, doi:10.1016/j.jma.2013.11.007

[15] J. B. Lin, X. Y. Wang, W. J. Ren, X. X. Yang, Q. D. Wang, Enhanced strength and ductility due to microstructure refinement and texture weakening of the GW102K alloy by cyclic extrusion compression, J. Mater. Sci. Technol., 32 (**2016**), 783–789, doi:10.1016/j.jmst.2016.01.004

[16] J. F. Jiang, Y. Wang, J. J. Qu, Microstructure and mechanical properties of AZ61 alloys with large cross-sectional size fabricated by multi-pass ECAP, Mater Sci. Eng. A, 560 (**2013**), 473–480, doi:10.1016/j.msea.2012.09.092

[17] L. W. Lu, C. M. Liu, Z. R. Yin, J. Zhao, L. Gan, Z. C. Wang, Double extrusion of Mg-Al-Zn alloys, Int. J. Adv. Manuf. Technol., 89 (**2017**), 869–875, doi:10.1007/s00170-016-9146-7

[18] H. Asgari, A. G. Odeshi, J. A. Szpunar, L. J. Zeng, E. Olsson, Grain size dependence of dynamic mechanical behavior of AZ31B magnesium alloy sheet under compressive shock loading, Mater. Charact., 106 (**2015**), 359–367, doi:10.1016/j.matchar.2015.06.030

[19] H. Chang, M. Y. Zheng, W. M. Gan, K. Wu, E. Maawad, H. G. Brokmeier, Texture evolution of the Mg/Al laminated composite fabricated by the accumulative roll bonding, Scripta Mater., 61 (**2009**) 7, 717–720, doi:10.1016/j.scriptamat.2009.06.014

[20] W. Guo, Q. D. Wang , B. Ye, H. Zhou, Microstructure and mechanical properties of AZ31 magnesium alloy processed by cyclic closed-die forging, J. Alloys Compd., 558 (**2013**), 164–171, doi:10.1016/j.jallcom.2013.01.035

[21] Q. S. Yang, B. Jiang, H. C. Pan, B. Song, Z. T. Jiang, J. H. Dai, L. F. Wang, F. S. Pan, Influence of different extrusion processes on mechanical properties of magnesium alloy, J. Magnesium Alloys, 2 (**2014**), 220–224, doi:10.1016/j.jma.2014.10.001

UDK 620.1:669.295:621.3.017.7
Original scientific article/Izvirni znanstveni članek

ISSN 1580-2949
MTAEC9, 51(6)1025(2017)

FORMATION MECHANISM OF DIFFUSION-REACTION LAYER FOR A Cu/Ti DIFFUSION COUPLE UNDER DIFFERENT HEATING METHODS

OBLIKOVANJE MEHANIZMA DIFUZIJSKO REAKCIJSKE PLASTI NA Cu/Ti POVRŠINI Z RAZLIČNIMI METODAMI SEGREVANJA

Liu Fei[1,2], Wu Mingfang[1], Pu Juan[1]

[1]Provincial Key Laboratory of Advanced Welding Technology, Jiangsu University of Science and Technology, Zhenjiang 212003, China
[2]Zhenjiang Technician Institute, Zhenjiang 212000, China
pu_juan84@163.com

Prejem rokopisa – received: 2017-05-23; sprejem za objavo – accepted for publication: 2017-06-22

doi:10.17222/mit.2017.062

Diffusion experiments with a Cu/Ti diffusion couple were conducted using the pulse-current-heating method and the conventional-heating method. The interfacial microstructure and the growth behavior of the diffusion-reaction layer were investigated with a scanning electron microscope (SEM), electron probe micro-analyzer (EPMA), energy dispersive spectrometer (EDS) and X-ray diffraction (XRD). The results showed that the pulse-current heating could accelerate the diffusion of Ti atoms into a Cu matrix, significantly improve the growth rate of the diffusion-action layer, located at the side of the Cu matrix and make the growth of the interfacial reaction layer follow the parabolic rule. Meanwhile, under the pulse-current heating, the stratification of the diffusion-reaction layer was not obvious. Correspondingly, under the conventional heating method, the stratification of the diffusion-reaction layer was obvious and each reaction layer had a single microstructure, which was consistent with the reactant from the corresponding Cu-Ti binary-alloy phase diagram.

Keywords: Cu/Ti diffusion couple, pulse-current heating, diffusion, interfacial microstructure, interfacial-layer growth

Avtorji prispevka so izvedli difuzijske eksperimente na paru Cu/Ti. Pri tem so difuzijski par ogrevali na dva različna načina; z uporabo postopka impulznega tokovnega ogrevanja in konvencionalnega postopka ogrevanja. Medfazno mikrostrukturo in rast difuzijsko-reakcijske plasti so analizirali z vrstičnim elektronskim mikroskopom (SEM), mikroanalizatorjem z elektronsko sondo (EPMA), energijskim disperzijskim spektrometrom (EDS) in rentgensko difrakcijsko analizo (XRD). Rezultati analiz so pokazali, da impulzno tokovno ogrevanje lahko pospeši difuzijo atomov Ti v matriko Cu in očitno izboljša hitrost rasti difuzijske plasti, ki se nahaja na strani Cu matrike. Pri tem kinetika rasti difuzijsko-reakcijske plasti sledi paraboličnemu zakonu. Niso pa opazili izrazitega plastenja difuzijsko- reakcijske plasti, ki je bilo očitno pri konvencionalnem načinu ogrevanja difuzijskega para. V tem primeru je imela vsaka reakcijska plast enovito mikrostrukturo, skladno z reaktantoma v binarnem faznem diagramu Cu-Ti.

Ključne besede: difuzijski par Cu/Ti, impulzno tokovno ogrevanje, difuzija, medfazna mikrostruktura, rast medfazne plasti

1 INTRODUCTION

Titanium alloys have been widely used in aerospace, national defense, medical treatment, etc. since 1950s due to their high strength, good corrosion resistance and excellent heat resistance. However, their application is restricted due to the high price. Therefore, it is of great importance to study the joining technologies applicable for titanium alloys and other materials. Currently, the main joining technologies include brazing[1,2], solid-phase diffusion welding,[3,4] superplastic forming and diffusion-bonding composite welding,[5] friction welding[6] and laser welding.[7] Diffusion welding has been widely used in the manufacture of titanium alloys that have a complex and thin-walled structure.[8]

A titanium alloy and copper alloy were joined with brazing and diffusion welding, respectively.[9,10] A comparative study showed that the microstructure and the strength of welded joints joined with two different methods show large differences. According to the Cu-Ti binary-alloy phase diagram,[11] titanium and copper generally cannot dissolve with each other. The solid solubility of titanium dissolved in copper is very small and the maximum solid solubility is ~5 % at 890 °C. Correspondingly, the solid solubility of copper dissolved in titanium is smaller and the maximum solid solubility is less than ~3 % at 798 °C. Several different kinds of interphases existed in a Cu-Ti binary-alloy system, and most of the interphases are intermetallic compounds.

The welding thermal process is a non-equilibrium thermodynamic process. It is difficult to simply judge the welding microstructure of titanium alloy and copper alloy joined by brazing and diffusion welding based on a Cu-Ti binary-alloy phase diagram. In this paper, diffusion experiments with a Cu/Ti diffusion couple were carried out using pulse-current heating and conventional heating at different heating temperatures and holding times. The effects of different heating methods and process parameters on the structure of an interfacial diffusion-reaction layer, together with the growth behavior of the diffusion-reaction layer under the condition of

pulse-current heating were carefully investigated. The related research is aimed to provide the necessary experimental data and theoretical analysis for predicting the structural type and growth characteristics of an interfacial reaction layer.

2 EXPERIMENTAL PART

2.1 Materials and methods

Cylindrical samples of pure copper and pure titanium (more than 99.99 %) with dimensions of $\phi 20 \times 3$ mm were used as the diffusion matrix. The samples were first mechanically polished, then polished with sand papers and finally cleaned with ultrasonic vibration. The samples were assembled in the form of pure copper/pure titanium/pure copper, then diffused and joined in a heating furnace using different heating methods. When the pulse-current heating process was used, the vacuum was not less than 13 Pa, the axial pressure load was 1 MPa and the duty cycle of direct-current pulse was 16/2 (on/off). Meanwhile, the heating rate was set as 100 °C/min, the heating temperature was 700 °C and the holding time was chosen in a range of 3–10 min. The samples were cooled inside the furnace to room temperature after diffuse joining. For comparison, the diffusion experiment under conventional heating was conducted using the same diffusion couple and the related processing parameters were set as follows: the thermal vacuum degree was not less than 1×10^{-2} Pa, the axial pressure load was 1 MPa, the heating temperature was 800 °C with holding times of 10–60 min and a heating speed of 100 °C /min.

The analysis samples were cut by wire cutting along the centerline, and the surfaces of the analysis samples were polished with different-grade sand papers with Nos.1–5. The diffusion-reaction areas of the copper/titanium samples were observed with a scanning electron microscope (SEM). The diffusion behavior between the Cu atoms and Ti atoms was analyzed with an electron-probe micro-analyzer (EPMA). The chemical compositions of feature points in the microstructure were detected with an energy dispersive spectrometer (EDS). The microstructure of the diffusion-reaction zone was characterized with X-ray diffraction (XRD).

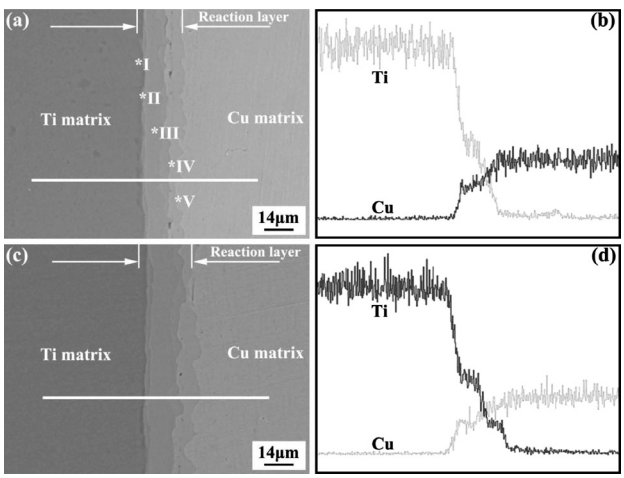

Figure 1: Morphology and elemental distribution of diffusion-reaction layer in the case of conventional heating: a) morphology image for the holding time of 30 min; b) EPMA line-scanning result for the holding time of 30 min; c) morphology image for the holding time of 60 min; d) EPMA line-scanning result for the holding time of 60 min

3 RESULTS AND ANALYSIS

3.1 Structure analysis of the diffusion-reaction layer under conventional heating

The diffusion-reaction experiments were carried on a Cu/Ti diffusion couple with a heating temperature of 800 °C, holding times of 10–60 min and axial pressure load of 1 MPa. **Figure 1** shows the morphology and elemental distribution of the diffusion-reaction layer at holding times of 30 min and 60 min.

Figures 1a and **1b** present SEM images and elemental-line scanning results for the sample with the holding time of 30 min. The results indicate that the inter-diffusion between the Cu atoms and Ti atoms occurred in the interface of the Cu/Ti diffusion couple. The deep-gray area on the left side is the Ti matrix, the gray region on the right side is the Cu matrix, and the middle region between them is the diffusion-reaction layer. The diffusion-reaction area is divided into five layers due to different contents of Ti atoms, namely, zones I–V. The width of zone I at the side of the Ti matrix is about 4–6 μm, formed due to the reaction of the Cu atoms and Ti atoms when the Cu atoms diffused into the Ti matrix (**Figure 1b**). When the Ti atoms diffused into the Cu matrix, zone II was formed at the side of the Cu matrix. Its width is about 1–2 μm. In addition, zone III, zone IV and zone V were formed along the depth direction of the Cu matrix. The widths of these three zones are (8–10, 2–3 and 5–7) μm, respectively. The total width of the diffusion-reaction layers is about 22–25 μm after the holding time of 30 min.

Figure 1c shows a secondary electronic image of the diffusion-reaction layer after the holding time of 60 min. **Figure 1d** displays the elemental-line scanning result for the corresponding diffusion-reaction layer (**Figure 1c**). This diffusion-reaction layer also has five layers and the total width of the diffusion-reaction layer is increased to 30–34 μm (**Figure 1c**), as compared with **Figure 1a**. The inter-diffusion behavior of the Cu atoms and Ti atoms in the Cu/Ti diffusion couple is more remarkable under the condition of conventional heating with the longer holding time of 60 min. Meanwhile, the rate of diffusion of the Ti atoms into the Cu matrix is higher than that of the Cu atoms into the Ti matrix. In order to determine the chemical composition of each reaction layer, EDS was employed to analyze the samples and the results are shown in **Table 1**. The compounds can be preliminary

determined based on the contents of the Ti atoms and Cu atoms for the feature points.

Table 1: EDS results for the interfacial reaction layer for conventional heating

Feature points	Ti	Cu	Compounds
I	95.78	4.22	(α-Ti)+Ti_2Cu
II	72.06	27.94	Ti_2Cu
III	51.46	48.54	TiCu
IV	23.23	76.77	$TiCu_4$
V	9.26	90.74	(Cu)+$TiCu_4$

In order to realize the diffusion of atoms, a driving force that can be either a concentration difference or a chemical potential difference is necessary. From the dynamic point of view, the inter-diffusion rate between the Cu atoms and Ti atoms was increased by increasing the temperature for the Cu/Ti diffusion couple. The driving force of diffusion was derived from the concentration difference for both sides of the interface. Meanwhile, as the diffusion rate of the Ti atoms was higher than that of the Cu atoms, the thickness of the diffusion-reaction layer at the side of the Cu matrix was increased significantly. From the view of thermodynamics, atoms always transferred spontaneously from the area of high chemical potential to the area of low chemical potential. As the chemical potential of Ti atoms was higher than that of Cu atoms, the gradient of chemical potential can also be deemed as a driving force that promoted the diffusion of the Ti atoms into the Cu matrix. According to the Cu-Ti binary-alloy phase diagram and reference[12], there is a variety of intermediate phases between these two elements. Most of them are intermetallic compounds, including $TiCu_4$, Ti_2Cu_3, Ti_3Cu_4, TiCu and Ti_2Cu. Based on the experimental results and the existing related researches, we can say that when the heating temperature was set as 800 °C and the holding time was 30 min, the reaction products of the Cu/Ti diffusion couple were (α-Ti)+Ti_2Cu in zone I, Ti_2Cu in zone II, TiCu in zone III, $TiCu_4$ in zone IV and (Cu)+$TiCu_4$ in zone V. Under the conventional-heating conditions with sufficient holding time, practical structures of the diffusion-reaction layers were consistent with the compounds from the Cu-Ti binary-alloy phase diagram. However, it should be noted that it was hard to form a continuous and compact interfacial reaction layer in the Cu/Ti diffusion couple under the condition of the present conventional heating. In addition, microvoids can be found in the initial interface.

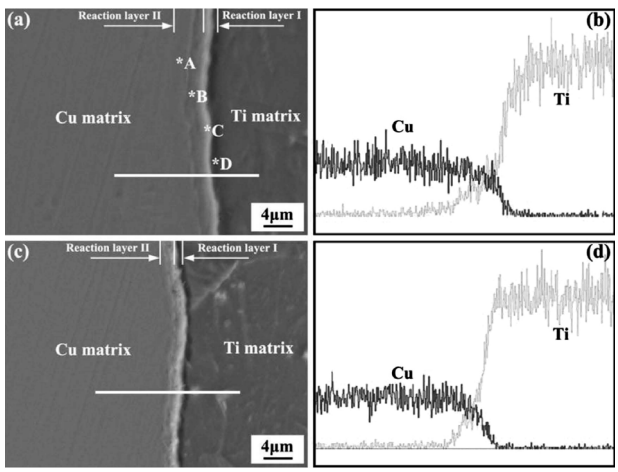

Figure 2: Morphology and element distribution of diffusion-reaction layer in the case of pulse-current heating: a) morphology image for the holding time of 6 min, b) EPMA line-scanning result for the holding time of 6 min, c) morphology image for the holding time of 3 min, d) EPMA line-scanning result for the holding time of 3 min

3.2 The structure of diffusion reaction layer under pulse current heating

For comparison, the diffusion experiment with the Cu/Ti diffusion couple was carried out under pulse-current heating at a temperature of 700 °C, holding times of 3–10 min and pulse-duty ratio of 16/2. **Figure 2** shows the morphology and elemental line-scanning results for the diffusion-reaction layer between the Cu matrix and the Ti matrix at holding times of 6 min and 3 min. **Table 2** lists EDS analysis results for feature points A, B, C and D.

Table 2: EDS results for the interfacial reaction layer for pulse-current heating

Feature points	Ti	Cu	Compounds
A	25.24	74.76	(Cu)+$TiCu_4$
B	30.42	69.58	(Cu)+$TiCu_4$
C	69.61	30.39	Ti_2Cu
D	97.53	2.47	(α-Ti)+Ti_2Cu

As shown in **Figure 2**, the Cu/Ti diffusion-reaction layer can be formed at different holding times. The width of the diffusion-reaction layer was 4–6 μm at the holding time of 3 min (**Figure 2a**) while it grew up to 10–12 μm at the holding time of 6 min (**Figure 2c**). When compared with the conventional heating method, a continuous and dense diffusion-reaction layer can be formed in a short holding time under the condition of pulse-current heating, proving that pulse-current heating can accelerate the process of interfacial reaction. **Figure 2b** shows the results of the elemental line-scanning analysis for the corresponding diffusion-reaction layer (**Figure 2a**). The diffusion of the Ti atoms into the Cu matrix can be clearly seen from **Figure 2b**. The depth of the titanium diffusion-reaction layer can be up to 10 μm. However, the diffusion of the Cu atoms into the Ti matrix is invisible. These results confirmed that under the effects of pulse-current heating, the diffusion of the Ti atoms into the Cu matrix was promoted while the diffusion of the Cu atoms into the Ti matrix was suppressed. Although the heating temperature was relatively low and the holding time was very short, the diffusion-reaction layer between the Cu matrix and Ti matrix was formed.

When combining the line-scanning results with the EDS analysis, the interface reaction layer can be generally divided into two zones: the initial interface reaction layer I for the Cu/Ti diffusion couple (a width of about 1 μm) and the reaction layer II along the depth direction of the Cu matrix (a width of about 10 μm). According to the data in **Table 2**, the contents of Cu and Ti in points A and B were almost equal. When combining the Cu-Ti binary-alloy phase diagram with the related researches, it can be inferred that the compounds in points A and B were composed of a Cu solid solution and $TiCu_4$ compound. Meanwhile, point C was composed of a Ti_2Cu compound and point D was composed of (α-Ti) and Ti_2Cu compounds. That is to say, the Ti_2Cu phase was formed in the reaction layer I, while the $TiCu_4$ phase was formed in the reaction layer II. Therefore, even though the heating temperature was only 700 °C and the holding time was only 6 min, the diffusion-reaction layer between the Cu matrix and the Ti matrix could still be formed under the condition of pulse current. When the holding time was prolonged, there was no obvious variation in the width of the reaction zone I, but the width of reaction zone II was increased remarkably.

Figure 2d shows the elemental line scanning of the diffusion-reaction layer between the Cu matrix and the Ti matrix at the holding time of 3 min. The elemental diffusion trends of the diffusion-reaction layer were approximately consistent with the results shown in **Figure 2b**. Namely, the diffusion rate of the Ti atoms into the Cu atoms was higher than that of the Cu atoms into the Ti atoms. The initial interfacial reaction layer I at the side of the Cu matrix was clearly visible, while the diffusion reaction layer II along the depth direction of the Cu matrix was invisible.

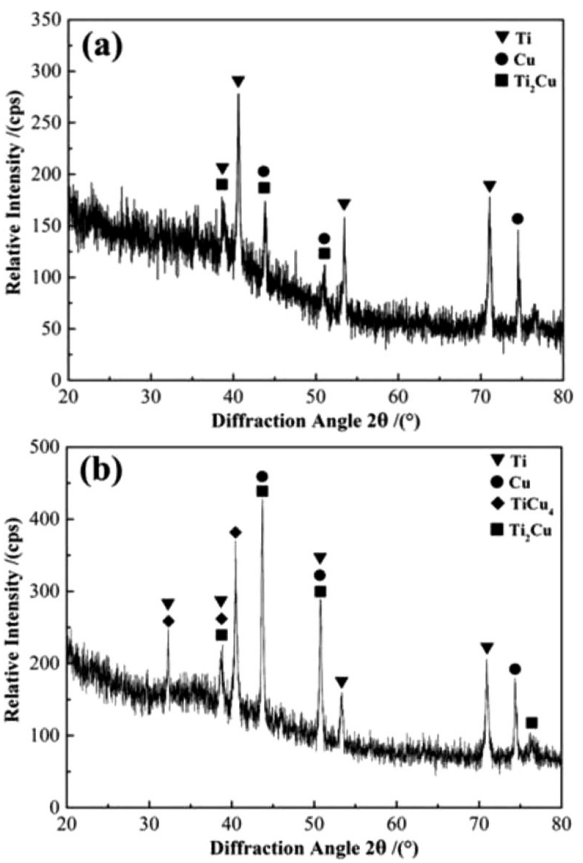

Figure 3: XRD test results for diffusion-reaction layer at the holding time of 6 min: phases of initial interface reaction layer I, b) phases of reaction layer II

To further clarify the structural constitution of the interfacial reaction layer for the Cu/Ti diffusion couple under pulse current, the samples were grinded layer by layer, and then the interfacial reaction layer was tested with XRD. The XRD results are shown in **Figure 3**. It can be seen that the compounds were mainly composed of $TiCu_4$ and Ti_2Cu at 700 °C, the holding time of 6 min and pulse-duty ratio of 16/2 (on/off).

Based on the above analysis, it can be concluded that the width of the Cu/Ti diffusion-reaction layer increased with the increasing holding time for either conventional-heating diffusion or pulse-current-heating diffusion. By contrast, pulse current could accelerate the diffusion rate of the Ti atoms into the Cu matrix and also promote the formation of the interface reaction layer. Meanwhile, pulse current could also suppress the diffusion of the Cu atoms into the Ti matrix. In the case of conventional-heating diffusion, each reaction layer had only one single phase. The phase of each reaction layer was consistent with the phase from the Cu-Ti binary-alloy phase diagram. However, for pulse-current-heating diffusion, the stratification phenomenon of the whole reaction layer was not obvious. The Ti_2Cu compound was formed at the initial interface, while the $TiCu_4$ compound was formed at the reaction layer along the depth direction of the Cu matrix. Although the diffusion of the Ti atoms into the Cu matrix was fast, no concentration gradient was formed in the whole reaction layer. It was inferred that pulse-current heating could change the structural constituent of the diffusion-reaction layer.

3.3 Growth of the interfacial reaction layer under pulse-current heating

According to the above analysis, the growth process of the interfacial reaction layer for the Cu/Ti diffusion couple under pulse-current heating could be divided into two stages, namely, (i) the nucleation and growth of a Ti_2Cu compound at the initial interface of the Cu/Ti diffusion couple, (ii) the nucleation and rapid growth of a Ti_4Cu compound at the side of the Cu matrix. During the first stage, a pure Cu/Ti diffusion couple was placed in a graphite heating body and pressure was pre-loaded with a pressure rod; the graphite heating body and the Cu/Ti diffusion couple were heated by pulsed direct current. The temperature at the initial interface was rapidly increased due to the heating of contact resistance. The inter-diffusion of the Ti atoms and Cu atoms was promoted; finally, the Ti_2Cu compound was formed.

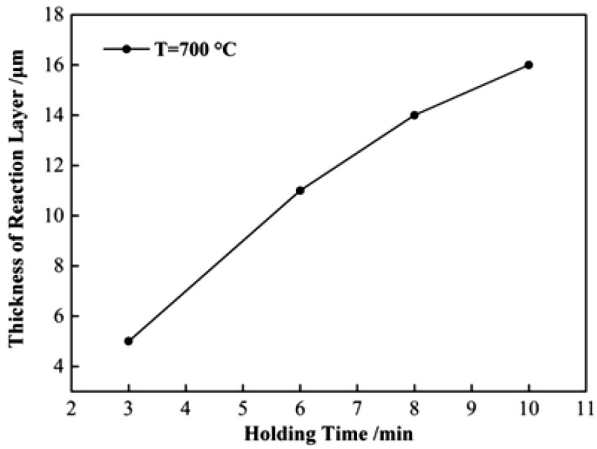

Figure 4: Relationship between the thickness of the interfacial reaction layer and the holding time under pulse-current heating

During the second stage, when the holding time was prolonged, free-state Ti atoms in the Ti matrix went across the Ti_2Cu compound layer, then they diffused into the Cu matrix and reacted with the Cu atoms; finally, the $TiCu_4$ compound was formed. The $TiCu_4$ reaction layer grew fast due to the higher diffusion rate of the Ti atoms. Meanwhile, the Cu matrix could provide enough free-state Cu atoms for the formation of a $TiCu_4$ diffusion-reaction layer. However, the diffusion rate of the Cu atoms into the Ti matrix was slow, and it took more time for the Cu atoms to pass through the Ti_2Cu reaction layer, resulting in a relatively slow growth rate of the Ti_2Cu diffusion-reaction layer. The growth rate of the whole reaction layer depends on the growth rate of the $TiCu_4$ compound.

According to **Figure 2** and the other experimental data, at the same heating temperature of 700 °C, axial pressure of 1MPa and pulse duty of 16/2, the average thickness values of the interfacial reaction layer of the Cu/Ti diffusion couple were (5, 11, 14 and 16) μm, corresponding with the holding times of 3, 6, 8 and 10 min. **Figure 4** shows the relationship between the holding time and the thickness of the diffusion reaction layer. The Y axis represents the thickness of the reaction layer and the X axis shows the square root of the holding time. It can be seen from Figure 4 that the growth of the interfacial reaction layer followed the parabolic law for the Cu/Ti diffusion couple under pulse-current heating.

4 CONCLUSIONS

Under the condition of pulse-current heating, the diffusion rate of the Ti atoms into the Cu matrix was accelerated, the growth rate of the interfacial reaction layer was promoted, and the growth of the interfacial reaction layer followed the parabolic law.

For pulse-current-heating diffusion, the formation of the stratification of the whole reaction layer was not obvious. A Ti_2Cu compound was formed at the initial interfacial layer while a single Ti_4Cu compound was formed in the depth direction of the Cu matrix.

For conventional-heating diffusion, a stratification of the whole reaction layer was obvious. If the holding time was long enough, the phase of each reaction layer was consistent with the phase from the Cu-Ti binary-alloy phase diagram.

Acknowledgements

This research was funded by the National Natural Science Foundation of China (No.51175239). The authors would like to express their gratitude to the technical stuff of the Provincial Key Laboratory of Advanced Welding Technology for various assistances.

5 REFERENCES

[1] X. P. Xu, H. Wang, J. S. Zou, C. Z. Xia, Interfacial structure and properties of Si_3N_4 ceramic and TiAl alloys brazed with Ti/Ag-Cu/Cu interlayers, Transactions of the China Welding Institution, 37 (**2016**) 12, 91–94, doi:10.3321/j.issn:0253-360X.2016.12.023

[2] M. F. Wu, Z. S. Yu, R. F. Li, A study of Ti/Fe contact reaction structures, Materials Science and Technology, 20 (**2004**) 5, 658–660, doi:10.1179/026708304225012080

[3] S. Kundu, S. Chatterjee, Interface microstructure and strength properties of diffusion bonded joints of Titanium-Al interlayer-18Cr-8Ni stainless steel, Materials Science and Engineering A, 527 (**2010**) 10–11, 2714–2719, doi:10.1016/j.msea.2009.12.042

[4] S. Kundu, S. Sam, S. Chatterjee, Interface microstructure and strength properties of Ti-6Al-4V and microduplex stainless steel diffusion bonded joints, Materials and Design, 32 (**2011**) 5, 2997–3003, doi:10.1016/j.matdes.2010.12.052

[5] Z. R. Lin, Z. Y. Zhang, W. D. Huang, An investigation of diffusion bonding under superplastic condition for Ti-6A-4V titanium alloys, Acta Aeronautica et Astronautica Sinica, 13 (**1992**) 5, 288–295, doi:10.3321/j.issn:1000-6893.1992.05.010

[6] J. Y. Li, L. H. Ni, X. Jin, Continuous drive friction welding procedures of TC4/T2 and microstructure and performance of dissimilar metal joints, Transactions of the China Welding Institution, 37 (**2016**) 9, 115–118, doi:10.3321/j.issn:0253-360X.2016.09.026

[7] R. F. Li, Z. G. Li, Y. Y. Zhu, L. Rong, A comparative study of laser beam welding and laser-MIG hybrid welding of Ti-Al-Zr-Fe titanium alloy, Materials Science and Engineering A, 528 (**2011**) 3, 1138–1142, doi:10.1016/j.msea.2010.09.084

[8] R. Yang, Y. S. Zhu, F. Y. Gao, Diffusion bonding for titanium alloy, Development and Application of Materials, 28 (**2013**) 5, 109–115, doi:10.3969/j.issn.1003-1545.2013.05.023

[9] R. K. Shiue, S. K. Wu, C. H. Chan, The interfacial reactions of infrared brazing Cu and Ti with two silver-based braze alloys, Journal of Alloys and Compounds, 372 (**2004**) 1–2, 148–157, doi:10.1016/j.jallcom.2003.09.155

[10] M. F. Wu, C. Yu, Z. S. Yu, K. Qi, R. F. Li, Dissolution behaviour of Ti/Cu contact reaction, Materials Science and Technology, 21 (**2005**) 2, 250–254, doi:10.1179/174328405X18683

[11] V. N. Eremenko, Y. I. Buyanov, S. B. Prima, Phase diagram of the system titanium-copper, Powder Metallurgy and Metal Ceramics, 5 (**1966**) 6, 494–502, doi:10.1007/BF00775543

[12] J. L. Murray, The Cu-Ti (Copper-Titanium) system, Journal of Phase Equilibria, 4 (**1983**) 1, 81–95, doi:10.1007/BF02880329

UDK 66.046.55:621.7:67.017
Original scientific article/Izvirni znanstveni članek

ISSN 1580-2949
MTAEC9, 51(6)1031(2017)

DE-OXIDATION OF PK942 STEEL WITH Ti AND Zr

DEZOKSIDACIJA JEKLA PK942 S Ti IN Zr

Mitja Koležnik[1], Jaka Burja[2], Barbara Šetina Batič[2], Aleš Nagode[3], Jožef Medved[3]

[1] Metal Ravne d.o.o., Koroška cesta 14, 2390 Ravne na Koroškem, Slovenia
[2]Institute of Metals and technology, IMT, Lepi pot 11, 1000 Ljubljana, Slovenia
[3]Faculty of Natural Sciences and Engineering Ljubljana, Aškerčeva cesta 12, 1000 Ljubljana, Slovenia
mitja.koleznik@metalravne.com

Prejem rokopisa – received: 2017-06-22; sprejem za objavo – accepted for publication: 2017-09-12

doi:10.17222/mit.2017.082

The effects of titanium and zirconium additions on the non-metallic inclusions and microstructure of PK942 (X11CrNiMo12) steel were investigated. Laboratory steel charges with additions of Ti, Zr and a combination of both elements were melted. The inclusions' size, quantity, distribution and composition were analysed using optical and scanning electron microscopy (SEM). Other than the difference in δ-ferrite quantity, there are no significant differences in the microstructure. The Ti and Zr additions had a significant effect on the non-metallic inclusions, and while the addition of Ti did have an effect on the composition of inclusions, the addition of Zr also had a great effect on the size distribution and the number of non-metallic inclusions. The result of the Zr addition was a large reduction in the total non-metallic inclusion surface area. The additions of both titanium and zirconium had similar effects to the addition of Zr. Thermodynamic reactions were considered to explain the modification of the non-metallic inclusions.

Keywords: non-metallic inclusions, clean steel, de-oxidation with Ti, de-oxidation with Zr, creep resistant steel

S pomočjo optične ter elektronske mikroskopije se je preiskal vpliv dezoksidacije jekla PK942 (X11CrNiMo12) s cirkonijem, titanom ter kombinacijo obeh. Poudarek raziskave je bil na spremembi velikosti, razporeditve ter sestave nekovinskih vključkov v jeklu PK942. Razen v majhni razliki deleža δ-ferita, ni bilo bistvenega vpliva na osnovno mikrostrukturo jekla. Večji vpliv pa se je pokazal na velikost, število ter kemično sestavo nekovinskih vključkov. Analiza nekovinskih vključkov je pokazala, da Ti vpliva predvsem na kemično sestavo, med tem ko ima Zr zelo velik vpliv tudi na velikostno porazdelitev ter število nekovinskih vključkov, rezultat česar je manjši skupni površinski delež nekovinskih vključkov. Dodatek kombinacije Zr in Ti ima podoben vpliv kot dodatek Zr, vendar v manjšem obsegu. Pri razlagi modifikacije vključkov so se upoštevale osnovne termodinamične reakcije oksidacije.

Ključne besede: nekovinski vključki, čistost jekla, dezoksidacija s Ti, dezoksidacija z Zr, jekla za lezenje

1 INTRODUCTION

The efficiency of steam turbines can be improved by increasing the maximum operating pressure and temperature, which are limited by the properties of the available materials.[1] The most widely used creep-resistant steels in a power plant are 9–12 % Cr martensitic steels, where the size, number and distribution of the precipitates affect the creep resistance.[2–6] They offer the best combination of high creep strength, high resistance against thermal fatigue, high steam oxidation resistance and good manufacturability at relatively low costs.[7] The steel grade PK942 (X11CrNiMo12) is a martensitic creep-resistant steel that is generally used for turbine blades and fittings.

These steels must fulfil very high quality standards in terms of the mechanical properties and microstructure. One of very important factors is the cleanliness of steel, which depends on the number, size, and distribution of non-metallic inclusions. The content of non-metallic inclusions depends on the control of melting, refining and casting of steel.[8] The use of de-oxidation agents is very important as they will greatly influence the formation of inclusions, both during refining and casting. De-oxidization is usually carried out through Al additions, but aluminates are hard and brittle, and are unfavourable. Alternatively, de-oxidation can also be performed with elements that have a very high chemical affinity for oxygen, like titanium and zirconium, this changes the size, number and distribution of non-metallic inclusions.[9] Zirconium and titanium additions are known to modify sulphide inclusions, cause grain refinement, reduce the grain growth during high-temperature annealing and in the heat-affected zone during welding, they also promote the precipitation of small nitride, carbide and carbonitride particles.[10–15] The use of both titanium and zirconium are known to reduce the size and improve the distribution of oxide inclusions in steel.[16]

The present investigation was undertaken with the objective of determining the effect of small additions of Zr, Ti and the combination of both elements, on the size, distribution and composition of inclusions in PK942 steel grade.

Table 1: Chemical compositions of the experimental charges / wt.%

sample	C	Si	Mn	Cr	Ni	Mo	V	Al	Ti	Zr	O	N	Fe
PK942	0.11	0.37	0.80	12.8	2.68	1.61	0.41	0.004	<0.001	<0.001	0.0126	0.038	Bal.
PK942Ti	0.12	0.39	0.80	12.6	2.67	1.60	0.40	0.006	0.018	<0.001	0.0119	0.045	Bal.
PK942Zr	0.10	0.26	0.58	12.4	2.69	1.62	0.37	0.005	<0.001	0.013	0.0148	0.038	Bal.
PK942TiZr	0.11	0.45	0.90	12.7	2.65	1.60	0.38	0.006	0.016	0.010	0.0105	0.038	Bal.

2 EXPERIMENTAL

2.1 Melting and casting

Experimental charges of PK942 (X11CrNiMo12, SINOX 4938) steel were remelted in a vacuum-induction-melting furnace under an inert Ar atmosphere. The four charges consisted of 8 kg of X11CrNiMo12 and minor additions of ferrosilicon (20 g), ferrovanadium (4g) and ferromanganese (50 g) were added to compensate for the oxidation losses. The first charge (PK942) was remelted without any additional alloys, the second charge (PK942Ti) was de-oxidised with the addition of ferrotitanium (70 % Ti), the third charge (PK942Zr) was de-oxidised by adding zirconium (99.8 % Zr), and the fourth charge (PK942TiZr) was de-oxidised by adding both ferrotitanium and Zr. The melt was cast into 88 mm × 88 mm moulds. The cast ingots were air cooled to room temperature.

2.2 Forging and heat treatment

Then the ingots were annealed at 720 °C to prevent stress cracking. The annealed ingots were then homogenized at 1180 °C for 6 hours. When the homogenization was complete the 88×88 mm ingots were hot forged into 30-mm diameter bars with a pneumatic forging hammer. After hot forging the samples were annealed at 720 °C for 1.5 h.

2.3 Sampling

The samples were then taken from the forged bars, in the longitudinal direction, as described in Figure 1.

2.4 Chemical analysis

The chemical analysis of the steel samples was made by time-of-flight mass spectrometers (TOFMS) LECO CS600 (C and S) and LECO TC436 (N and O), by Coupled Plasma-Optical Emission Spectrometers (ICP-OES) Varian 730-ES (Ti and Zr), and by Optical Emission Spectroscopy (OES) ARL 3460 (Si, Mn, Cr, Ni, Mo, V and Al).

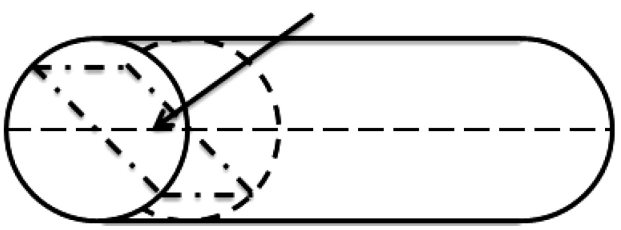

Figure 1: Site of the sample extraction

2.5 Metallography

The metallographic analysis and the determination of the prior austenite grain size according to ASTM E112[17] were made with an optical microscope (Olympus DP70). The samples for optical microscopy were etched with Vilella's reagent, while the samples for electron microscopy were only polished.

The electron microscopy and EDS analysis were made in a SEM (Jeol-JSM6500F). The non-metallic inclusion analysis was made with an INCA FEATURE in a SEM Jeol-JSM6510. The total analysis area for each sample was 9×10^6 μm^2.

2.6 Thermodynamic

The calculation of the Gibbs free energy and its dependence on the temperature were made with HTCS 8 software.

3 RESULTS AND DISCUSSION

The chemical analyses of the four different charges PK942, PK942Ti, PK942Zr and PK942TiZr are given in **Table 1**. The most important variations of the experimental charges in comparison to PK942 are 0.018 % of mass fractions of Ti in PK942Ti, 0.013% of mass fractions of Zr in PK942Zr, and 0.016 % of mass fractions of

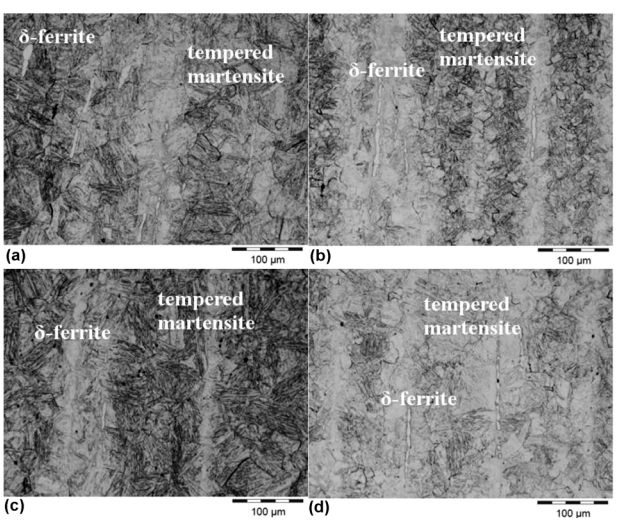

Figure 2: Microstructure of quenched and tempered sample a) PK942, b) PK942Ti, c) PK942 Zr, d) PK942TiZr

Ti and 0.01 % of mass fractions of Zr in PK942TiZr, as can be seen in **Table 1**.

The chemical analyses showed that the oxygen content in the charges varies from 0.0105 % to 0.0148 % of mass fractions, while the nitrogen content is 0.038 % of mass fractions, except for PK942Ti, where it is 0.045 % of mass fractions. These values of the measurements can be considered to be roughly the same for practical purposes. Although the higher nitrogen content could be attributed to the formation of titanium nitrides in the liquid melt.

The microstructures are shown in **Figure 2a** to **2d**. All four types of steel contain martensite with small δ-ferrite islands in the segregation areas. The prior austenite grain size of all the samples was 5 according to ASTM E112.[17] The occurrence of δ-ferrite islands is less frequent in the PK942Zr sample, which may be explained by the fact that ZrO_2 is a heterogeneous nucleation site during the solidification of austenite, therefore inhibiting δ-ferrite nucleation.[18] This can be beneficial as δ-ferrite can be harmful to the final properties and the hot working is reduced by annealing.[19] Other than the difference in δ-ferrite, there are no significant differences in the microstructure.

3.1 INCA-feature

The automatic non-metallic inclusion analysis made by the INCA Feature revealed significant differences in the non-metallic inclusion content and chemistry between the samples. The graph in **Figure 3** shows the total area of all the inclusions and the number of inclusions found in the INCA-feature analysis. The total analysis area for each sample was 9×10^6 μm^2.

The results of the Inca feature analysis are given in **Figure 3**. The non-metallic inclusion area drastically decreases with the Zr additions, but the number of inclusions, however, sharply increases. This means that Zr additions cause the formation of numerous small non-metallic inclusions. The explanation for the smaller ZrO_2 non-metallic inclusions, especially in comparison to the alumina inclusions, is the lower interfacial energy and better wettability. During solidification the ZrO_2 particles are engulfed by the solidification front, while the alumina particles are pushed from the solidification front.[20]

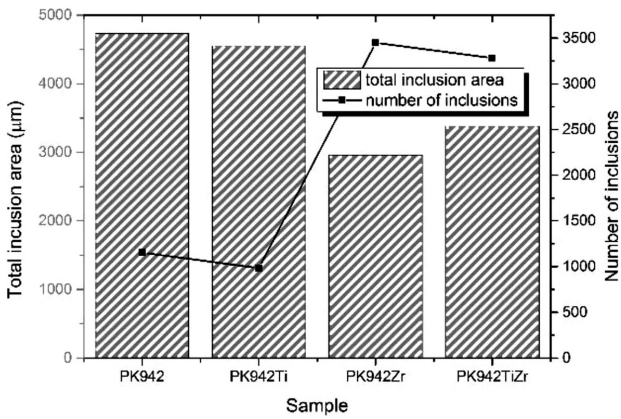

Figure 3: Total inclusion area and number of inclusions for each sample

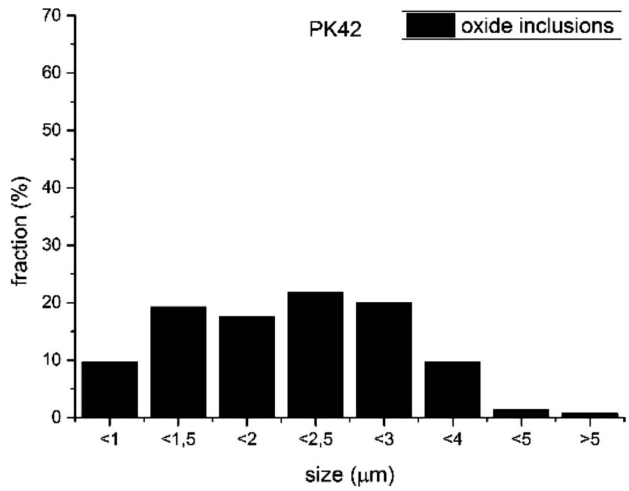

Figure 4: Size distribution of non-metallic inclusions for sample PK942

The Ti additions have no significant effect on the total surface and the number of inclusions. The combined addition of Ti and Zr results in a decrease in the total inclusion area and an increase in the number of inclusions.

The distribution of inclusions in each sample according to their diameter is shown in **Figures 4–7**. It can be observed that while the PK942 and PK942Ti samples (**Figures 4–5**) have a relatively uniform distribution of inclusions of different sizes, the majority of the inclusions in the PK942Zr and PK942TiZr samples (**Figures 6–7**) are smaller than 1 μm. This is in good agreement with the research of A. V. Karasev and H. Suito, where the majority of the Zr de-oxidation product inclusions were less than 1 μm in diameter.

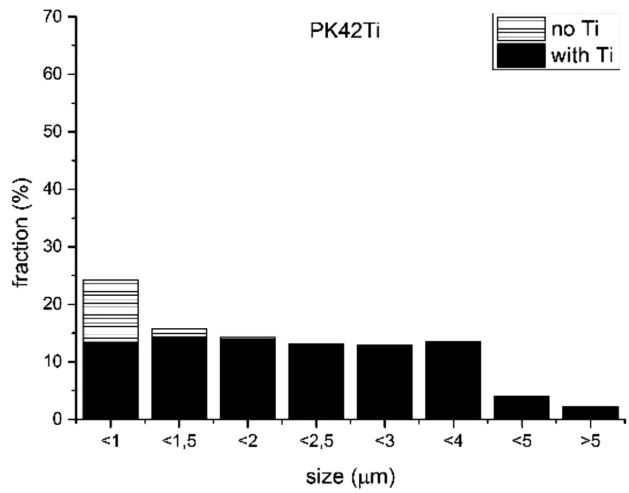

Figure 5: Size distribution of non-metallic inclusions for sample PK942Ti

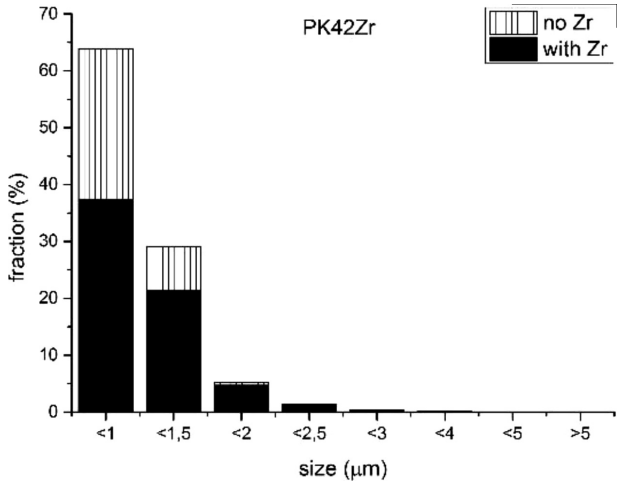

Figure 6: Size distribution of non-metallic inclusions for sample PK942Zr

The non-metallic inclusions in PK942 are relatively equally distributed among the sizes from 1 to 4 μm. The inclusions are relatively small but compared to **Figure 6** (PK942Zr and PK942TiZr) they are large. The PK942 sample has the highest surface area of non-metallic inclusions, compared to the other samples in **Figure 3**.

For PK942Ti the inclusion size and distribution are comparable to PK942, but most of the inclusions were modified by the Ti, especially the larger inclusions. Only a few smaller inclusions contain no titanium. The analysis of the non-metallic inclusions is very similar to PK942, both in the distribution of the non-metallic inclusion size as well as in the non-metallic inclusion surface area.

The addition of Zr drastically changed the inclusion size distribution, as the majority of the inclusions (over 60 %) are smaller than 1 μm in diameter. The majority of the inclusions also contain Zr. The highest percentage of inclusions without Zr is smaller than 1 μm in diameter. The share of non-modified inclusions is larger than in the PK942Ti sample. The overall inclusion surface area is the smallest, as can be seen in **Figure 3**, but the number of inclusions is the highest.

The combination of Ti and Zr additions has a high percentage of modified inclusions, similar to PK942Ti, and the majority of the inclusions are smaller than 1 μm in diameter, similar to PK942Zr. The overall surface area of the non-metallic inclusions is higher than in PK942Zr, but still much lower than in PK942 and PK942Ti (**Figure 3**).

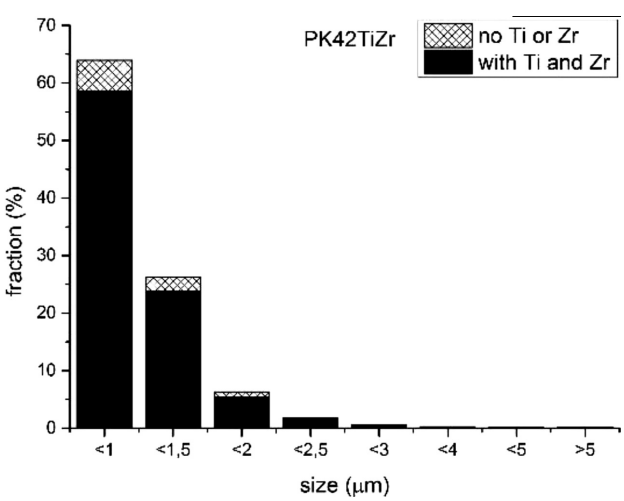

Figure 7: Size distribution of non-metallic inclusions for the sample PK942TiZr

3.2 Thermodynamics

When adding elements like Ti and Zr the basic thermodynamic reactions must be considered. For steelmaking the reactions with oxygen must be considered when estimating the alloy addition yield. **Figure 8** shows a diagram with the Gibbs free energy and its dependence on the temperature in degrees Celsius. Titanium has a high affinity for oxygen, higher than silicon, while zirconium has higher affinity for oxygen, even higher than aluminium, as can be seen in **Figure 8**. The high affinity for oxygen is one of the reasons so much of both titanium and zirconium are present in the non-metallic inclusions. The exact thermodynamic values were taken from the HTCS 8 software, and are given in **Table 2** at 1600 °C.

Table 2: Reactions and associated values of ΔH, ΔS and ΔG at 1600 °C

Reaction	ΔH (kJ)	ΔS (J/K)	ΔG (kJ)
$4/3Al+O_2(g)=2/3Al_2O_3$	-1120.9	-215.7	-716.8
$2Ca+O_2(g)=2CaO$	-1288.9	-226.2	-910.5
$4/3Cr+O_2(g)=2/3Cr_2O_3$	-751.9	-166.8	-439.5
$2Mn+O_2(g)=2MnO$	-812.1	-175.7	-482.9
$Si+O_2(g)=SiO_2$	-946.3	-197.9	-575.7
$Ti+O_2(g)=TiO_2$	-937.5	-175.8	-608.1
$Zr+O_2(g)=ZrO_2$	-1080.6	-175.8	-751.3

The reactions of the different alloying elements were calculated to represent the reduction of 1 mole of $O_2(g)$.

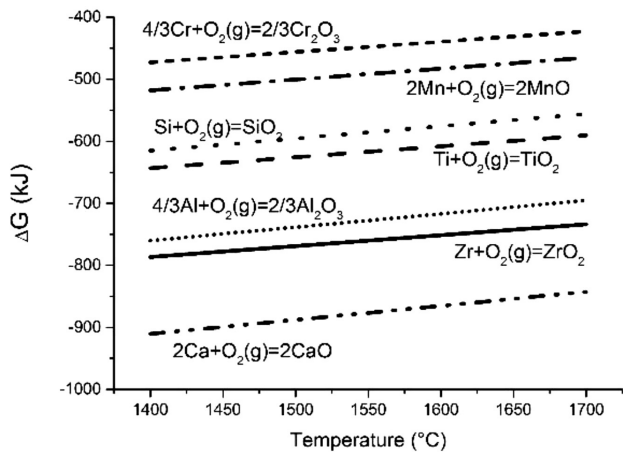

Figure 8: Gibbs free energy for the formation of different oxides

Table 3: Chemical composition of the typical oxide inclusion in **Figure 9**

sample	wt. %*									
	O	S	Zr	Ti	Cr	Mn	V	Si	Al	Fe
PK942-Spect1	40.1	/	/	/	4.3	25.4	/	20.4	/	9.8
PK942Ti-Spect1	14.52	/	/	9.57	10.32	1.22	1.65	5.13	0.97	56.62
PK942Ti-Spect2	34.04	/	/	41.18	6.63	5.03	6.28	/	0.75	6.09
PK942Ti-Spect3	/	/	/	12.34	12.90	1.19	2.64	/	/	70.93
PK942Ti-Spect4	32.00	/	/	32.54	7.50	4.53	4.66	1.29	0.93	16.55
PK942Zr-Spect1	27.57	/	67.57	/	0.78	/	/	0.68	/	3.39
PK942Zr-Spect2	28.65	/	26.92	/	15.62	9.59	2.43	1.15	0.66	14.97
PK942Zr-Spect3	31.92	/	35.25	/	7.68	3.95	1.18	4.78	/	15.24
PK942TiZr-Spect1	24.9	/	50.7	7.0	4.2	1.6	0.8	/	0.5	10.3
PK942TiZr-Spect2	5.9	13.5	12.6	5.1	7.3	28.4	1.5	/	0.4	25.3
PK942TiZr-Spect3	/	/	/	/	14.0	1.2	0.6	0.6	/	83.6

*The carbon content was omitted from the results as it cannot be properly measured by the SEM EDS method and would only potentially confuse the reader into thinking there were carbides in the inclusions.

According to **Figure 8**, zirconium oxide is more stable than aluminium oxide, which means that zirconium will be a better de-oxidiser than aluminium. This explains why a large amount of the non-metallic inclusions contain zirconium. Zirconium reduced most of the inclusions in the melt and formed new, smaller inclusions and completely changed the size distribution and the amount of the non-metallic inclusions (**Figure 6**). Titanium, however, forms less-stable oxides than aluminium, but since there were no aluminium additions to the melt, it also acted as a strong de-oxidiser. Titanium only partially reduced the pre-existing inclusions; therefore, it did not have a profound effect on the number and size distribution of the non-metallic inclusions, but titanium was present in the majority of the inclusions (**Figure 5**).

The combined addition of both titanium and zirconium had a similar effect on the size and distribution of the non-metallic inclusions to that of the zirconium addition, but with a large majority of the inclusions modified by both Ti and Zr (**Figure 7**).

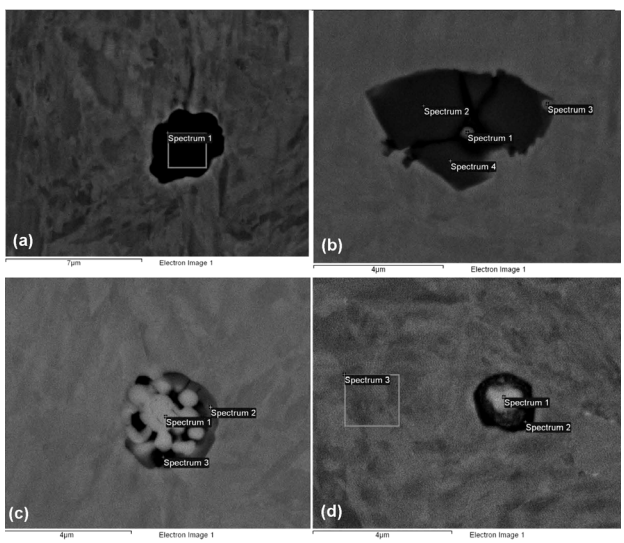

Figure 9: Typical oxide inclusions from samples a) PK942, b) PK942Ti, c) PK942 Zr, d) PK942TiZr

3.3 EDS

Typical samples of oxide inclusions are shown in **Figure 9a** to **9d**. The analysed non-metallic inclusions are oxides as they represent the bulk of the inclusions. The PK942 sample contains oxide non-metallic inclusions that are mostly manganese silicates, as shown in **Figure 9a/Table 3**. The de-oxidation with titanium results in the formation of titanium oxides as it has a higher affinity for oxygen than Mn and Si (**Figure 9b/Table 3**). Due to the strong de-oxidation nature of Zr, ZrO_2 inclusions are formed first and then provide nucleation for many different phases,[13,23,24] for example, the Zr-Ti-O inclusion in **Figure 9d/Table 3**. PK942TiZr has a MnS attached, ZrO_2 provides the nucleation sites for MnS as they have small misfit in the lattice parameters.[16,23] This is why zirconium additions are known to improve the impact toughness through sulphide modification.[10]

The SEM EDS results show that the complexity of the non-metallic inclusions is increased with Ti, Zr and Ti+Zr de-oxidation. The SEM micrograph in **Figure 9c** also shows that the larger zirconium oxides are mostly agglomerated smaller ZrO_2 spheres with the attachment of other oxides.

4 CONCLUSIONS

No significant changes other than a decreased content of δ-ferrite in the zirconium de-oxidised sample were observed in the microstructure when titanium or both titanium and zirconium were added. However, there was a significant impact on the non-metallic inclusions.

The addition of titanium did not have any significant effect on the size distribution and the number of non-metallic inclusions, but it did have a significant

effect on the composition of the non-metallic inclusions, as a majority of the inclusions contained Ti.

The addition of zirconium had a great effect on the size distribution and the number of non-metallic inclusions. The inclusions were significantly smaller and the number was much higher (300 % compared to PK942), the result was a large reduction in the total non-metallic inclusion surface area (37 % reduction). Most of the inclusions contained Zr. This means that the de-oxidation with zirconium is potentially beneficial for the production of clean steel.

The addition of both titanium and zirconium also resulted in smaller (over 60 % of non-metallic inclusions are smaller than 1 μm) but more numerous non-metallic inclusions that had a reduced total non-metallic inclusion surface area (28.5 %) in comparison to the PK942 sample. The vast majority of inclusions contain both Ti and Zr.

5 REFERENCES

[1] H. K. D. H. Bhadeshia, Design of ferritic creep-resistant steels, ISIJ Int. 41 (2001) 626–640

[2] B. Žužek, F. Vodopivec, B. Podgornik, M. Jenko, M. Godec, Calculation of accelerated stationary creep rate activation energy for a steel microstructure with a uniform distribution of carbide particles, Mater. Tehnol., 46 (**2012**) 661–664

[3] B. Žužek, F. Vodopivec, M. Jenko, B. Podgornik, Effect of creep strain on creep rate in the temperature range 550–640 °C, Mater. Tehnol., 48 (**2014**) 545–548.

[4] F. Vodopivec, F. Kafexhiu, B. Žužek, B. Podgornik, Glide Stress by Stationary Creep of Tempered Martensite with Polyhedral Particles, Steel Res. Int., 88 (**2017**), 1600200, doi:10.1002/srin.201600200

[5] F. Vodopivec, F. Kafexhiu, B. Žužek, Effect of Ferrite Lattice Vacancies on Creep Rate of the Steel X20CrMoV121 in the Range 763-913 K, Steel Res. Int., 88 (**2017**), e201600315, doi:10.1002/srin.201600315

[6] B. Žužek, F. Kafexhiu, B. Podgornik, F. Vodopivec, Effect of carbides size and distribution on creep rate, Metalurgija, 56 (2017), 323–325

[7] F. Abe, T. Kern, R. Viswanathan, 1st ed., Creep-resistant steels, Woodhead Publishing Limited, Cambridge, 2008, 678

[8] C. Mapelli, Non-metallic inclusions and clean steel, Metall. Ital., 100 (2008), 43–52

[9] Y. Li, X.L. Wan, W.Y. Lu, A.A. Shirzadi, O. Isayev, O. Hress, K.M. Wu, Effect of Zr-Ti combined deoxidation on the microstructure and mechanical properties of high-strength low-alloy steels, Mater. Sci. Eng. A., 659 (**2016**), 179–187, doi:10.1016/j.msea.2016.02.035

[10] H. Suito, A.V. Karasev, M. Hamada, R. Inoue, K. Nakajima, Influence of Oxide Particles and Residual Elements on Microstructure and Toughness in the Heat-Affected Zone of Low-Carbon Steel Deoxidized with Ti and Zr, ISIJ Int., 51 (**2011**), 1151–1162, doi:10.2355/isijinternational.51.1151

[11] J. Janis, A. Karasev, K. Nakajima, P. Jönsson, Effect of Secondary Nitride Particles on Grain Growth in a Fe-20 mass% Cr Alloy Deoxidised with Ti and Zr, ISIJ Int., 53 (**2013**), 476–483, doi:10.2355/isijinternational.53.476

[12] L. Zhang, T. Kannengiesser, Austenite grain growth and microstructure control in simulated heat affected zones of microalloyed HSLA steel, Mater. Sci. Eng. A., 613 (**2014**), 326–335, doi:10.1016/j.msea.2014.06.106

[13] T.N. Baker, Role of zirconium in microalloyed steels: a review, Mater. Sci. Technol., 31 (**2015**), 265–294, doi:10.1179/1743284714Y.0000000549

[14] C. Wang, Z. Wang, G. Wang, Effect of Hot Deformation and Controlled Cooling Process on Microstructures of Ti – Zr Deoxidized Low Carbon Steel, ISIJ Int., 56 (2016), 1800–1807, doi:10.2355/isijinternational.ISIJINT-2016-106

[15] P. V. Bizyukov, S.R. Giese, Effects of Zr, Ti and Al Additions on Nonmetallic Inclusions and Impact Toughness of Cast Low-Alloy Steel, J. Mater. Eng. Perform., 26 (2017), 1878–1889, doi:10.1007/s11665-017-2583-0

[16] Y. Du, K.M. Wu, L. Cheng, Y. Li, O. Isayev, O. Hress, Effect of Zr–Ti deoxidisation on the hydrogen-induced cracking of X65 pipeline steels, Mater. Sci. Technol., 32 (**2016**), 728–735, doi:10.1080/02670836.2016.1157971

[17] ASTM International, ASTM E112-13 Standard Test Methods for Determining Average Grain Size, Subcommittee E04.08 on Grain Size, 2013, doi:10.1520/E0112

[18] H. Suito, H. Ohta, S. Morioka, Refinement of solidification microstructure and austenite grain by fine inclusion particles, ISIJ Int., 46 (**2006**), 840–846. doi:10.2355/isijinternational.46.840

[19] F. Tehovnik, F. Vodopivec, L. Kosec, M. Godec, Hot ductility of austenite stainless steel with a solidification structure, Mater. Tehnol., 40 (**2006**), 129–137

[20] H. Ohta, H. Suito, Dispersion Behavior of MgO, ZrO2, Al2O3, CaO-Al2O3 and MnO-SiO2 Deoxidation Particles during Solidification of Fe-10mass%Ni Alloy, ISIJ Int., 46 (**2006**), 22–28, doi:10.2355/isijinternational.46.22

[21] A. V Karasev, H. Suito, Quantitative evaluation of inclusion in deoxidation of Fe-10 mass% Ni alloy with Si, T, Al, Zr, and Ce, Metall. Mater. Trans. B Vol.30B, 30B (**1999**), 249–257, doi:10.1007/s11663-999-0054-1

[22] A. V. Karasev, H. Suito, Nitride Precipitation on Particles in Fe–10mass%Ni Alloy Deoxidized with Ti, M (M=Mg, Zr and Ce) and Ti/M, ISIJ Int., 49 (**2009**), 229–238, doi:10.2355/isijinternational.49.229

[23] H. Ohta, H. Suito, Precipitation and Dispersion Control of MnS by Deoxidation Products of ZrO2, Al2O3, MgO and MnO – SiO2 Particles in Fe – 10mass % Ni Alloy, ISIJ Int., 46 (**2006**), 480–489

[24] Y. Min, X. Li, Z. Yu, C. Liu, M. Jiang, Characterization of the Acicular Ferrite in Al-Deoxidized Low-Carbon Steel Combined with Zr and Mg Additions, Steel Res. Int., 87 (**2016**), 1503–1510, doi:10.1002/srin.201500440

UDK 620.193:62-4-023.731:669.017.1
Original scientific article/Izvirni znanstveni članek

ISSN 1580-2949
MTAEC9, 51(6)1037(2017)

CORROSION ON POLISHED AND LASER-TEXTURED SURFACES OF AN Fe–Mn BIODEGRADABLE ALLOY

PRIMERJAVA KOROZIJSKIH LASTNOSTI POLIRANE IN LASERSKO TEKSTURIRANE POVRŠINE BIORAZGRADLJIVE ZLITINE Fe–Mn

Matej Hočevar[1], Črtomir Donik[1], Irena Paulin[1], Aleksandra Kocijan[1], Franc Tehovnik[1], Jaka Burja[1], Peter Gregorčič[2], Matjaž Godec[1]

[1]Institute of Metals and Technology, Lepi pot 11, 1000 Ljubljana, Slovenia
[2]Faculty of Mechanical Engineering, University of Ljubljana, Aškerčeva 6, 1000 Ljubljana, Slovenia
matej.hocevar@imt.si

Prejem rokopisa – received: 2017-08-21; sprejem za objavo – accepted for publication: 2017-09-12

doi:10.17222/mit.2017.140

Fe-based biodegradable alloys such as Fe–Mn are interesting for biodegradable implants; however, their corrosion rate for such applications is too low. Here, nanosecond-laser surface texturing is applied as a successful surface treatment for increasing the degradation rate of an Fe–Mn alloy. Laser texturing increases the surface area by increasing the surface porosity and generating a super-hydrophilic surface. Electrochemistry tests revealed that the laser-textured samples have a higher corrosion rate than a polished sample, thus enhancing the biodegradability of the Fe–Mn alloy. EDS analyses revealed a significantly higher content of Mn on the surface in the oxidized layer compared to the bulk Fe–Mn composition, which is one of the reasons for the increased corrosion rate. This work demonstrates the potential of laser-treated surfaces of biodegradable metals for biomedical applications.

Keywords: Fe–Mn alloy, laser texturing, corrosion, biodegradable, EDS analyses

Biološko razgradljive zlitine, kot so na primer Fe–Mn zlitine, so zanimive za uporabo v obliki biološko razgradljivih implantantov, vendar je njihova hitrost korozije za ciljne aplikacije še vedno prenizka. Lasersko teksturiranje površine predstavlja uspešno površinsko obdelavo za povečanje hitrosti razgradnje Fe–Mn zlitine. Obdelava površine z laserjem poveča delež izpostavljene površine na račun večje poroznosti, obenem pa je novonastala površina superhidrofilna. Elektrokemijski testi so pokazali, da imajo vzorci, obdelani z laserjem, večjo stopnjo korozije v primerjavi s poliranimi vzorci, s čimer se poveča biorazgradljivost zlitine Fe–Mn. EDS analiza je pokazala povečano vsebnost Mn na površini v oksidirani plasti v primerjavi s kemijsko sestavo osnovnega materiala Fe–Mn, kar predstavlja eno od razlag za povečanje hitrosti korozije. Raziskava dokazuje potencial laserske obdelave površine biološko razgradljivih kovin za biomedicinske aplikacije.

Ključne besede: zlitina Fe–Mn, lasersko teksturiranje, korozija, biorazgradljivost, EDS analiza

1 INTRODUCTION

In recent years, biodegradable metals, such as Fe and Mg alloys, have emerged as a promising alternative in bone surgery, orthopaedic and cardiovascular applications.[1–4] The advantages of biodegradable metals are temporary support during tissue healing, progressive degradation, as well as reducing the long-term risks and side effects.[1,2,5,6] Despite the high potential of these Fe-based materials, which possess similar mechanical properties to stainless steel, they exhibit one main weakness – the corrosion rate is too slow.[6–8] However, with the addition of Mn as an alloying element, a trace element necessary in many enzymatic reactions, the corrosion rate is enhanced.[2,9] Although the degradation is faster it is still too low, which represents a major problem for these recently developed Fe–Mn alloys. Another way to influence the corrosion rate of an Fe–Mn alloy without changing its chemical composition is to modify the surface morphology via mechanical treatments, including machining, sand blasting and laser surface modification.[10–15] Increased surface areas, porous surfaces and surfaces with increased wettability (super-hydrophilic surfaces) have higher corrosion rates.[11,16,17] However, not so many studies has been made on biodegradable Fe metals, and many of the existing treatments are usually applied to biocompatible materials with passivating surfaces such as AISI 316L stainless steel, titanium alloys, cobalt-chromium alloys and other similar alloys to improve the corrosion properties.[11,18,19]

The aim of the present study was to investigate the influence of a laser surface treatment on the corrosion behaviour of the Fe–Mn alloy due to changes in the surface properties. In contrast to other authors the content of Mn in our study was below 20 % of mass fractions, with no additional changes in the chemical composition. Like the majority of the previous studies to simulate *in-vivo* conditions, the corrosion properties were investigated using Hank's solution.

2 EXPERIMENTAL PART

2.1 Material preparation

An Fe-Mn alloy with 17 % of mass fractions of Mn was produced from pure Fe with the addition of Mn to the alloy. The laboratory material was made in a 20 kg Leybold Heraeus vacuum induction furnace. The two 60 mm × 60 mm × 500 mm ingots of Fe-Mn alloy were cast and hot rolled to 60 mm × 20 mm × 150 mm. The hot-rolled material was solution annealed at 1200 °C and quenched in oil. The chemical composition of the Fe–Mn alloy was determined with an X-ray fluorescence spectrometer XRF (Thermo Scientific Niton XL3t GOLDD+) and a carbon and sulphur analyser (ELTRA CS-800). The chemical composition of produced Fe-Mn alloy in % of mass fractions of: 0.58 % C, 0.067 % Si, 17.0 % Mn, 0.051 % Cu, 0.31 % Mo, 0.058 % Ti, balance Fe.

2.2 Surface modification

The Fe–Mn samples were cut into 15 mm × 15 mm size squares and prepared by wet grinding down to 1200 grit followed by polishing down to 1 µm with a diamond suspension to produce a smooth mirror finish. Selected samples were further textured by using a nanosecond laser (Nd:YAG) with a wavelength of 1064 nm and pulse duration of 95 ns. The beam spot size was 0.05 mm and it was led in lines with a velocity of 1.6 mm/s using a scanning head. The scan line separation equalled 50 µm. The texturing was performed with a pulse energy of 0.6 mJ and frequency of 1kHz. Before laser texturing, the samples were cleaned with detergent, rinsed thoroughly with water and immersed in an ultrasonic bath in absolute ethanol for 12 min.

2.3 Electrochemical measurements

Electrochemical measurements were performed on polished and laser-treated Fe–Mn samples at room temperature in a simulated physiological Hank's solution, containing 8 g/L NaCl, 0.40 g/L KCl, 0.35 g/L $NaHCO_3$, 0.25 g/L NaH_2PO_4, 0.06 g/L Na_2HPO_4, 0.19 g/L $CaCl_2$, 0.41 g/L $MgCl_2$, 0.06 g/L Mg_SO_4 and 1 g/L glucose, stabilized at pH = 7.8. All the chemicals were from Merck, Darmstadt, Germany. A three-electrode, flat BioLogic® corrosion cell (volume 0.25 L) was used for the corrosion measurements. The test specimen was employed as the working electrode (WE). The reference electrode (RE) was a saturated calomel electrode (SCE, 0.242 V vs. SHE) and the counter electrode (CE) was a platinum mesh. Electrochemical measurements were recorded using a BioLogic® Modular Research Grade Potentiostat/Galvanostat/FRA Model SP-300 with an EC-Lab® software V11.10. The specimens were immersed in the solution 1 h prior to the measurement in order to stabilize the surface at the open-circuit potential (OCP). The linear polarization measurements were performed at ± 25 mV according to the OCP, using a scan rate of 0.01 mV s^{-1}.

2.4 Surface and metallographic investigation

The surface morphologies of the polished and laser-textured samples were examined with a scanning electron microscope (SEM JEOL JSM-6500F) coupled with an energy-dispersive spectrometer (EDS INCA ENERGY 400) and a non-contact Alicona G4 3D optical Infinite-Focus Measuring (IFM) device. A cross-section of the laser-textured samples was studied using EDS line scan and EDS mapping analyses.

3 RESULTS AND DISCUSSION

3.1 Surface characterization

3D optical measurements (**Figure 1**) and SEM images (**Figure 2**) of the laser-modified sample reveal 100-µm-deep visible micro-channels, separated by 50 µm. The bimodal structure with a typical dimension of 10 µm is formed at the top of these micro-channels due to laser ablation and melting. This nanostructured surface is covered by a Fe–Mn oxide layer (**Figure 2b**). A 3D profile of the polished surface is shown in **Figure 1b**, where an ultra-smooth surface is visible with a surface roughness S_a < 0.04 µm compared to the laser-textured ultra-rough sample with S_a > 25 µm. Additionally, the laser-textured sample exhibited super-hydrophilic behaviour after the treatment (θ = 0°), whereas the static contact angle on the polished surface is approaching the hydrophobic area (θ = 70°). As previously shown by other authors[11,16,17] the increased surface roughness,

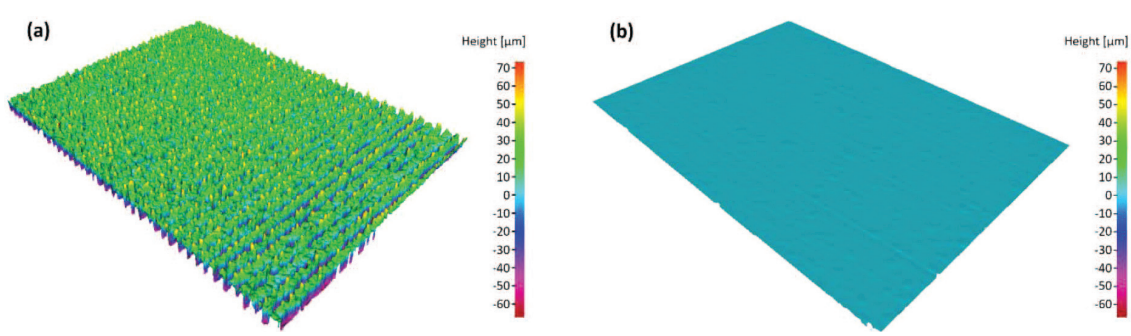

Figure 1: 3D height image representing the surface topography of a) laser-textured Fe–Mn sample and b) polished Fe–Mn sample

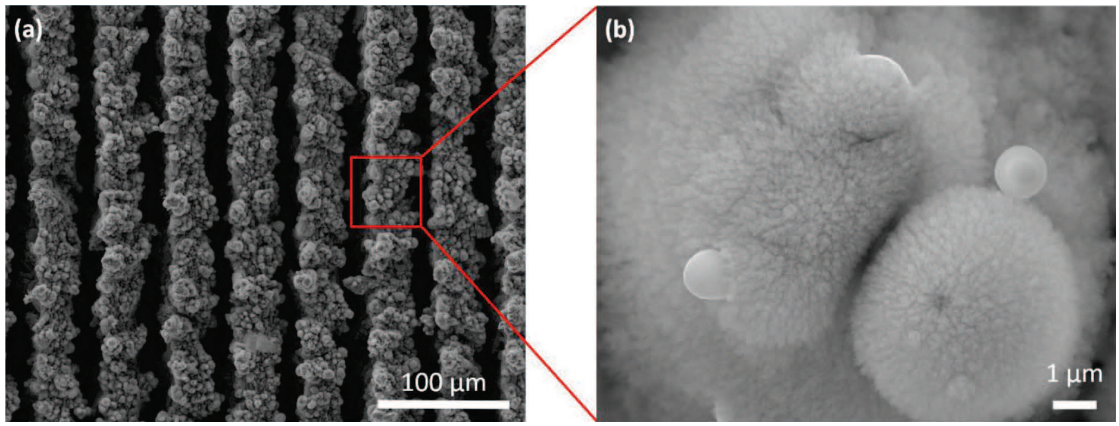

Figure 2: a) SEM image of surface topography of Fe–Mn laser-textured sample with micro-channels and b) highly magnified nanostructured surface covered by Fe–Mn oxide layer

porosity and also the super-hydrophilic behaviour of laser-treated Fe–Mn, significantly enhance the corrosion rate compared to the polished sample.

EDS analyses revealed a noticeable surface oxide layer. From the surface to the bulk the concentration of O is decreasing with increased Mn concentration (**Figures 3** and **4**). This is a known mechanism for increasing the corrosion rate.[20] This increase of Mn causes depletion of the Fe in the oxide layer and the ratio shifts to Mn > Fe (**Figures 3** and **4**).

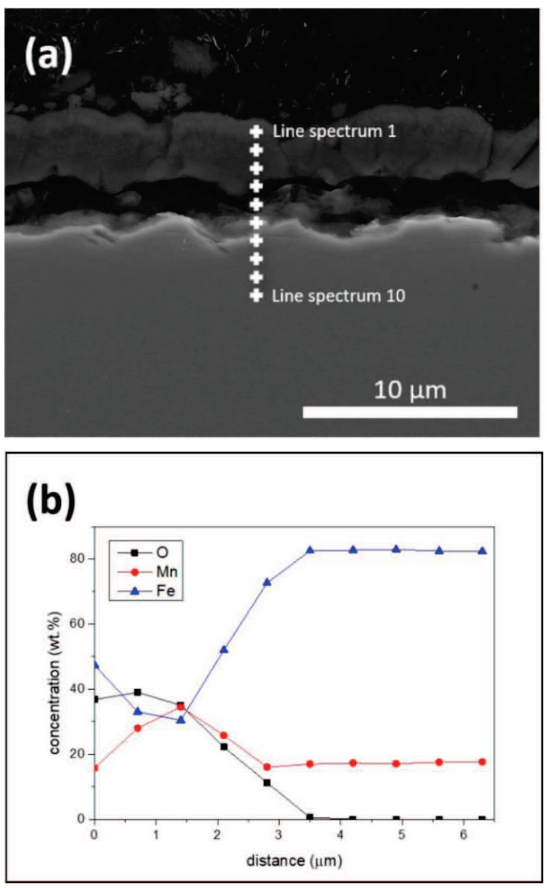

Figure 3: a) SEM cross-section image of laser-textured Fe–Mn sample and b) the corresponding EDS line scan

3.2 Electrochemical measurements

3.2.1 Linear polarization

Figure 5 shows the linear polarization curves for the polished and laser-textured Fe–Mn samples in a simulated physiological Hank's solution at pH = 7.8. The calculations from the linear polarization measurements used the Equation (1):

$$R_p = \beta_a \beta_c / (2.3\ I_{corr}\ (\beta_a + \beta_c)) \quad (1)$$

The polarization resistance, R_p, is evaluated from the linear polarization curves by applying a linear least-squares fit of the data around OCP, ± 10 mV. The corrosion current, I_{corr}, is calculated from R_p, the least-squares slope, and the Tafel constants, β_a and β_c, of 120 mV decade^{-1}. The value of $E_{(I=0)}$ is calculated from the least-squares intercept. The corrosion rates were calculated using the following conversion in Equation (2):

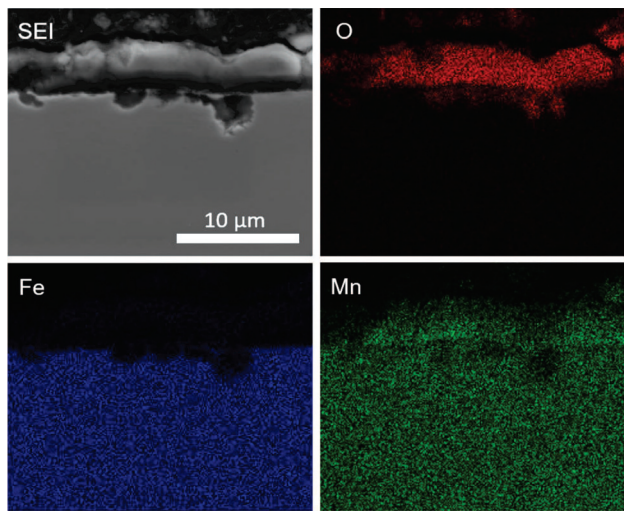

Figure 4: SEM cross-section image of laser-textured Fe–Mn sample and corresponding EDS elemental maps showing composition (O, Fe, Mn)

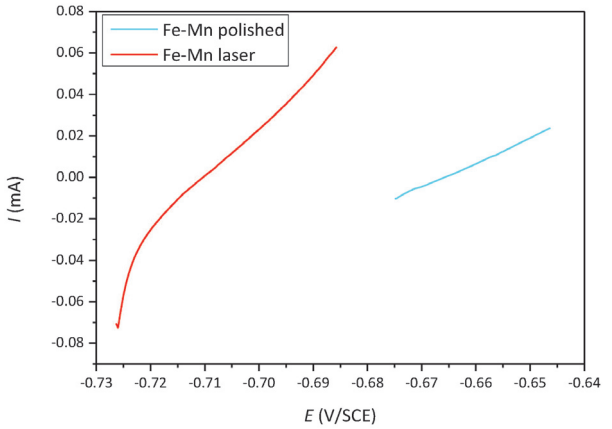

Figure 5: Linear polarization curve for polished and Fe–Mn laser-textured samples

$$v_{corr} = C(EW/d)(I_{corr}/A), \quad (2)$$

where EW is the equivalent weight of the sample in g, A is the sample area in cm^2, d is its density in g/cm^3, and C is a conversion constant that is dependent upon the required units. The results from the laser-treated Fe–Mn demonstrate steeper linear polarization curves and therefore a lower corrosion resistance compared the other two samples of polished Fe–Mn alloy, which have curves with similar inclines. The corrosion parameters calculated from the linear polarization with potentiodynamic measurement data in a simulated physiological Hank's solution indicated that the corrosion stability is higher for the polished Fe–Mn than for the laser-textured surface. A higher corrosion rate indicates better biodegradability of laser-textured Fe–Mn sample. This was proven with the higher corrosion currents (I_{corr}), higher corrosion rates (v_{corr}) and lower polarization resistances (R_p), compared to the polished sample (**Table 1**). These results corroborate the results of earlier studies,[21,22] where the corrosion rate is directly linked to the roughness and hydrophobicity.

Table 1: Corrosion characteristics of studied materials calculated from linear polarisation measurements

	I_{corr} /μA	E_{corr} /mV	v_{corr} / nm year^{-1}	R_p/W
Fe–Mn laser	70.6	–775	770	395
Fe–Mn polished	11.4	–705	123	850

4 CONCLUSIONS

Laser structuring using a nanosecond laser creates a super-hydrophilic surface with an increased exposed surface area containing nanostructured high-temperature oxides. In the present study, an electrochemical investigation confirmed that the laser treatment of the Fe–Mn alloy increases the corrosion rate by more than six times compared to the polished Fe–Mn alloy. The EDS line scan and the mapping showed a corrosion-favourable chemical composition changes, with Mn increasing and Fe depleting in the exposed surface layer. The results in our study revealed that an increased exposed porous surface, super-hydrophobicity and Fe depletion in the oxide layer are the three main reasons leading to an increased biodegradability of the Fe–Mn alloy. We have shown that laser-surface texturing has a high potential for surface modification in biomedical applications, since the proposed approach might also be applicable to other biodegradable metals to increase the biodegradation.

Acknowledgement

The authors acknowledge the financial support from the Slovenian Research Agency (research core funding Nos. P2-0132 and P2-0392).

5 REFERENCES

[1] A. Francis, Y. Yang, S. Virtanen, A.R. Boccaccini, Iron and iron-based alloys for temporary cardiovascular applications, J. Mater. Sci. Mater. Med., 26 (**2015**), 138, doi:10.1007/s10856-015-5473-8

[2] H. Hermawan, Biodegradable Metals: From Concept to Applications, Springer, Berlin Heidelberg, 2012, doi:10.1007/978-3-642-31170-3

[3] J. Cheng, B. Liu, Y.H. Wu, Y.F. Zheng, Comparative in vitro Study on Pure Metals (Fe, Mn, Mg, Zn and W) as Biodegradable Metals, J. Mater. Sci. Technol., 29 (**2013**), 619–627, doi:10.1016/j.jmst.2013.03.019

[4] H. Hermawan, D. Mantovani, Degradable metallic biomaterials: the concept, current developments and future directions, MINERVA Biotecnol., 21 (**2009**), 207–216

[1] L. Tan, X. Yu, P. Wan, K. Yang, Biodegradable Materials for Bone Repairs: A Review, J. Mater. Sci. Technol., 29 (**2013**), 503–513, doi:http://dx.doi.org/10.1016/j.jmst.2013.03.002

[5] M. P. Staiger, A. M. Pietak, J. Huadmai, G. Dias, Magnesium and its alloys as orthopedic biomaterials: A review, Biomaterials, 27 (**2006**), 1728–1734, doi:10.1016/j.biomaterials.2005.10.003

[6] Z. Zhen, T. XI, Y. Zheng, A review on in vitro corrosion performance test of biodegradable metallic materials, Trans. Nonferrous Met. Soc. China, 23 (**2013**), 2283–2293, doi:10.1016/S1003-6326(13)62730-2

[7] B. Liu, Y. F. Zheng, Effects of alloying elements (Mn, Co, Al, W, Sn, B, C and S) on biodegradability and in vitro biocompatibility of pure iron, Acta Biomater., 7 (**2011**), 1407–1420, doi:10.1016/j.actbio.2010.11.001

[8] H. Hermawan, D. Dubé, D. Mantovani, Developments in metallic biodegradable stents, Acta Biomater., 6 (**2010**), 1693–1697, doi:10.1016/j.actbio.2009.10.006

[9] J. Zhou, Y. Yang, M. Alonso Frank, R. Detsch, A. R. Boccaccini, S. Virtanen, Accelerated Degradation Behavior and Cytocompatibility of Pure Iron Treated with Sandblasting, ACS Appl. Mater. {&} Interfaces, 8 (**2016**), 26482–26492, doi:10.1021/acsami.6b07068

[10] U. Trdan, M. Hočevar, P. Gregorčič, Transition from superhydrophilic to superhydrophobic state of laser textured stainless steel surface and its effect on corrosion resistance, Corros. Sci., (**2017**), doi:10.1016/j.corsci.2017.04.005

[11] L. De Lara, R. Jagdheesh, J. L. Ocana, Corrosion resistance of laser patterned ultrahydrophobic aluminium surface, Mater. Lett., 184 (**2016**), 100–103, doi:10.1016/j.matlet.2016.08.022

[12] M. S. Brown, C. B. Arnold, Fundamentals of Laser-Material Interaction and Application to Multiscale Surface Modification, in: K. Sugioka, M. Meunier, A. Piqué (Eds.), Laser Precis. Microfabr., Springer Berlin Heidelberg, Berlin, Heidelberg, 2010: 91–120, doi:10.1007/978-3-642-10523-4_4

[13] M. Svantner, M. Kucera, S. Houdkova, J. Riha, Influence of laser ablation on stainless steel corrosion behaviour, in: Met. 2011 20TH Anniv. Int. Conf. Metall. Mater., Tanger LTD, Keltickova 62, Slezska, Ostrava 710 00, Czech Republic, 2011: 752–757

[14] A. Kocijan, I. Paulin, C. Donik, M. Hocevar, K. Zelic, M. Godec, Influence of Different Production Processes on the Biodegradability of an FeMn17 Alloy, Mater. Tehnol., 50 (**2016**), 805–811, doi:10.17222/mit.2016.055

[15] G. Ryan, A. Pandit, D. P. Apatsidis, Fabrication methods of porous metals for use in orthopaedic applications, Biomaterials, 27 (**2006**), 2651–2670, doi:10.1016/j.biomaterials.2005.12.002

[16] Z. Zhen, T. Xi, Y. Zheng, A review on in vitro corrosion performance test of biodegradable metallic materials, Trans. Nonferrous Met. Soc. China, 23 (**2013**), 2283–2293, doi:10.1016/S1003-6326(13)62730-2

[17] Y. F. Zheng, X. N. Gu, F. Witte, Biodegradable metals, Mater. Sci. Eng. R Reports, 77 (**2014**), 1–34, doi:10.1016/j.mser.2014.01.001

[18] M. T. Mohammed, Z. A. Khan, A. N. Siddiquee, Surface Modifications of Titanium Materials for developing Corrosion Behavior in Human Body Environment: A Review, Procedia Mater. Sci., 6 (**2014**), 1610–1618, doi:10.1016/j.mspro.2014.07.144

[19] A. Kawashima, K. Asami, K. Hashimoto, Effect of Manganese on The Corrosion Behavior of Chromium-Bearing Amorphous Metal-Metalloid Alloys, Sci. Reports Res. Institutes Tohoku Univ. Ser. A-PHYSICS Chem. Metall., 29 (**1981**), 276–283

[20] J. E. Tang, M. Halvarsson, H. Asteman, J. E. Svensson, Microstructure of oxidised 304L steel and the effects of surface roughness on oxidation behaviour, in: R.W.I.G.K.R.C.C.M.G.A. Streiff (Ed.), 2001: 205–214

[21] A. Dunn, K. L. Wlodarczyk, J. V Carstensen, E. B. Hansen, J. Gabzdyl, P. M. Harrison, J. D. Shephard, D. P. Hand, Laser surface texturing for high friction contacts, Appl. Surf. Sci., 357 (**2015**), 2313–2319, doi:10.1016/j.apsusc.2015.09.233

UDK 620.1/.2:620.19:532.6
Original scientific article/Izvirni znanstveni članek

ISSN 1580-2949
MTAEC9, 51(6)1043(2017)

COMPARISON OF THE SURFACE AND ANTICORROSION PROPERTIES OF SiO_2 AND TiO_2 NANOPARTICLE EPOXY COATINGS

PRIMERJAVA POVRŠINSKIH IN PROTIKOROZIJSKIH LASTNOSTI EPOKSIDNIH PREVLEK OBOGATENIH S SiO_2 IN TiO_2 NANOVKLJUČKI

Marjetka Conradi, Aleksandra Kocijan

Institute of Metals and Technology, Lepi pot 11, 1000 Ljubljana, Slovenia
marjetka.conradi@imt.si

Prejem rokopisa – received: 2017-08-21; sprejem za objavo – accepted for publication: 2017-10-02

doi:10.17222/mit.2017.137

In this article we compare the morphology, wetting and anticorrosion properties of fluorosilane-modified TiO_2, FAS-TiO_2/epoxy and SiO_2, FAS-SiO_2/epoxy coatings. Thirty-nanometre TiO_2 and SiO_2 nanoparticles were spin coated onto the AISI 316L steel substrate and covered with a thin epoxy layer for nanoparticle fixation. The morphology of the coatings was analysed with SEM imaging and the average surface roughness (S_a), and it showed a homogeneous FAS-TiO_2 nanoparticle distribution in the coating, whereas the FAS-SiO_2 nanoparticles tended to agglomerate. Static water contact angles were measured to evaluate the wetting properties, indicating the highly hydrophobic nature of both coatings. Potentiodynamic measurements showed that the addition of nanoparticles to the epoxy coating significantly improved the corrosion resistance of the AISI 316L stainless steel.

Keywords: TiO_2, SiO_2, epoxy, coatings, wetting, corrosion

V članku primerjamo morfologijo, omočitvene lastnosti in antikorozijske lastnosti s fluorosilanom oblečenih TiO_2, FAS-TiO_2/epoksi in SiO_2, FAS-SiO_2/epoxy prevlek. 30-nm TiO_2 in SiO_2 nanodelce smo na jekleno podlago tipa AISI 316L nanesli s "spin coaterjem" ter jih prekrili s tanko plastjo epoksidne smole, ki je zagotovila fiksacijo nanodelcev na površini. Morfološke lastnosti prevlek smo analizirali s SEM mikroskopijo ter z meritvami povprečne hrapavosti površine (S_a). Pokazali smo, da so FAS-TiO_2 nanodelci v prevleki enakomerno razporejeni, medtem, ko FAS-SiO_2 nanodelci kažejo visoko stopnjo aglomeracije. Omočitvene lastnosti prevlek smo določili z meritvami statičnih kontaktnih kotov, ki so pokazale hidrofobne lastnosti tako FAS-TiO_2/epoksi kot tudi FAS-SiO_2/epoksi prevlek. Potenciodinamske meritve potrjujejo, da z dodatkom nanodelcev epoksi, zaščitnim prevlekam izrazito izboljšamo korozijsko obstojnost nerjavnega jekla AISI 316L.

Ključne besede: TiO_2, SiO_2, epoksi, prevleke, omočitvene lastnosti, korozija

1 INTRODUCTION

Designing a solid surface with specific surface characteristics, such as wetting properties, mechanical resistance, anticorrosion properties, etc., is challenging in several applications in aerospace, marine, biomedicine etc[1,2]. Therefore, the surface modification of engineering metallic materials, such as the most commonly used austenitic stainless steel (AISI),[3,4] by various coatings represents an important subject in the field of enhancing particular surface properties, mechanical as well as anticorrosion properties.

Epoxy coatings serve as an excellent physical barrier for metallic surface protection due to their good mechanical and electrical insulating properties, chemical resistance and strong adhesion to different substrates. However, the highly cross-linked structure of an epoxy resin often makes epoxy coatings susceptible to the propagation of cracks and damage by surface abrasion and wear.[5] It has been shown that the implementation of various nanoparticles like SiO_2, TiO_2, ZnO, CuO, etc. additionally improves the performance of coatings.[6] Nanoparticles also enhance the corrosion protection properties of the epoxy coatings by decreasing the porosities due to the small size and high specific area.

The hierarchical structures of nanoparticle/epoxy composites can, on the other hand, also change the wetting characteristics of the surface. It is well known that the surface roughness can enhance both hydrophobicity and hydrophilicity.[7,8] In combination with the nanoparticle surface chemistry (i.e., functionalization) we can control the wetting characteristics of epoxy coatings[9] that additionally allows for an improvement of the anticorrosion properties.

Here we report on a comparison of the surface and anticorrosion properties of hydrophobic FAS-TiO_2/epoxy and FAS-SiO_2/epoxy coatings. The morphology and wetting properties are characterized as well as the anticorrosion properties through potentiodynamic measurements.

2 EXPERIMENTAL PART

Materials. Austenitic stainless steel AISI 316L (17 % Cr, 10 % Ni, 2.1 % Mo, 1.4 % Mn, 0.38 % Si, 0.041 % P,

0.021 % C, <0.005 % S in mass fraction) was used as a substrate.

A biocompatible epoxy EPO-TEK 302-3M (EPOXY TECHNOLOGY, Inc.) was mixed in the producer-prescribed two-component *w*/% ratio 100:45. 30-nm TiO_2 nanoparticles with mean were provided by Cinkarna Celje, whereas the 30-nm SiO_2 nanoparticles were supplied by Cab-O-Sil.

Surface functionalization. For hydrophobic effect as well as for homogenization of nanoparticle distribution, SiO_2 and TiO_2 particles were functionalized in 1 % of volume fractions of ethanolic fluoroalkylsilane or FAS17 ($C_{16}H_{19}F_{17}O_3Si$) solution.

Steel substrate preparation. Prior to the application of the coating, the steel discs of 25 mm diameter and with a thickness of 1.5 mm were diamond polished following a standard mechanical procedure and then cleaned with ethanol in an ultrasonic bath.

Coating preparation. To improve the SiO_2 and TiO_2 nanoparticles' adhesion, the diamond-polished AISI 316L substrate was spin-coated with a thin layer of epoxy and then cured for 3 h at 65 °C. To ensure good surface coverage, five drops (20 µL) of 3 % of mass fractions of TiO_2/SiO_2 nanoparticle ethanolic solution were then spin-coated onto an epoxy-coated AISI 316L substrate and dried in an oven for approximately 20 min at 100 °C. Finally, the coatings were covered with another thin layer of epoxy for particle fixation and then cured for 3 h at 65 °C.

Scanning electron microscopy (SEM). SEM analysis using FE-SEM Zeiss SUPRA 35VP was employed to investigate the morphology of the nanoparticle coatings' surfaces, which were sputtered with gold prior to imaging.

Contact-angle measurements. The static contact-angle measurements of water (W) on the nanoparticle coatings were performed using a surface-energy evaluation system (Advex Instruments s.r.o.). Liquid drops of 5 µL were deposited on different spots of the substrates to avoid the influence of roughness and gravity on the shape of the drop. The drop contour was analysed from the image of the deposited liquid drop on the surface and the contact angle was determined by using Young-Laplace fitting. To minimize the errors due to roughness and heterogeneity, the average values of the contact angles of the drop were calculated approximately 30 s after the deposition from at least five measurements on the studied coated steel. All the contact-angle measurements were carried out at 20 °C and ambient humidity.

Surface roughness. Optical 3D metrology system, model Alicona Infinite Focus (Alicona Imaging GmbH), was used for the surface-roughness analysis. At least three measurements per sample were performed at a magnification of 20× with a lateral resolution of 0.9 µm and a vertical resolution of about 50 nm. IF-Measure-Suite (Version 5.1) software was later on used to calculate the average surface roughness, S_a, for each sample, based on the general surface-roughness equation (Equation (1)):

$$Sa = \frac{1}{L_x}\frac{1}{L_y}\int_0^{L_x}\int_0^{L_y}\left|z(x,y)\right|\mathrm{d}x\mathrm{d}y \qquad (1)$$

where L_x and L_y are the acquisition lengths of the surface in the x and y directions and $z(x,y)$ is the height. The size of the analysed area was 1337×540 µm^2.

Electrochemical measurements. Electrochemical measurements were performed on the epoxy-coated, FAS-SiO_2/epoxy-coated and FAS-TiO_2/epoxy-coated AISI 316L stainless steel in a simulated physiological Hank's solution, containing 8 g/L NaCl, 0.40 g/L KCl, 0.35 g/L $NaHCO_3$, 0.25 g/L $NaH_2PO_4{\cdot}2H_2O$, 0.06 g/L $Na_2HPO_4{\cdot}2H_2O$, 0.19 g/L $CaCl_2{\cdot}2H_2O$, 0.41 g/L $MgCl_2{\cdot}6H_2O$, 0.06 g/L $MgSO_4{\cdot}7H_2O$ and 1 g/L glucose, at pH = 7.8 and 37 °C. All the chemicals were from Merck, Darmstadt, Germany. The measurements were performed by using BioLogic Modular Research Grade Potentiostat/Galvanostat/FRA Model SP-300 with an EC-Lab Software and a three-electrode flat corrosion cell, where the working electrode (WE) was the investigated specimen, the reference electrode (RE) was a saturated calomel electrode (SCE, 0.242 V vs. SHE) and the counter electrode (CE) was a platinum net. The potentiodynamic curves were recorded at the open-circuit potential (OCP), starting the measurement at 250 mV vs. SCE more negative than the OCP. The potential was increased using a scan rate of 1 mV s^{-1}.

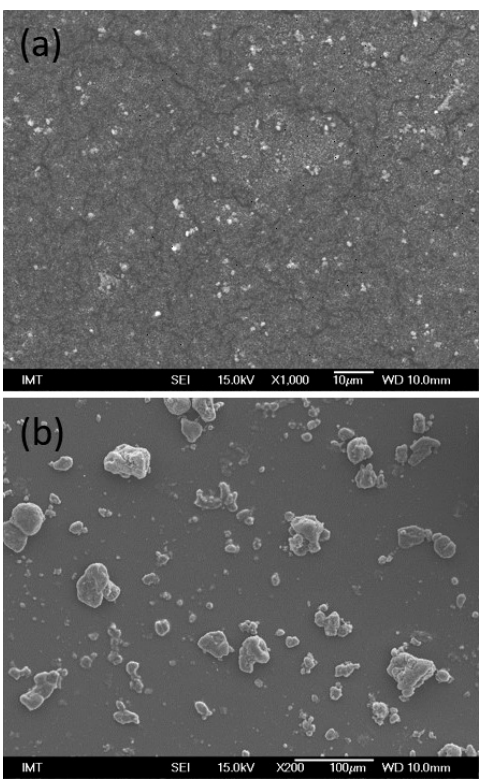

Figure 1: SEM images of the surface morphology of: a) FAS-TiO_2/epoxy and b) FAS-SiO_2/epoxy coatings

3 RESULTS AND DISCUSSION

3.1 Surface morphology

Figure 1 compares the morphology of the FAS-TiO_2/epoxy and FAS-SiO_2/epoxy coatings. The SEM images reveal a distinctive morphology between the two coatings that is reflected in the different length scale of the agglomerate formation, which is also reflected in a discrepancy in the average surface roughness S_a (**Table 1**). FAS-TiO_2/epoxy coatings (**Figure 1a**) are characterized with a more refined structure that is a consequence of the better FAS-TiO_2 nanoparticle dispersion with less agglomeration on the micrometre scale. FAS-SiO_2/epoxy coatings, in contrast, are characterized by severe agglomeration (**Figure 1b**) and randomly distributed agglomerates from nanometres to a few micrometres in diameter. This suggests that the FAS functionalization works well with homogenization of TiO_2 nanoparticle distribution, but has no effect on the homogenization of the SiO_2 nanoparticle distribution.

3.2 Wetting properties

To analyse the surface wettability, we performed five static contact-angle measurements with water (W) on different spots all over the sample and used them to determine the average contact-angle values of the coating with an estimated error in the reading of $\theta \pm 1.0°$.

In the first step we prepared the superhydrophobic FAS-TiO_2 and FAS-SiO_2 surfaces by spin-coating the AISI+epoxy substrate with FAS-TiO_2 and FAS-SiO_2 nanoparticles. The corresponding static water contact angles are reported in **Table 1**. Nanoparticle fixation with a thin layer of hydrophilic epoxy ($\theta^w = 71.8°$) eliminated the superhydrophobic effect; however, a substantial degree of hydrophobicity that is necessary for desirable anticorrosion properties[10] was retained, as reported in **Table 1**. The retained high degree of hydrophobicity is most probably a combination of surface roughness and the originally superhydrophobic nature of the FAS-TiO_2 and FAS-SiO_2 nanoparticles. In addition, the top layer of epoxy also smoothened the coating, which is reflected in the reduced average surface roughness, S_a, of the AISI+epoxy+TiO_2/SiO_2+epoxy surfaces compared to the AISI+epoxy+TiO_2/SiO_2 surfaces. This is most probably due to the fact that epoxy fills the space between the nanoparticle agglomerates and reduces the height variation over the whole surface, and therefore also S_a.

There is, however, a noticeable difference in the static water contact angles and a difference by a factor of 10 in the value of the average surface roughness, S_a, As reported in **Table 1**, the FAS-SiO_2/epoxy coating is rougher and more hydrophobic compared to the FAS-TiO_2/epoxy coating. The difference in the average surface roughness was already expected from the surface morphology analysis (**Figure 1**) due to the severe SiO_2 nanoparticle agglomeration compared to the TiO_2 coated surface. The increased hydrophobicity of the FAS-SiO_2/epoxy coating can, on the other hand, be attributed to the more pronounced micro- to nanoparticle-textured surface with a refined roughness structure.[9]

Table 1: Comparison of the static water contact angles (θ^W) and the average surface roughness (S_a) of the FAS-TiO_2/epoxy and FAS-SiO_2/epoxy coatings

Substrate	Contact angle θ^w (°)	Roughness S_a (µm)
epoxy	71.8	0.02
AISI+epoxy+TiO_2	150.1	0.41
AISI+epoxy+SiO_2	155.4	3.69
AISI+epoxy+TiO_2+epoxy	121.1	0.23
AISI+epoxy+SiO_2+epoxy	130.6	2.34

3.3 Potentiodynamic measurements

Figure 2 shows the potentiodynamic behaviour of the FAS-TiO_2/epoxy-coated, FAS-SiO_2/epoxy-coated and epoxy-coated AISI 316L stainless steel in a simulated physiological Hank's solution. The polarization and the passivation behaviour of the tested material after the surface modification was studied. The corrosion potential (E_{corr}) for the epoxy coating in the Hank's solution was approximately –256 mV vs. SCE, for the FAS-TiO_2/epoxy-coated AISI 316L it was –335 mV vs. SCE and for FAS-SiO_2/epoxy-coated AISI 316L it was –407 mV vs. SCE. After the Tafel region, the investigated sample exhibited a broad passive range followed by the breakdown potential (E_b). The passivation range of the FAS-TiO_2/epoxy-coated and FAS-SiO_2/epoxy-coated AISI 316L specimen was moved to the significantly lower corrosion-current densities compared to the pure epoxy-coated AISI 316L. We established that the addition of nanoparticles to the epoxy coating significantly

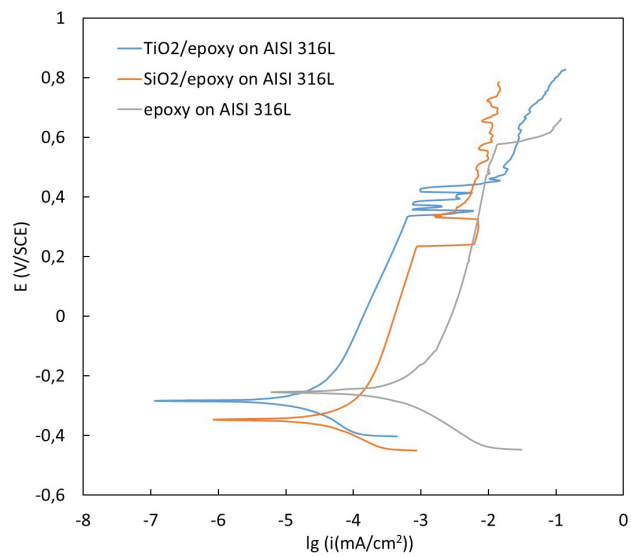

Figure 2: Potentiodynamic curves for FAS-TiO_2/epoxy-coated, FAS-SiO_2/epoxy-coated and epoxy-coated AISI 316L substrate in a simulated physiological Hank's solution

enhanced the corrosion resistance of the AISI 316L stainless steel compared to the pure epoxy coating, especially in the case of the FAS-TiO_2/epoxy coating. The corrosion parameters calculated from the potentiodynamic measurements showed decreased corrosion-current densities and increased the polarisation resistances of the specimens coated with FAS-TiO_2/epoxy and FAS-SiO_2/epoxy coating compared to the pure epoxy coating (**Table 2**). The superior protective properties of the FAS-TiO_2/epoxy coating were attributed to the more uniform distribution of the FAS-TiO_2 nanoparticles within the coating.

Table 2: Corrosion parameters calculated from the potentiodynamic measurements

Material	$E(I=0)$ (mV)	I_{corr} (μA)	R_p (kΩ)	v_{corr} (nm/year)
epoxy coated AISI 316L	–256	0.33	78	1.1
SiO_2/epoxy coated AISI 316L	–407	0.06	557	0.7
TiO_2/epoxy coated AISI 316L	–335	0.02	1500	0.2

4 CONCLUSIONS

We analysed the morphology of FAS-TiO_2/epoxy and FAS-SiO_2/epoxy coatings showing that the FAS functionalization works well with the homogenization of the TiO_2 nanoparticle distribution, but has no effect on the homogenization of the SiO_2 nanoparticle distribution, as these tend to agglomerate. This is directly reflected in the SEM image analysis and the average surface-roughness measurements. The wetting properties evaluation reveals the superhydrophobic nature of the FAS-TiO_2 and FAS-SiO_2 nanoparticle coatings prior to the epoxy layer's deposition for the nanoparticle fixation. This suggests that hydrophilic epoxy eliminates the superhydrophobic effect, retaining, however, a high degree of hydrophobicity that is a consequence of the combination of surface roughness and the originally superhydrophobic nature of the FAS-TiO_2 and FAS-SiO_2 nanoparticles. There is also a noticeable difference in the static water contact angles between the FAS-TiO_2/epoxy and the FAS-SiO_2/epoxy coatings, the FAS-SiO_2/epoxy coatings being more hydrophobic due to the more pronounced micro- to nanoparticle-textured surface with a refined roughness structure. The corrosion evaluation showed the significantly enhanced corrosion resistance of the AISI 316L stainless steel with the addition of nanoparticles to the epoxy coating compared to the pure epoxy coating, especially in the case of the FAS-TiO_2/epoxy coating. The uniform distribution of the FAS-TiO_2 nanoparticles within the coating plays a crucial role in the superior protective properties of the coating.

Acknowledgements

This work was carried out within the framework of the Slovenian research project J2-7196: Antibakterijske nanostrukturirane zaščitne plasti za biološke aplikacije, financed by the Slovenian Research Agency (ARRS).

5 REFERENCES

[1] B. Xue, L. Gao, Y. Hou, Z. Liu, L. Jiang, Temperature Controlled Water/Oil Wettability of a Surface Fabricated by a Block Copolymer: Application as a Dual Water/Oil On–Off Switch, Adv. Mater., 25 (**2013**), 278–283, doi:10.1002/adma.201202799

[2] Y. Tian, B. Su, L. Jiang, Interfaces: Interfacial Material System Exhibiting Superwettability, Adv. Mater., 26 (**2014**), 6872, doi:10.1002/adma.201470276

[3] M. A. M. Ibrahim, S. S. A. El Rehim, M. M. Hamza, Corrosion behavior of some austenitic stainless steels in chloride environments, Mat. Chem. Phys., 115 (**2009**), 80–85, doi:10.1016/j.matchemphys.2008.11.016

[4] T. Hryniewicz, R. Rokicki, K. Rokosz, Corrosion characteristics of medical-grade AISI Type 316L stainless steel surface after electropolishing in a magnetic field, Corrosion 64, (**2008**), 660–665, doi:10.5006/1.3279927

[5] B. Wetzel, F. Haupert, M. Q. Zhang, Epoxy nanocomposites with high mechanical and tribological performance, Comp. Sci. Technol. 63, (**2003**), 2055–2067, doi:10.1016/s0266-3538(03)00115-5

[6] Y. Qing, Facile fabrication of superhydrophobic surfaces with corrosion resistance by nanocomposite coating of TiO_2 and polydimethylsiloxane. Colloids and Surfaces a-Physicochemical and Engineering Aspects, 484 (**2015**), 471–477, doi:10.1016/j.colsurfa.2015.08.024

[7] R. N. Wenzel, Resistance of solid surfaces to wetting by water, Ind. Eng. Chem., 28 (**1936**), 988–944, doi: 10.1021/ie50320a024

[8] C. S. Baxter, Wettability of porous surfaces, Trans. Faraday Soc., 40 (**1944**), 546–551

[9] M. Conradi, A. Kocijan, Fine-tuning of surface properties of dual-size TiO_2 nanoparticle coatings. Surface & coatings technology, 304 (**2016**), 486–491, doi:10.1016/j.surfcoat.2016.07.059

[10] Y. Qian, Y. Li, S. Jungwirth, N. Seely, Y. Fang, X. Shi, The Application of Anti- Corrosion Coating for Preserving the Value of Equipment Asset in Chloride-Laden Environments: A Review, Int. J. Electrochem. Sci., 10 (**2015**), 10756–10780

MATERIALI IN TEHNOLOGIJE

MATERIALS AND TECHNOLOGY

Letnik / Volume 51 2017

ISSN 1580-2949

IMT Ljubljana, Lepi pot 11, 1000 Ljubljana, Slovenija

MATERIALI IN TEHNOLOGIJE / MATERIALS AND TECHNOLOGY

VSEBINA / CONTENTS
LETNIK / VOLUME 51, 2017/1, 2, 3, 4, 5, 6

2017/1

2017/3

MATERIALI IN TEHNOLOGIJE / MATERIALS AND TECHNOLOGY

AVTORSKO KAZALO / AUTHOR INDEX

LETNIK / VOLUME 51, 2017, 1–6, A–Ž

MATERIALI IN TEHNOLOGIJE / MATERIALS AND TECHNOLOGY

VSEBINSKO KAZALO / SUBJECT INDEX

LETNIK / VOLUME 51, 2017, 1–6

Kovinski materiali – Metallic materials

Anorganski materiali – Inorganic materials

Organski materiali – Organic materials

Polimeri – Polymers

Gradbeni materiali – Materials in Civil Engineering

Nanomateriali in nanotehnologije – Nanomaterials and nanotechnology

Numerične metode – Numerical methods

Predgovor urednika – Editorial preface

50 let revije – 50th anniversary MIT

MEGATEL

poslovna IP telefonija

instrumentalia

Instrumentalia, d.o.o.
Leskoškova cesta 9 E
SI – 1000 Ljubljana
Tel: + 386 1 524 0196
Fax: + 386 1 524 0198
GSM: + 386 51 385 007

TA Instruments

INŠTITUT ZA KOVINSKE MATERIALE IN TEHNOLOGIJE

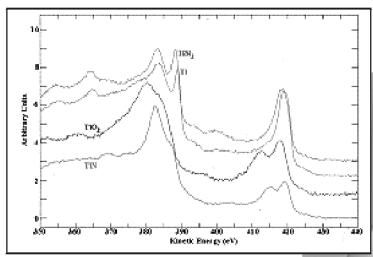

AES spekter štirih različnih kemijskih stanj titana (levo)

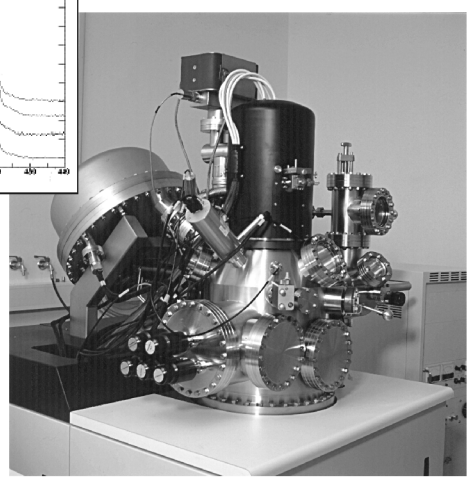

Elektronski spektrometer Microlab 310-F za HRAES, SAM, SEM in XPS analize površin

Elektronski mikroskop Jeol JSM-6500F opremljen z ED, WD in EBSD

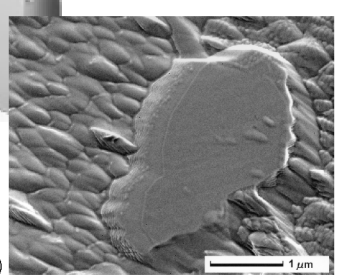

Zrno kromovega karbida (desno)

Naslov:
IMT, Lepi pot 11,
SI-1000 Ljubljana,
Slovenia
Tel.: +386 1 4701 800,
Faks: +386 1 4701 939
http://www.imt.si,
e-pošta: imt@imt.si

Tlačna tehtnica RUSKA 2465A za kalibracije merilnikov tlaka

AKREDITACIJSKA LISTINA
ST. L-030
INŠTITUT ZA KOVINSKE MATERIALE IN TEHNOLOGIJE
Laboratorij za metrologijo tlaka
Lepi pot 11, Ljubljana
SIST EN ISO/IEC 17025
dr. Božan Godec

Akreditacijska listina L-030

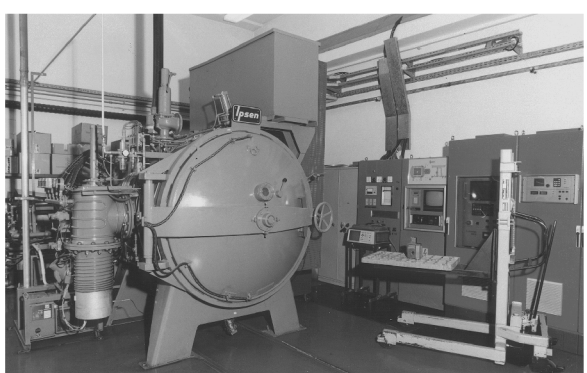

Vakuumska peč VTTC-324R za toplotno obdelavo kovinskih materialov

METAPLAS IONON HZIW 600/1000 peč za nitriranje v pulzirajoči plazmi

impol

aluminijska industrija 1825-2000

IMPOL d.d.
Partizanska 38
2310 Slovenska Bistrica
SLOVENIJA

tel: +386-2-8453 100
fax:+386-2-8181 219

e-mail: info@impol.si
http://www.impol.si

IZDELKI IZ ALUMINIJA: palice in cevi, profili, pločevine, folije

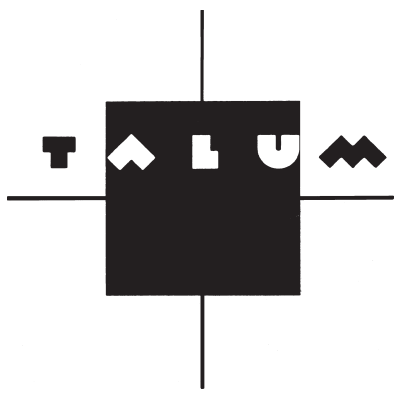

TALUM, d.d., KIDRIČEVO
Tovarniška ulica 10
2325 Kidričevo, Slovenia
Telephone: +386 2 799 51 00
Telefax: +386 2 799 51 03

INSTRUCTIONS FOR AUTHORS

1 SUBMISSION OF MANUSCRIPT

An electronic version (using Microsoft Word or similar) of the manuscript, complete with abstract, keywords, figures and tables must be submitted to the MIT Editorial Office (mit@imt.si) as an e-mail attachment.

All contributions must be written in Slovene or English, following the MIT template.

The manuscript must be accompanied by the MIT checklist, data and cover letter.

Authors must provide the details of two potential reviewers who can make an independent assessment of the quality of the manuscript. The purpose of the reviewing procedure is to have the manuscripts evaluated objectively, and so suggested reviewers with local affiliations and who may be too closely associated with the authors, will be disregarded.

Authors must provide details of two potential referees who are not associated with the specific study, nor with the general research activities of the authors.

After the review process the manuscript will be returned to the author, with the decision of the Editor and, if appropriate, the reviews of the referees. If the paper is accepted the author will be asked to amend the manuscript in accordance with the referees' comments and return it to the MIT Editorial Office.

Authors must state that the results in their manuscript have not been published before, nor are they included in a paper that has been submitted to another journal.

Upon acceptance of an article, the copyright is transferred to the publisher. This transfer will ensure the widest possible dissemination of the article.

1.1 Preparation of the manuscript

The paper must be as short as possible and should not exceed 4-6 printed pages (approx. 20.000 characters). Papers presented at conferences must be restricted to 2-4 printed pages (approx. 10.000 characters).

Title page

Papers must have a concise but informative title, which should not exceed one line. The words from the title must be suitable for indexing and searching.

The title must be followed by the name(s) of the author(s) and by the name and address of the institution(s) where the work was carried out. An e-mail address for the contact author must be supplied.

Abstract

Papers must include an abstract, which should provide an overview of the content and conclusions of the paper and highlight the new information they contain. The abstract must be understandable in isolation and written in the past tense, because it refers to work that was already done.

The length of the abstract should not exceed 250 words.

Keywords

The author must supply 3–4 keywords that describe the content of the article and are suitable for indexing and searching.

1.2 Symbols, equations (units of measurement)

Units of measurement must comply with the Law of Units of Measurement and Measures (Official Gazette of the Republic of Slovenia 2001/26), i.e., international SI units.

Equations must be marked on the right-hand side of the text with numbers in round brackets.

Symbols in text should be written as text, not as equation.

1.3 Tables

Tables must be clearly referred to in the text using Arabic numerals.

Each table must have a title which makes the general meaning understandable without reference to the text.

1.4 Figures

Figures are reduced to a single-column width (7.9 cm) except in special cases (max. printed size ˜16 cm).

The lettering used on a figure should be chosen so that after reduction the height of numbers and capital letters falls within the range (1.2–2.4) mm.

Lines and arrows should also be of sufficient thickness so as to remain clear after the reduction process.

Figures must be saved in any supported format, e.g. JPG, TIFF.

Figures and figures captions must be inserted in the text.

Illustrations can be printed in colour when they are judged by the Editor to be essential to the presentation. Further information concerning colour illustrations and the costs to the author can be obtained from the publisher. Colour figures can be included, but with an additional page charge of €80.

Maximum number of figures and tables in paper is 10, for papers presented at conferences must be restricted to 8.

1.5 References

The references must be collected at the end of the article, and numbered in the order of their appearance in the text.

Each reference must be complete, the use of ibid., idem., et al., etc. is not permitted.

References to unpublished or not readily accessible reports must be avoided.

References must be cited in English.

All references should have a DOI number, if it exists for the given reference.

Authors should avoid self-citing in the references as far as possible.

In the list of references, monographs, articles in journals, journals, contributions to conference proceedings, patent documents, electronic monographs, articles and other electronic documents must be cited in accordance with the following examples:

1. **Monographs**
   H. Ibach, H. Luth, Solid State physics, 2nd ed., Springer, Berlin 1991, 245
2. **Articles in journals**
   T. Mauder, J. Stetina, Improvement of the casting of special steel with a wide solid liquid interface, Mater. Tehnol., 50 (**2015**) 1–2, doi:10.17222/mit.2014.122
3. **Contributions to conference proceedings, symposiums or conferences**
   I. Rak, M. Kocak, V. Gliha, N. Gubeljak: Fracture behaviour of over-matched high strength steel welds containing soft root layers, Proc. of the 2nd Inter. Symp. on Mis-Matching of Interfaces and Welds, Reinsford, 1997, 627–641
4. **Contributions in electronic form/online**
   • Articles: M. P. Wnuk: Principles of fracture mechanics for space applications, http://mit.imt.si/Revija/izvodi/kzt996/wnuk.pdf, 30.01.2000
   • Other: http://www.imt.si/, 15.03.2016
5. **Standards**
   ISO 15787:2001(E) Technical product documentation, Heat treated ferrous part, Presentation and indication ISO Committee, Geneve

SPECIAL NOTICE TO AUTHORS

In the past few years we have received an increasing number of articles that include computer simulations, with 3D colour images as a result. As the journal charges €80 per page for colour printing, some authors have decided to convert their colour images to grey-scale images. We believe that this lessens both the impact and the clarity of the results. Since the Materials and Technology journal consistently strives for better quality presentation and a higher impact factor, we will be rejecting articles of this type.

2 ARTICLE PROOFS

Authors will receive a set of proofs. They are requested to return the proofs with any corrections within two days. In the case of a delay the Editor will postpone publication of the article until the article proof is received.

3 COPYRIGHT

In addition to the paper, authors must also enclose a written statement that the paper is original work and has not been published in this form anywhere else and that it is not under consideration for publication elsewhere.

On publication, copyright will pass to the publisher. The Journal of Materials and Technology must be stated as the source in all later publications.

The Editorial Board of the Journal of Materials and Technology:

- decide whether to accept a paper for publication;
- obtain professional reviewers for papers and decide on any proposals to shorten or extend them;
- obtain correct terminology and edit language.

The e-files of papers will be kept in the archives of the Materials and Technology journal.

4 PUBLICATION FEE

Authors will be asked to pay a publication fee for each article before its publishing in MIT journal. After the article has been accepted for publishing, this fee needs to be paid. The fee is € 300 for regular articles, and € 150 for articles, presented at ICMT annual conference in Portorož. The additional cost for coloured printing for one page is € 80. These fees do include value-added tax (VAT).

ELECTRONIC ACCESS

http://mit.imt.si

ISSN 1580-2949